GLUON POLARIZATION IN THE PROTON: CONSTRAINTS AT LOW X FROM THE MEASUREMENT OF THE DOUBLE LONGITUDINAL SPIN ASYMMETRY FOR FORWARD-RAPIDITY HADRONS WITH THE PHENIX DETECTOR AT RHIC

BY

CAMERON PALMER MCKINNEY

DISSERTATION

Submitted in partial fulfillment of the requirements
for the degree of Doctor of Philosophy in Physics
in the Graduate College of the
University of Illinois at Urbana-Champaign, 2015

Urbana, Illinois

Doctoral Committee:

Professor Naomi Makins, Chair
Professor Matthias Grosse Perdekamp, Director of Research
Professor John Stack
Professor Scott Willenbrock

Abstract

In the 1980s, polarized deep inelastic lepton-nucleon scattering experiments revealed that only about a third of the proton's spin of $\frac{1}{2}\hbar$ is carried by the quarks and antiquarks, leaving physicists with the puzzle of how to account for the remaining spin. As gluons carry roughly 50% of the proton's momentum, it seemed most logical to look to the gluon spin as another significant contributor. However, lepton-nucleon scattering experiments only access the gluon helicity distribution, Δg, through effects on the quark distributions via scaling violations. Constraining Δg through scaling violations requires experiments that together cover a large range of Q^2. Such experiments had been carried out with unpolarized beams, leaving $g(x)$ (the unpolarized gluon distribution) relatively well-known, but the polarized experiments have only thus far provided weak constraints on Δg in a limited momentum fraction range.

With the commissioning in 2000 of the Relativistic Heavy Ion Collider, the first polarized proton-proton (pp) collider, and the first polarized pp running in 2002, the gluon distributions could be accessed directly by studying quark-gluon and gluon-gluon interactions. In 2009, data from measurements of double longitudinal spin asymmetries, A_{LL}, at the STAR and PHENIX experiments through 2006 were included in a QCD global analysis performed by Daniel de Florian, Rodolfo Sassot, Marco Stratmann, and Werner Vogelsang (DSSV), yielding the first direct constraints on the gluon helicity. The DSSV group found that the contribution of the gluon spin to the proton spin was consistent with zero, but the data provided by PHENIX and STAR was all at mid-rapidity, meaning Δg was constrained by data only a range in x from 0.05 to 0.2, leaving out helicity contributions from the huge number of low-x gluons. A more recent analysis by DSSV from 2014 including RHIC data through 2009 for the first time points to significant gluon polarization at intermediate momentum fractions, meaning gluon polarization measurements may be more interesting than anticipated, especially at momentum fractions where no constraints exist as of yet.

A forward detector upgrade in PHENIX, the Muon Piston Calorimeter (MPC), was designed with the purpose of extending the sensitivity to Δg to lower x. Monte Carlo simulations indicate that measurements of hadrons in the MPC's pseudorapidity of range $3.1 < \eta < 3.9$ probe asymmetric collisions between high-x quarks and low-x gluons, with the x of the gluons reaching below

0.01 at a collision energy $\sqrt{s} = 500\,GeV$. We access Δg through measurements of A_{LL} for electromagnetic clusters in the MPC; this thesis details the measurement from the Run 11 (2011) data set at $\sqrt{s} = 500\,GeV$. We find $A_{LL} \approx 0$, but the statistical uncertainties from this measurement mean we likely cannot resolve the small expected asymmetries. However, improved techniques for determining the relative luminosity between bunch crossings with different helicity configurations will allow data from a much larger data set in Run 13 to be most impactful in constraining Δg, whereas previous measurements of A_{LL} have had difficulties limiting the systematic uncertainty from relative luminosity.

In this thesis, we begin by presenting an overview of the physics motivation for this experiment. Then, we discuss the experimental apparatus at RHIC and PHENIX, with a focus on those systems integral to our analysis. The analysis sections of the thesis cover calibration of the Muon Piston Calorimeter, a careful examination of the relative luminosity systematic uncertainty, and the process of obtaining a final physics result.

Acknowledgments

I owe the completion of this thesis in large part to the support and efforts of a great number of people, and I want to specifically mention a fraction of those here. First, I want to extend my appreciation to the PHENIX collaboration as a whole. The dedication and commitment to excellence of the leadership and senior members of PHENIX permeates through to everyone involved with the experiment, and I never encountered anyone who was not glad to share their expertise when I needed help. The conveners of the Spin Physics Working Group, particularly Oleg Eyser, Itaru Nakagawa, Ralf Seidl, Sasha Bazilevsky, and Xiaorong Wang, have facilitated frequent in-depth discussions of challenging analyses while providing valuable insight in their own right.

I have been fortunate enough to work more closely with fantastic mentors and colleagues who continually impress me with their intelligence, work ethic, and willingness to help others. Chief among my mentors is my advisor, Matthias Grosse Perdekamp, whose optimism and enthusiasm can convince anyone he works with that their work is both doable and worth doing. Our frequent discussions at lunch on a wide range of topics outside the realm of physics have also been appreciated and have helped me to understand how the work we can do as physicists and as citizens in general can be impactful. Mickey Chiu, as the head of the MPC group and my unofficial co-advisor, has always made himself available as an invaluable resource and has helped to coordinate the research of countless MPC analyzers, even after assuming the role of Director of Operations in PHENIX.

Furthermore, I have had the pleasure of working with a top-of-the-line group of post-docs and graduate and undergraduate students in our UIUC group. I wish to thank all of them for their support and friendship, specifically Beau Meredith, John Koster, Young Jin Kim, Francesca Giordano, IhnJea Choi, Martin Leitgab, Michael Murray, Scott Wolin, Daniel Jumper, and Pedro Montuenga.

I am additionally grateful to our business managers in the Nuclear Physics Laboratory during my tenure, Penny Sigler and Mike Suchor, who have always run a tight ship and have allowed us physicists to spend our time doing physics.

Moving beyond PHENIX and UIUC, I want to express my sincerest gratitude to my family for their love, support, and confidence. My parents always fostered

in me an appreciation for science, between family trips to parks and museums, libraries and bookstores, and the countryside to watch meteor showers. They, my brothers and sisters-in-law, my in-laws, and my extended family have been my cheering section throughout my studies.

Finally, my wife, Beth, deserves special recognition for being on the front lines. Always with a steady dose of love, cheer, encouragement, and prayers, she has been willing and able to pull me through the toughest challenges in graduate school and is now doing the same with the challenges of parenthood. I am extremely excited to celebrate with her the conclusion of this chapter and the beginning of the next chapter of our lives.

Contents

Chapter 1

Introduction

1.1 A brief history of the proton

The field of nuclear physics can be said to have begun with the gold foil scattering experiment of Hans Geiger, Ernest Marsden, and Ernest Rutherford beginning in 1908. J. J. Thompson, who discovered the electron in 1897, proposed a model of the atom as a number of electrons N with total charge $-Ne$ embedded within a sphere of uniform positive charge $+Ne$[1, 2]. This model predicted that positively-charged alpha particles (i.e. doubly-charged helium ions) would only be deflected by small amounts in interactions with atoms, as electrons were known to be too light to significantly alter the path of the heavier alpha particles, and the diffuse positive charge in the model (especially when considered in tandem with the embedded negative charges) could not create an electric field strong enough to deflect the particles by more than a few hundredths of a degree. However, Geiger and Marsden found that while many of the alpha particles did only experience small deflections, some were deflected by large angles, and 1 in 8000 were deflected by more than 90°[3]. Rutherford's analysis of the results from the experiment indicated that the atom contained a very small nucleus of positive charge that contained nearly all of the mass of the atom[4, 5]. In later experiments, Rutherford found that upon bombarding nitrogen and other light elements with alpha particles, fast particles with one unit of positive charge were emitted; the proton, a building block of all nuclei, had been discovered[6].

The story of the proton (particularly in relation to the topic of my thesis) also features the work of Otto Stern, who helped to show that particles have an intrinsic angular momentum that can be observed via the particle's interaction with magnetic fields[7]. The proton was measured to have an angular momentum along any chosen axis of $\frac{1}{2}\hbar$, the same as for the electron, where $\hbar = \frac{h}{2\pi}$, and h is Planck's constant, integral to the field of quantum mechanics. Intertwined with Planck's constant and quantum mechanics is the quantization of angular momentum; which can only exist in chunks (quanta) of $\frac{1}{2}\hbar$. Another peculiarity of quantum mechanics concerns the statement that the measured angular momentum is always $\frac{1}{2}\hbar$. The total angular momentum of the proton and other spin-$1/2$ particles is in fact $\frac{\sqrt{3}}{2}\hbar$, but one must measure the angular momentum with respect to some axis, and the result of that measurement will always be $\frac{1}{2}\hbar$.

The strength of the interaction of this spinning positive charge with a magnetic field, or the proton's magnetic moment, was thought to be known from calculations by Paul Dirac. However, Stern found that the magnetic moment was larger than predicted by a factor of between two and three. As the calculations by Dirac assumed the particle was pointlike, this large magnetic moment was evidence for a yet-unknown internal structure of the proton.

In the 1960s, the internal structure of the proton was confirmed by experiments at the Stanford Linear Accelerator Center involving the scattering of high-energy electrons off of protons, reminiscent of Rutherford's discovery of the internal structure of atoms through his scattering experiments[8]. In the experiments at SLAC, the proton is probed by a virtual photon exchanged between the electron and the target proton, transferring a certain amount of momentum. In the process, the proton absorbs kinetic energy and can break apart, meaning the scattering is inelastic. The length scale at which the proton is probed depends on the wavelength of the virtual photon and therefore the inverse of the photon's momentum. It was expected that higher-energy, shorter-wavelength photons corresponding to a larger loss of momentum from the electron would "see" a smaller sphere of charge inside the proton, which was thought to have more-or-less evenly distributed charge. As the probability of an interaction occurring between an electron and a proton, referred to as the cross section, depends on how much charge the photon sees, the cross section was expected to fall off steeply as the energy of the virtual photon increased. Instead, what was found was that above a certain energy, the cross section remained roughly constant—the amount of charge seen by a photon was independent of the length scale. This result indicated that there were point-like objects inside the proton, which were eventually shown to correspond to theoretical constructs called quarks (and their antiparticle counterparts, antiquarks) which had been hypothesized as the fundamental building blocks of an ever-increasing collection of known subatomic particles[9, 10, 11].

Experiments involving electron-proton and neutrino-proton scattering yielded more information about quarks: quarks were found to be spin-$1/2$ particles[1]; quarks have fractional charges of $+2/3e$ or $-1/3e$ with the antiquarks carrying the same magnitude of charge but with opposite sign; there are six flavors[2] of quarks and six corresponding antiquarks; there are three valence quarks in the proton that determine the proton's quantum numbers; there exists in addition to the valence quarks a sea of quark-antiquark pairs with smaller fractions of the proton momentum; and in total, the quarks and antiquarks carry around 50% of the total momentum of the proton.

[1] In particle physics, it is customary to work with a system of units where $\hbar = 1$, so particles with spin of $\frac{1}{2}\hbar$ are called spin-$1/2$ particles. We follow this convention except when the $\hbar$ is needed for clarity.

[2] The flavors of quark are called up, down, strange, charm, top, and bottom. Of these, only the up quark and antiquark (u,$\bar{u}$), the down quark and antiquark (d,$\bar{d}$), and the strange quark and antiquark (s, $\bar{s}$) are found in the proton as the masses of the other quarks are greater than the proton mass.

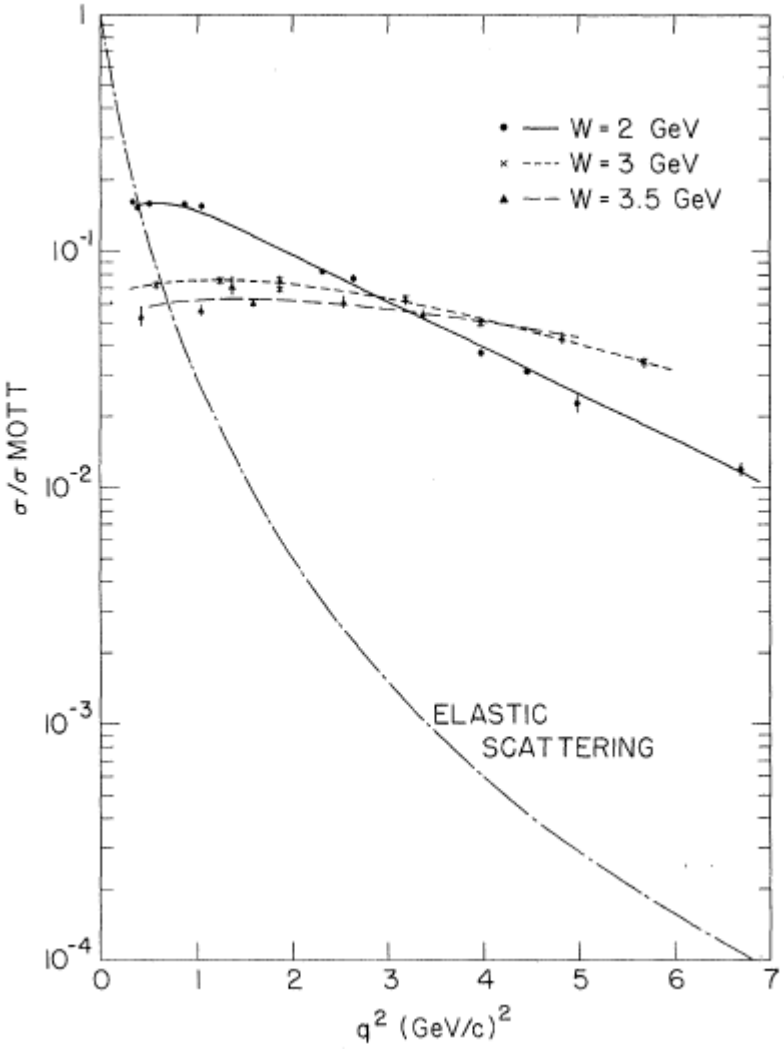

Figure 1.1: Cross sections for inelastic electron-proton scattering from SLAC/MIT experiments[8]. The cross sections are normalized by the Mott scattering cross section, which describes the scattering of spin-1/2 particles off of a heavy target, and are compared to expectations from elastic scattering.

The remaining 50% of the momentum of the proton comes from a massless particle called the *gluon*[12]. The concept of the gluon was developed alongside the quark models for subatomic structure; the gluon receives its name from the fact that it carries the *strong force* that binds quarks together in the proton. The nature of the interaction between quarks and gluons is central to this thesis and will be discussed in more detail in the next section. For now, we will simply state that the existence of the gluon was experimentally confirmed by detecting the experimental signature of a gluon being emitted by a quark produced via e^+e^- annihilation, and the gluons were found to be spin-1 particles like photons (which mediate the electromagnetic force) but in contrast to quarks.

1.2 The proton spin puzzle

We have arrived at a description of the proton, a composite spin-$1/2$ particle comprised of irreducible spin-$1/2$ quarks and antiquarks as well as spin-1 gluons, known collectively as partons. The momentum contributions of these constituents was known from electron, muon, and neutrino scattering experiments, but these experiments involved unpolarized beams and targets and could therefore not yield information about the alignment of the spins of the constituent particles. Polarized beams and targets were being developed alongside the unpolarized scattering experiments though, meaning the spin of the proton could be studied in detail. It would be natural to assume that the proton's spin of $1/2$ arises from the three valence quarks, with one of the spins oriented antiparallel to the other two. Experimenters from multiple collaborations all found however that the quarks inside the proton in total only carry about 25% of the proton's spin: the proton spin crisis was born.

1.2.1 The pieces

We can easily identify the possible sources of the proton's spin of $1/2$. The quarks each carry intrinsic spin angular momentum of $1/2$, which is to say if one measures a single quark's spin with respect to the axis of the proton's spin (which we call the z-axis), the result will be $+1/2$ if the quark's spin is parallel to the proton's or $-1/2$ if it is antiparallel. The total contribution of the quark spins is the difference between the numbers of parallel and antiparallel quark spins times $1/2$, which is represented as $\Delta\Sigma$. The quarks can also have orbital angular momentum with respect to the proton's spin axis, ΔL_q, from their motion in the proton. The orbital angular momentum can only be integer multiples of $\hbar$, with the sign of the contribution again depending on the direction of the orbital angular momentum vector compared to the proton's spin axis. Analogously, the gluons can also contribute spin ΔG and orbital angular momentum ΔL_g, both in integer multiples of $\hbar$. Then, representing the spin contributions from quarks as $\Delta\Sigma$ and gluons as ΔG, we write a decomposition of the proton's longitudinal

spin, or the spin of the proton in the direction of its momentum[3]:

$$\frac{1}{2} = \frac{1}{2}\Delta\Sigma + \Delta G + \Delta L_q + \Delta L_g. \tag{1.1}$$

As mentioned above, the total quark contribution is fairly well-known from lepton scattering experiments. The orbital angular momentum distributions are under investigation via the measurement of transverse momentum dependent (TMD) distribution functions. The gluon contribution ΔG is constrained to a small degree in lepton scattering experiments through the interaction of gluons with quarks (the gluons themselves do not interact directly with leptons as the gluons have no electric or weak charge). The best constraints on ΔG currently available are from polarized proton-proton collisions at RHIC. How we learn about ΔG from polarized proton-proton collisions is the topic of the next section, when we introduce some formalism and look at the scattering process in more detail.

1.3 Accessing ΔG in polarized proton-proton collisions

1.3.1 Quantum chromodynamics[4]

The theory of quantum chromodynamics (QCD) describes the strong force, interactions between the quarks and gluons that comprise the proton. QCD derives its name from the color charge carried by quarks or gluons. Quarks can have one of three color charges, antiquarks have one of three corresponding anticolor charges, and gluons carry one of eight color/anticolor combinations. That the gluons carry the color charge differentiates the strong force from the electromagnetic force (where the corresponding force-carrying particle, the photon, is chargeless) in very significant ways. For example, gluons can temporarily fluctuate into a quark-antiquark pair as photons can. This sea quark-antiquark pairs popping into and out of existence tend to arrange themselves in the presence of color charge (say, a quark) to effectively screen the amount of color charge visible outside of the region near the color charge. The result is that the strength of a QCD interaction, represented by the strong interaction coupling constant α_S, depends on the distance scale at which the interaction occurs. As mentioned above, the scale is governed by the four-momentum transfer in the interaction, which is denoted by q. The Lorentz-invariant quantity is the four-momentum squared, which for a virtual particle is negative, so by convention we refer to

[3] This decomposition of the proton spin, proposed by Jaffe and Manohar, emphasizes the individual partonic contributions to the proton spin. For more details regarding proton spin decompositions, see [13].

[4] We present a basic overview here. For textbooks with a more detailed introduction of the topic, as well as some interesting historical backdrop, see [14, 15, 16].

the quantity Q^2:

$$Q^2 \equiv -q^2 \equiv -(four - momentum\, transfer)^2. \tag{1.2}$$

Conceptually, as Q^2 increases, one can peer deeper inside the cloud of quark-antiquark pairs and see more of the unscreened color charge, so α_s would be expected to increase. This description does align with what we see in quantum electrodynamics[5], but in QCD, the gluons themselves carry a color charge and an anticolor charge and arrange themselves in such a way that the effective charge of the bare quark is spread out rather than screened. Recalling the discussion of electron-proton scattering in section 1.1, for a charge spread out over some volume, we expect the strength of an interaction with that charge to decrease with increased Q^2 and shorter length scales. So, in QCD, changes in Q^2 have competing effects on α_S: screening caused by quark-antiquark pairs and antiscreening caused by gluons. Which of the two effects dominates depends on the number of flavors of quark n_f and the number of colors N (which determines the number of gluons):

$$\frac{\partial \alpha_s}{\partial log(Q^2)} = (2n_f - 11N)\frac{\alpha_s^2}{2\pi}. \tag{1.3}$$

Since there are three colors and six flavors of quark, $(2n_f - 11N)$ is negative, and the coupling constant α_s decreases with increasing Q^2 and increases with decreasing Q^2. The behavior of α_s in both of these directions is important. The behavior at large energies and short length-scales gives rise to the property of QCD called *asymptotic freedom*. In this regime, quarks in the proton can be approximated as free quarks, not interacting with other partons. This enables calculations in QCD using perturbation theory (pQCD), wherein simplified calculations with analytic solutions are carried out, while correction terms to the simplified calculations come with factors of α_s and become negligible because of the smallness of α_s. In the low-Q^2 regime, on the other hand, α_s becomes large (~ 1) for length scales on the order of the size of a nucleon. Here, the correction terms from pQCD do not become negligible, so QCD calculations describing interactions at this level are impossible. Furthermore, the strength of the strong interaction actually increases with increasing distance. As a result, as two color charges separate, the potential energy between them grows to the point where it becomes more energetically favorable for additional quark-antiquark pairs to form, with all quarks, antiquarks, and gluons ending up in color-neutral hadrons. There have been no detections of individual quarks, antiquarks, or gluons—they obey a principle of QCD called *confinement*, and the process by which quarks, antiquarks, and gluons all end up as hadrons in the final state is known as *fragmentation*[6].

[5] Quantum electrodynamics is the quantum field theory of the electromagnetic force.

[6] We also refer to the resulting cascade of particles in the direction of the fragmenting parton as a jet.

In scattering experiments, the main quantity of interest is the rate of particle production in the acceptance of the detectors. The rate depends on the specifics of the experiment, such as the number of particles in the beam, the frequency at which particles are incident on either a target or particles in another colliding beam, and the spatial extent of the beam. Therefore, the quantity compared between experiments is an intrinsic probability of particles colliding and interacting in a certain way, and this probability is referred to as the cross section, σ. The cross section is related to the rate of interactions:

$$\sigma = \frac{rate}{\mathcal{L}}, \tag{1.4}$$

where $\mathcal{L}$ is the luminosity, which, for a collider with beams a and b and numbers of particles in the beams N_a and N_b intersecting with a frequency f in a cross-sectional area A, is given by

$$\mathcal{L} = \frac{N_a N_b f}{A}. \tag{1.5}$$

The cross section is generally measured over some period of time, where we talk about an integrated luminosity and a total yield of interactions detected Y, rather than a rate:

$$\int \mathcal{L} dt = \frac{Y}{\sigma}. \tag{1.6}$$

1.3.2 Proton-proton collisions: parton distribution functions, the partonic cross section, and fragmentation functions

The framework of pQCD is suitable for calculating fundamental short-range interactions between partons but not the complex long-range interactions in hadrons where the effective α_s is large. The QCD cross section of a high-energy proton-proton collision where the quarks are considered asymptotically free can be *factorized* into three components which can be analyzed separately and combined into a final result. We schematically present such a collision in Figure 1.2. The first non-calculable portion of the cross section parameterizes the internal structure of the proton in the initial state in terms of *parton distribution functions* (PDFs). These functions describe the number density of a given parton (a d-quark or gluon, for example) with a certain fraction x of the total momentum of the proton, described at a factorization scale[7] μ^2 which is generally set to the squared four-momentum transfer in the interaction Q^2 or the square of the transverse momentum p_T^2 of the final state hadron, as Q^2 is not directly

[7] The dependence of the PDFs on the length scale can be thought of a reshuffling of terms between the hard scattering component of the cross section and the PDF (or the fragmentation function). For example, a gluon radiated before the scattering by one of the interacting quarks could be included in the pQCD calculation of the hard scattering cross section. Alternatively, the scale can be chosen such that the correction enters as a modification of the PDF of the parton instead.

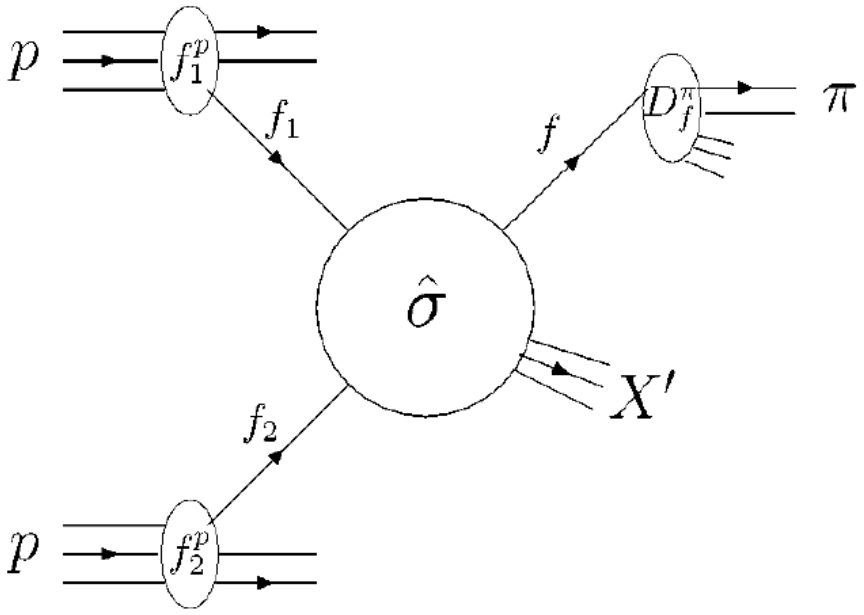

Figure 1.2: Schematic representation of an inelastic proton-proton scattering event[17]. A parton from each of the colliding protons (represented by three lines representing the three valence quarks) participates in the fundamental hard scattering interaction, which is calculable in pQCD. Emerging from the interaction are two partons that fragment into colorless particles. A hadron (in this figure, a pion denoted by π) from one of the fragmentation processes is detected in the final state.

measured in pp collisions. By this definition, we have the following identities:

$$\begin{aligned} \#\, of\, partons\, of\, flavor\, a &= \int_0^1 f_a(x, Q^2) dx, \\ total\, momentum\, from\, flavor\, a &= \int_0^1 x f_a(x, Q^2) dx, \end{aligned} \tag{1.7}$$

where f_a is the PDF for parton a, often written more simply[8] as $a(x, Q^2)$.

The hard scattering process between the two partons is the piece calculable in pQCD; its value depends on the partons involved and the kinematics of the scattering as well as a renormalization scale (also generally set to Q^2 or p_T^2) that is related to how divergences in the pQCD calculation are handled. The final-state non-calculable portion of the cross section concerns fragmentation, the transition from the quarks and/or gluons leaving the hard scattering process to the color-neutral hadrons. The form of these fragmentation functions resembles the parton distribution functions; they are written $D_{i\to h}(z,\, \mu^2)$ and are interpreted as the probability for a hadron h to be produced from the fragmentation of a parton i, while z is the fraction of the parton's total momentum carried by the hadron. We combine these components to write down the cross section for a proton-proton scattering event $pp \to hX$, where the protons have momenta P_a and P_b and the final-state hadron has momentum p_h, suppressing the theoretical scale dependence for conciseness[18]:

$$\begin{aligned} \sigma^{pp\to hX} = \sum_{a,b,c=u,d,s,g\ldots} \int_0^1 dx_a \int_0^1 dx_b \int_0^1 dz_c [f_a(x_a) f_b(x_b) \\ \times \hat{\sigma}^{ab\to cX}(x_a P_a, x_b P_b, {}^{p_h}/_z) D_{c\to h}(z_c)]. \end{aligned} \tag{1.8}$$

The summation over quark flavors and the gluon represents the combinations of two initial state partons and the final state parton involved in the 2-to-2 scattering process that can contribute to the total cross section. The integrals over x and z cover the entire range of possible momenta that the colliding partons and the fragmented hadron can have. Conceptually, then, we get a "piece" of the cross section from the probability that:

- a parton is found from each of the colliding protons, one with flavor a and momentum fraction x_a and the other with flavor b and momentum fraction x_b. The probability to find such partons are given in by the PDFs f_a and f_b in Equation 1.8;
- the partons a and b undergo elastic scattering, leading to parton c and another parton exiting the hard scattering process. The probability of

[8] For example, a general quark PDF is written $q(x, Q^2)$, the u-quark distribution as $u(x, Q^2)$, and the gluon distribution as $g(x, Q^2)$.

this interaction is given by the parton-level cross section $\hat{\sigma}$;

- and the parton c, a product of the hard scattering interaction, fragments into the hadron h with a probability dependent on the momentum of the hadron: $D_{c\to h}(z_c)$.

1.3.3 Polarized proton-proton collisions

We can generalize Equation 1.8, which makes no reference to the polarization of the protons or the quarks and gluons, to the case of polarized pp collisions. As mentioned in section 1.1, the polarization measured along any axis for a spin-$1/2$ particle is $\pm\frac{1}{2}\hbar$. Consequently, quarks and gluons in the proton can be found with either the same or opposite helicity as the proton. The unpolarized parton distribution functions $f(x, Q^2)$ are a sum of contributions of the aligned $(+)$ and antialigned $(-)$ partons:

$$f(x, Q^2) = f^+(x, Q^2) + f^-(x, Q^2), \tag{1.9}$$

and the difference of the spin-separated PDFs we call the helicity parton distribution functions:

$$\Delta f(x, Q^2) = f^+(x, Q^2) - f^-(x, Q^2). \tag{1.10}$$

The total spin contributed to the proton from a particular flavor of quark or a gluon can be found by taking the product of the parton's spin with the integral of the helicity distribution over all x:

$$\begin{aligned} \Delta\Sigma(Q^2) &= \frac{1}{2}\sum_{a=q,\bar{q}}\int_0^1 \Delta f_a(x, Q^2)dx, \\ \Delta G(x, Q^2) &= \int_0^1 \Delta g(x, Q^2)dx, \end{aligned} \tag{1.11}$$

where $\Delta\Sigma$ is the contribution from all flavors of quarks and antiquarks.

With polarized partons undergoing the hard scattering process, helicity-conservation effects come into play, and $\hat{\sigma}^{ab\to cX}$ has a different value depending on whether the two colliding partons have the same or opposite helicity ($++$ or $+-$ referring to the sign of the helicity of the two partons). Similarly to the helicity PDFs, we have a spin-dependent parton-level cross section:

$$\begin{aligned} \hat{\sigma}^{ab\to cX} &= (\hat{\sigma}^{ab\to cX})^{++} + (\hat{\sigma}^{ab\to cX})^{+-}, \\ \Delta\hat{\sigma}^{ab\to cX} &= (\hat{\sigma}^{ab\to cX})^{++} - (\hat{\sigma}^{ab\to cX})^{+-}. \end{aligned} \tag{1.12}$$

For our purposes, we only consider fragmentation functions from unpolarized quarks, meaning the fragmentation function $D_{c\to h}(z)$ is the same in the unpo-

larized and helicity-dependent cross sections.

With the above definitions in mind, we now can see how the gluon helicity distribution, $\Delta g(x, Q^2)$, is accessed at RHIC. We formulate a cross section asymmetry that is the difference between the cross sections for protons with the same helicity versus the opposite helicity. The expression looks similar in form to the unpolarized cross section of Equation 1.8, but the PDFs and parton-level cross section have been replaced by their helicity-dependent analogues. Measuring a difference in cross sections and normalizing by the unpolarized cross section greatly simplifies the analysis because detector acceptances and efficiencies are assumed to be independent of the spin states of the interacting protons, meaning these effects cancel out in the ratio. The double longitudinal spin asymmetry A_{LL} is defined as

$$A_{LL} = \frac{\sigma^{++} - \sigma^{+-}}{\sigma^{++} + \sigma^{+-}} = \frac{\Delta\sigma}{\sigma}, \tag{1.13}$$

where the helicity superscripts now refer to the helicities of the colliding protons rather than the partons and $\Delta\sigma$ is the cross section with the helicity-dependent parton distribution functions and partonic cross section substituted for their unpolarized counterparts from Equation 1.8:

$$\Delta\sigma^{pp\to hX} = \sum_{a,b,c=u,d,s,g\ldots} \int_0^1 dx_a \int_0^1 dx_b \int_0^1 dz_c [\Delta f_a(x_a)\Delta f_b(x_b) \times \Delta\hat{\sigma}^{ab\to cX}(x_a P_a, x_b P_b, {}^{p_h}/_z) D_{c\to h}(z_c)]. \tag{1.14}$$

The asymmetry A_{LL} is sensitive to $\frac{\Delta q(x)}{q(x)}\frac{\Delta g(x)}{g(x)}$ through quark-gluon scattering processes and $\frac{\Delta g(x)}{g(x)}\frac{\Delta g(x)}{g(x)}$ through gluon-gluon scattering. The partonic cross section asymmetry $\hat{a}_{LL}$ modulates the strength of the overall asymmetry to the helicity PDFs and can be thought of as an analyzing power. The partonic cross section is a function of the center-of-mass scattering angle and the types of partons involved in the scattering. The value of $\hat{a}_{LL}$ for various processes from pQCD calculations is shown in Figure 1.3.

In terms of measuring the asymmetry, we start with Equation 1.13 and consider the $\sigma^{++(+-)}$ terms. We have a relation between cross sections and the particle yield N (e.g. number of pions, electrons, scaler counts), given by

$$\sigma = \frac{N}{L}, \tag{1.15}$$

where the N must be corrected for detector efficiency and acceptance effects:

$$N = \frac{N_{meas}}{\epsilon_{det}\epsilon_{acc}}. \tag{1.16}$$

We assume that the efficiencies are the same for same-sign and opposite-sign helicity crossings, so they factor out and cancel in the ratio in Equation 1.13.

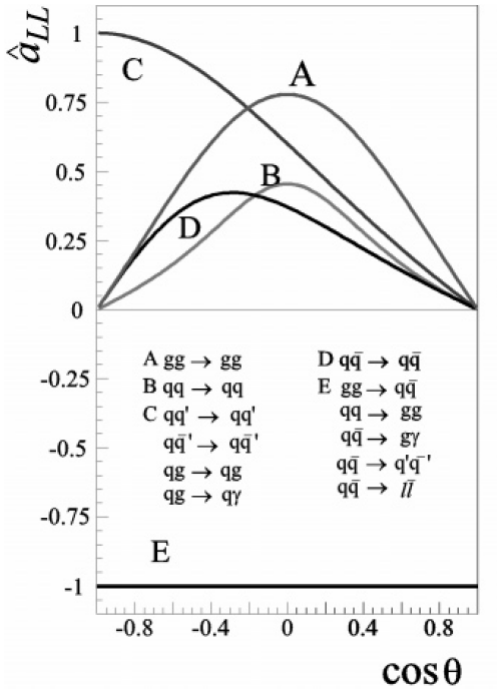

Figure 1.3: The analyzing power $\hat{a}_{LL}$ for scattering processes in pp collisions, taken from [17].

We then have

$$A_{LL} = \frac{1}{|P_b P_y|} \frac{\frac{N^{++}}{L^{++}} - \frac{N^{+-}}{L^{+-}}}{\frac{N^{++}}{L^{++}} + \frac{N^{+-}}{L^{+-}}}, \tag{1.17}$$

where the polarization factors counter the dilution of the asymmetry due to the less-than-perfect polarization of the beams. We usually combine the L^{++} and L^{+-} terms into a ratio $R = \frac{L^{++}}{L^{+-}}$ called the relative luminosity.The uncertainty on the ratio R, quantified by differing results from separate luminosity monitors, is the main systematic error on the asymmetry measurement and is the subject of chapter 4. Substituting R into Equation 1.17, we arrive at the following form of A_{LL} corresponding to what we measure in PHENIX:

$$A_{LL} = \frac{1}{|P_b P_y|} \frac{N^{++} - RN^{+-}}{N^{++} + RN^{+-}}. \tag{1.18}$$

The most abundant hadrons produced in high-energy collisions are the charged and neutral pions, π^+, π^-, and π^0, as they have the smallest mass among hadrons and therefore require the least amount of energy to produce. The π^0's, which are a superposition of a $u\bar{u}$ pair and a $d\bar{d}$ pair, decay via the electromagnetic force nearly instantaneously before they have traveled even tens of nanometers. The most common decay channel is to two photons; for our asymmetry measurement, we measure the yield of π^0's evidenced by the signature of the two resulting high-energy photons in the detector.

1.4 Description of kinematics

In a hard scattering QCD interaction between protons, two partons collinear with the protons with momenta x_1P_1 and x_2P_2 interact through the exchange of a gluon[9] with squared four=momentum $q^2 = -Q^2$. The two partons exiting the hard interaction fragment, and a hadron deposits energy in a detector. We characterize the hadron by its energy, its transverse momentum p_T (transverse to the beam axis) defined as

$$p_T = \sqrt{p_x^2 + p_y^2}, \tag{1.19}$$

and its pseudorapidity η, defined in terms of the angle θ between the hadron and the beam axis as

$$\eta = -ln[tan(\frac{\theta}{2})]. \tag{1.20}$$

The pseudorapidity is 0 for particles scattered at a right angle to the beam axis, while $\eta \to \infty$ along the positive direction of the beam axis and $\eta \to -\infty$ in the backward direction.

1.5 Global QCD analyses

In order to extract information about the helicity PDFs through asymmetry measurements in pp, the other components of the polarized and unpolarized cross sections need to be constrained. The *universality* of the factorized components of cross sections is assumed, meaning those components are independent of the type of experiment in which they arise. In other words, a parton distribution or fragmentation function measured in a lepton scattering experiment will be the same as one found from a proton-proton collision and so on. Different types of experiment are better suited to provide different pieces of information. For instance, electron-positron colliders have simple initial states with no parton distribution functions to worry about, but the e^+e^- annihilation produces quark-antiquark pairs that fragment into hadrons in the final state. Studying the production rates of hadrons with a range of momenta allows for precise determination of fragmentation functions. Also, recall from section 1.1 that lepton-proton scattering experiments have placed strong constraints on the unpolarized PDFs. In general, theorists perform fits to data from many different experiments at different center of mass energies and Q^2 to determine the long-range interactions not calculable in pQCD. This type of analysis is known as a *global analysis.*

[9] In the vast majority of cases, the partons interact via the strong force, exchanging a gluon. In a small fraction of collisions, the partons can exchange a W or Z boson (the force carriers of the weak force) or a photon (the force carrier of the electromagnetic force).

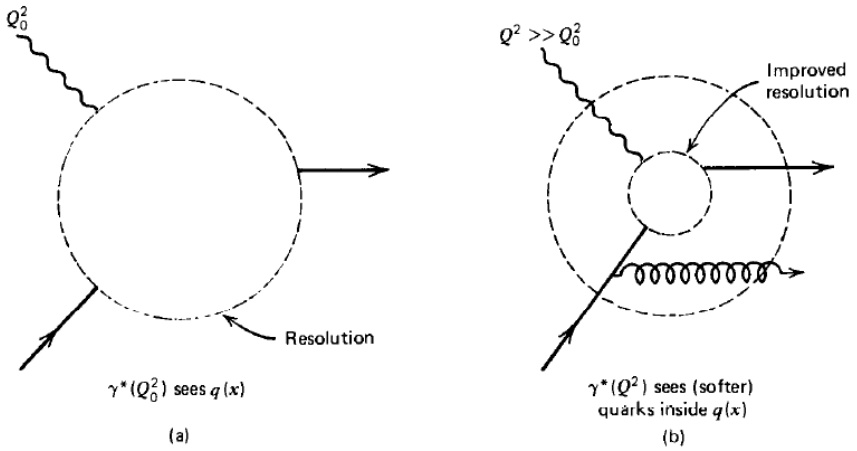

Figure 1.4: Conceptual picture of DGLAP evolution taken from [15]. Moving to a higher-Q^2 probe reveals more details about the radiation and splitting of partons into more partons at lower x.

1.5.1 Q^2 evolution of parton distribution functions and fragmentation functions

Because the parton distribution functions have a dependence on a theoretical scale that is generally set to the Q^2 or p_T^2 at which a measurement takes place, care must be taken when comparing data from multiple experiments. The dependence on Q^2 is related to the splitting of gluons into quark-antiquark pairs; at higher Q^2, more of these processes are resolved, and as a result, the a certain fraction of the proton's momentum is distributed among a larger number of partons which individually have smaller momentum fractions. The result is that the parton distribution functions are shifted to smaller x at higher Q^2. The equations describing the evolution of the PDFs with Q^2 were worked out by Dokshitzer, Gribov, Lipatov, Altarelli, and Parisi[19, 20, 21]. The DGLAP equations have the following form:

$$\frac{d}{d\,log(Q^2)} f_q(x,Q^2) = \frac{\alpha_S}{2\pi}\int_x^1 \frac{dy}{y}(f_q(y,Q^2)P_{qq}(\frac{x}{y}) + g(y,Q^2)P_{qg}(\frac{x}{y}),$$
$$\frac{d}{d\,log(Q^2)} f_g(x,Q^2) = \frac{\alpha_S}{2\pi}\int_x^1 \frac{dy}{y}(g(y,Q^2)P_{gg}(\frac{x}{y}) + \sum_i f_{q_i}(y,Q^2)P_{gq}(\frac{x}{y})), \tag{1.21}$$

where the P are splitting functions that can be interpreted at leading order as the probability for a parton to result from radiative processes from a quark or gluon. An example of how changing Q^2 affects a parton distribution function is given in Figure 1.5.

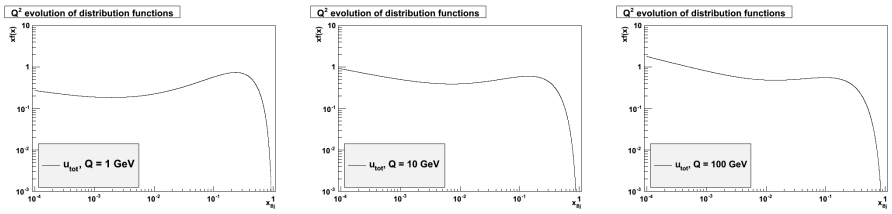

Figure 1.5: The u-quark parton distribution function $f_u(x)$ from the CTEQ6M PDF set at three values of Q shows how the PDF evolves at different scales.

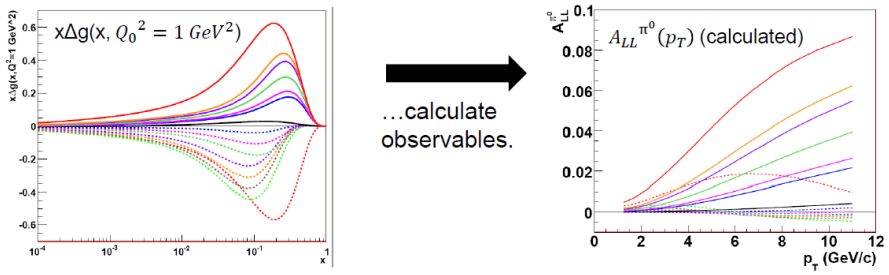

Figure 1.6: An illustration of how a range of input helicity PDFs (from a global analysis by the GRSV group[23]) corresponds to a range of computed observables[24]. Note how the largest gluon helicity shown on the left, the solid red line, corresponds to the largest asymmetry on the right.

1.5.2 Fitting the parton distribution functions to data

To extract information about parton distribution functions from data, theorists first need to calculate observables based on models of the parton distribution functions. A thorough but accessible description of how this is accomplished for the helicity PDFs is presented by the DSSV group[22]. To summarize, as a first step, each of the helicity distributions is parameterize in the following way at an "input scale" of $\mu_0 = 1\,GeV$:

$$x\Delta f_i(x,\mu_0^2) = N_i x^{\alpha_i}(1-x)^{\beta_i}(1+\gamma_i\sqrt{x}+\eta_i x), \tag{1.22}$$

where N_i, α_i, β_i, γ_i, and η_i are parameters of the function. The form of the parameterization is flexible enough to accommodate desired behaviors in the limits of $x \to 1$ and $x \to 0$ as well as sign-changes in the PDFs as x is varied. Assumptions about the form of the PDFs in the low-x and high-x limits place constraints on the parameters as do considerations of flavor symmetries. The PDFs are also constrained by quark counting rules and positivity bounds, which for example limit the number of partons with a certain polarization to be less than or equal to the total number of that parton.

The parameterized PDFs are then evolved from the input scale μ_0 to the scale of a particular experiment μ (see subsection 1.5.1), and an observable is computed. For example, a common observable used for the helicity PDFs is the A_{LL} as in Equation 1.13 and Equation 1.14. The resulting observable

is compared to the actual data points provided by the experiment, and the parameters of Equation 1.22 are varied to minimize the χ^2. Uncertainty bands on the helicity PDFs are mapped out by varying the fit parameters until the χ^2 values reach some distance from the minimum; the DSSV group and other analyzers of global QCD data have found that uncertainty bands that cover $\frac{\Delta\chi^2}{\chi^2} = 2\%$ tend to encompass the "best fit" PDFs resulting from successive iterations of the global analyses.

1.5.3 Current knowledge of parton distribution functions

While DIS experiments have been successful in determining the polarized parton distributions for quarks, they are not as useful in constraining $\Delta g(x, Q^2)$. As mentioned above, the only constraints placed on $\Delta g(x, Q^2)$ from inclusive DIS arise from the DGLAP evolution equations which describe the interdependence of $\Delta q(x, Q^2)$ and $\Delta g(x, Q^2)$ as Q^2 varies. Polarized experiments have covered a fairly limited range of Q^2 though, meaning $\Delta g(x, Q^2)$ is only weakly constrained.

Under the assumption of universality, theorists and experimentalists can attempt to simultaneously fit PDFs or polarized PDFs to cross sections measured at various DIS and proton-proton scattering experiments. The CTEQ (Coordinated Theoretical-Experimental Project on QCD) collaboration has performed such a global fit for unpolarized PDFs, most recently in collaboration with Jefferson Lab in 2013[25], while de Florian, Sassot, Stratmann, and Vogelsang (DSSV) continually work on fits for polarized PDFs[22]. Presently, the unpolarized PDFs and the total $u-$ and d-quark polarized distributions are well-known, whereas the polarized sea-quark PDFs are less well-constrained, and the polarized gluon PDF is weakly constrained, particularly at high and low x (see Fig. 1 and Fig. 2). The PHENIX experiment at RHIC is working towards measurements that will specifically help to constrain the polarized sea-quark and gluon PDFs.

Data from the RHIC experiments STAR and PHENIX provides the strongest constraints on the gluon polarization thus far. While lepton-hadron scattering experiments have provided strong constraints on the quark distribution functions on account of the direct (leading order in pQCD) interactions between leptons and quarks, these experiments are only sensitive to the electrically neutral gluons through DGLAP evolution of the quark distribution functions. Additionally, before 2009, measurements of A_{LL} in PHENIX and RHIC were confined to final states detected in a limited range of scattering angle near $\theta = 90°$. As we will discuss in detail later on, this means that the polarizations of gluons is unconstrained at low momentum fractions, where the total number of gluons is very large compared to the other parton densities. Measuring A_{LL} at kinematics that provide information on the gluon helicity for low-x is the focus of this measurement.

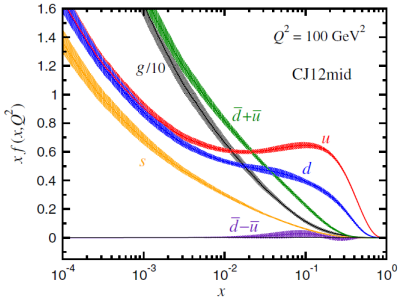

(a) PDFs from CJ12 global fit, from [25]; note the factor of x on the y-axis and the 1/10 factor applied to the gluon distribution.

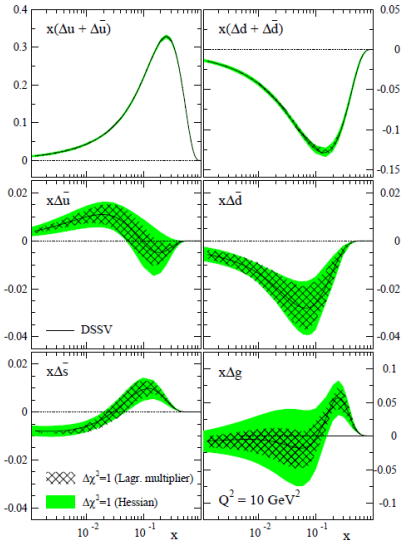

(b) Polarized PDFs from global fit by DSSV from 2009[22]; note the factor of x on the y-axes.

Figure 1.7: Parton distribution functions extracted from global QCD data.

Chapter 2

Experimental overview

2.1 The Relativistic Heavy Ion Collider

PHENIX is located at the Relativistic Heavy Ion Collider (RHIC) at Brookhaven National Laboratory on Long Island, NY[26, 27] . The construction of the collider along with PHENIX and three other experiments, called STAR, BRAHMS, and PHOBOS, was completed in 1999. Of these experiments, the multi-purpose experiments STAR and PHENIX are the two that remain operational; a Drell-Yan experiment called AnDY ran at the BRAHMS interaction point from 2011-2013. The purpose of RHIC was chiefly to collide heavy ions to reach the high energy densities required to observe a predicted phase of matter called the quark-gluon plasma. The existing linear accelerator at BNL had the ability to accelerate polarized protons however, and advances in spin-rotator technology (particularly in collaboration with the RIKEN research institute in Japan) allowed the plans for RHIC to extend to studying the spin structure of the proton as the world's only polarized proton-proton (pp) collider.

Since the first physics running in 2000, RHIC has demonstrated impressive flexibility both in heavy ion and polarized proton running. For the heavy ion programs, RHIC has collided deuterons as well as copper, gold, uranium, and aluminum ions at energies of $3.85\,GeV/nucleon$ to $100\,GeV/nucleon$. To study spin physics, RHIC has collided transversely and longitudinally polarized protons at center-of-mass energies up to $\sqrt{s} = 510\,GeV$ with polarizations above 50%, and this year for the first time, polarized protons have been collided with heavy ions at energies of $100\,GeV/nucleon$[29].

2.1.1 Accelerator chain

We provide a brief summary here of the production, acceleration, storage, and collision of polarized protons at RHIC; a more detailed explanation can be found in [30]. On the order of 10^{12} polarized H^- ions are produced by an optically pumped polarized ion source. The H^- ions are accelerated to an energy of $200\,MeV$ by a linear accelerator and are stripped of their electrons, leaving polarized protons to be injected into the Alternating Gradient Synchrotron (AGS) Booster. The AGS Booster accelerates the protons to $1.5\,GeV$ and delivers them to the larger Alternating Gradient Synchrotron, where the protons reach

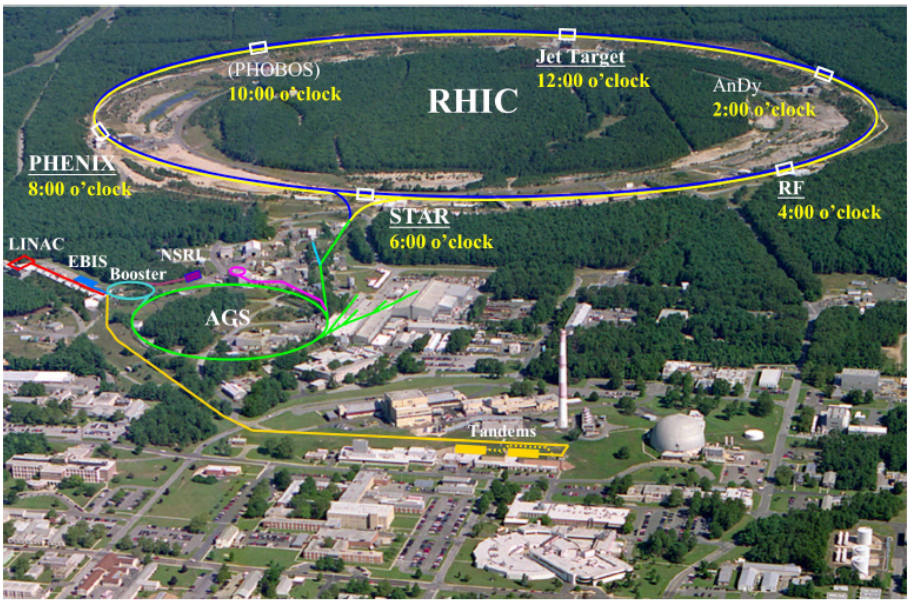

Figure 2.1: An overview of the RHIC/AGS accelerator complex at Brookhaven National Laboratory[28].

energies of $25\,GeV$. Finally, the bunch of protons, having at this point closer to 10^{11} protons, is injected into one of two storage rings in RHIC with a circumference of $3.8\,km$. The two rings store counter-rotating beams, called the blue and yellow beams, which each hold up to 120 bunches of ions separated by $106\,ns$, and all bunches can be filled in about 10 minutes. There are nine consecutive unfilled buckets at the end of the 120 crossings referred to as the abort gap that allows kicker magnets the time to ramp up to deflect the beam into beam dumps when the beams need to be aborted. The luminosity and profile of bunches in the beams are monitored by a system of wall current monitors. These monitors measure voltage from an image current generated on a conducting pipe by the ions in the beam. This current is forced across a resistive gap allowing a voltage to be read out; every five minutes, the voltage is sampled for approximately $12\,\mu s$ at intervals of $0.05\,ns$, giving a picture of the charge in both beams at every point around the ring as the duration of the sampling corresponds to the revolution period of the protons.

The bunches from the two beams are brought into collision via steering magnets and focusing magnets at up to four collision points; the width of the bunches in the longitudinal direction is such that nearly all collisions between protons in the two bunches take place in a range of $\pm 150\,cm$ from the nominal interaction point. Even with 100 billion protons in each of the intersecting bunches, though, collisions between protons are extremely rare. For each crossing of bunches, we see on the order of one inelastic pp collision.

One set of injected bunches in each beam is allowed to remain in the beam for a number of hours (in Run 11 generally not more than six hours) until the

luminosity and polarization deteriorate past the point of usefulness at which point the beams are dumped. The period of running from one store of protons or ions is called a fill. PHENIX further divides the fill into data-taking segments of up to an hour-long called runs (not to be confused with the Run, as in Run 11, which refers to a year of data taking). Restarting the data acquisition system in PHENIX more frequently allows the shift crew to debug the detectors and electronics systems, preventing problems from compromising an entire fill's worth of data.

2.1.2 Spin rotators, spin patterns, and Siberian snakes

Helical dipole magnets are employed at RHIC in order to manipulate the direction of the spin of the polarized protons. This capability is needed for two purposes—to deliver transversely or longitudinally polarized protons to PHENIX and STAR and to maintain a high level of polarization in the proton bunches. The spin rotators are located on either side of the PHENIX and STAR experiments and change the polarization direction of the protons, which circulate with their spins transversely up or down with respect to their momentum direction, to a positive or negative helicity state. For each of the ≈ 107 filled bunches, the blue beam bunch and yellow beam bunch together can have one of four helicity configurations: the blue and yellow bunches can both have either positive or negative helicity, or the blue bunch can have positive helicity and the yellow bunch negative, or vice versa. For analyses of double spin asymmetries, yields from the same-sign (both positive or both negative) and opposite-sign (one positive, one negative) bunches are grouped together. To avoid time- or crossing-dependent effects that cause systematic differences between the helicity configurations, the helicities of the blue and yellow bunches are organized in patterns consisting of repeating groups of 8 crossings that sample each helicity configuration twice. In Run 11, four such spin patterns were used. For two patterns, the pattern of same-sign and opposite-sign crossings, denoted by S and O, is "SOOSOSSO" beginning with the first crossing, labeled crossing 0. One of the two patterns has all helicities multiplied by -1 relative to the other. Similarly, the other two spin patterns are arranged as "OSSOSOOS," again beginning with crossing 0 and having a relative sign difference of -1 in the bunch helicities.

The purpose of the other group of helical dipole magnets in the accelerators, the Siberian snakes, is to counter the effect of depolarization resonances while the protons are being accelerated or stored. The depolarization resonances occur due to disturbances to the proton's spin from focusing magnets or imperfections in the magnetic fields that maintain the proton's vertical polarization. The disturbances are amplified when they occur at the same frequency as the precession of the proton's spin. The Siberian snakes in RHIC flip the spin of the protons by 180° twice for each orbit in RHIC, with the result that the effect of

destabilizing magnetic fields on the protons' spins cancel out during the course of a complete orbit. The AGS also uses partial Siberian snakes to avoid the depolarizing resonances.

2.1.3 RHIC Polarimetry

The polarization of the beams in RHIC is measured at the 12 o'clock position in the ring by two subsystems, the proton-carbon (pC) and the hydrogen jet (H-jet) polarimeters. Both measure left-right asymmetries in the elastic scattering of the polarized protons in the beam off of a target. The protons in the H-jet target are polarized, allowing an absolute polarization of the beam to be determined, but the rate of interactions between the beam protons and the dilute gas jet is small resulting in large statistical uncertainties. The pC polarimetry measurement is complementary in the sense that it measures a very high rate of interactions, allowing for quick measurements that can determine the change in beam polarization over time. However, the carbon target is unpolarized, and the polarization measurements from the pC system need to be calibrated with the results from the H-jet polarimeter.

Additionally, there are detectors along the beam pipe at experiments at RHIC known as Zero Degree Calorimeters that monitor the luminosity of the beams by detecting neutrons from diffractive interactions between protons. In PHENIX, an array of scintillator strips called the Shower Maximum Detector determines the position of the neutrons with the resolution needed to measure a left-right asymmetry. By analyzing this asymmetry, a local polarization measurement can be done that confirms that the colliding protons are successfully rotated to longitudinal polarization for collisions in PHENIX during longitudinal pp running.

2.2 The PHENIX detector

The array of detectors that comprise the PHENIX experiment are located at 8 o'clock on the RHIC ring[31]. PHENIX consists of groups of detectors covering sections around the collision point and serving various purposes:

- The central arm is comprised of two spectrometers that each cover $|\eta| < 0.35$ and 90° in ϕ. The central arm provides tracking and calorimetry.
- The muon arm covers $1.2 < |\eta| < 2.4$ and is used for identifying, tracking, and triggering on high-p_T muons.
- The Muon Piston Calorimeter (MPC) sits in a hole around the beam pipe in the muon arms. It covers $3.1 < |\eta| < 3.9$ and 2π azimuthally and was designed to study nucleon structure at low momentum fraction x.
- There are also detectors used for event characterization; the Beam-Beam Counter (BBC), a pair of detectors encircling the beam pipe at $\pm 144\,cm$

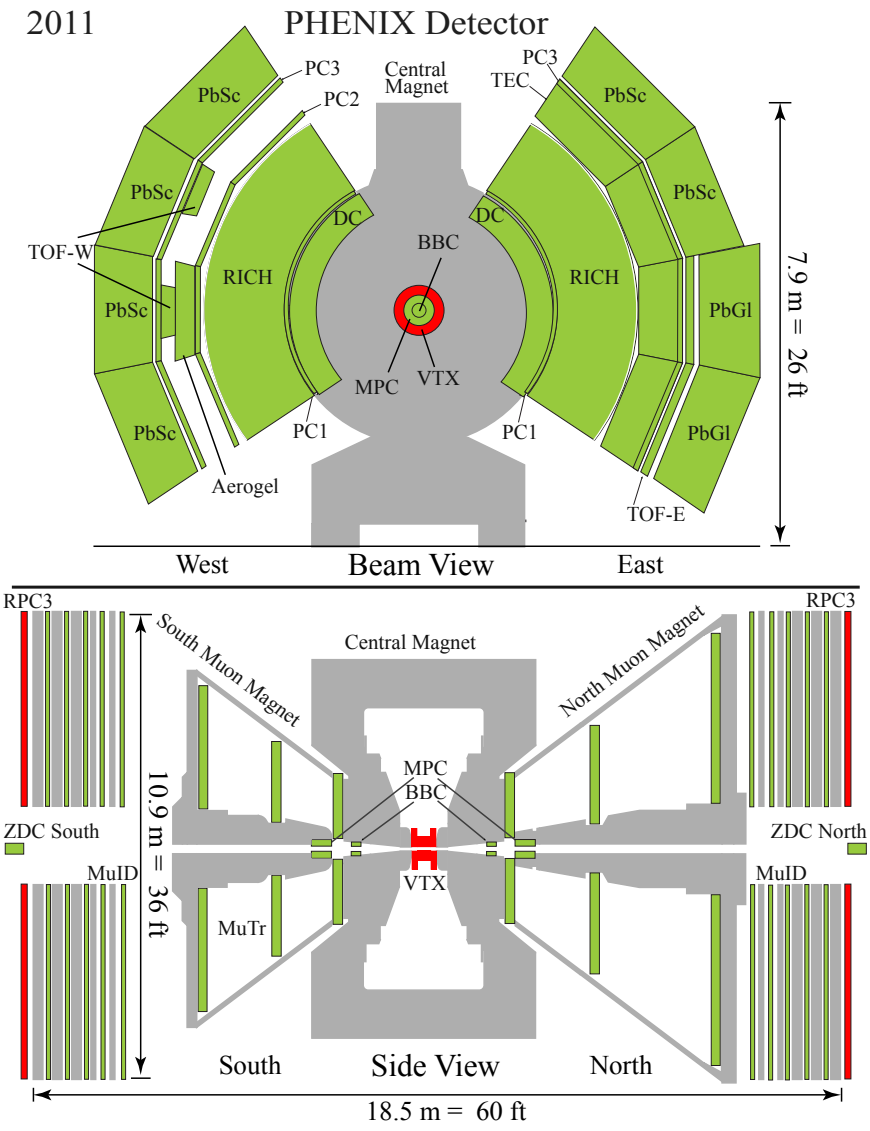

Figure 2.2: View of the PHENIX detector systems for Run 11 (2011).

which PHENIX uses as a minimum bias trigger for inelastic pp collisions, and the Zero Degree Calorimeter, which sits on the beam axis at $\pm 18\,m$ and monitors the luminosity by detecting neutrons from diffractive pp interactions.

For the purposes of our measurement, we only include data collected by the MPC, BBC, and ZDC; we briefly introduce the BBC and the ZDC here, while the MPC will be covered in more detail below.

Coordinates We will also refer to coordinates with respect to PHENIX in this thesis. For reference, the x-axis and y-axis are perpendicular to the beam, with the x-axis being horizontal and the y-axis vertical. The z-axis is along the beam, with $z = 0\,cm$ being the center of PHENIX. We refer to the polar angle, or the angle between a vector and the beam axis, as θ, while the azimuthal angle around the beam axis is referred to as ϕ.

2.2.1 The Beam-Beam Counter

The Beam-Beam Counter (BBC) is comprised of two cylindrical Cherenkov detectors, one located at $z = +144\,cm$ along the beam axis and the other at $-144\,cm$ (referred to as the BBCN and BBCS respectively, for north and south)[32]. The counters each have 64 elements, consisting of a quartz radiator with a thickness of $3\,cm$ mounted on a photomultiplier tube, arranged from $r = 10\,cm$ from the center of the beam pipe to $r = 30\,cm$. The photomultiplier tubes are read out to give charge and timing information with a timing resolution of about $50\,ps$. This information is used in the PHENIX trigger system to determine whether data from a particular crossing should be written to disk. Additionally, collisions resulting in at least one hit photomultiplier tube in the BBCS and the BBCN can use the high-precision timing information to reconstruct the collision vertex with a precision of a few centimeters via the relation

$$z_{vtx} = \frac{t_S - t_N}{2} \times c,$$

based on the time required for a particle moving at the speed of light to travel the differing distances to the south and north detectors. The requirement that at least one tube in each of the counters is hit also serves as the minimum bias trigger (sometimes with an additional restriction on z_{vtx}) and as a method for counting inelastic pp collisions.

2.2.2 The Zero Degree Calorimeter

The Zero Degree Calorimeters (ZDC) are hadron calorimeters located $18\,m$ from the center of PHENIX between the blue and yellow beam pipes just after they split[33]. Their location along the collision axis of the beams and far from the collision point means they cover a very high pseudorapidity of $|\eta| > 6$. The

calorimeters are designed to detect low p_T neutral particles emerging from pp interactions, and coincidences between the north and south arms are used as a luminosity monitor similar to the BBC, but with poorer timing (and therefore z_{vtx}) resolution. In between the first two layers of the calorimeters is the Shower Maximum Detector, which as mentioned in subsection 2.1.3 allows sufficient position resolution to measure an asymmetry in the neutron yields as an indicator of the beam polarizations.

2.2.3 Data acquisition (DAQ) system

The data acquisition system at PHENIX[34] has to be able to write a large volume of data, quickly sift through an even larger amount of data, and combine information from all of the detector components in PHENIX in order to function properly. Each detector system has a front-end electronics module (FEM) that digitizes the raw analog signals from the detector and temporarily stores the data in a buffer to wait for a trigger decision indicating whether the data should be written out. The FEMs also send the data needed to determine whether or not an event is "interesting" to a system called the Local Level-1 (LL1), which processes the data and passes along an "accept" signal (a trigger) if programmable conditions are met. The Global Level-1 (GL1) system looks at the output from the various LL1 systems and makes a decision about whether or not data from a crossing should be recorded. In the event that the GL1's conditions are met and the DAQ is not in a busy state, it signals the FEMs via each system's Granule Timing Module (which also ensures that the various detectors are synchronized by passing along a beam clock timing signal). At this point, the FEMs send their data to a Data Collection Module (DCM) which feeds into a Sub-Event Buffer and finally an Assembly Trigger Processor. These last two systems handle the combining of data from the various subsystems into "events," any higher-level trigger decisions needed, and the sending of the complete events' data to hard disks.

From the prospective of a data analyzer in PHENIX, the final product is a set of Data Summary Tables, or DSTs, that are the result of production software running over raw data files. The DST files contain all of the data relevant for an analysis for a particular detector subsystem and class of event in a human-understandable format. For example, such a file for the MPC contains (among other things) the location and energies for hits in the detector from events meeting a specified trigger condition. The majority of the analysis is performed using a framework of C++ libraries called ROOT[35]. ROOT provides various data structures that are generally useful to particle physics analysis; in particular, data can be organized in a tree structure that tracks the link between all data common to a certain event. This allows analysis code to be written to comprehensively process a single event while ROOT and a PHENIX-specific interface to the DSTs called Fun4All handle the running of each event through the analysis

code.

2.2.4 Scaler boards

The DAQ system includes additional components called scaler boards, which count the number of triggers that occur over the course of the run. The scaler boards preserve information that would normally be lost due to limits on the speed of writing data to disk. Certain triggers fire at a rate at which writing out data for each incidence would be impossible. Therefore, only a small, randomly-sampled fraction of events selected by these triggers can be fully written out. The scaler boards at least allow us to track how often the trigger conditions in the detector systems were met.

There are three sets of scaler boards in PHENIX that we use in this analysis: the GL1 scalers, the GL1p scalers, and the STAR scalers[36]. The GL1p and STAR scalers each count triggers on a crossing-by-crossing basis, allowing for the relative luminosity between bunches of different helicity configurations to be determined. The GL1p board can scale four trigger inputs. In Run 11, these were the BBCLL1(>0 tubes) trigger, which requires a hit in the BBCS and the BBCN as well as $|z_{vtx}| < 30\,cm$; the *BBCnarrow* trigger, which again requires a coincidence between the BBCS and BBCN but has a stricter vertex cut of $|z_{vtx}| < 15\,cm$; the *ZDCwide* trigger, which requires a coincidence between the north and south arms of the ZDC and $|z_{vtx}| < 150\,cm$; and the *ZDCnarrow* trigger, which requires a ZDC coincidence and $|z_{vtx}| < 30\,cm$. The STAR scalers include these four triggers as well as a *BBCwide* trigger with no vertex cut and a clock trigger which counts the number of bunch crossings during a run. The STAR scalers also store information on whether the DAQ was available to write data for particular crossings, allowing us to distinguish between "raw" (all crossings) and "live" crossings. The GL1 boards scale the total number of triggers integrated over all crossings. We use the GL1 as a cross-check to the results we see from the GL1p and the STAR scalers. The scaler boards play a central role in the relative luminosity analysis discussed in detail in chapter 4.

2.3 The Muon Piston Calorimeter

The Muon Piston Calorimeter (MPC) is a forward calorimeter upgrade to PHENIX designed, constructed, and installed between 2005 and 2008[37]. University of Illinois scientists[1] led the proposal, development, and construction of the detector, which had the scientific goals of measuring transverse single spin asymmetries, measuring the double longitudinal spin asymmetry at low-x, and looking for signs of low-x gluons reaching a saturation point (i.e. the Color Glass Condensate) in heavy ion collisions[38].

[1] Professor Matthias Grosse Perdekamp, post-doctoral researcher Mickey Chiu, and graduate students John Koster and Beau Meredith.

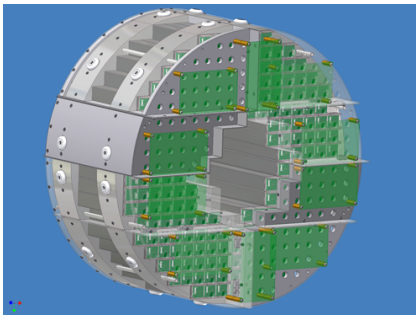

(a) CAD drawing of one arm of the Muon Piston Calorimeter.

(b) One arm of the MPC in its position around the beam pipe in the muon piston.

Figure 2.3: The Muon Piston Calorimeter

There were very limited options for placement of the MPC in PHENIX, and the design of the detector reflects those limitations. The detectors are restricted in size because they sit in a hole between the muon arm magnet yoke and the beam pipe; the hole has an a diameter of $45\,cm$, while beam pipe-related structures provide an inner diameter minimum of 6.5 inches in the south arm and 4.62 inches in the north arm. These considerations most obviously constrain the geometric acceptance of the MPC, but they also impact the choice of the crystal used for the calorimetry. As we will discuss below, photons and electrons incident on the calorimeter initiate showers of particles with a lateral extent that depends on the material used in the calorimeter. In order to best be able to resolve multiple hits[2] in such a small space, we need to use crystals that limit the lateral development of showers as much as possible. The measure of this property for calorimeter materials is the Molière radius, and lead tungstate ($PbWO_4$) crystals were ultimately chosen for their small Molière radius, which is of roughly the same size as the transverse size of the crystals. The dimensions of the crystals are $2.2 \times 2.2 \times 18\,cm^3$, where the first two dimensions are transverse to the beam direction and the third is in the direction of the beam, and the MPCS contains 196 such crystals while the MPCN has 220.

The scintillation light generated by showers in the crystals needs to be quickly converted into an amplified charge that can be read out. Considerations both of limited space in the z direction and strong magnetic fields due to the muon arm magnets lead to the choice of avalanche photodiodes (APDs) to measure the light output from the crystals. The APDs convert light to electron-hole pairs via the photoelectric effect. The electrons are accelerated by a strong electric field in the APD generated by a high reverse bias voltage, creating an avalanche of electrons through ionization. The APDs are attached to the end of the crystals facing the collision point and are soldered to preamplifiers.

Groups of APDs are serviced by one of ten driver boards in each arm of the MPC. The driver boards both supply the high voltage to the APDs and receive and transmit the output from the preamplifiers attached to the APDs. The

[2] A "hit" is a general term for a measured particle incident on a detector.

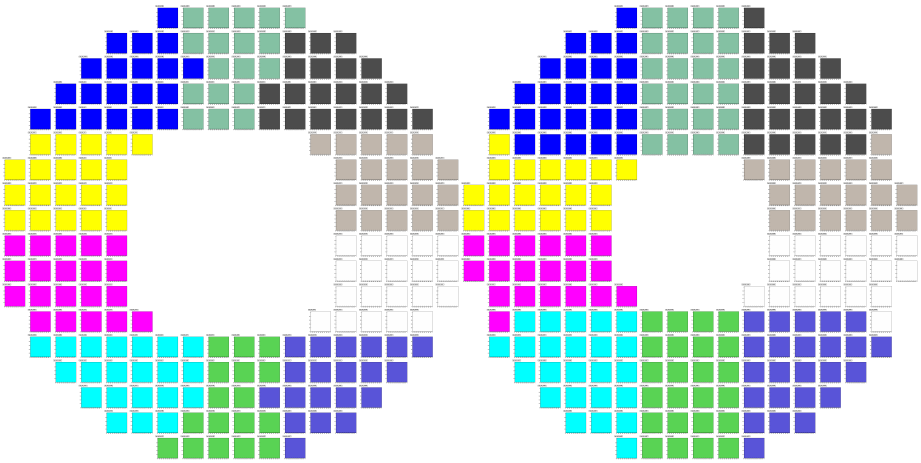

Figure 2.4: Diagrams of tower locations in the MPCS (left) and MPCN (right). The groups of same-colored towers are connected to the same driver board, with ten boards for the south arm and ten for the north arm.

signals from the preamplifiers are again amplified by the driver boards and sent to receiver boards, which converts the signal into a form that can be handled by spare FEMs from the PHENIX central arm Electromagnetic Calorimeter (EMCal).

2.3.1 Calorimetry overview

As mentioned above, the $PbWO_4$ crystals are particularly suitable for use in the MPC. Here, we describe the basics of calorimetry for particle physics to explain the usefulness of our choice of crystal. For a more detailed description, refer to the review article we summarize here (from which we take the equations below)[39] or a book that covers a broader range of techniques and detectors for particle physics and the interaction of high-energy particles with matter in general[40]. High-energy electrons or photons incident on the $PbWO_4$ crystals deposit their energy mainly through a cyclical process of the pair production of electrons and positrons by high-energy photons and the subsequent emission of photons by the electrons and positrons through bremsstrahlung radiation. These processes create a shower of particles with the average energy of the particles decreasing as the shower progresses (as the energy from the initial particle is spread between larger and larger numbers of particles). Finally, the cascading photons and electrons have sufficiently small energy for energy loss via exciting or ionizing atoms in the $PbWO_4$ to become significant. As the affected atoms de-excite or recombine with electrons, scintillation light is emitted and transmitted through the crystal to the APD where it is converted to an electrical signal to be read out.

The electromagnetic showering process is quantified by parameters that depend on the properties of the $PbWO_4$ crystals. The length in a material over

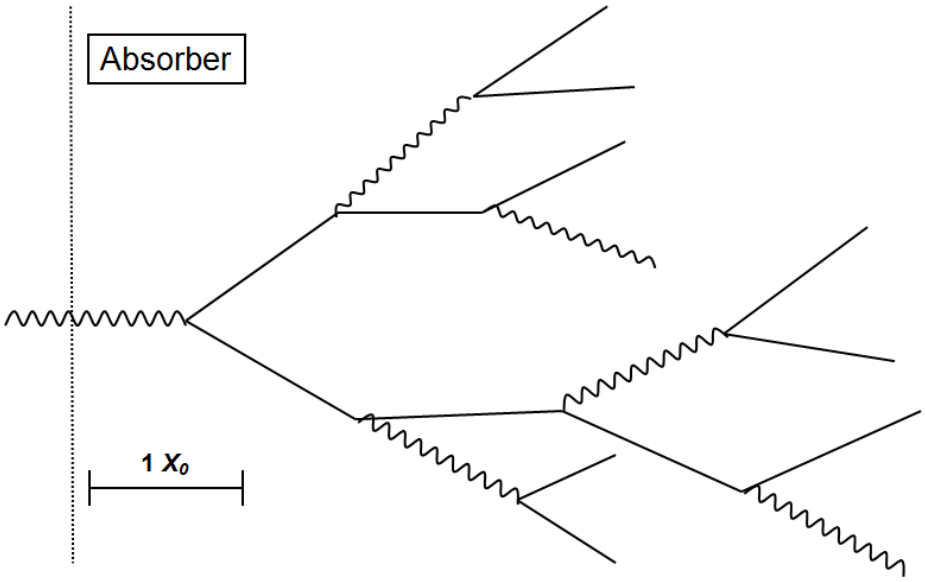

Figure 2.5: A simplified sketch of the electromagnetic showering process for a photon incident on the $PbWO_4$ absorber/scintillator crystals. The photon (wavy line) creates an electron-positron pair (solid lines), which in turn radiate photons through bremsstrahlung radiation, creating a cascade.

which an electron loses all but $1/e$ of its energy to radiation is called the radiation length, X_0. Quantitatively, the energy of the loss by electrons in material is given by the relation

$$-\frac{dE}{dX} = \frac{E}{X_0}. \tag{2.1}$$

The radiation length is also on the order of the mean distance a photon will travel in the crystal before producing an e^+e^- pair; a photon beam with initial intensity I loses intensity to pair production at a rate given by

$$-\frac{dI}{dX} = \frac{X}{\frac{7}{9}X_0}. \tag{2.2}$$

Therefore, the number of radiation lengths spanned by a physical crystal determines how much of an incident particle's energy will be lost to the crystal. Lead tungstate was chosen as the material for the MPC crystals partly due to its short radiation length of only $0.89\,cm$, meaning the $18\,cm$-long crystals span 20 radiation lengths. The length of the crystals is such that a $1\,GeV$ photon incident on the crystal will deposit about 95% of its energy. The shower also spreads transversely due to multiple scattering with a characteristic radius also related to the radiation length. The Moliére radius corresponds to the radius of a cylinder that contains on average 90% of the energy deposited by the shower and is approximated by

$$R_M(g/cm^2) = 21\,MeV\frac{X_0}{\epsilon(MeV)}, \tag{2.3}$$

where $\epsilon \approx 9\,MeV$ (for $PbWO_4$) is the "critical energy" at which energy loss from ionization equals the energy loss from radiation.

2.3.2 LED monitoring system

The MPC is also outfitted with an LED light distribution system used for monitoring changes in the detector response due to aging and temperature effects[41]. There are six hollow Teflon boxes called homogenizers mounted to the MPCs. The boxes each contain two blue LEDs and a red LED, a bundle of optical fibers for delivering light from the box to individual crystals, and a PIN diode that measures the light output from the LED for normalization purposes. A signal synchronized to a laser triggering system in PHENIX is sent to the boxes at regular intervals to fire the LEDs. The response of each crystal is measured and compared to the reading from the PIN diode, and we track the variation in the results throughout Run 11. We use this data to correct for time-dependent changes in the effective gain of the detector as we will describe in section 5.2.

2.3.3 Readout

The FEMs[3] store information about the signals generated in the MPC in Analog Memory Units (AMUs) while they wait for a trigger decision from the GL1 (see subsection 2.2.3). The signal from each tower is sampled once every beam crossing, and information from 64 crossings can be stored at once. The information stored includes a sample of the voltage waveform, a sample of an amplified waveform for better sensitivity to low-energy deposits in the MPC, and a timing measurement. The FEMs also form sums of charge collected from 2x2 and 4x4 groups of towers to use in generating the trigger output for the MPC. If the GL1 sends the accept signal to the GTM for the MPC, the FEMs digitize the analog information in the AMUs for readout. At this point, the stored samples from the two waveforms are digitized into a low-gain ADC value and a high-gain ADC value (the latter corresponding to the sample from the amplified waveform) and a TDC value which are sent to the DCM. The ADC values from the 4th crossing before the current one are also read out; these are subtracted from the ADC readings from the current crossing to account for the possibility that residual charge from a previous hit in the detector could not have yet dissipated, meaning the waveform from the current crossing is sitting atop a "pedestal" that inflates the measurement of the charge from the current crossing. Another pedestal resulting from electronics noise is common to all ADC measurements in the MPC and is therefore subtracted off as well.

[3] The MPC uses FEMs identical to those used by the central arm electromagnetic calorimeter, the EMCal[42].

2.3.4 Triggers

The MPC FEMs are also responsible for sending trigger information used by PHENIX in determining which events to be recorded. The FEMs compare energy sums within 4x4 groups of towers to three separate thresholds to make trigger decisions. The triggers are called, from lowest-energy threshold to highest-energy, 4x4c, 4x4a, and 4x4b. Our analysis uses a data set comprised of events that fired the MPC 4x4a and/or the MPC 4x4b trigger as well as those which fire the MPC 4x4c trigger in conjunction with a trigger from the central arm detector suite. The triggering system for the MPC is covered in much greater detail in reference [37].

2.3.5 Clustering

During the data production that converts raw data from the MPC to the MPC DSTs (see subsection 2.2.3), a clustering algorithm is run to associate groups of towers containing energy from a single electromagnetic shower. A detailed description of the process can be found in [43]. Essentially, all contiguous towers reading an energy above a minimum threshold are grouped as a single cluster. The shape of the energy distribution from an electromagnetic shower over the towers in a cluster has a known functional form; information about the shower shape is used to distinguished electromagnetic showers from noise, hadronic showers, or a single tower background that will be discussed further in subsection 6.1.1.

Chapter 3

Motivation for the Forward A_{LL} Measurement

PHENIX and STAR have provided constraints to ΔG through measurements of A_{LL} at mid-rapidity in Runs 3, 5, 6, and 9. However, these measurements access only the gluon spin over a limited range of x "truncated" moment $\Delta G^{[0.05,0.2]} = \int_{0.05}^{0.2} dx \Delta g(x)$, based on the kinematics of collisions that result in high-p_T particles at mid-rapidity[22]. A major objective of the RHIC Spin Program is to extend the kinematic range of x that is accessed, as the truncated moments $\Delta G^{[0,0.05]}$ and $\Delta G^{[0.2,1]}$ are presently unconstrained by experimental data[44]. Here we make the case using PYTHIA simulations that we can access the low-x range where the gluon distributions dominates via measurements with the MPC. Due to the positivity constraint that $|\Delta g(x)| < g(x)$ and the very small gluon density at large x, $\Delta G^{[0.2,1]}$ is expected to be < 0.1 for $Q^2 = 10\, GeV^2$. On the other hand, at low x, the gluon density becomes very high, giving $\Delta g(x < 0.05)$ a large range of possible values. Our simulations indicate that we can probe the gluon helicity down to $x \sim 10^{-3}$ with measurements involving the MPC. Hard scattering interactions detected by the MPC are also shown by pQCD calculations to be mainly quark-gluon interactions.

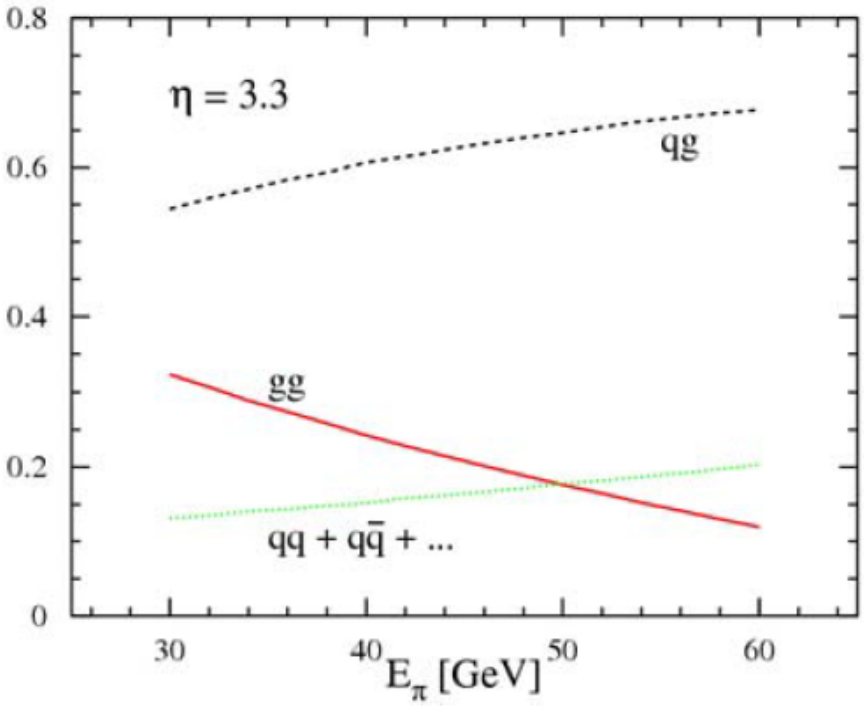

Figure 3.1: Fraction of hard pp interactions resulting from qg, qq, and gg scattering processes at $\eta = 3.3$ over a range of π^0 energies[38].

In this chapter, in addition to examining the accessible range of x, we also show projected $A_{LL}^{\pi^0}$'s for the 2009 models of $\Delta g(x)$ from the DSSV group[22], as well as for hypothetical models of $\Delta g(x)$ that differ from DSSV in the low-x region not currently constrained by data.

3.1 Extending sensitivity to ΔG at PHENIX to low x

The primary means of accessing $\Delta G = \int_0^1 \Delta g(x)dx$ at RHIC is through measuring double-spin asymmetries, A_{LL}, for inclusive hadron or jet production. Previous measurements of this asymmetry in jet and π^0 production at STAR[45, 46] and π^0 and η production at PHENIX[47, 48, 49] have only covered a range in momentum fractions from about 0.05 to 0.2. The range in x is limited by the kinematics of measuring jets and π^0's at mid-rapidity, meaning that the momenta of the interacting partons from the two protons are roughly equal. The relationship between x and the rapidity is shown by the following relation at leading order for interacting collinear partons with momentum fractions x_1 and

x_2 with outgoing rapidities[1] y_3 and y_4 and transverse momentum p_T:

$$\begin{aligned} x_1 &= \frac{p_T}{\sqrt{s}}(e^{y_3} + e^{y_4}) \\ x_2 &= \frac{p_T}{\sqrt{s}}(e^{-y_3} + e^{-y_4}). \end{aligned} \tag{3.1}$$

For $\eta \approx 0$, the exponentials in the expressions for x_1 and x_2 are all close to 1, and x_1 and x_2 are similar. The rapidities of the outgoing partons cannot be measured directly; instead, we use π^0's as proxies for the outgoing jets. In PHENIX, the MPC allows an extension of the measured x-range to lower x by extending the acceptance in PHENIX to larger y. For π^0's detected at forward pseudorapidities, there is a higher likelihood that the interacting partons had largely asymmetric momenta, with a high-x quark striking a low-x gluon for example. Additionally, the selection of this scenario can be enhanced by requiring two π^0's in a single arm ("north" or "south") of the MPC. In this case, the presence of both jets in the forward direction indicates a large boost of the center-of-momentum frame of the interacting partons. We further ensure that the two π^0's represent two jets, rather than a single jet yielding two π^0's, by introducing a minimum separation in ϕ between the π^0's. The width of a jet is such that it cannot span "back-to-back" π^0's in the MPC, so requiring $|d\phi| > \frac{\pi}{2}$ should select scattering events with two distinct forward jets [2](Figure 3.2).

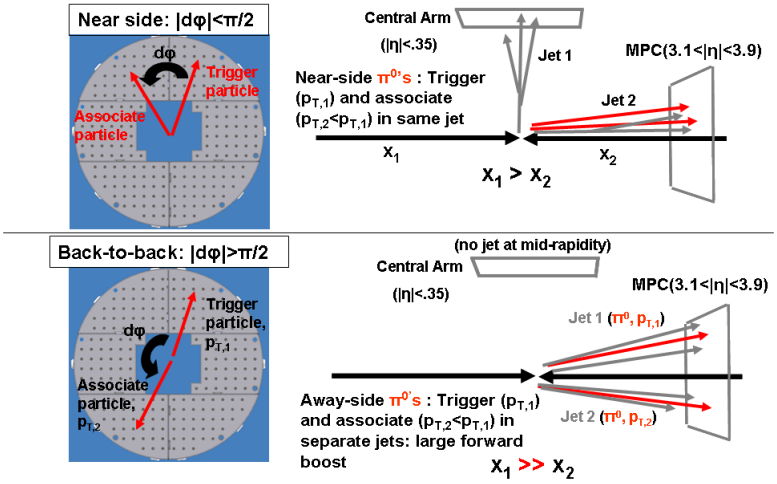

Figure 3.2: Kinematics of away-side cut: In di-jet events, we tag one jet with a high-p_T π^0. The second (associate) π^0 can either be in the same jet or an opposite jet. If the associate is in an opposite jet, most likely there is a forward boost to the system and $x_1 \gg x_2$.

Finally, to have the highest sensitivity to ΔG, we want to select scattering events that feature a quark-gluon interaction. Since $A_{LL} \propto \Delta f_a \Delta f_b$ and Δq

[1]The rapidity is defined as $y = \frac{1}{2} ln(\frac{E+|\boldsymbol{p}|c}{E-|\boldsymbol{p}|c})$ and is approximately equal to the pseudorapidity for highly relativistic particles.

[2]The $|d\phi|$ cut has been employed successfully for forward-forward di-hadron correlations in dA and pp collisions, where in that analysis, one of the π^0's is a merged cluster[50].

is large and well-known at large x, we expect larger asymmetries from quark-gluon scattering than from gluon-gluon scattering. We can tune the process fractions, the relative ratio of each scattering process, by adjusting a lower limit on transverse momentum (p_T) of the detected π^0's. Having a minimum p_T cut also ensures that we are in a hard-scattering domain where pQCD is applicable.

3.1.1 Determining the accessed range in x from simulation

To determine the accessible range of x in measurements involving the MPC, 210 million proton-proton collisions were generated using the event generator PYTHIA[51]. In order to ensure that enough statistics were produced in the sample for high-p_T events, the simulation was divided into 5 sets of 42 million events each that differed only in the limits placed on the p_T of produced jets. The bins used were 2-5 GeV/c, 5-10 GeV/c, 10-20 GeV/c, 20-30 GeV/c, and 30-45 GeV/c. In order to determine the statistical uncertainty, all events were multiplied by a scale factor determined by the cross section reported by PYTHIA. Because the integrated luminosity $\int Ldt = N_{events}/\sigma$, we know what integrated luminosity a set of simulated events represents. We can then scale the events by a factor so that this integrated luminosity matches the projected luminosity to be achieved at RHIC. At the time the simulations were conducted, it had been estimated that around $\int Ldt = 300\,pb^{-1}$ of $p+p$ data would be taken at $\sqrt{s} = 500\,GeV$ by 2015[52]. In the simulated data, there were 41 million events generated for the lowest p_T bin, and PYTHIA reports a total cross section for these events of $34\,mb$. The scale factor for these events then is $300\,pb^{-1} \times \frac{34\,mb}{41M}$. Applying the scale factor in this way also ensures that the high-p_T events from simulation are not overrepresented, since their scale factors are small due to their comparatively small cross sections. The error bars were scaled up by additional factors of 2, 4, or 6 depending on the channel and p_T to represent trigger turn-on and prescale factors. These scaling factors were chosen such that the error bars in the simulation approximate the error bars from previous data sets for the same integrated luminosity.

We are interested in determining how the use of the MPC for single- and double-π^0 A_{LL} measurements can select specific ranges of x of the two interacting partons. To this end, distributions of x_1 and x_2 were produced for two π^0's in the central arm (Figure 3.3 (a)), single π^0's in the central arm (b), a trigger π^0 in the MPC with a second π^0 in the central arm (c), one π^0 in the north MPC and one in the south MPC (d), single π^0's in the MPC (e), and two π^0's in one arm of the MPC (f). The optimal p_T cuts for the trigger and associate π^0's were determined from a previous simulation. We found that increasing the minimum p_T for both the trigger and associate particles led to larger separa-

tions between the x_1 and x_2 peaks and lower $< x_2 >$[3], but as the p_T cuts were increased, statistics became severely limited. The best compromise was determined to be using the cuts $p_{T,trigger} > 3.0\,GeV/c$ and $p_{T,assoc.} > 1.5\,GeV/c$ for the di-hadron channels. In the $A_{LL}^{\pi^0}$ projections for di-hadron channels, events with trigger $p_T > 3.0\,GeV/c$ are included, while for single hadron channels, π^0's with $p_T > 1.0\,GeV/c$ were accepted.

A description of the final cuts used in these simulation studies is as follows: a π^0 from PYTHIA is considered to be in the MPC if its pseudorapidity falls within the MPC's fiducial acceptance: $-3.7 < \eta < -3.1$ for the south MPC and $3.1 < \eta < 3.9$ for the north MPC. There are no requirements requiring the decay photons to be in the MPC acceptance for the purposes of these simplified simulations. For a π^0 to be in the central arm, it must satisfy $|\eta| < 0.35$. For single π^0 channels, $p_T > 1.0\,GeV/c$, and for two-π^0 channels, $p_{T,1} > 3.0\,GeV/c$ and $p_{T,2} > 1.5\,GeV/c$. Lastly, for the MPC-MPC and central arm-central arm channels, it is required that $|d\phi| > \frac{\pi}{2}$. The resulting distributions for x_1 and x_2 from the simulations are shown in Figure 3.3. They are arranged with channels involving the central arm along the top row and those involving only the MPC along the bottom row. From the shapes and means of the distributions, it can be seen that generally, the central arm single- and double-π^0 channels feature more symmetric interactions with respect to x_1 and x_2, with a lower range for x_1 and a higher range for x_2. Moving forward to look at the MPC-central arm channel and the MPC single- and double-π^0 channels, the distributions become more asymmetric, with x_1 moving to higher x as x_2 shifts to lower x. In particular, the MPC double-π^0 channel features the (narrowly) lowest $< x_2 >$ as well as the largest $< x_1 > - < x_2 >$. While the mean of the x_2 distribution for this channel is still only around a few times 10^{-2}, there is a peak in the distribution below 10^{-3}, meaning we can hope to be sensitive to Δg in that region. From these simulations, we see that a measurement of $A_{LL}^{\pi^0}$ in the MPC can probe $\Delta g(x)$ for $x \approx 5 \times 10^{-3}$ and, depending on the statistics collected, as low as $x \sim 10^{-3}$.

[3]In general, as we see in Equation 3.1, increasing p_T results in higher x. However, requiring a high-p_T particle in our simulations helped to single out hard scattering interactions where Equation 3.1 holds. For softer interactions, other effects become significant and the relationship between x and η becomes less clear.

Figure 3.3: Distributions for the momentum fractions x_1 and x_2 as reported by PYTHIA for different measurements involving the central arm and MPC.

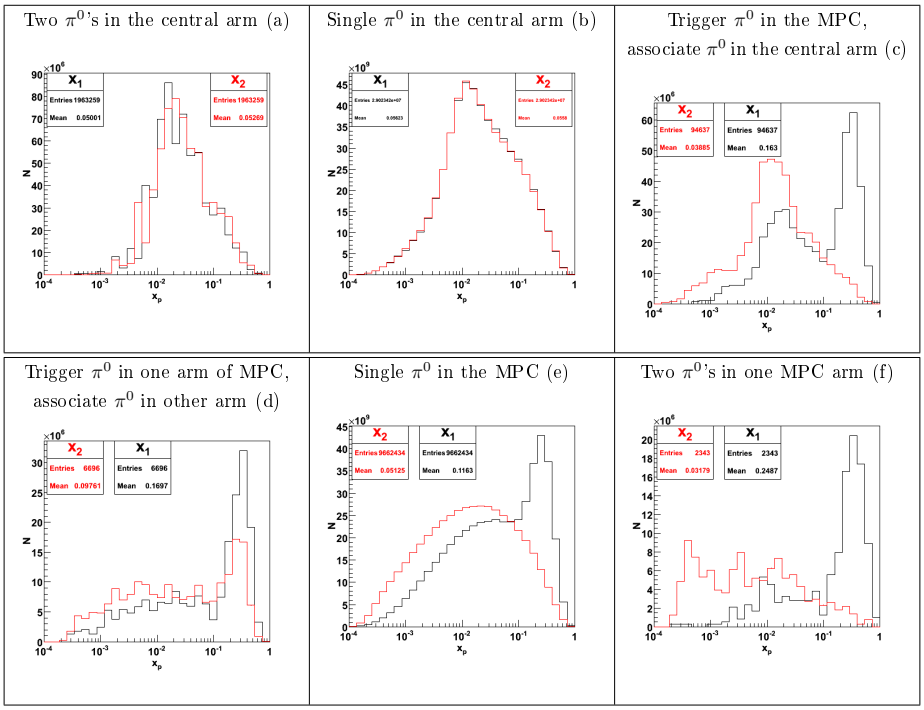

3.2 A_{LL} projections

From the simulations, it is also possible to generate projections of asymmetries that can be measured with the MPC along with their statistical uncertainties. For polarized protons, we can write for the difference between the spin-dependent cross sections, $\Delta\sigma = \sigma^{++} - \sigma^{+-}$:

$$\Delta\sigma^{p+p\to\pi^0+X} = \sum_{a,b,c} (\Delta f_a(x_a, Q^2) \otimes \Delta f_b(x_b, Q^2)$$

$$\otimes \Delta\hat{\sigma}^{a+b\to c+X}(x_a, x_b, Q^2, z) \otimes D_{c\to\pi^0}(z_c, Q^2)). \tag{3.2}$$

The asymmetry that we wish to measure is the ratio of this difference to the spin averaged cross section: $A_{LL} \equiv \frac{\sigma_{++}-\sigma_{+-}}{\sigma_{++}+\sigma_{+-}} = \frac{\Delta\sigma}{\sigma}$. Following the procedure in [53], the projected asymmetry is calculated as follows. One histogram is filled by p_T bin with all accepted π^0's (or π^0 pairs) weighted with only the luminosity scaling factor to give the unpolarized cross section. A second histogram is filled for each π^0 or π^0 pair, with each weighted by the luminosity scaling factor in addition to the hadronic double spin asymmetry for the parent event:

$$w(x_A, x_B, \hat{s}, \hat{t}, \hat{u}, Q^2) = \frac{\Delta f_A}{f_A}\frac{\Delta f_B}{f_B}\hat{a}_{LL}. \tag{3.3}$$

Here, Δf is the polarized PDF, f is the corresponding unpolarized PDF, the subscripts A and B refer to the partons participating in the scattering event. $\hat{a}_{LL}$ is the partonic asymmetry, $\frac{\Delta\hat{\sigma}}{\hat{\sigma}}$,which depends on the types of the interacting partons and the kinematic Mandelstam variables $\hat{s}$, $\hat{t}$, and $\hat{u}$, where the hats indicate reference to the scattering partons rather than the nucleons. This partonic asymmetry can be calculated from leading order pQCD; the formulas for each process type are provided in Table Table 3.1[4][54]. The fragmentation functions $D_{c\to\pi^0}(z_c, Q^2)$ from the cross sections cancel on an event-by-event basis, so they are dropped from the weight. After weights for all events have been calculated, the weighted histogram is divided by the unweighted histogram to give $A_{LL}^{\pi^0}$ for the selected channel. Errors were calculated as $\frac{1}{\sqrt{N_{counts}}}$, where the counts were scaled to represent 300 pb^{-1} of data as mentioned previously. Additionally, the beam polarizations are accounted for in the errors as a $\frac{1}{P^2}$ term; the assumed polarization for this study is $P = 0.55$. A last adjustment to the error bars was made by comparing errors from simulation to errors from previous analyses, assuming the same polarization and integrated luminosity for the simulated data set. The scale factors needed to match the simulation error bars to the errors from a data analysis were noted and applied to the final projections. These factors should help to account for trigger prescaling and efficiency effects as well as any inaccuracies in PYTHIA's generation of π^0 yields. Systematic uncertainties are not shown in the projection plots, but a rough relative luminosity uncertainty of 10^{-4} is included in the uncertainties listed in Table 3.2.

Table 3.1: Leading order partonic asymmetries $\hat{a}_{LL}$ by process[54].

PYTHIA process number	Parton process $ab \to cd$	Partonic asymmetry $\hat{a}_{LL} = \frac{\Delta\sigma_{ab}^{cd}}{\sigma_{ab}^{cd}}$
11	$qq \to qq$	$\frac{\hat{t}^2+\hat{u}^2-\frac{2}{3}\hat{t}\hat{u}-\frac{\hat{t}^4+\hat{u}^4}{\hat{s}^2}}{\hat{t}^2+\hat{u}^2-\frac{2}{3}\hat{t}\hat{u}+\frac{\hat{t}^4+\hat{u}^4}{\hat{s}^2}}$
	$qq' \to qq'$	$\frac{\hat{s}^2-\hat{u}^2}{\hat{s}^2+\hat{u}^2}$
	$q\bar{q}' \to q\bar{q}'$	$\frac{\hat{s}^2-\hat{u}^2}{\hat{s}^2+\hat{u}^2}$
12	$q\bar{q} \to q\bar{q}$	$\frac{\frac{\hat{s}^4-\hat{t}^4}{\hat{u}^2}-(\hat{s}^2+\hat{t}^2-\frac{2}{3}\hat{s}\hat{t})}{\frac{\hat{s}^4+\hat{t}^4}{\hat{u}^2}+(\hat{s}^2+\hat{t}^2-\frac{2}{3}\hat{s}\hat{t})}$
	$q\bar{q} \to q'\bar{q}'$	-1
13	$q\bar{q} \to gg$	$\frac{8}{3}\frac{\hat{t}^2+\hat{u}^2}{\hat{t}\hat{u}} - 6\frac{\hat{t}^2+\hat{u}^2}{\hat{s}^2}$
28	$qg \to qg$	$\frac{\hat{s}^2-\hat{u}^2}{\hat{s}^2+\hat{u}^2}$
53	$gg \to q\bar{q}$	-1
68	$gg \to gg$	$\frac{2\frac{\hat{s}^2}{\hat{t}\hat{u}}+\frac{\hat{t}\hat{u}}{\hat{s}^2}-3}{3-\frac{\hat{s}\hat{u}}{\hat{t}^2}-\frac{\hat{s}\hat{t}}{\hat{u}^2}-\frac{\hat{t}\hat{u}}{\hat{s}^2}}$

[4]While writing this section, a bug was discovered in the code for calculating the partonic asymmetries for the weight. The effect of the bug is that both $q\bar{q}$ processes (process number 12) have the asymmetry of the $q\bar{q} \to q\bar{q}$ process, rather than the second one having an asymmetry of -1. However, this process accounts for $< 0.05\%$ of events, so the effect on the projected A_{LL} is small.

3.2.1 PDF Sets Used for $A_{LL}^{\pi^0}$ Projections

In generating the weights for the asymmetries (Equation 3.3), for the unpolarized PDFs $f_{A,B}$ we use fits from a QCD global analysis by the CTEQ (Coordinated Theoretical-Experimental Project on QCD) collaboration [55]. For the polarized PDFs $\Delta f_{A,B}$, we use results from de Florian, Sassot, Stratmann, and Vogelsang (DSSV)[22]. Presently, the unpolarized PDFs and the total $u-$ and d-quark polarized distributions are well-known, whereas the polarized sea-quark PDFs are less well-constrained, and the polarized gluon PDF is weakly constrained, particularly at high and low x (see Figure 1.7). To examine the effect of different models of $\Delta g(x)$ on $A_{LL}^{\pi^0}$, we also generate projected asymmetries for models of $\Delta g(x)$ that differ from DSSV's best fit.

3.2.2 Modified $\Delta g(x)$ Functions

Because we are interested in possible divergences from the DSSV fit to $\Delta g(x, Q^2)$ for low x where there is a lack of data, we constructed hypothetical low-x tails to examine the effect on $A_{LL}^{\pi^0}$. The Δg's we use, in addition to the standard fit DSSV-STD and its upper and lower uncertainty limits DSSV-MAX, and DSSV-MIN, were of the form

$$\Delta g(x, Q^2 = 10\, GeV^2) = \begin{cases} k \times \text{DSSV-MAX} & x < 0.05 \\ \text{DSSV-STD} & x > 0.05 \end{cases}. \tag{3.4}$$

The constants k were chosen to give values of $\Delta G^{[10^{-3},1.0]}$ ranging from -.7 to .7. Similarly, we generated A_{LL} projections for $\Delta g(x) = k \times$ DSSV-MAX over the whole range of x. The Q^2 evolution of the gluon PDF was assumed to be independent of the scale factor k and was taken from grids provided by DSSV.

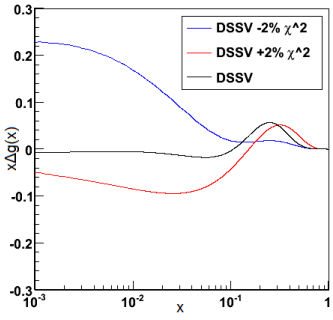

Figure 3.4: $\Delta g(x)$ from standard DSSV fit, as well as DSSV MIN and MAX from $\Delta\chi^2 = +/-2\%$. All functions are scaled by x.

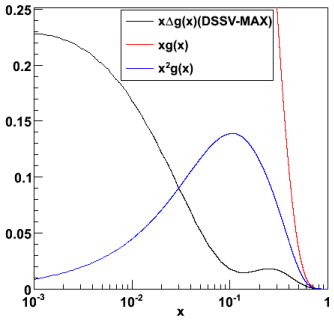

Figure 3.5: DSSV-MAX $\Delta g(x)$ compared to $g(x)$(red) and $xg(x)$(blue). All functions are scaled by a factor of x.

3.2.3 A_{LL} Simulation Results

Projected asymmetries were generated for each of 19 handmade Δg's overall. A sample of results from these projections is shown in Figure 3.6 and . The values of $< A_{LL}^{\pi^0} >$ listed in the table are from fitting the plots of A_{LL} vs. p_T to a constant, and a common factor of 10^{-4} is dropped from all numbers for readability. In the Single π^0 MPC channel, the first point is excluded from the fit because the dominance of statistics in the lowest p_T bin resulted in the fit reporting the value of $A_{LL}^{\pi^0}$ at that point as the constant. Of particular relevance for our physics analysis is the small size of the projected asymmetries, even for models of gluon polarization on the upper end of the range consistent with experimental data to this point. The simulations point to asymmetries smaller than 10^{-3} which would be too small to be seen with the levels of systematic uncertainty present in A_{LL} measurements at PHENIX in 2009. This concern motivates our work to limit our systematic uncertainty from our measurement of the relative luminosity to on the order of 10^{-4}, as we will discuss in depth in chapter 4.

Even from this limited sample of data, it is possible to identify trends that point to the low-x region's being probed. First, as a sanity check, it is clear that the magnitude of the asymmetry increases for all channels as the chosen $\Delta G^{[10^{-3},1.0]}$ increases, and the asymmetry appears to be sensitive to the sign of ΔG. However, when comparing the increase in $A_{LL}^{\pi^0}$ as $\Delta G^{[10^{-3},1.0]}$ is ratcheted up, the change is much more dramatic for the "forward" channels involving the MPC than for the "central" channels. The modification of $\Delta g(x)$ to bring about the increase in the truncated moment all occurs at low x. Since the central channels access less of this range, they are less affected by the modification. However, the forward measurements that do probe the low-x region are very sensitive to differences in the form of $\Delta g(x)$ in that region. Of the two forward channels, the single π^0 channel is more sensitive to ΔG because of the higher statistics available. More concretely, the single π^0 MPC measurement could measure a total gluon polarization of 0.35 at around a 2σ difference from zero. For a $\Delta G^{[10^{-3},1.0]}$ equal to .7 (for the unscaled DSSV-MAX), the difference from zero increases to 5σ. The asymmetries for the di-hadron channel are indeed larger, indicating a narrower focus on the lower x region of the gluon distribution. Unfortunately, unlike for the single pion measurement, statistical uncertainties factor in even more heavily than projected systematic uncertainties.

Table 3.2

Table 3.2: Sample of projected $A_{LL}^{\pi^0}$'s fit to a constant, uncertainties, and # of sigmas from 0 with a common factor of 10^{-4} omitted. The error $\Delta A_{LL}^{\pi^0} = \sqrt{(\Delta A_{LL}^{stat})^2 + (\Delta A_{LL}^{sys})^2}$, using projected $A_{LL}^{sys} = 10^{-4}$. "CA" refers to the central arm.

$\Delta g(x) \Longrightarrow$	DSSV-STD	DSSV-MAX	DSSV-MAX at low x	$\propto$DSSV-MAX $\Delta G^{[10^{-3},1.0]} = -0.35$	$\propto$DSSV-MAX $\Delta G^{[10^{-3},1.0]} = 0.1$
Single π^0 CA	$-.1 \pm 1.0(.1\sigma)$	$3.8 \pm 1.0(4\sigma)$	$2.9 \pm 1(2.9\sigma)$	$-0.4 \pm 1(-0.39\sigma)$	$0.22 \pm 1(0.22\sigma)$
Double π^0 CA	$1.9 \pm 5.8(.3\sigma)$	$2.7 \pm 5.8(.5\sigma)$	$2.2 \pm 4.4(0.5\sigma)$	$-0.75 \pm 4.4(-0.17\sigma)$	$0.032 \pm 4.4(0.0073\sigma)$
π^0 MPC+π^0 CA	$-.026 \pm 6.4(.004\sigma)$	$6.4 \pm 6.4(1\sigma)$	$4.8 \pm 6.6(0.73\sigma)$	$-1.8 \pm 6.6(-0.28\sigma)$	$0.64 \pm 6.6(0.098\sigma)$
Single π^0 MPC	$-.32 \pm 1.2(.3\sigma)$	$6.5 \pm 1.0(5\sigma)$	$6.4 \pm 1.4(4.7\sigma)$	$-3.7 \pm 1.4(-2.7\sigma)$	$0.75 \pm 1.4(0.56\sigma)$
Double π^0 MPC	$-.34 \pm 14.(.02\sigma)$	$12. \pm 14.(.9\sigma)$	$9.8 \pm 6.2(1.6\sigma)$	$-6.5 \pm 6.2(-1\sigma)$	$0.81 \pm 6.2(0.13\sigma)$
π^0 MPC N+π^0 MPC S	$-.24 \pm 10.(.02\sigma)$	$7.6 \pm 10.(.7\sigma)$	$6.5 \pm 4.8(1.4\sigma)$	$-2.9 \pm 4.8(-0.6\sigma)$	$0.63 \pm 4.8(0.13\sigma)$

Figure 3.6: Sample A_{LL} Projections for different channels and Δg's; only statistical errors shown (does not include projected systematic error of $\sim 10^{-4}$).

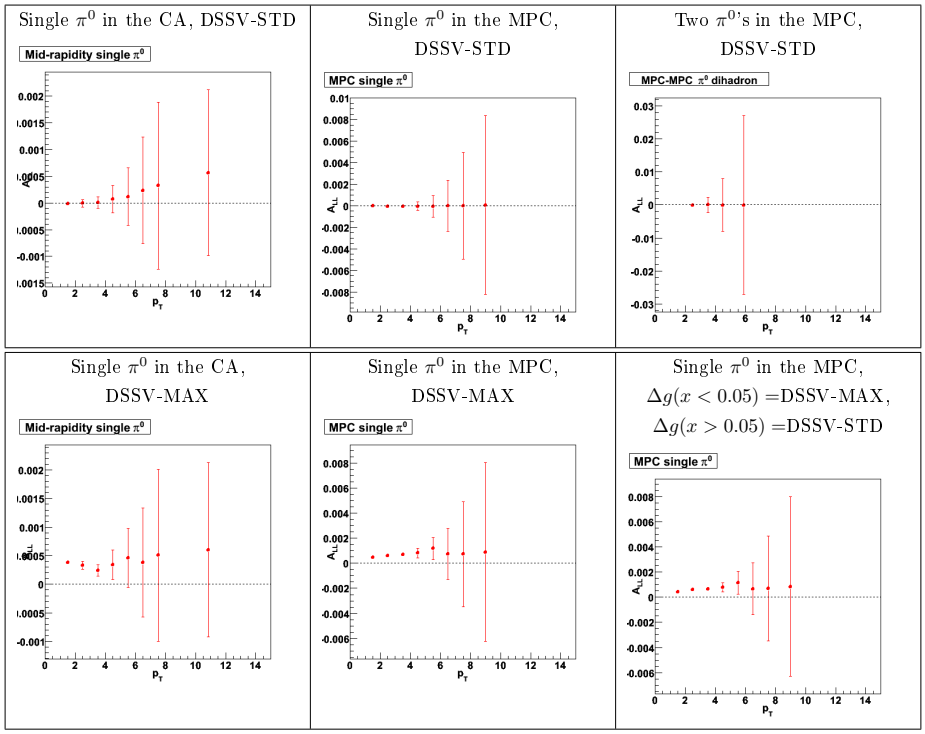

3.3 Effect of multi-parton interactions and initial- and final-state radiation in PYTHIA

Some of the results from PYTHIA differ from what would be expected from a leading order treatment of calculations of kinematics of the involved processes. This leads to some features of the distributions of x_1 and x_2 that may not

be physical. The main discrepancy is in the range of x accessed by the central arm. Previous studies in PHENIX have shown that for $p+p$ collisions at $\sqrt{s} = 500\,GeV$, the lower limit of x probed by the central arm is about 5×10^{-3} for $2.0\,GeV/c < p_T < 2.5\,GeV/c$, with $< x >\sim$a few times 10^{-2}. The distributions in this note on the other hand show the central arm probing x below 10^{-3}. Furthermore, the x_1 range for single π^0's in the MPC shows a broad second hump in addition to the high x quark peak that resembles the x_2 distribution. This symmetrical portion of the distributions is not fully understood for the forward-boosted collisions that result in π^0's in the MPC. Finally, upon closer examination of kinematic variables on an event-by-event basis, we see a significant number of events where $x_2 \gg x_1$, indicating a large boost in the direction of the south MPC, but π^0's still show up in the north MPC, or vice versa. This collection of evidence points toward a weakened connection between the kinematics of the hard scattering event and the π^0's in the final state.

Two tunable features of events in PYTHIA can possibly explain these discrepancies: Multi-Parton Interactions (MPIs) and initial- and final-state radiation (ISR+FSR). In an event with MPIs, there can be multiple binary interactions between partons in the colliding protons in addition to the hardest scattering event that is reported by PYTHIA. These can yield additional π^0's that pass our kinematic cuts and are weighted and counted in the same way as π^0's from the primary interaction. For example, consider an event with two scattering processes: a primary collision (a) and a secondary collision (b). For the primary collision, we take $x_1^a \gg x_2^a$. This type of collision should result in a forward boost and π_a^0's in the forward direction. In the secondary collision, we can instead have $x_1^b \ll x_2^b$, with π_b^0's detected in the opposite arm of the MPC. However, because PYTHIA only reports x_1^a and x_2^a for each event, the π_b^0's will be mistakenly treated as if they also originated in the primary collision. As a result, we can see π^0's in the opposite arm of the MPC than would be expected from kinematic considerations based on the reported x_1 and x_2.

ISR and FSR also can confuse the issue of the proper x_1 and x_2 to use as the arguments to the parton distribution functions. When the partons involved in the hard scattering process radiate gluons, their momentum fractions change. Additionally, it is possible that the radiated gluons themselves enter the hard scattering process. Finally, because the radiation processes can themselves be hard, it is possible that gluons radiated in the initial or the final state fragment directly into π^0's that pass the kinematic cuts. It is possible that given our leading-order calculation of $A_{LL}^{\pi^0}$ and the partonic asymmetries for the projections, we should not include MPIs, ISR, or FSR from PYTHIA. As a low-level illustration of the effects of MPIs, ISR, and FSR, we include two x distributions for single π^0's for a smaller set of PYTHIA events with MPIs, ISR, and FSR switched off.

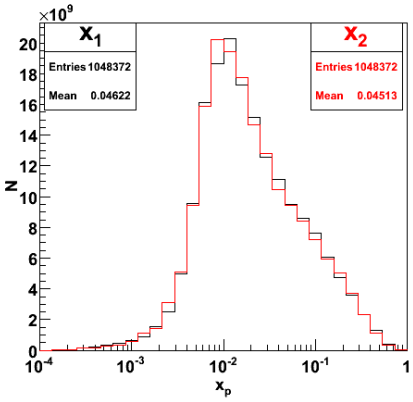

Figure 3.7: x distributions for single π^0's in the central arm with MPIs, ISR, and FSR switched off

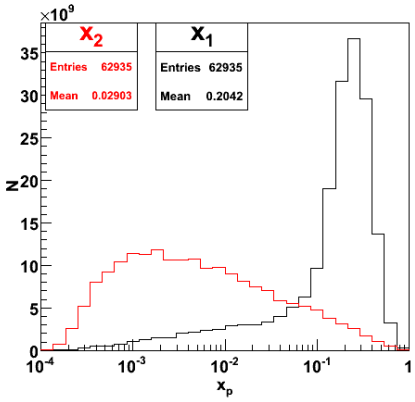

Figure 3.8: x distributions for single π^0's in the MPC with MPIs, ISR, and FSR switched off

Chapter 4

Relative Luminosity Analysis

4.1 Overview

One of the main challenges faced in calculating $A_{LL} = \frac{1}{P_b P_y} \frac{N^{++} - RN^{+-}}{N^{++} + RN^{+-}}$ to high precision is determining R, the ratio of the luminosity in same-sign helicity collisions versus opposite-sign helicity collisions. Particularly in view of the $150\,pb^{-1}$ of integrated luminosity recorded in Run 13 (compared to the $16.7\,pb^{-1}$ in Run 11), we hope to push the uncertainty on relative luminosity down to the order of 10^{-4}. This note is a continuation of work done towards improving the precision of our relative luminosity measurement over the years in PHENIX, most recently by groups at Stony Brook University and the University of Illinois at Urbana-Champaign[56, 57, 58]. In this note, however, we are working chiefly with scalers with no vertex cut[1], as this has been enabled by the STAR scalers which allow a wider variety of scaler data to be collected. For a summary of the scalers used in this section, see subsection 2.2.4.

As has been the practice in PHENIX, we use the BBC to determine relative luminosity due to its good z-vertex resolution and high rates. Nevertheless, we must be careful not to blindly trust the yields measured by the BBC as representative of the true collision rate. In order to maximize our confidence in the collision rates as measured by the BBC, we eliminate runs or crossings with abnormalities in the scaler data through an extensive quality assurance analysis (section 4.2). Additionally, the limitation that the BBC can only count one coincidence in a crossing necessitates a rate-dependent correction that accounts for crossings with multiple collisions (section 4.3). Finally, we limit the possibility of the BBC itself measuring an A_{LL} through comparison with the luminosity measured in the second luminosity monitor in PHENIX, the ZDC (section 4.4). It is the size of the asymmetry $A_{LL}(\frac{ZDCwide}{BBCwide})$ and its pattern dependence that serve as our primary estimators of δR.

This chapter ends with a discussion on the crossing dependence of the pileup corrected $\frac{ZDCwide}{BBCwide}$ ratio that is the main driver of poor $\sqrt{\chi^2/NDF}$ values in bunch-fitting $A_{LL}(\frac{ZDCwide}{BBCwide})$ calculations (section 4.6).

[1] The $ZDCwide$ trigger actually has a cut at $|z| = 150\,cm$, corresponding to the location of the BBC to avoid the ZDC sampling collisions where the BBC has no acceptance. In practice, this does not make much difference, as the average of $\frac{ZDC(no\,vtx.\,cut)}{ZDCwide}$ is 1.5×10^{-5}.

4.2 Scaler data quality assurance

In PHENIX, we have a number of cross-checks on the "goodness" of the scalers that record the number of triggers from the BBC and ZDC on a run-by-run, crossing-by-crossing basis. The triggers are recorded by the GL1 scalers, which sum scalers over all crossings, and the GL1p and STAR scalers, which count triggers from each of the 120 bunch crossings over the course of a run. We look for consistency in the data as reported by the three systems and exclude runs or crossings where discrepancies indicate glitches in the DAQ. Abnormal data from the scalers, such as a large number of counts in the abort gaps where no collisions occur, can point to problems with the beam during certain runs. The shift crews responsible for collecting data during Run 11 also report in logbooks when they encounter problems during a run that could lead to suspect data. These considerations all factor into whether a particular run or crossing is included in the final analysis as detailed below.

4.2.1 Run-level QA cuts

Missing STAR scaler data In 29 of the 432 runs designated as "Physics" runs, there is no STAR scaler data available, making the runs unusable for our analysis.

STAR scaler bunch structure problems The abort gaps and the four "empty-full" crossings where only either the blue beam or yellow beam is filled are identifiable as crossings where the STAR scalers show greatly reduced counts in the BBC and the ZDC. In some cases, the gap is "misaligned," not comprised of crossings 111-119, but the alignment can be fixed by hand. In other cases, the abort gap seems to be missing altogether, indicating a malfunction in the scalers. These problematic runs are excluded from the analysis.

STAR scaler ZDC bunch structure problems We exclude a handful of runs where the normal bunch structure is present in the BBC scalers, but problems in the ZDC electronics lead to the abort gaps not appearing in the ZDC scalers.

STAR-GL1 scaler mismatch The GL1 boards, which integrate trigger counts over all 120 bunch crossings, provide another cross-check on the accuracy of the readings from the STAR scalers. The STAR scalers have a slightly delayed start time at the beginning of each run, resulting in distributions of $\frac{STAR\,scalers}{GL1\,scalers}$ that peak between 0.99 and 1.0. We require that this fraction for the clock triggers, *BBCwide* triggers, *BBCnarrow* triggers, and *ZDCwide* triggers, falls between 0.99 and 1.0 for all runs included in the analysis.

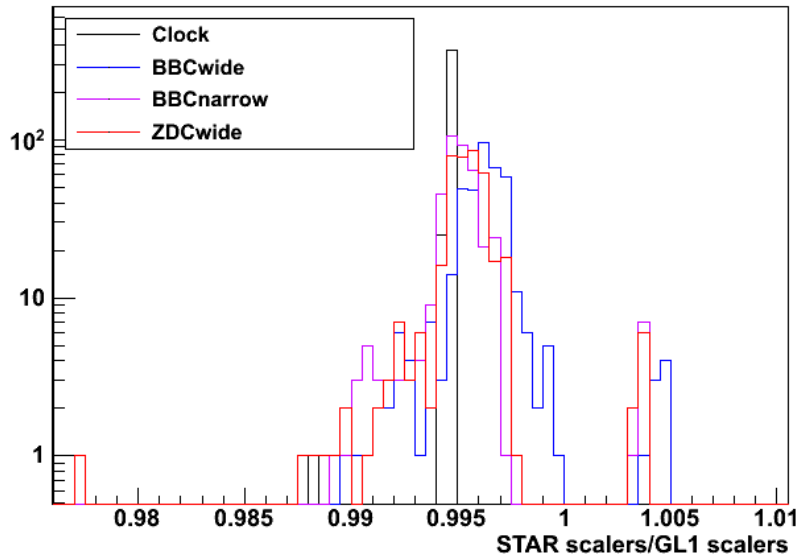

Figure 4.1: Distribution of ratios of STAR scalers to GL1 scalers from each run.

STAR-GL1p scaler mismatch The STAR scalers can also be compared to the GL1p scalers on a crossing-by-crossing level. Individual crossings where the ratio of the two scalers falls outside of a range from 0.998 to 1.004 are considered bad, and these are excluded (see below in the bunch-level QA section). However, runs with more than six of these bad crossings are removed entirely from the analysis.

Empty crossing issues In each run, crossings 38, 39, 78, 79, and 111-119 are expected to have few collisions recorded by the STAR scalers due to either or both of the beams having no proton bunch at that crossing. In a number of runs, there are either additional "empty" crossings before or after the expected ones, or some of the crossings expected to be empty register numbers of collisions consistent with the interaction of two bunches. It is not known whether these runs exhibit a problem in the timing of the electronics or if there are actual irregularities in the bunch structure in RHIC, but we exclude these runs in any case.

Early runs We exclude the period in Run 11 before run 336000, which is characterized by somewhat unstable beam performance in RHIC, as evidenced by a low fraction of runs declared suitable for physics analysis, high backgrounds, and large variations in the ratio of single-arm to coincidence counts in the ZDC and the ratio of ZDC coincidences to BBC coincidences.

4.2.2 Bunch-level QA

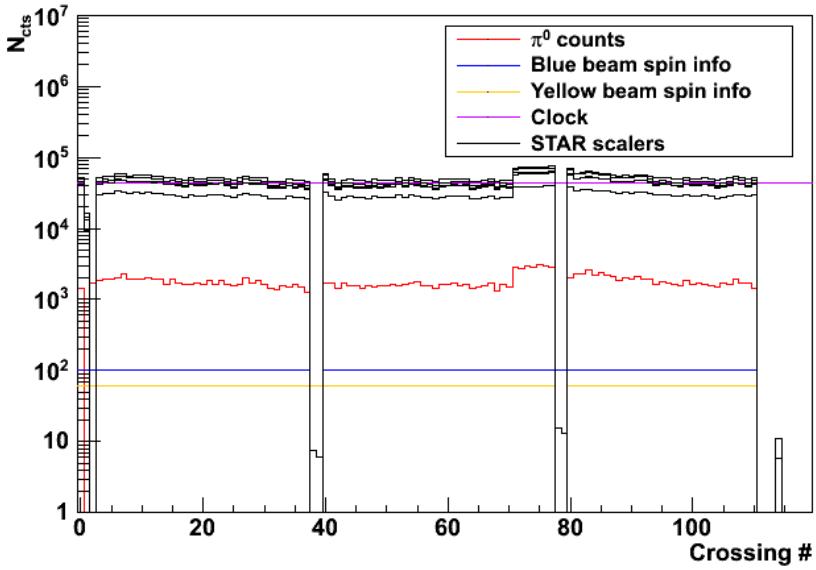

Figure 4.2: Database information for individual bunches from one run. The number of $\pi^0 s$ reconstructed from MPC analysis is also included. The STAR scaler histograms are scaled to appear together on the plot, and the beam spin information is a constant if a reported helicity is present in the spin database and zero otherwise.

In addition to excluding entire runs from the final analyzed data set, we drop individual crossings on a run-by-run basis based on criteria listed below.

Spin information QA The blue and yellow bunches in each crossing are filled with either positive or negative helicity, and this information is recorded in a database. Bunches that are either unfilled or missing their helicity identification are excluded from the analysis. In general, these are crossings 38, 39, 78, and 79, which are the so-called "empty-full" crossings where only either the blue or yellow beam is filled, and crossings 111 through 119, the abort gap, which are never filled in either beam.

STAR scaler outliers For each run, we plot the value of each of the six STAR scalers we use versus bunch crossing. We fit these to a constant using an algorithm that ignores outliers to get the run average. Then, any crossing i for which $scaler_i < 0.5 \times (scaler\, average\, for\, run)$ or $scaler_i > 2 \times (scaler\, average\, for\, run)$ is excluded.

STAR-GL1p mismatch In comparing the STAR scalers to the GL1p scalers, we find that the ratio for the majority of crossings in all good runs falls between 0.998 and 1.004. Crossings where this is not the case in any of

the scalers present in both the STAR scalers and the GL1p (i.e. *BBC30cm, BBCnarrow, ZDCwide,* and *ZDCnarrow)* are excluded.

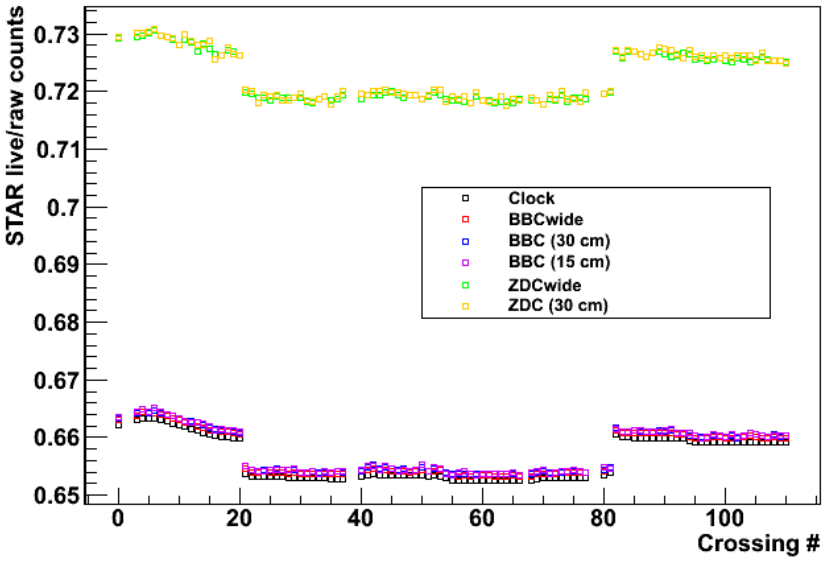

Figure 4.3: Trigger live times from the STAR scalers.

Livetime issues/crossing analysis QA In Run 11, there were large variations in livetime, the ratio of triggers when the DAQ was live (ready to write data) to total triggers, over the course of the 120 crossings (see Figure 4.3) . In particular, there is a large drop around crossing 20 and a "recovery" after crossing 82. The presence of the abort gap from crossings 111-119 and the empty-full crossings also affect the livetime of the early crossings. We find that because the effect of livetime on the ZDC and BBC is different, including crossings around these points can have unusual effects on the calculated asymmetries between the BBC and the ZDC. For this reason, we exclude crossings 0, 21, 40, 80, 81, and 82.

4.2.3 Scaler data QA Summary

The final relative luminosity analysis encompasses data from 23,305 good crossings in 239 good runs. The results of the QA are shown in Figure 4.4. The good runs are listed in Appendix A.

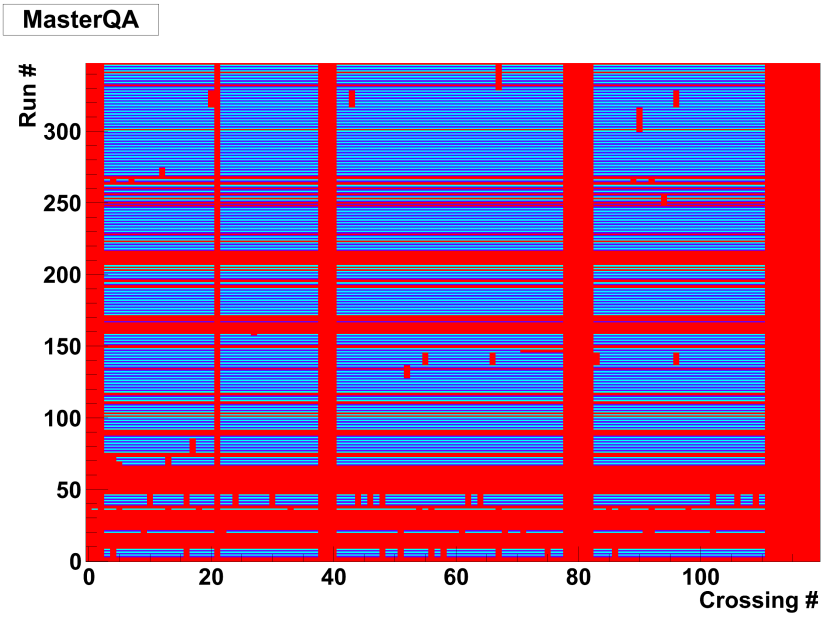

Figure 4.4: Master QA plot for Run 11 scaler data. Bad bunches are marked red; the alternating shades of blue distinguish consecutive runs. The run counters in the y-axis are assigned sequentially to runs but do not correspond to the actual run numbers in the database.

4.3 Pileup correction

The BBC and ZDC triggers fire for any crossing where a hit was recorded in both arms of the detector, but only one coincidence can be counted in a given crossing. For crossings with a single collision, no confusion is possible, and the detectors will record a trigger with some efficiency if the one collision results in hits in both arms of the detector. The situation is more complicated for the case where there are two collisions in a single crossing. The detectors can miscount the number of collisions that would individually create a coincidence (or "visible" collisions) in two ways:

(a) Two collisions occur, each resulting in hits in both arms; one coincidence trigger reported.

(b) Two collisions occur, with one resulting in a hit in the south arm and the other resulting in a hit in the north arm; a coincidence is reported, whereas neither of the two collisions individually would be counted.

Of course, there can be more than two collisions in a crossing, and the above effects extend to those cases as well. Both of these miscounting possibilities must be accounted for in order to accurately determine the true number of collisions from the BBC and ZDC scaler data. Qualitatively, if a detector has a higher probability of detecting hits in both arms from a single collision, effect (a) dominates at high rates, and the detector will undercount the true number

of collisions. If the detector instead has a higher probability of detecting a hit from a collision in only one arm, the dominant effect from multiple collisions is the accidental coincidences of effect (b), and the detector will overcount the true number of visible collisions.

4.3.1 Derivation of the pileup correction

We now turn to the question of formalizing the pileup correction, following a derivation by members of the ATLAS collaboration.[59]. We start with a true rate $\mu = \frac{N_{collisions}}{N_{clock}}$, representing the average number of inelastic pp collisions per bunch crossing. We assume that the number of collisions in a crossing obeys Poisson statistics, such that, for the rate μ, the probability of n collisions occurring in a crossing is

$$P(n;\,\mu) = \frac{\mu^n e^{-\mu}}{n!}. \tag{4.1}$$

We also define efficiency for a given detector to "see" a hit from a collision in the south arm, the north arm, or both arms as ϵ_S, ϵ_N, and ϵ_{NS} respectively; this efficiency by definition incorporates the detector's acceptance. The true rates of hits in the detector then are $\mu_S = \mu\epsilon_S$, $\mu_N = \mu\epsilon_N$, and $\mu_{NS} = \mu\epsilon_{NS}$. By extension, we also have $\epsilon_{OR} = \epsilon_S + \epsilon_N - \epsilon_{NS}$ as the efficiency of at least one arm of the detector seeing a hit from a collision[2]. Finally, we have actual observed single-arm and coincidence rates, $\frac{N_S}{N_{clock}}$, $\frac{N_N}{N_{clock}}$, and $\frac{N_{NS}}{N_{clock}}$. With these assumptions and definitions, we can begin to work out the relation between true and observed rates.

Our goal is to determine the value of $\mu_{vis} = \mu\epsilon_{NS}$ from the scaler values N_S, N_N, N_{NS}, and N_{clock}. We have that the probability of detecting a coincidence in a detector (P_{AND}) is one minus the probability of detecting zero hits in at least one arm (we will call this $P_{0,\,OR}$), or

$$P_{AND} = 1 - P_{0,\,OR} = 1 - (P_{0,S} + P_{0,N} - P_{0,N\,\&\&\,0,S}), \tag{4.2}$$

where the final term is the probability that neither arm sees a hit. The probability for each term on the right-hand side can be determined from the Poisson distribution:

$$\begin{aligned}\frac{N_{NS}}{N_{clock}} &= 1 - (\frac{(\mu\epsilon_S)^0 e^{-\mu\epsilon_S}}{0!} + \frac{(\mu\epsilon_N)^0 e^{-\mu\epsilon_N}}{0!} - \frac{(\mu\epsilon_{OR})^0 e^{-\mu\epsilon_{OR}}}{0!}) \\ &= 1 - e^{-\mu\epsilon_S} - e^{-\mu\epsilon_N} + e^{-\mu(\epsilon_S+\epsilon_N-\epsilon_{NS})}.\end{aligned} \tag{4.3}$$

[2]This follows from the relation $P(A\,or\,B) = P(A) + P(B) - P(A\&\&B)$.

Finally, we introduce the single-arm to double-arm hit ratios[3],

$$k_{N(S)} = \frac{\epsilon_{N(S)}}{\epsilon_{NS}}. \tag{4.4}$$

Substituting these ratios into Equation 4.3, the relation simplifies:[4]

$$\begin{aligned} \frac{N_{NS}}{N_{clock}} &= 1 - e^{-\mu\epsilon_{NS}k_S} - e^{-\mu\epsilon_{NS}k_N} + e^{-\mu\epsilon_{NS}(k_S+k_N-1)} \\ &= 1 - e^{-\mu_{NS}k_S} - e^{-\mu_{NS}k_N} + e^{-\mu_{NS}(k_S+k_N-1)}. \end{aligned} \tag{4.5}$$

This equation cannot be solved for the true rate μ_{NS} analytically, but given the measured rate $\frac{N_{NS}}{N_{clock}}$ and k_N and k_S, we can find μ_{NS} numerically.

4.3.2 Determination of singles-to-doubles ratios for the ZDC and the BBC

The singles-to-doubles ratios can be found from the single-arm and coincidence scalers available in the STAR scalers. However, these scalers also depend on rate due to pileup, so we attempt to correct for this before calculating k_N and k_S. We already have the framework above to derive the relation between the single-arm scaler counts and the true rate of collisions visible to a single arm of the detector:

$$\begin{aligned} \frac{N_{S(N)}}{N_{clock}} &= 1 - P_{0,S(N)} = 1 - e^{-\mu\epsilon_{S(N)}} \\ \mu\epsilon_{S(N)} &= \mu_{S(N)} = -ln(1 - \frac{N_{S(N)}}{N_{clock}}). \end{aligned} \tag{4.6}$$

If we plug Equation 4.6 into Equation 4.3, we have the following:

$$\frac{N_{NS}}{N_{clock}} = 1 - e^{ln(1-\frac{N_S}{N_{clock}})} - e^{ln(1-\frac{N_N}{N_{clock}})} + e^{ln(1-\frac{N_S}{N_{clock}})}e^{ln(1-\frac{N_N}{N_{clock}})}e^{\mu\epsilon_{NS}},$$

which after simplifying the exponentials and taking the logarithm gives us an equation for the rate-corrected coincidence rate in terms of only the observed scalers:

$$\mu_{NS} = ln(1 - \frac{N_S}{N_{clock}} - \frac{N_N}{N_{clock}} + \frac{N_{NS}}{N_{clock}}) - ln(1 - \frac{N_S}{N_{clock}}) - ln(1 - \frac{N_N}{N_{clock}}). \tag{4.7}$$

These pileup-corrected values for the singles and doubles rates are what we use to calculate k_N and k_S, but why can we not just jump straight to using Equation 4.7 for our pileup-corrected rates instead of using Equation 4.5? There are two difficulties with the "scalers-only" approach to the pileup corrections.

[3] In PHENIX, this value is often defined as the ratio of exclusive single-arm counts to the double-arm counts such that $k'_{N(S)} = \frac{\epsilon_{N(S)} - \epsilon_{NS}}{\epsilon_{NS}} = k_{N(S)} - 1$ in terms of the definitions used in this section.

[4] Using the exclusive singles-to-doubles ratio, $k_{N(S)} \rightarrow 1 + k'_{N(S)}$, so $\frac{N_{NS}}{N_{clock}} = 1 - e^{-\mu_{NS}(1+k_s)} - e^{-\mu_{NS}(1+k_N)} + e^{-\mu_{NS}(1+k_S+k_N)}$.

For one, the singles-to-doubles ratios are essentially ratios between efficiencies and acceptances and should be rate-independent properties of the detectors and their geometry.We see however that even after attempting to correct out the rate dependence, the values we find for k_N and k_S vary over the range of rates found in Run 11.

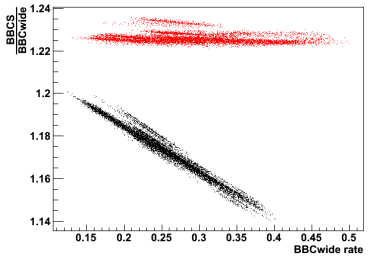

(a) The rate-corrected BBC singles-to-doubles ratio k_S (red) shows a much smaller dependence on the rate than the uncorrected ratio (black).

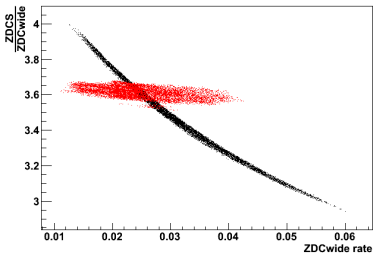

(b) The rate correction has a stronger effect on the ZDC rate and singles-to-doubles ratio. The red points are $(1 - k_S)$ (or the exclusive singles-to-doubles ratio) for plotting purposes.

Figure 4.5: Corrected and uncorrected singles-to-doubles ratios.

We take a closer look at the rate dependence in Figure 4.6. Secondly, the use of single-arm scalers directly in calculating the pileup correction makes the result more susceptible to noise and backgrounds which affect single-arm counts more than coincidences.

The scalers-only pileup corrections (Equation 4.6 and Equation 4.7) do a reasonable job of removing the rate dependence from k_S and k_N, but a small effect persists.

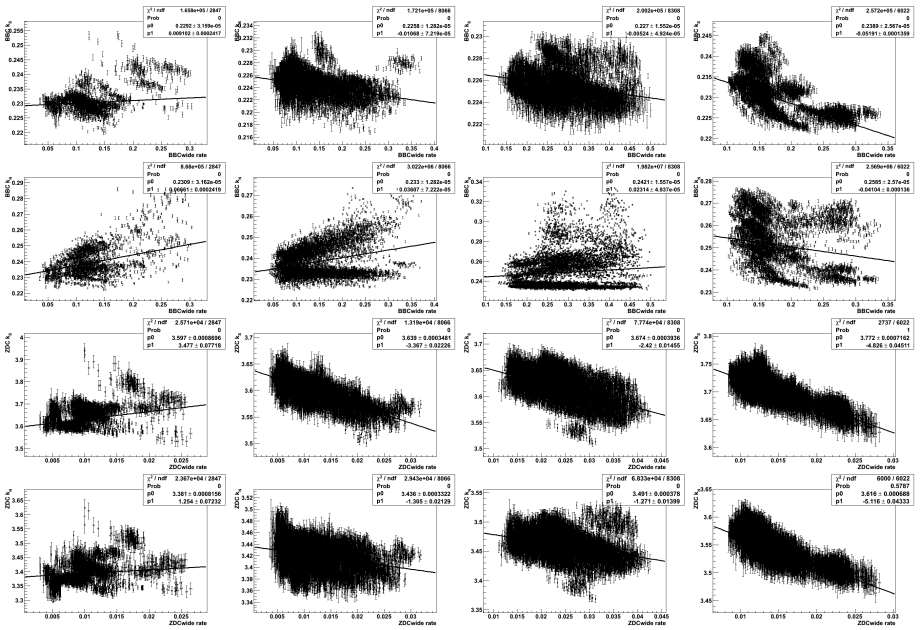

Figure 4.6: Plots showing the extrapolation to zero rate of, from top to bottom, BBC k_S, BBC k_N, ZDC k_S, and ZDC k_N. The columns represent the four sections of Run 11 with distinctive properties referred to in later in this note, with later sections being further to the right.

A few features are already notable from the data shown in Figure 4.6. For instance, the first column of plots, representing runs earlier than run 336000, display singles-to-doubles ratios that are erratic and do not follow the trends seen in the later data. This is one motivation for that section of the run to be excluded from the final analysis. Moreover, the values of BBC k_N in the first three sections of the run show a splitting that corresponds to different behavior of the BBCN single-arm scaler between alternating crossings. This abnormality is thought to be due to a timing issue in the BBC electronics. Additionally, there is a difference between the ZDC k_S and k_N on the order of 0.2 for all sections of Run 11. This difference has also been seen in runs from other years as well. For these reasons, and because the pileup correction treats k_S and k_N symmetrically, we use the value we find of k_S for both k_S and k_N for the BBC and the ZDC. Ultimately, this choice is justified by our finding that the smallest rate dependence in the BBC and ZDC scalers remains when using these values.

We assume that the best estimate for the singles-to-doubles ratios would be at low rates where multiple collisions are less of a factor, so we plot $k_{S(N)}$ vs. rate, fit to a line, and extrapolate to find the singles-to-doubles ratio at zero rate. As we will show in the next section, changing behavior of the detectors and the beam over time leads to a partitioning of the Run 11 data set into four groups of runs. We find k_N and k_S separately for these four sections. The resulting fits can be seen in Figure 4.6.

Run range	BBC k_S	BBC k_N	ZDC k_S	ZDC k_N
331130-336000	0.2292	0.2309	3.597	3.381
336000-338000	0.2258	0.2330	3.694	3.436
338000-339700	0.2292	0.2241	3.665	3.495
339700-340515	0.2389	0.2585	3.772	3.616

Table 4.1: Summary of results of singles-to-doubles ratio determination

In practice, there is still enough variation in k_N and k_S within each section to justify an attempt to determine the ratios on even shorter timescales. We find that the statistics and lever arm in the *ZDCwide* rates on the level of an individual run are not quite sufficient to give stable fits and values of k_N and k_S. However, if we consider each fill individually, we find values that agree well with the "section-level" values while giving us increased sensitivity to fluctuations in the singles-to-doubles ratios. For these reasons, for each fill, we use one value of BBC k_S for BBC k_S and k_N for all crossings, and likewise for the ZDC. For the uncertainties on k_N and k_S, we use the approximate spread on the values at a given rate over a section of the run. We conservatively estimate that $\delta(BBC\,k_S) = \pm 0.005$ and $\delta(ZDC\,k_S) = \pm 0.05$.

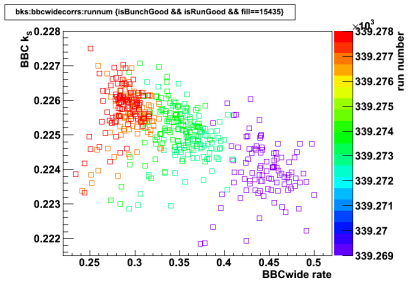

(a) Rate dependence of BBC $k'_S = k_S - 1$ for a single fill. Each point represents one crossing from the fill, and the colors represent runs in the fill. The rate dependence within a single run is not strong enough to extrapolate from, but a clear correlation is seen over the entire fill.

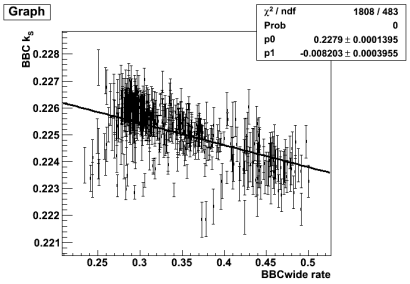

(b) The same plot as 4.7a without run numbers, but error bars and a linear fit have been added to show the extrapolation to the zero-rate value of BBC $k_S = 0.2279$.

Figure 4.7: Determination of BBC k_S for a single fill.

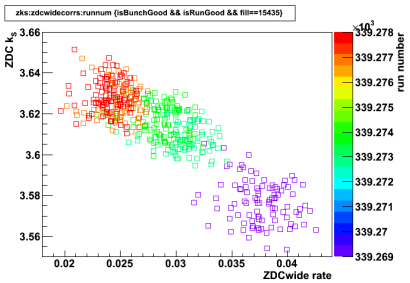

(a) Rate dependence of ZDC $k'_S = k_S - 1$ for a single fill. Each point represents one crossing from the fill, and the colors represent runs in the fill. The rate dependence within a single run is not strong enough to extrapolate from, but a clear correlation is seen over the entire fill.

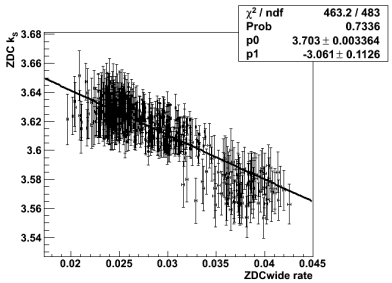

(b) The same plot as 4.8a without run numbers, but error bars and a linear fit have been added to show the extrapolation to the zero-rate value of ZDC $k'_S = 3.703$.

Figure 4.8: Determination of ZDC k_S for a single fill.

4.3.3 Effect of the pileup correction

As mentioned before, detectors that see a large singles-to-doubles ratio are likely to overcount collisions due to accidental coincidences from multiple collisions in a single crossing hitting a single arm of the detector, whereas detectors with a small singles-to-doubles ratio undercount collisions because multiple collisions resulting in true coincidences in a single crossing will only be recorded as a single coincidence. We see this dichotomy clearly in the pileup corrections to the raw *BBCwide* and *ZDCwide* trigger counts. For our calculated values of k_S and k_N, the *BBCwide* counts need to be multiplied by a factor greater than one that grows as the rate increases. Conversely, the *ZDCwide* counts are multiplied by a factor smaller than one that decreases with increasing rate.

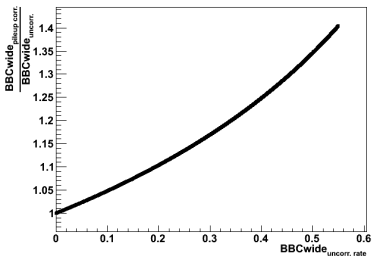

(a)

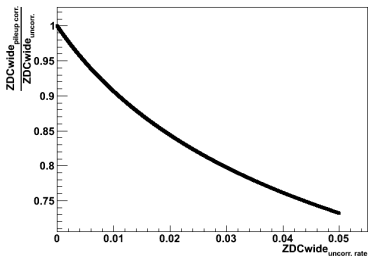

(b)

Figure 4.9: Pileup correction factors for the BBC (a) and ZDC (b).

The necessity of the pileup correction is clearly demonstrated via a ratio between the scalers from the two detectors, $\frac{ZDCwide}{BBCwide}$. Ideally, the two detectors count coincidences at a rate directly proportional to the true luminosity, so the two scalers would be related by a factor that is constant with respect

to rate. With no pileup correction applied, the ratio increases drastically with rate. Particularly because our estimate for the uncertainty on the relative luminosity measurement depends on $\frac{ZDCwide}{BBCwide}$ asymmetries, the correction is needed to ensure that the rates we measure in one detector are consistent with the other and that both are proportional to the true collision rate. As shown in Figure 4.10, the pileup corrections successfully eliminate the rate dependence of the $\frac{ZDCwide}{BBCwide}$ ratio.

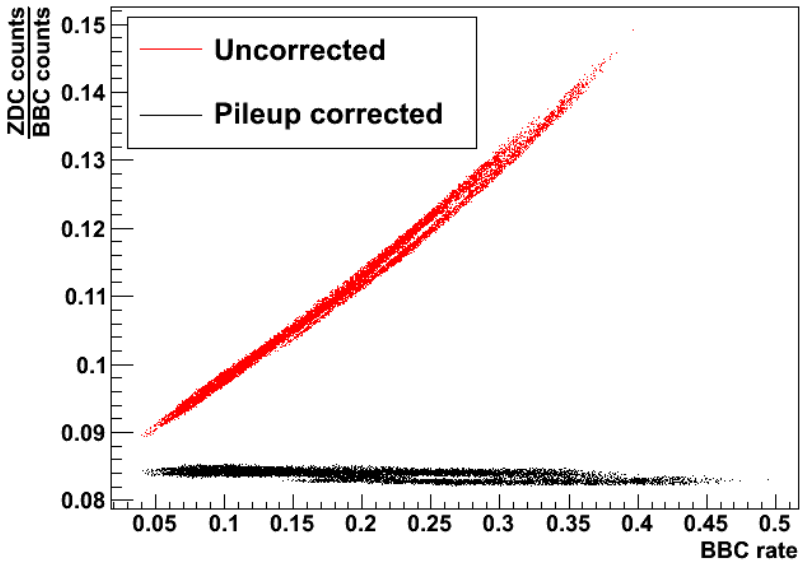

Figure 4.10: The effect of the pileup correction applied to the BBC and the ZDC on the ratio $\frac{ZDCwide}{BBCwide}$ is shown. Each point represents one crossing from one run, and all crossings from Run 11 that pass the data QA in Run 11 are included.

To wrap up the discussion from the previous section on the determination of the singles-to-doubles ratios, we include a comparison of the $\frac{ZDCwide}{BBCwide}$ ratios for one section of the run using the scalers-only pileup correction and the k_S, k_N pileup correction, showing the improvement resulting from using the latter method.

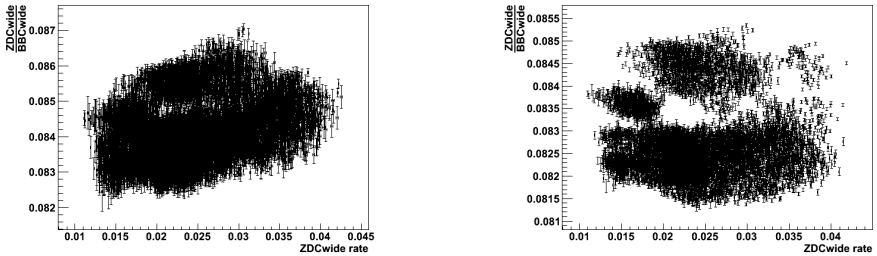

(a) Rate-dependence of $\frac{ZDCwide}{BBCwide}$ using the scalers-only pileup correction (Equation 4.7).

(b) Rate-dependence of $\frac{ZDCwide}{BBCwide}$ using the pileup correction with k_N and k_S (Equation 4.5). No clear rate-dependence remains over a wide range of rates.

Figure 4.11: Comparison of pileup correction methods.

After the pileup corrections have been applied to the *BBCwide* and *ZDCwide* scalers, we can take a wide look at the scaler ratios from every crossing over the entirety of Run 11. We find the data arranges into four well-defined groups based on run number. Of the four groups, the first is not used in the analysis, the middle two show reasonably consistent values of $\frac{ZDCwide}{BBCwide}$ over a wide range of *BBCwide* rates, and the last group is usable despite difficulties with the bunch storage system that arose leading to wide bunches and a larger range of $\frac{ZDCwide}{BBCwide}$.

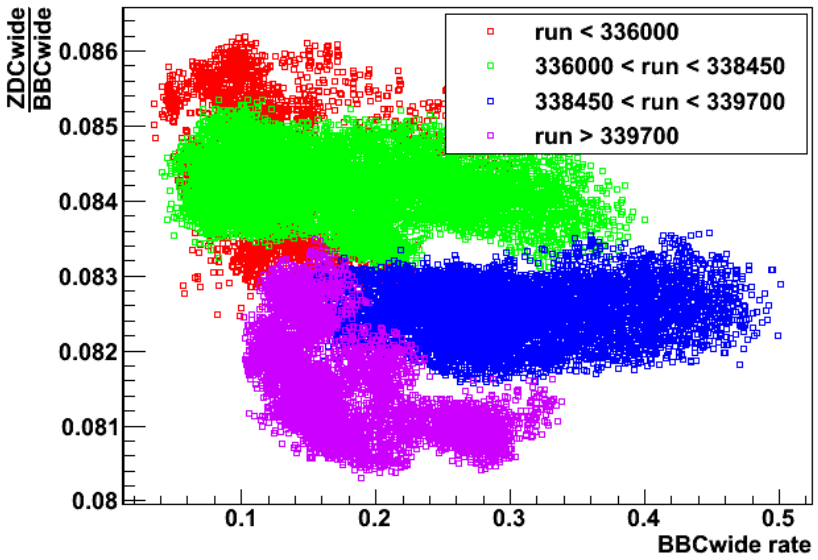

Figure 4.12: The pileup corrected $\frac{ZDCwide}{BBCwide}$ ratios when plotted against rate fall in different regions depending on run number.

4.4 Constraining A_{LL} in the BBC with the ZDC

Even if we assume that the BBC and the scalers are all working perfectly, and we are able to correctly account for the possibility of multiple collisions in a single crossing, we could still run into difficulties if a true physics asymmetry is measured in the BBC. Such an asymmetry would lead to the BBC measuring different numbers of collisions in same-sign and opposite-sign crossings for the same beam, and the measured relative luminosity would not be the proper normalization for the MPC asymmetry.

For example, if the same physical and positive A_{LL} exists for the p_T sampled by the BBC and the MPC, then both detectors will count higher yields for same-sign collisions than opposite sign collisions, such that $N^{++} = (1+\delta)N^{+-}$ for both detectors. With this assumption, we recall the formula we use to calculate A_{LL},

$$A_{LL}^{MPC\,clus.}(BBC\,lumi) = \frac{1}{|P_b P_y|}\frac{N_{MPC}^{++} - \frac{N_{BBC}^{++}}{N_{BBC}^{+-}}N_{MPC}^{+-}}{N_{MPC}^{++} - \frac{N_{BBC}^{++}}{N_{BBC}^{+-}}N_{MPC}^{+-}}, \tag{4.8}$$

and it is clear that no asymmetry will be measured despite our assumption that A_{LL} exists and is positive.

We employ the other luminosity monitor in PHENIX, the ZDC, as assurance that the BBC is not measuring an A_{LL} that cancels with an asymmetry in the MPC. While the MPC and BBC both sample hard collisions between protons, the ZDC samples double-diffractive interactions, and the chances are remote that the same A_{LL} would be generated by two completely different physics processes. We calculate an asymmetry in the ZDC with the respect to the BBC in an analogous manner as we do for the MPC:

$$A_{LL}^{ZDC.}(BBC\,lumi) = \frac{1}{P_b P_y}\frac{N_{ZDC}^{++} - \frac{N_{BBC}^{++}}{N_{BBC}^{+-}}N_{ZDC}^{+-}}{N_{ZDC}^{++} - \frac{N_{BBC}^{++}}{N_{BBC}^{+-}}N_{ZDC}^{+-}}, \tag{4.9}$$

$$\delta A_{LL}^{ZDC}(BBC\,lumi) = \frac{1}{P_b P_y}\frac{2\frac{N_{BBC}^{++}}{N_{BBC}^{+-}}N_{ZDC}^{++}N_{ZDC}^{+-}}{(N_{ZDC}^{++}+N_{ZDC}^{+-})^2}\times \sqrt{(\frac{\delta N_{ZDC}^{++}}{N_{ZDC}^{++}})^2 + (\frac{\delta N_{ZDC}^{+-}}{N_{ZDC}^{+-}})^2 + (\frac{\delta N_{BBC}^{++}}{N_{BBC}^{++}})^2 + (\frac{\delta N_{ZDC}^{+-}}{N_{BBC}^{+-}})^2}. \tag{4.10}$$

We calculate the δN from the raw scaler counts in each crossing i as binomial errors on the rate $r_i = \frac{N_i}{N_{clocks,i}}$:

$$\frac{\delta N_i}{N_{clocks,i}} = \sqrt{\frac{r_i(1-r_i)}{N_{clocks,i}}}, \tag{4.11}$$

taking the error on the number of clock triggers as negligible compared to the

error on the counts from the BBC and ZDC. This error is scaled by the pileup correction factor, and the errors N_i are summed in quadrature to give the final δN^{++} and δN^{+-}. The polarization values P_b and P_y are fill-averaged values provided by the the CNI polarimetry group within the RHIC Spin Group[60].

The overall asymmetry $A_{LL}^{ZDC}(BBC\,lumi)$, or $A_{LL}(\frac{ZDC}{BBC})$, is calculated in the same way as $A_{LL}(\frac{MPC}{BBC})$. The asymmetry is calculated for each run individually, and then the resulting run-by-run asymmetries are fit to a constant. For consistency, the same QA cuts are applied to the data for this analysis as for the MPC analysis, with the exception of those cuts specific to problems with the MPC.

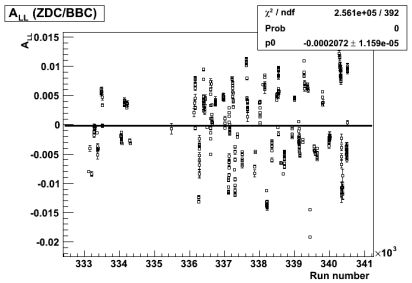

(a) $A_{LL}(\frac{ZDC}{BBC})$ with minimal QA and no pileup corrections.

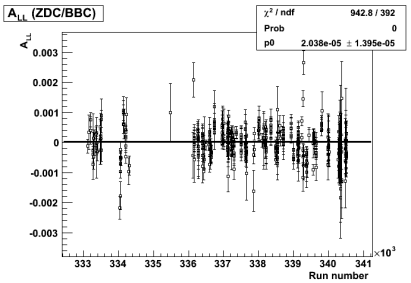

(b) $A_{LL}(\frac{ZDC}{BBC})$ with pileup corrections but minimal QA.

Figure 4.13: Uncorrected $A_{LL}(\frac{ZDC}{BBC})$ examples.

The effect of the pileup correction on $A_{LL}(\frac{ZDC}{BBC})$ can be seen in Figure 4.13. Without the pileup corrections to the *BBCwide* and *ZDCwide* scalers, the $\frac{\chi^2}{NDF}$ of the fit of the run-by-run asymmetries to a constant is ~ 650; with the pileup corrections applied, the $\frac{\chi^2}{NDF}$ is already down to less than 3.

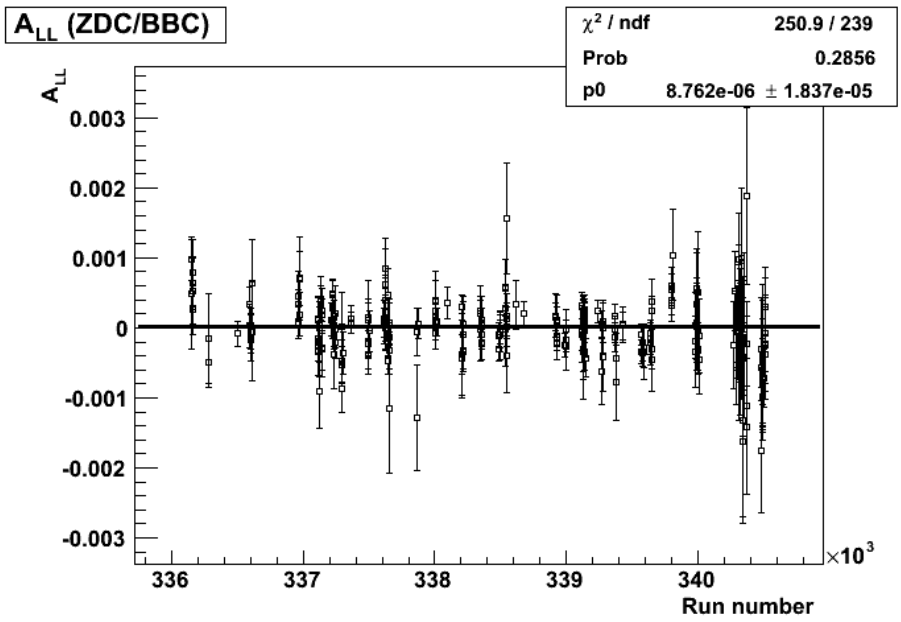

Figure 4.14: Final $A_{LL}(\frac{ZDC}{BBC})$ after the pileup correction and data QA have been applied.

With the full data quality assurance cuts applied, problematic crossings and runs have been removed, bringing the $\frac{\chi^2}{NDF}$ to 1 and the value of $A_{LL}(\frac{ZDC}{BBC}) = 7.298 \times 10^{-6} \pm 1.837 \times 10^{-5}$. Generally, the central value of $A_{LL}(\frac{ZDC}{BBC})$ has been quoted as δR, the uncertainty on the relative luminosity. As our result is consistent with zero and smaller than the error on our fit, we instead quote the error on the fit, 1.837×10^{-5}, as the statistical component of δR.

4.5 Checks on systematic errors

As additional verification of the data, our quality assurance methods, and our calculations, we carry out a number of analyses as cross checks. First, we check for consistency in $A_{LL}(\frac{ZDC}{BBC})$ between the four spin patterns used at RHIC during Run 11 to ensure that the beam is not affected by the particular sequence of same-sign and opposite-sign crossings. We also compare the asymmetry in even crossings versus odd crossings to check for effects resulting from the separate trigger circuits in some PHENIX systems that handle alternating crossings. A third test involving the double spin asymmetry is a bunch shuffling analysis wherein asymmetries are calculated with randomized spin patterns to confirm that the statistical error we report accurately reflects the spread of asymmetries that would be seen if we could repeat our measurement a large number of times. The last systematic effect we attempt to account for involves the pileup correction; by scanning through a range of values of the singles-to-doubles ratios that are inputs to the pileup correction, we see how uncertainty in our determination of those values propagates to an uncertainty in the final asymmetry.

4.5.1 Systematic uncertainty from the determination of k_N and k_S

We follow the suggestion of previous A_{LL} analyzers and approximate the impact of our uncertainty in k_N and k_S by varying these parameters and comparing the resulting asymmetries. As mentioned at the end of subsection 4.3.2, a conservative estimate of our uncertainty in the value of BBC k_S is $\delta(BBC\,k_S) = \pm 0.005$, while $\delta(ZDC\,k_S) = 0.05$. We scan seven values each of BBC and ZDC k_S in the range covered by the estimated uncertainty for a total of 49 calculations of A_{LL}.

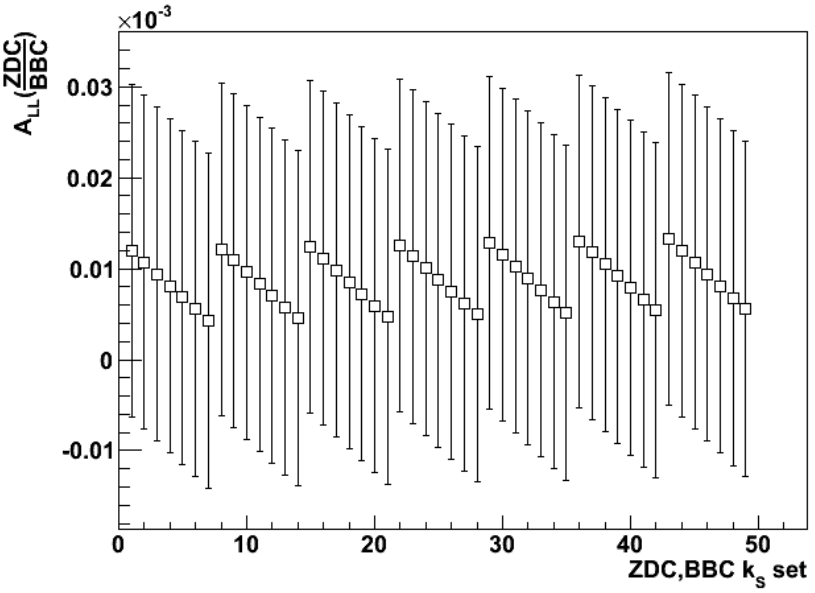

Figure 4.15: Results of scan through BBC and ZDC k_S values. The groups of seven points have a single value of BBC k_S, increasing from left to right. Within each group, the value of ZDC k_S increases from left to right.

The largest of any of the 49 calculated asymmetries with varying k_S is $A_{LL}(\frac{ZDC}{BBC}, BBC\,k_S = BBC\,k_S(std.)+0.005, ZDC\,k_S = ZDC\,k_S(std.)-0.05) = (1.32 \pm 1.83) \times 10^{-5}$.

4.5.2 $A_{LL}(\frac{ZDC}{BBC})$ by spin pattern

Ideally, any double spin asymmetry we measure would be due to a true difference in the pp cross section depending on the helicities of the colliding protons. In practice, differences in the performance of the detectors and/or electronics between the same-sign and opposite-sign crossings could lead to false asymmetries. Any differences in rates between crossing types that are not fully accounted for by the pileup corrections would also show up as a false asymmetry. As we will see in section 4.6, a crossing-dependent variation in the ratio of *ZDCwide*

to *BBCwide* scalers can lead to an asymmetry that is independent of physics considerations.

The false asymmetries cause maximal splitting between the two "SOOS" patterns and the two "OSSO" patterns (defined by the pattern of same-sign and opposite-sign blue and yellow beam helicities in the first four crossings) shown in Table 4.2.

Table 4.2: Spin pattern definitions for Run 11

Spin Pattern		Crossings 0-7
P0 (SOOS)	Blue beam helicity	$+-+--+-+$
	Yellow beam helicity	$++--+-+-$
P1 (SOOS)	Blue beam helicity	$-+-++-+-$
	Yellow beam helicity	$--++--++$
P2 (OSSO)	Blue beam helicity	$+-+--+-+$
	Yellow beam helicity	$--++--++$
P3 (OSSO)	Blue beam helicity	$-+-++-+-$
	Yellow beam helicity	$++--+-+-$

For example, consider a hypothetical distribution of scalers (BBC and ZDC) that are functions of the crossing numbers only: $N_{BBC(ZDC)}(crossing)$. We then choose a spin pattern such that the scalers are summed according to their crossing types, and we plug these totals into Equation 4.9:

$$P_b P_y A_{LL}^{SOOS}(\frac{ZDC}{BBC}) = \frac{N_{ZDC}^{++} - \frac{N_{BBC}^{++}}{N_{BBC}^{+-}} N_{ZDC}^{+-}}{N_{ZDC}^{++} + \frac{N_{BBC}^{++}}{N_{BBC}^{+-}} N_{ZDC}^{+-}}.$$

If we instead use the other type of spin pattern (switching from SOOS to OSSO), the result is that the identification of each crossing type switches such that in Equation 4.9, $N^{++} \rightarrow N^{+-}$. Making this substitution back into the formula for the asymmetry, we obtain the same result, but with a minus sign:

$$\begin{aligned} P_b P_y A_{LL}^{OSSO}(\frac{ZDC}{BBC}) = & \quad \frac{N_{ZDC}^{+-} - \frac{N_{BBC}^{+-}}{N_{BBC}^{++}} N_{ZDC}^{++}}{N_{ZDC}^{+-} + \frac{N_{BBC}^{+-}}{N_{BBC}^{++}} N_{ZDC}^{++}} = \frac{\frac{N_{BBC}^{++}}{N_{BBC}^{+-}} N_{ZDC}^{+-} - N_{ZDC}^{++}}{\frac{N_{BBC}^{++}}{N_{BBC}^{+-}} N_{ZDC}^{+-} + N_{ZDC}^{++}} \\ = & \quad -P_b P_y A_{LL}^{SOOS}(\frac{ZDC}{BBC}). \end{aligned} \tag{4.12}$$

Therefore, we take differences in $A_{LL}(\frac{ZDC}{BBC})$ to be indicative of a false asymmetry that depends on the details of our particular measurement in PHENIX rather than a physics asymmetry. We place limits on the size of this type of false asymmetry by calculating the asymmetry separately for the four spin patterns. We demonstrate in Figure 4.16 that the asymmetries from all four patterns are

consistent with zero and with one another (within 1σ).

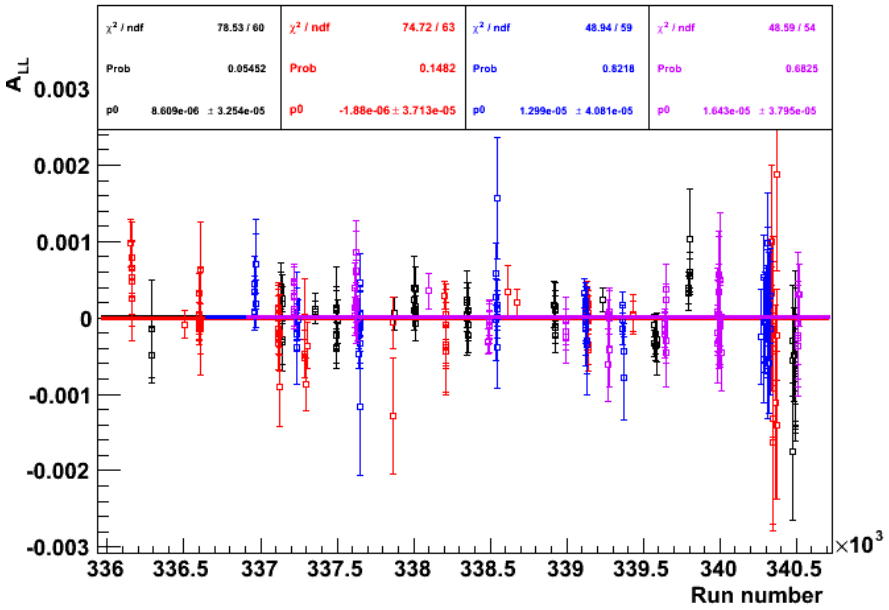

Figure 4.16: Double spin asymmetries are shown calculated separately for fills in Pattern 0 (black, SOOS-type), Pattern 1 (red, SOOS-type), Pattern 2 (blue, OSSO-type), and Pattern 3 (violet, OSSO-type). The asymmetries from the four patterns are consistent with zero and with one another, and the fits have reasonable values of χ^2/NDF.

4.5.3 Parity-violating single-spin asymmetries

We also construct the longitudinal single spin asymmetries between the ZDC and the BBC for the blue (yellow) beam,

$$A_{L,b(y)}(\frac{ZDC}{BBC}) = \frac{1}{P_{b(y)}} \frac{N^+_{ZDC} - \frac{N^+_{BBC}}{N^-_{BBC}} N^-_{ZDC}}{N^+_{ZDC} + \frac{N^+_{BBC}}{N^-_{BBC}} N^+_{ZDC}},$$

where the $N^+$is the sum of all scalers in crossings where the blue (yellow) beam has helicity of $+1$, while N^- is the sum for crossings where the beam has helicity -1.

A non-zero asymmetry would violate parity conservation, which is impossible for the strong force. In fact, as can be seen in Figure 4.17, a large asymmetry is seen in both beams. The cause of this asymmetry is unknown at present, but the interplay between beam angles or offsets and a physical A_N in the beam resulting from residual transverse polarization seems to be a good candidate, as proposed by Andrew Manion and Kieran Boyle[61]. It appears that the single spin asymmetry in the scalers does not negatively impact our double spin asymmetry measurements though; any problem would show up as a non-zero double spin asymmetry in the scalers, which we do not see.

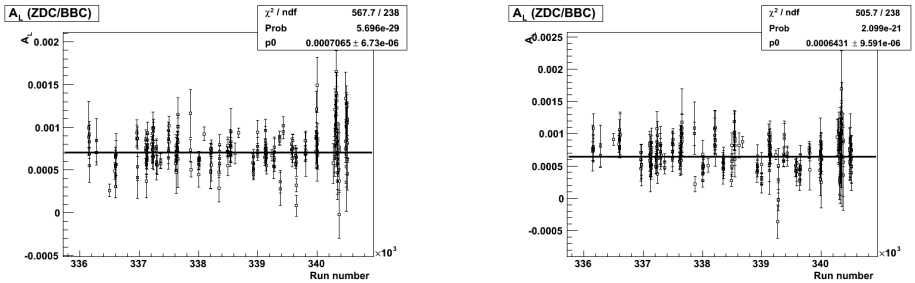

(a) $A_L(\frac{ZDC}{BBC})$ for the blue beam.

(b) $A_L(\frac{ZDC}{BBC})$ for the yellow beam.

Figure 4.17: $A_L(\frac{ZDC}{BBC})$ results showing a non-zero parity-violating asymmetry.

4.5.4 Bunch shuffling

The bunch shuffling test has previously been carried out on final physics asymmetries (e.g. $A_{LL}^{\pi^0}$) as a check for systematic errors and the accurate determination of statistical errors. For completeness, I perform the test here on $A_{LL}(\frac{ZDC}{BBC})$. For each run, we randomly assign the blue and yellow helicities for each crossing. With these randomized spin patterns, we recalculate $A_{LL}(\frac{ZDC}{BBC})$. As the bunch shuffling eliminates any relationship between the assigned helicities of a crossing and the true helicities, the effective polarization of the shuffled data is zero, meaning we expect asymmetries that are consistent with zero within the statistical uncertainties. The shuffling procedure is repeated 10,000 times for each run to get a distribution of asymmetries. We find the total asymmetry for each of the 10,000 shuffles from a fit to the asymmetry vs. run number (as in the physics case), and we generate a histogram filled with the value of $\frac{A_{LL}}{\delta A_{LL}(stat.)}$ for each shuffle. We expect the resulting distribution to be centered at zero to reflect the unpolarized nature of the shuffled data, and the width of the distribution should be near one if the statistical errors on $A_{LL}(\frac{ZDC}{BBC})$ are accurately determined.

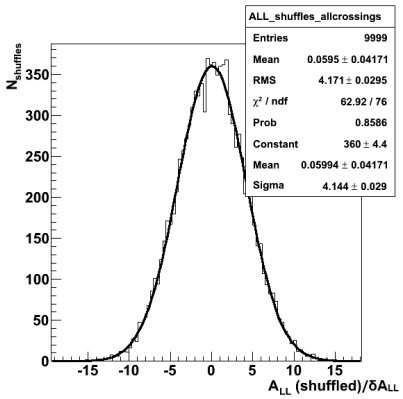

(a) $A_{LL}(\frac{ZDC}{BBC})$ bunch shuffling distribution. Each entry is $\frac{A_{LL}}{\delta A_{LL}}$ for the entire Run 11 data set (with QA cuts). For this distribution, $\sigma = 4$, in contrast to the expectation that $\sigma = 1$.

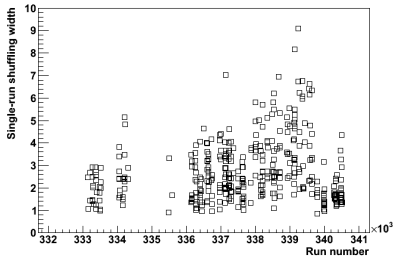

(b) Bunch shuffling widths for individual runs. No runs are excluded from this plot by run QA, though runs with extremely large widths are not shown due to the y-axis scale.

Figure 4.18: $A_{LL}(\frac{ZDC}{BBC})$ bunch shuffling results.

However, it is clear from Figure 4.18 that the bunch shuffling test fails badly for the scaler asymmetries. The same behavior is seen in the bunch shuffling of the single-spin asymmetries as well. It appears that the statistical errors significantly underrepresent actual fluctuations in the data. In contrast to our findings from the bunch shuffling procedure, in our final result for $A_{LL}(\frac{ZDC}{BBC})$ in Figure 4.14, the $\frac{\chi^2}{NDF}$ is essentially 1, indicating that the statistical errors used are appropriate. Ultimately, we find that the large shuffling widths are caused by variations of the ratio of ZDC to BBC scalers over the 120 crossings in a run. This variation is significant compared to the statistical error, but normal spin patterns employed at RHIC were designed to limit the impact on asymmetries of such crossing-dependent fluctuations. Bunch shuffling leads to unphysical distributions of same-sign and opposite-sign crossings that cause a crossing dependence of $\frac{ZDCwide}{BBCwide}$ to become problematic. We investigate this concept further in section 4.6.

4.5.5 Even-odd separated $A_{LL}(\frac{ZDC}{BBC})$

The difference in BBC k_N between even-numbered and odd-numbered crossings motivates the calculation of $A_{LL}(\frac{ZDCwide}{BBCwide})$ for even and odd crossings separately.

Figure 4.19: $A_{LL}(\frac{ZDC}{BBC})$ for even and odd crossings separately.

(a) $A_{LL}(\frac{ZDC}{BBC})$ for even crossings only.

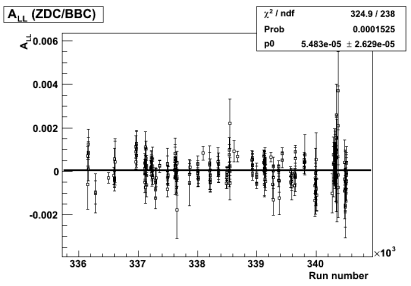

(b) $A_{LL}(\frac{ZDC}{BBC})$ for odd crossings only.

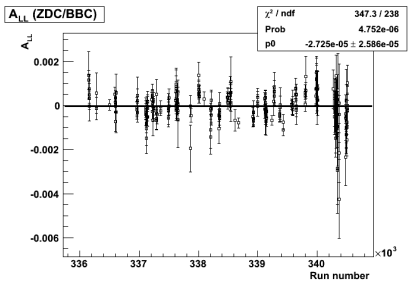

The χ^2/NDF of the fits as well as the size of the asymmetries are a bit worse than for the combined even and odd crossings. This is likely an artifact of the same effect causing the wide shuffling widths, namely the crossing dependence of the $\frac{ZDCwide}{BBCwide}$ ratio. As mentioned in the previous subsection, this effect is mitigated by the close and even distribution of same-sign and opposite-sign crossings that ensures that both types of crossings sample similar $\frac{ZDCwide}{BBCwide}$ ratios over the course of the 120 crossings. The spacing between crossing types is increased when only considering every second crossing in a run. We demonstrate in Figure 4.20 the continued deterioration of the asymmetry fits for increased crossing spacing by considering asymmetries comprised from data only from every third crossing, every fourth crossing, and so on.

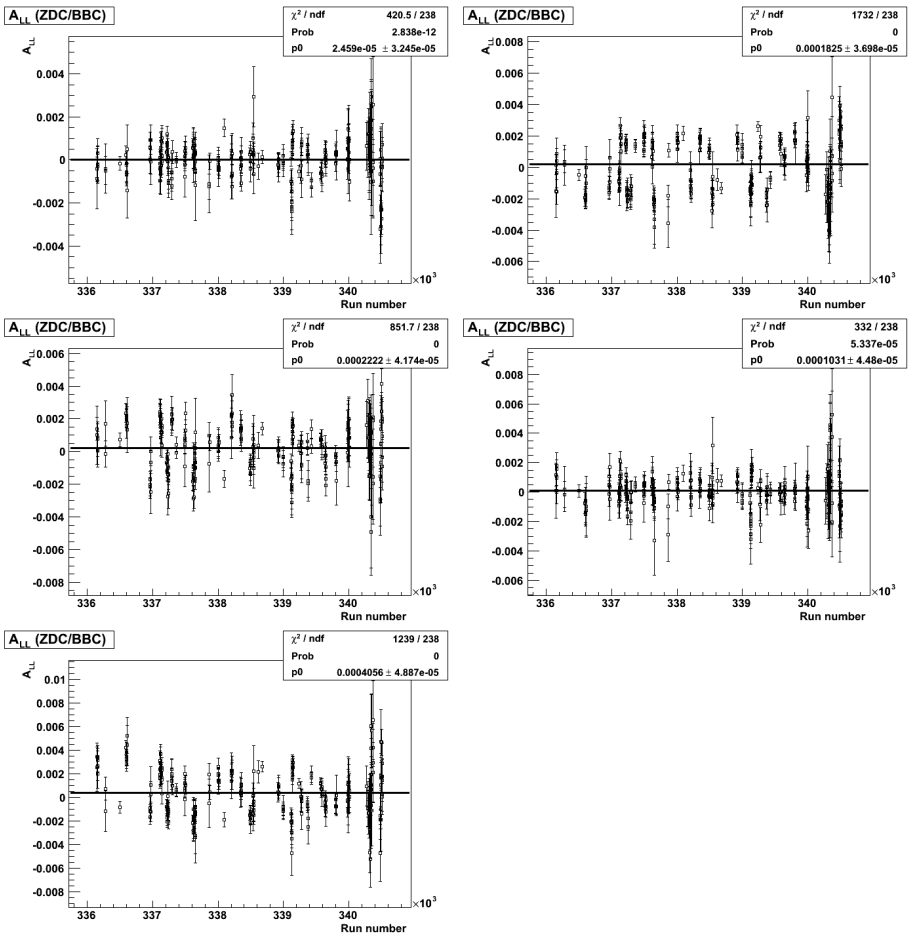

Figure 4.20: $A_{LL}(\frac{ZDCwide}{BBCwide})$ for every n^{th} crossing, for $n = 3$ to $n = 7$. For $n = 8$, the crossings included in the analysis would all be either same-sign or opposite-sign due to the periodicity of the spin pattern, so no asymmetry can be calculated.

4.6 Variation in $\frac{ZDCwide}{BBCwide}$ with crossing number

We found in the course of the relative luminosity analysis that while on a large scale (e.g. the sections of Run 11 used for determining k_N and k_S), the pileup corrections are effective and sufficient for ensuring consistent luminosity measurements between the ZDC and the BBC, this is not the case on the level of an individual run (see Figure 4.21). The problem is evident when considering a method of determining the run-by-run asymmetry via the bunch fitting method[5]. In this method, we define a function relating the $\frac{ZDCwide}{BBCwide}$ at each crossing n_C to the blue and yellow beam helicities for that crossing and a "raw"

[5]The bunch fitting method is mathematically equivalent to calculating A_{LL} by summing scalers in same-sign and opposite-sign crossings as is done in this chapter. The fitting method gives more information (via the χ^2/NDF) about how "well-behaved" the data is on a crossing-to-crossing level.

asymmetry:

$$(\frac{ZDCwide}{BBCwide})_{n_C} = \alpha(1 + S_{y,n_C} S_{b,n_C} \epsilon_{LL}), \tag{4.13}$$

where $S_{b(y),n_C} = +1$ if the blue (yellow) bunch at crossing n_C has positive helicity and -1 if it has negative helicity, and $\epsilon_{LL} = P_b P_y A_{LL}(\frac{ZDCwide}{BBCwide})$. Attempting to fit data with large non-statistical fluctuations in $\frac{ZDCwide}{BBCwide}$ with Equation 4.13 yields very large values of χ^2/NDF that call into question the validity of the fit.

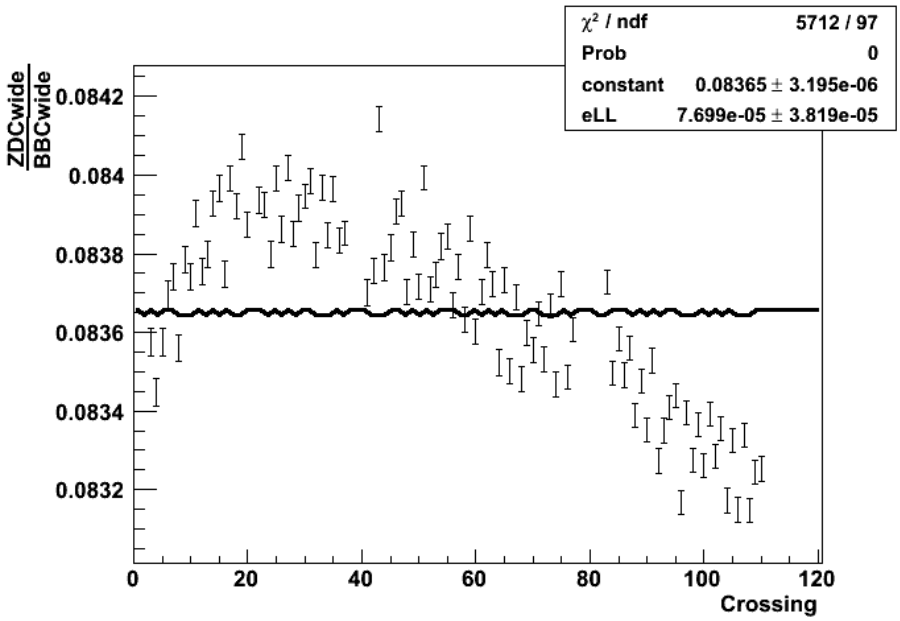

Figure 4.21: The scaler ratios from run 339134 show the characteristic relation to crossing number, peaking around crossing twenty and consistently falling off during the remaining crossings. The fit parameters show the result of the bunch fitting method for this run (Equation 4.13).

We can clarify the impact of the variation in $\frac{ZDCwide}{BBCwide}$ on our asymmetry calculations by rewriting Equation 4.9 with neither the ZDC nor BBC distinguished as the "yield" detector or the "relative luminosity" detector:

$$A_{LL}^{ZDC.}(BBC\,lumi) = \frac{1}{|P_b P_y|} \frac{\frac{N_{ZDC}^{++}}{N_{BBC}^{++}} - \frac{N_{ZDC}^{+-}}{N_{BBC}^{+-}}}{\frac{N_{ZDC}^{++}}{N_{BBC}^{++}} - \frac{N_{ZDC}^{+-}}{N_{BBC}^{+-}}}. \tag{4.14}$$

We see here that $A_{LL}(\frac{ZDC}{BBC})$ compares the pileup corrected $\frac{ZDCwide}{BBCwide}$ ratios in same-sign crossings to the ratios in opposite-sign crossings. We would expect this difference to be negligible in the absence of a physical asymmetry in particle production between the same-sign and opposite-sign crossings. However, we see from the average values of $\frac{ZDCwide}{BBCwide}$ as a function of crossing number that an opposite-sign crossing could have a smaller $\frac{ZDCwide}{BBCwide}$ than a same-sign crossing simply by having a larger crossing number.

Fortunately, we will see in the final calculation of $A_{LL}(\frac{ZDC}{BBC})$ that this problem is not fatal. The spin patterns employed at RHIC ensure an even distribution of ++ and +- crossings, such that the average crossing number of the crossing types are near one another. Roughly speaking, we have that the ratios $\frac{ZDCwide}{BBCwide}$ are modified by a crossing-dependent factor:

$$\frac{ZDCwide}{BBCwide} \rightarrow \frac{ZDCwide}{BBCwide} \times f(crossing\,\#). \tag{4.15}$$

If we assume that $\frac{ZDCwide}{BBCwide}$ has no double spin asymmetry, then the A_{LL} we measure is only sensitive to differences in the values of f between ++ and +- crossings. Abbreviating the crossing number as n_C, we have

$$A_{LL}(\frac{ZDC}{BBC}) \sim < f(n_C) >_{++\,crossings} - < f(n_C) >_{+-\,crossings}\,. \tag{4.16}$$

Finally, as $f(n_C)$ is more or less linear, we estimate that $< f(n_C) >= f(< n_C >$), so we write

$$A_{LL}(\frac{ZDC}{BBC}) \propto f(< n_C >_{++\,crossings}) - f(< n_C >_{+-\,crossings}),$$

which goes to zero as the difference in average crossing number between same-sign and opposite-sign crossings goes to zero.

While we escape trouble with the crossing-dependent $\frac{ZDCwide}{BBCwide}$ ratio when considering the overall $A_{LL}(\frac{ZDC}{BBC})$, the pattern is problematic in other ways. First, a method for determining $A_{LL}(\frac{ZDC}{BBC})$ on a run-by-run basis using a method known as bunch fitting yields fits with very large values of $\frac{\chi^2}{NDF}$ (see the fit parameters in Figure 4.22, for example), complicating the identification of the bunch-by-bunch statistical errors with true statistical fluctuations. A second point, related to the first, is that the bunch shuffling check on systematic errors breaks down. Finally, from a philosophical standpoint, if our goal is to precisely understand the relationship between the BBC's measurement of relative luminosity and the true relative luminosity and to confirm our understanding with the ZDC, we would like to understand why the two detectors count differently with respect to one another as a function of crossing number. We discuss attempts to address these issues in a future section. In the meantime, we will show how the $\frac{ZDCwide}{BBCwide}$ variations lead to large bunch shuffling widths and why this effect is not a concern for the final analysis.

4.6.1 Effect of crossing-dependent $\frac{ZDCwide}{BBCwide}$ variation on bunch shuffling widths

We return to Equation 4.14 and consider how bunch shuffled asymmetries are affected by a systematic variation in the ratio $\frac{ZDCwide}{BBCwide}$ that depends on crossing number. As explained in the previous section, such a variation is not problematic as long as same-sign and opposite-sign crossings are "evenly distributed"

over crossing numbers as they are in the data. However, bunch shuffling creates helicity configurations where same-sign crossings (or more accurately, crossings that have been randomly assigned a same-sign configuration) are more concentrated at early or late crossings compared to opposite-sign crossings. The strong correlation between crossing number and $\frac{ZDCwide}{BBCwide}$ means that for earlier crossings, $\frac{ZDCwide}{BBCwide}$ is larger than in later crossings. Therefore, when calculating $A_{LL}(\frac{ZDC}{BBC})$, a shuffle with more same-sign crossings at early crossings will tend to have larger values that enter into the positive term of the numerator of Equation 4.14, while the opposite-sign crossings at later crossings have smaller $\frac{ZDCwide}{BBCwide}$ values entering into the negative term in the numerator. The resulting $A_{LL,shuf.}(\frac{ZDCwide}{BBCwide})$ will be positive by virtue of whatever effect causes $\frac{ZDCwide}{BBCwide}$ to vary with crossing number, independent of a difference between the cross sections of same-sign and opposite-sign crossings. This effect is stronger for runs with larger slopes in the relation between $\frac{ZDCwide}{BBCwide}$ versus crossing number, while the effect is mitigated somewhat in runs with less statistics, where the increased uncertainty on $\frac{ZDCwide}{BBCwide}$ from crossing to crossing can mask the crossing dependence to some degree.

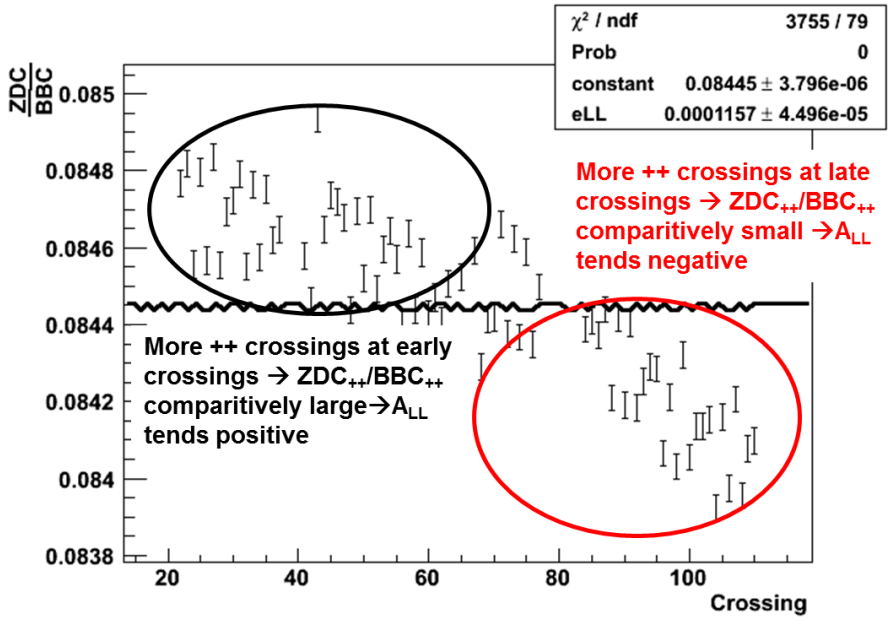

Figure 4.22: $\frac{ZDCwide}{BBCwide}$ vs. crossing for one run; disparity in the locations of same-sign and opposite-sign crossings can lead to false asymmetries.

We can demonstrate that the unexpectedly large bunch shuffled asymmetries arise from unphysical helicity configurations by defining a scaler-weighted average crossing number for same-sign and opposite-sign crossings:

$$< SS\,crossings >= \frac{\sum_{SS\,crossings} n_C \times BBCwide}{\sum_{SS\,crossings} BBCwide},$$

$$< OS\,crossings >= \frac{\sum_{OS\,crossings} n_C \times BBCwide}{\sum_{OS\,crossings} BBCwide}.$$

We take the difference between these two terms as a measure of the evenness of the distribution of crossing types. We then, for one run, compute these values for the 10,000 bunch shuffles and plot the resulting asymmetries against the evenness measure.

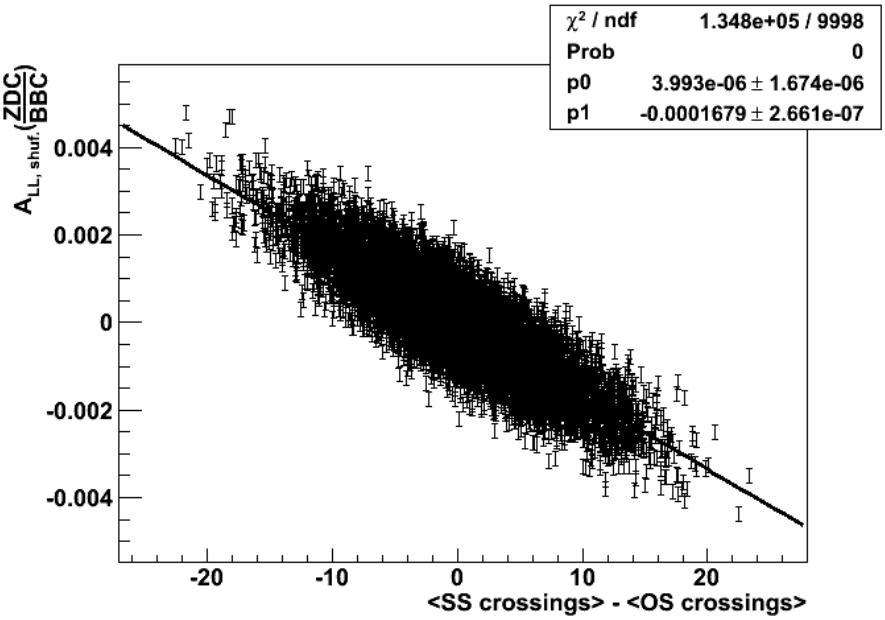

Figure 4.23: Bunch shuffled $A_{LL}(\frac{ZDC}{BBC})$'s for a single run (338677) are plotted against the difference in average crossing number for same-sign and opposite-sign collisions for each shuffle.

The results shown in Figure 4.23 are in line with expectations. When $< SS\,crossings > - < OS\,crossings >$is negative, the same-sign crossings are more concentrated at low crossing numbers where $\frac{ZDCwide}{BBCwide}$ is relatively large compared to the opposite-sign crossings concentrated at higher crossing numbers, leading to a positive $A_{LL}(\frac{ZDC}{BBC})$. The opposite is true when $< SS\,crossings > - < OS\,crossings >$is positive. We see in the data throughout Run 11 a relationship between the spread in $\frac{ZDCwide}{BBCwide}$ for a run, the average number of $BBCwide$ counts in a crossing from that run, and the width of the run's bunch shuffling distribution (see Figure 4.24).

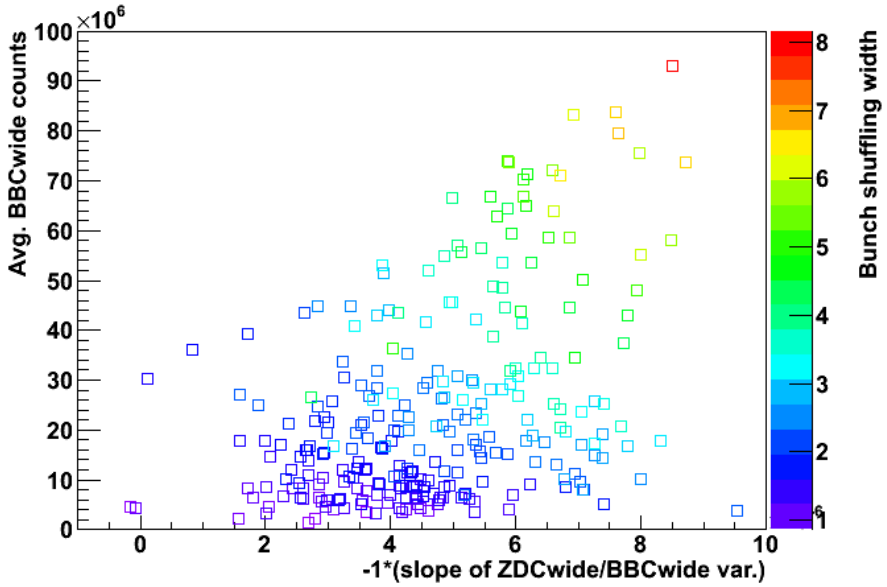

Figure 4.24: The effect of $\frac{ZDCwide}{BBCwide}$ variation and statistical precision on bunch shuffling widths in the data is shown in this 2D histogram. For small average $BBCwide$ counts, the statistical error bars cover the variation in $\frac{ZDCwide}{BBCwide}$ (as measured by the slope vs. crossing) to some extent, reducing the effect on the bunch shuffling widths. The measurement of $\frac{ZDCwide}{BBCwide}$ for each crossing becomes more precise with increasing $BBCwide$ counts, at which point the effect of increasing slopes of $\frac{ZDCwide}{BBCwide}$ on bunch shuffling widths becomes apparent.

While the widths of the bunch shuffling distributions are adversely affected by the crossing dependence of $\frac{ZDCwide}{BBCwide}$, we show through our determination of $A_{LL}(\frac{ZDC}{BBC})$ that the problem has a negligible impact on our final uncertainty on relative luminosity. In Figure 4.25, we plot $A_{LL}(\frac{ZDC}{BBC})$ vs. $< SS\,crossings > - < OS\,crossings >$instead of run number, fit to a constant in 4.25a and a line in 4.25b .

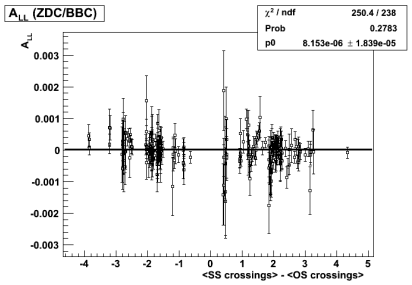

(a) $A_{LL}(\frac{ZDC}{BBC})$ vs. $< SS\,crossings > - < OS\,crossings >$ fit to a constant.

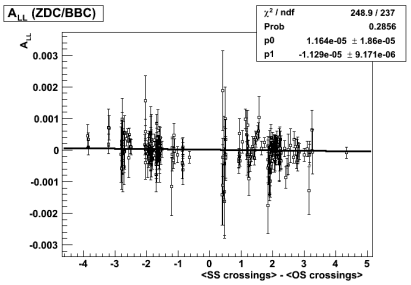

(b) $A_{LL}(\frac{ZDC}{BBC})$ vs. $< SS\,crossings > - < OS\,crossings >$ fit to a line; this fit only offers a minuscule improvement in $\frac{\chi^2}{NDF}$ compared to the constant fit. There is a slight dependence of $A_{LL}(\frac{ZDC}{BBC})$ on the helicity configuration, but only at a level slightly above 1σ.

Figure 4.25: Dependence of $A_{LL}(\frac{ZDC}{BBC})$ on distribution of same-sign and opposite-sign crossings.

We further confirm our hypothesis that the increased bunch shuffling widths come from the form of $\frac{ZDCwide}{BBCwide}$ vs. crossing number by generating test cases of data for hypothetical runs. The typical spread in $\frac{ZDCwide}{BBCwide}$ over a run is $(\frac{ZDCwide}{BBCwide})_{max} - (\frac{ZDCwide}{BBCwide})_{min} = 0.001$. We use spreads of 0, 0.0004, 0.001, and 0.003 in the test data. As mentioned before, the total number of scaler counts in a run also determines how statistically significant a given spread of scaler ratio values is, so we tune this number as well. We choose a typical value of $BBCwide$ to generate one test data set, and two other sets are generated with $\frac{1}{3}$ and 3 times the typical value of $BBCwide$.

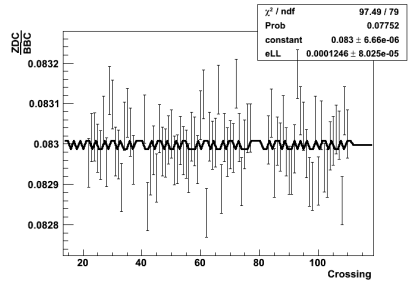

(a) A test run of data generated with the assumption that $\frac{ZDCwide}{BBCwide}$ does not depend on crossing number. The scalers in each crossing are randomly shifted according to a Gaussian error distribution.

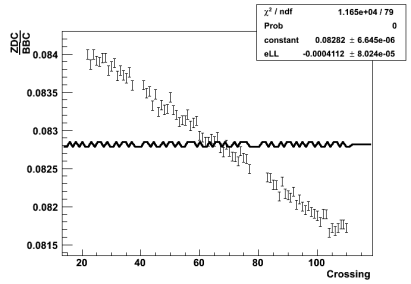

(b) A test run of data generated with a large variation in $\frac{ZDCwide}{BBCwide}$ and a large number of statistics. Both are about $3x$ what is seen in a typical run of real data.

Figure 4.26: Examples of $\frac{ZDCwide}{BBCwide}$ vs. crossing from test data.

We bunch shuffle the test data sets in the same manner as for the real data; the results are shown in Figure 4.27. We see that as the slope of the correlation between $\frac{ZDCwide}{BBCwide}$ and crossing number increases (moving down the

rows in Figure 4.27), the bunch shuffling widths increase from around one to greater than eight, with increased statistical precision (moving to the right in Figure 4.27) amplifying the effect of the slope on the widths even further.

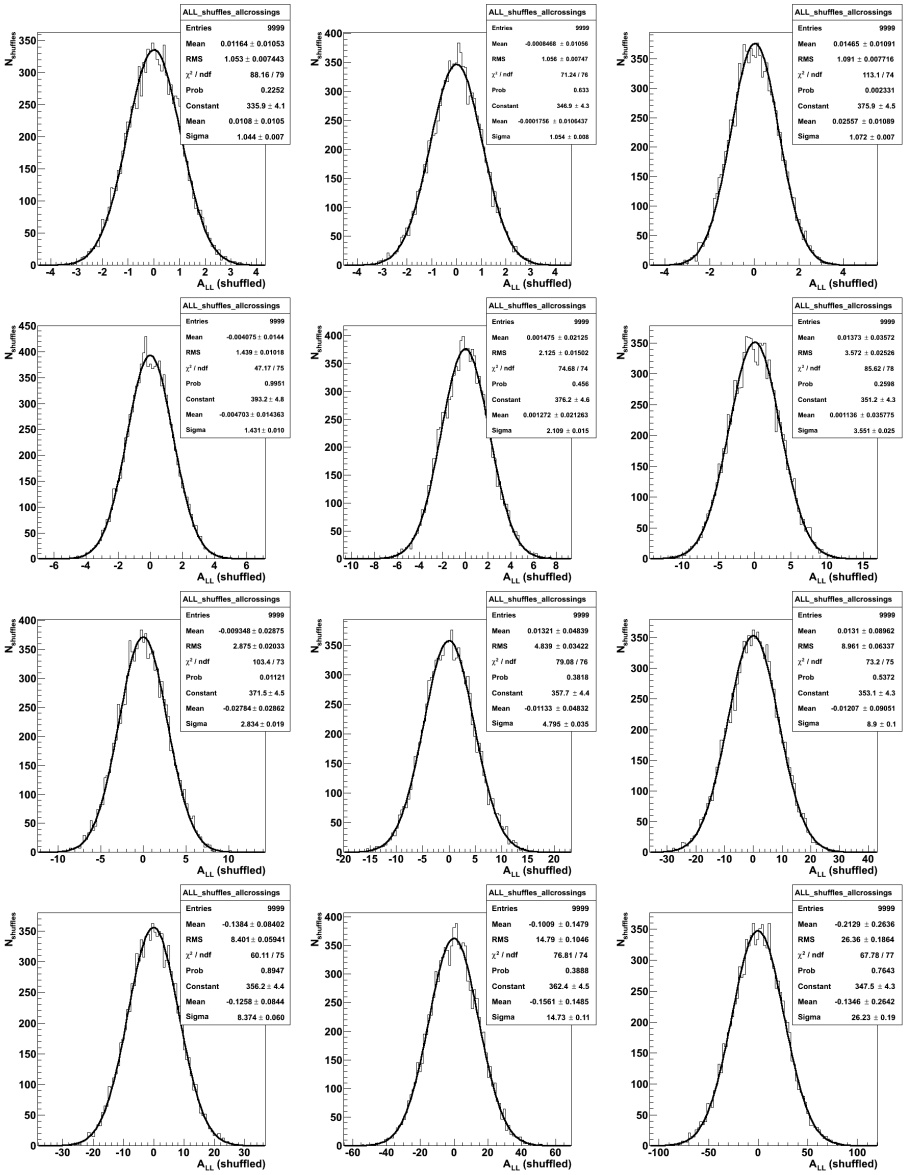

Figure 4.27: Bunch shuffling for test data. Each row represents one choice for the spread in $\frac{ZDCwide}{BBCwide}$ as discussed in the text, with the spread starting at 0 in the top row and increasing for the following rows. Each column represents one of the selection for the total $BBCwide$ counts; the first column is $\frac{1}{3}$ of the typical value, the middle column is the typical value, and the third column is 3 times the typical value.

4.6.2 The nature of the $\frac{ZDCwide}{BBCwide}$ dependence on crossing number

Even if the combination of statistics and the crossing dependence of the scaler ratio $\frac{ZDCwide}{BBCwide}$ in Run 11 is not enough to significantly increase our uncertainty in determining relative luminosity, this may not be the case in future runs with higher luminosity, longer runs, and different variations of $\frac{ZDCwide}{BBCwide}$ with crossing number. For this reason, we have undertaken further studies of this systematic effect in hopes of understanding the cause.

4.6.2.1 Form of the dependence

The qualitative features of the graph of $\frac{ZDCwide}{BBCwide}$ vs. crossing are very similar across all runs and all sections of Run 11. The main feature is a linearly decreasing trend starting around crossing 20 with notable outliers that tend to fall around the empty-full crossings. The first twenty crossings are less consistent but tend to have $\frac{ZDCwide}{BBCwide}$ scaler ratios that begin at nearly the same level as some of the later crossings but quickly rise to a peak around crossing 20. To demonstrate the universality of this effect, we plot the scaler ratio and crossing number for each crossing passing QA cuts from all runs in a section of Run 11.

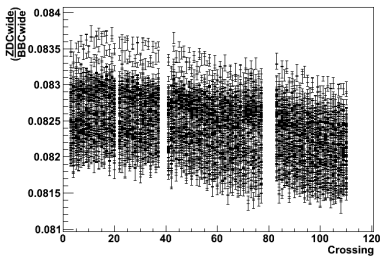

(a) ZDC-to-BBC ratios from all good crossings from runs between 338450 and 339700.

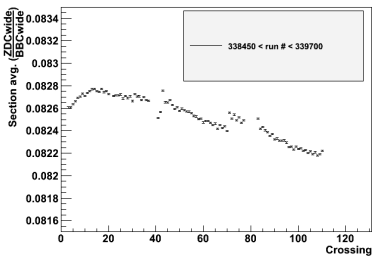

(b) For each crossing, the statistics-weighted average for all crossings in a section of Run 11 is plotted against the crossing number.

Figure 4.28: Scaler ratios vs. crossing for runs between 338450 and 339700.

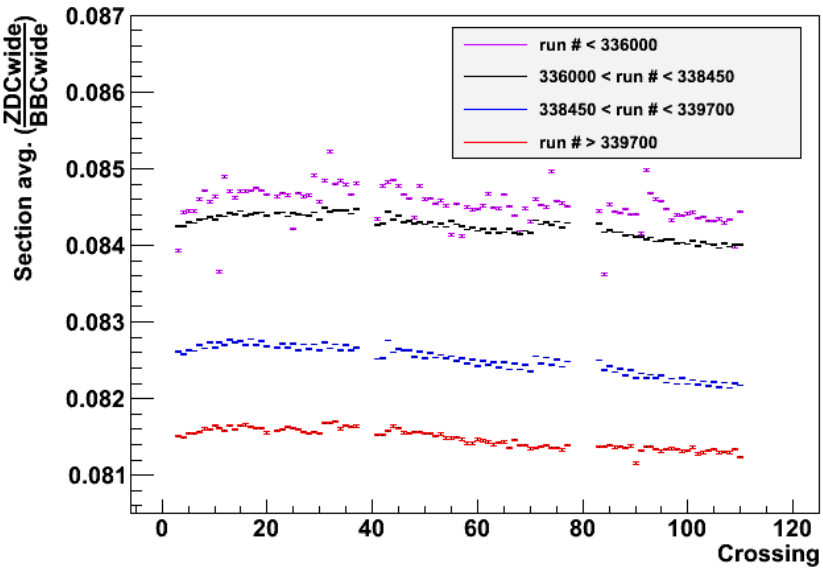

Figure 4.29: Scaler ratio splines for the four sections of Run 11.

We can also examine the strength of the correlation between $\frac{ZDCwide}{BBCwide}$ and crossing number for each run. This correlation can be measured either by a correlation factor or from the slope of a linear fit to $\frac{ZDCwide}{BBCwide}$ vs. crossing number. The correlation factor between the set of ordered pairs $(\frac{ZDCwide}{BBCwide}, n_C)$ in a run is given by

$$corr(\frac{ZDCwide}{BBCwide}, n_C) = \frac{cov(\frac{ZDCwide}{BBCwide}, n_C)}{\sigma_{\frac{ZDCwide}{BBCwide}} \sigma_{n_C}}.$$

The correlation factor method is disadvantageous in that it does not account for error bars, while using the slope instead as a measure of correlation can tell us how big of an effect results from the correlation but not how good the correlation is. For both measures, we exclude the first 20 crossings that tend not to follow the same trend as the remaining crossings, as discussed above.

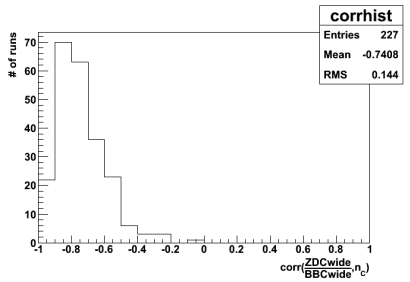

(a) The distribution of correlation factors between the scaler ratios and crossing number within individual runs is shown. Nearly all runs show a significant negative correlation meaning $\frac{ZDCwide}{BBCwide}$ decreases with increasing crossing number.

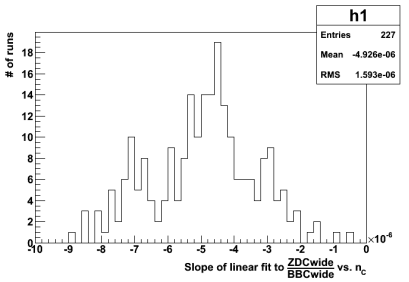

(b) Slopes of linear fits to the data are all negative. A slope of -5×10^{-6} over 90 crossings (from 20 to 110) corresponds to a decrease in the scaler ratio of 0.00045 or a change of -0.5% for a typical $\frac{ZDCwide}{BBCwide}$ of 0.083.

Figure 4.30: Strength of correlation between scaler ratio and crossing number in individual runs.

4.6.2.2 Correlation between the scaler ratio and other variables

We have other information in the data on the level of an individual crossing, including coincidence rates, singles rates, singles-to-doubles ratios, and measures of the width of the collision vertex distribution[6]. By looking at how this other data varies with crossing number and for correlations between these data and the scaler ratios, we try to understand the underlying cause of the crossing dependence of $\frac{ZDCwide}{BBCwide}$. We present here distributions of correlation factors on the level of individual runs between $\frac{ZDCwide}{BBCwide}$ and these data.

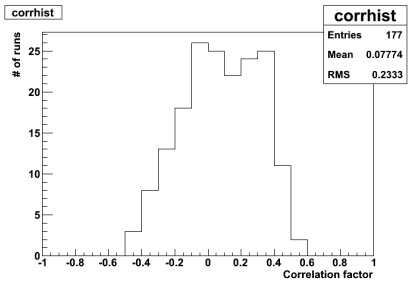

(a) Run-by-run correlation factors between $\frac{ZDCwide}{BBCwide}$ and $BBCwide$ rate.

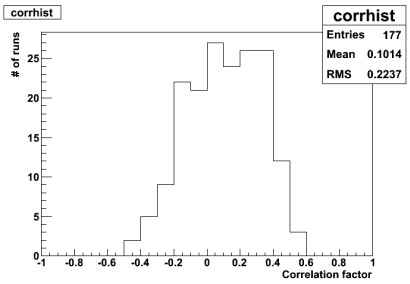

(b) Run-by-run correlation factors between $\frac{ZDCwide}{BBCwide}$ and $ZDCwide$ rate.

Figure 4.31: Correlations between scaler ratios and coincidence rates.

[6]We use wall current monitor data from each crossing to generate unbiased vertex distributions. For more details, see [58].

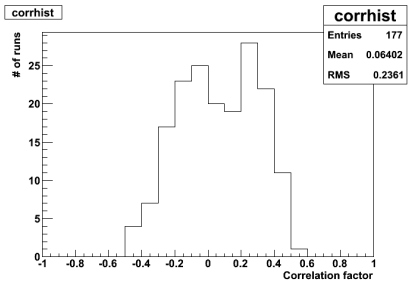

(a) Run-by-run correlation factors between $\frac{ZDCwide}{BBCwide}$ and $BBCS$ exclusive single-arm rate.

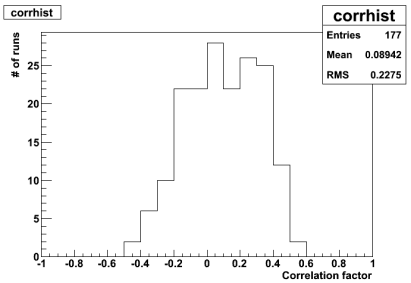

(b) Run-by-run correlation factors between $\frac{ZDCwide}{BBCwide}$ and $ZDCS$ exclusive single-arm rate.

Figure 4.32: Correlations between scaler ratios and south arm exclusive singles rates.

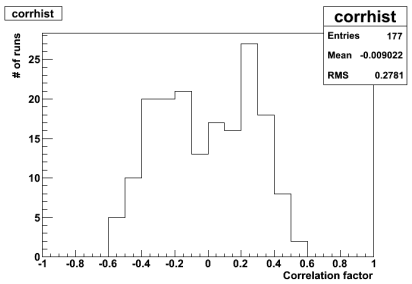

(a) Run-by-run correlation factors between $\frac{ZDCwide}{BBCwide}$ and the $BBCN$ exclusive single-arm rate.

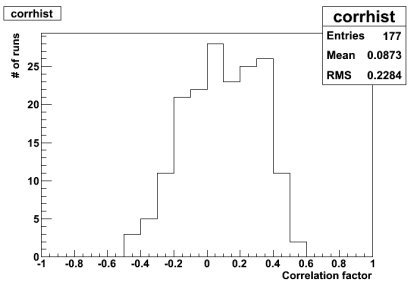

(b) Run-by-run correlation factors between $\frac{ZDCwide}{BBCwide}$ and $ZDCN$ exclusive single-arm rate.

Figure 4.33: Correlations between scaler ratios and north arm exclusive singles rates.

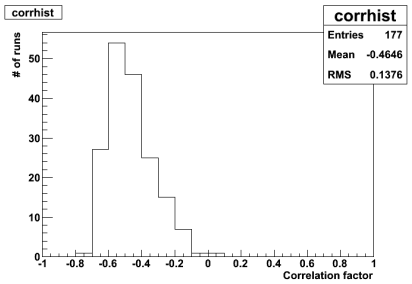

(a) Run-by-run correlation factors between $\frac{ZDCwide}{BBCwide}$ and $BBC\,k_S$.

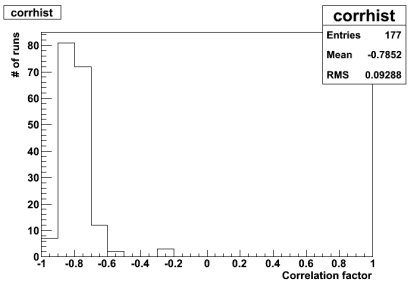

(b) Run-by-run correlation factors between $\frac{ZDCwide}{BBCwide}$ and $ZDC\,k_S$.

Figure 4.34: Correlations between scaler ratios and singles-to-doubles ratios.

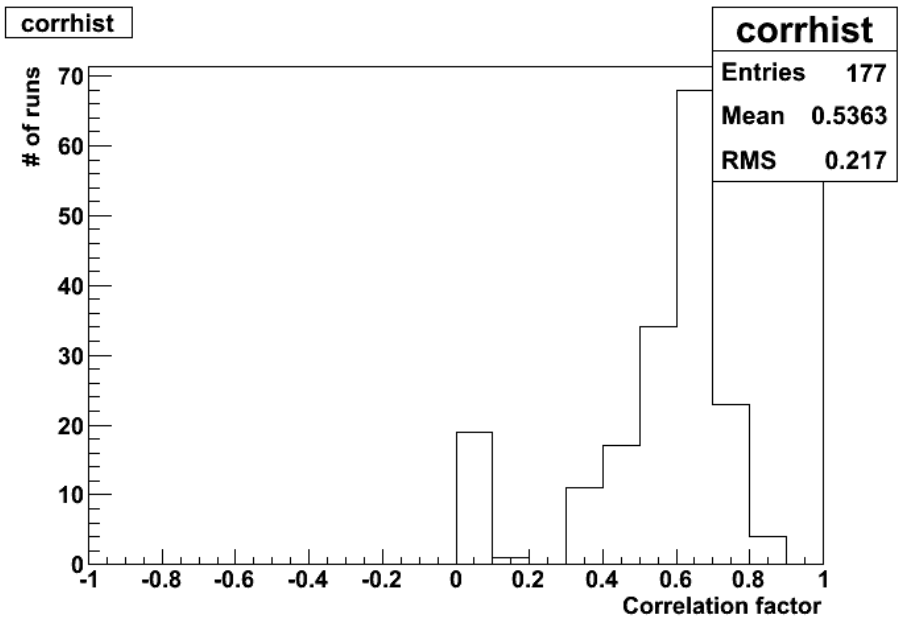

Figure 4.35: Run-by-run correlation factors between $\frac{ZDCwide}{BBCwide}$ and the widths of the vertex distributions derived from wall current monitor data.

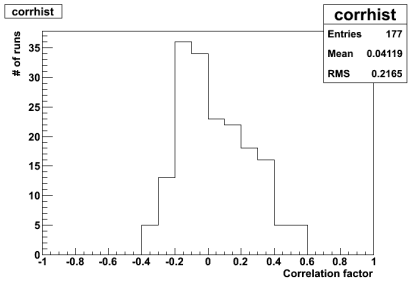

(a) Run-by-run correlation factors between $\frac{ZDCwide}{BBCwide}$ and BBC vertex distribution RMS.

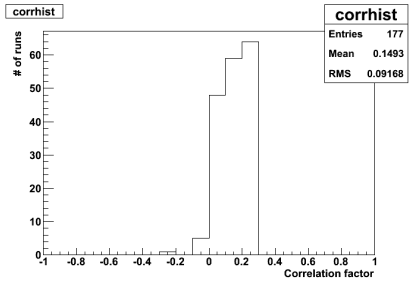

(b) Run-by-run correlation factors between $\frac{ZDCwide}{BBCwide}$ and ZDC vertex distribution RMS.

Figure 4.36: Correlations between scaler ratios and width of vertex distributions.

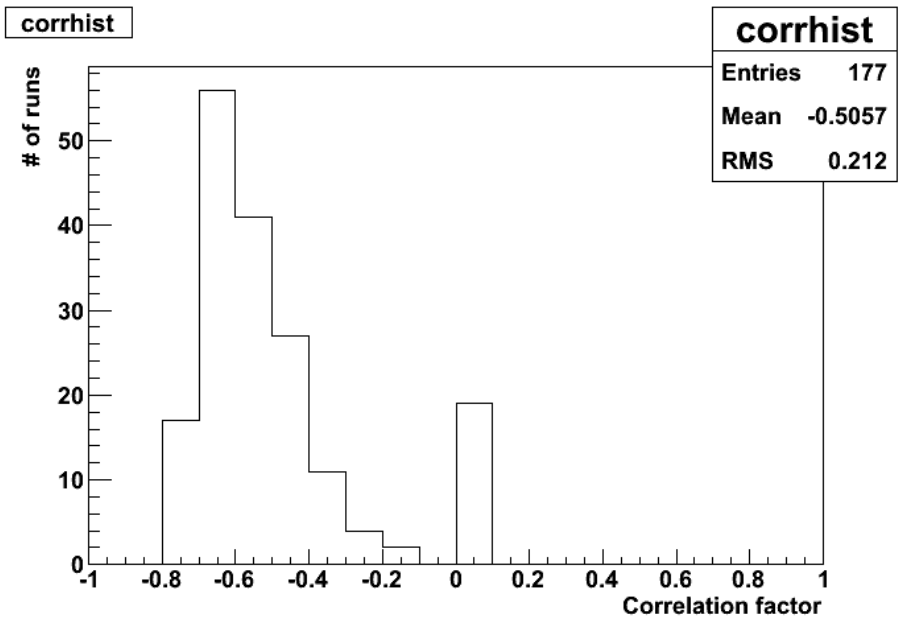

Figure 4.37: Correlation factors between $ZDC\,k_S$ and width of vertex distributions derived from wall current monitor data.

4.6.3 Possible sources of variation in scaler ratio vs. crossing number

From the plots in subsubsection 4.6.2.2, we see that the best candidates for a strong correlation to the scaler ratio are the singles-to-doubles ratio (especially $ZDC\,k_S$) and the width of the collision vertex distribution as taken from wall current monitor data. On the whole, we do not see evidence for a correlation between $\frac{ZDCwide}{BBCwide}$ and single-arm or coincidence rates, though there may be some slight correlations due to correlations between the rates and the other variables.

Variation of singles-to-doubles ratios within single runs We first consider the possible correlation between crossing-to-crossing variations and the singles-to-doubles ratios. For the purpose of this exercise, we will look at run 338925 from fill 15419. Over the range of crossings in this run, the scaler ratio drops from 0.0829 around crossing 20 to 0.0823 around crossing 100, so we have a percent change of 0.7%. In Figure 4.39, we show the variation in the singles-to-doubles ratios through the run. In order to use our method of extrapolating to zero rate to find k_S for the pileup correction, we can only choose a single value of k_S for each fill, and we ignore the crossing dependence of the singles-to-doubles ratios in applying the pileup correction. This imprecision could theoretically lead to a crossing-dependent error in the pileup correction that could cause the variation in the scaler ratio. The "raw" BBCS singles-to-doubles ratios (not extrapolated to zero rate) fall in a range from 0.223 to 0.225. Shifting this

range to the zero-extrapolated value for the fill of 0.22937 and taking from the data $BBCwide_{uncorr.} = 0.26$, we find that the range of $BBC\,k_S$ values could account for a change in the corrected $BBCwide$ rate of 0.03%. Similarly, the range in $ZDC\,k_S$ of ~ 0.03 could lead to a change in the $ZDCwide$ rate of 0.3%. While this gets factor gets close to the 0.7% difference in the scaler ratio from crossing 20 to crossing 100, the change would be applied in the wrong direction. The later crossings have larger $ZDC\,k_S$ than the early crossings; as a larger $ZDC\,k_S$ yields a smaller corrected $ZDCwide$ rate, the effect of implementing the varying $ZDC\,k_S$ would be to further decrease the $\frac{ZDCwide}{BBCwide}$ ratio at higher crossing numbers. For this reason, it seems more plausible that the crossing-dependent variation of the singles-to-doubles ratio has a cause in common with the scaler ratio variation rather than being the cause of the variation through pileup corrections.

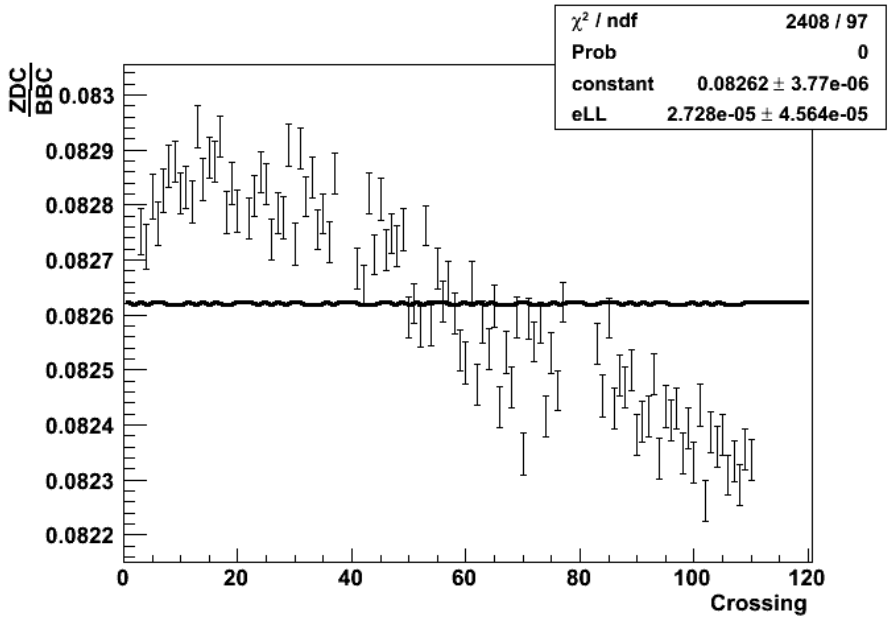

Figure 4.38: $\frac{ZDCwide}{BBCwide}$ ratios for Run 338625.

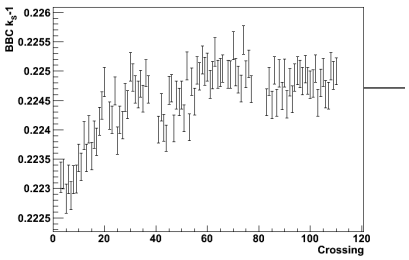

(a) Run-by-run correlation factors between $\frac{ZDCwide}{BBCwide}$ and BBC vertex distribution RMS.

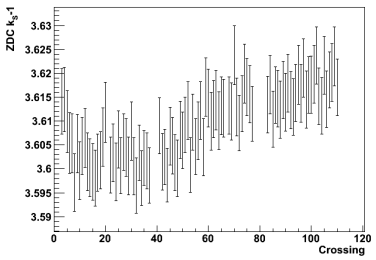

(b) Run-by-run correlation factors between $\frac{ZDCwide}{BBCwide}$ and ZDC vertex distribution RMS.

Figure 4.39: BBC and ZDC south arm singles-to-doubles ratios vs. crossing for Run 338925.

Crossing dependence of collision vertex distribution widths Trends similar to what we see in the plots of $\frac{ZDCwide}{BBCwide}$ vs. crossing are also present in plots of vertex distribution width vs. crossing (see Figure 4.40).

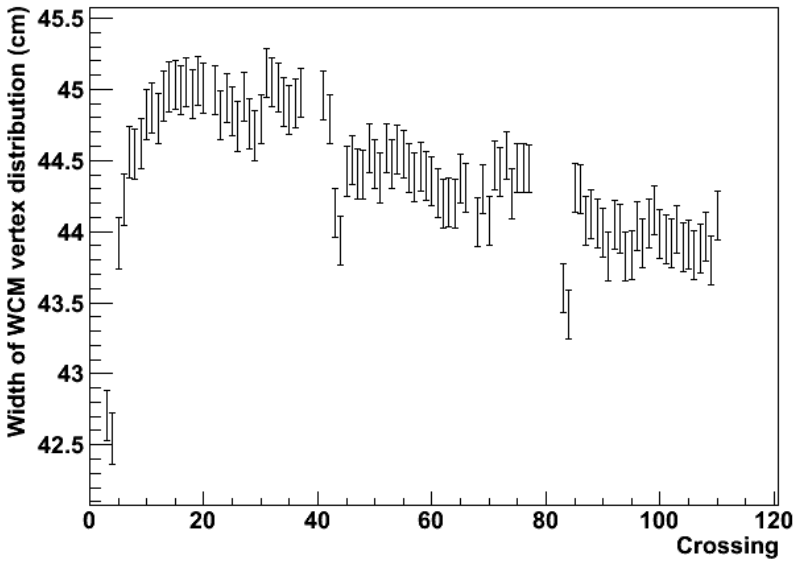

Figure 4.40: Vertex distribution widths for Run 338925

The scaler ratio could be sensitive to the vertex widths due to differences in acceptance between the BBC and the ZDC. Theoretically, the scaler ratio variation could also be a result off the limited ZDC resolution in conjunction with the fiducial vertex cut at $150\,cm$ for the *ZDCwide* trigger; we eliminated this second possibility by generating the scaler ratios using a simple ZDC coincidence trigger from the STAR scalers that did not include a vertex cut. There was no noticeable difference in the crossing dependence of the scaler ratios.

As for detector acceptance effects, the ZDC is located at $|z| = 18\,m$, we

assume its acceptance is flat within $z = \pm 150\,cm$. We know from Vernier scans in Run 11, though, that the BBC acceptance falls off compared to the ZDC as $|z|$ approaches 150 cm[62].

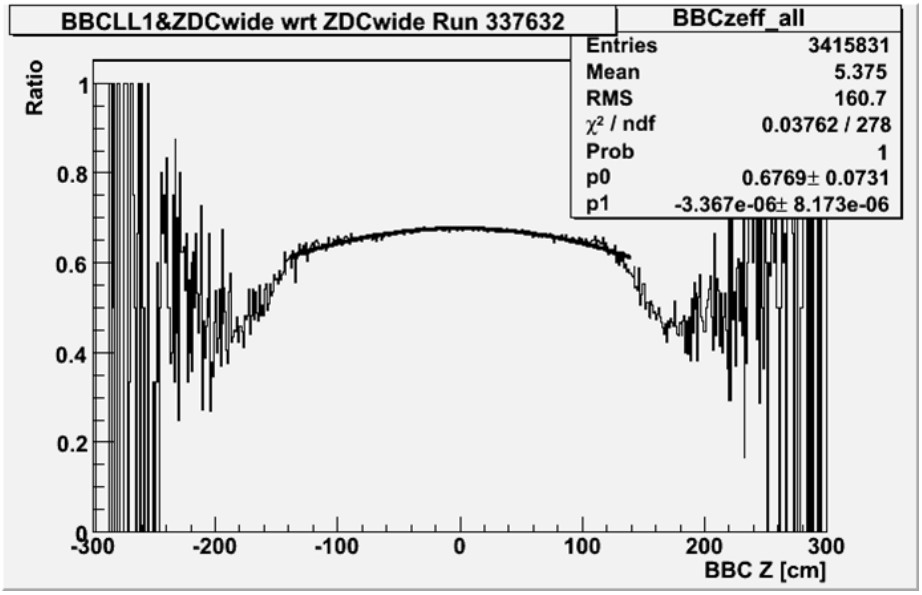

Figure 4.41: Plot of BBC acceptance as a function of $|z|$. The data shown is $\frac{(BBCwide\,\&\&\,ZDCwide)}{ZDCwide}$.

We can use the acceptance function, $a_{BBC}(z) = p_0 + p_1 z^2$, taken from the fit to modify the raw *BBCwide* scalers by a factor that increases with increasing vertex distribution width to account for would-be coincidences that are lost due to the BBC's limited acceptance at large $|z|$. To determine the correction factor, we generate a Gaussian $g(z, vtx\,RMS)$ centered at $z = 0\,cm$ with a width taken from the wall current monitor data and a flat function, $a_{flat}(z)$ with the same $p0$ as the acceptance function. The correction factor is the ratio of the integral of the Gaussian with no acceptance modification to the integral of the acceptance-modified Gaussian:

$$f_{acc} = \frac{\int_{-150}^{150} g(z, vtx\,RMS) \times a_{flat}(z) dz}{\int_{-150}^{150} g(z, vtx\,RMS) \times a_{BBC}(z) dz}. \tag{4.17}$$

The correction factor is applied to the *BBCwide* scalers before pileup corrections. We use a typical *BBCwide* rate of 0.26 to demonstrate the final impact on the rates, as a correction applied before pileup corrections will lead to a different pileup correction factor as well.

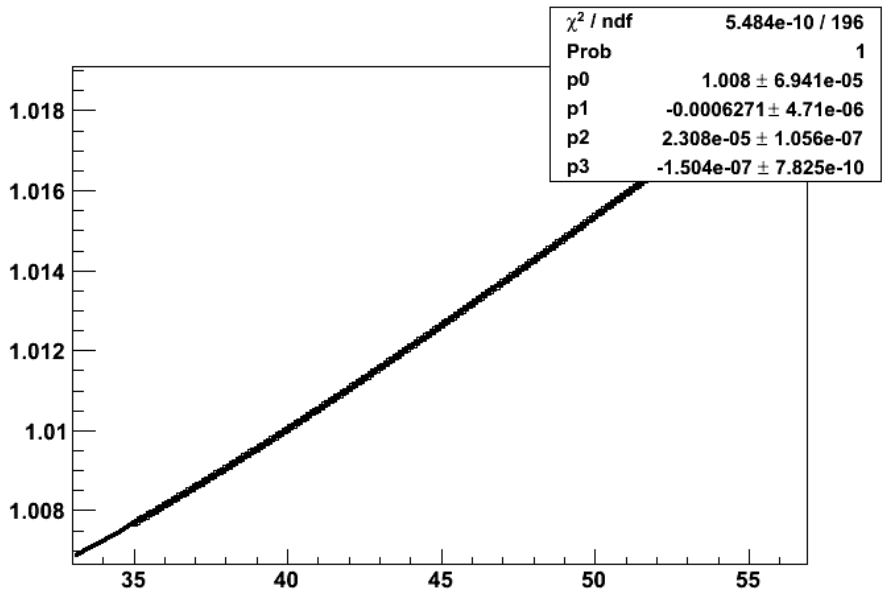

Figure 4.42: Effect of z-dependent BBC acceptance on final *BBCwide* rates.

In Figure 4.42, we see that over the range of vertex widths seen during the course of Run 11, the BBC acceptance factor can change by around 1%. However, the majority of fills have a spread in vertex distribution widths less than $2.5\,cm$ with none greater than $4\,cm$; therefore, a more realistic expectation of the effect of an acceptance correction is on the order of 0.1%, too small to account for the $\frac{ZDCwide}{BBCwide}$ crossing dependence. Additionally, any correlation between $\frac{ZDCwide}{BBCwide}$ and vertex width is washed out when considering crossings from many fills simultaneously in most of Run 11. Interestingly, after the 9 MHz radio frequency system involved in confining protons in bunches failed around run 339700, a strong correlation between the scaler ratio and the vertex width reappears along with larger vertex widths in general for the rest of the run.

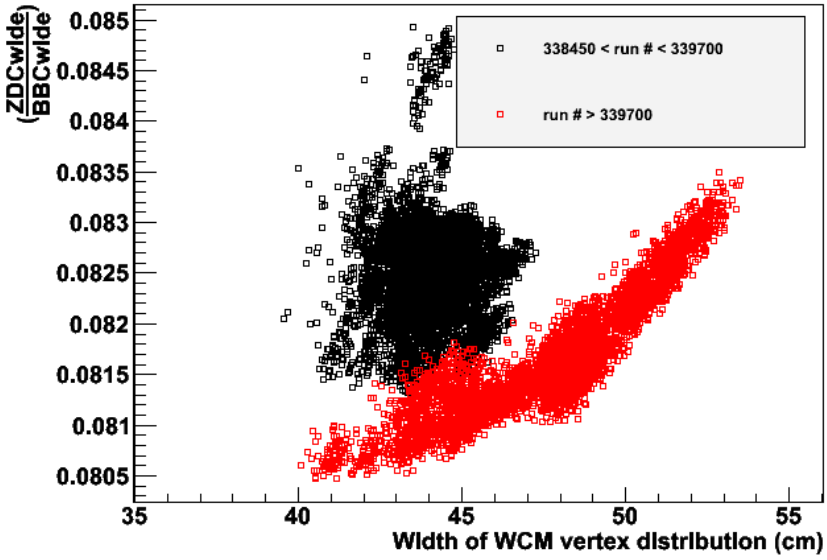

Figure 4.43: Relation between scaler ratios and vertex distribution widths, before and after the failure of the 9 MHz RF cavity around run 339700.

4.7 Summary of relative luminosity status

For the beam intensity in Run 11, the pileup corrections work sufficiently well and the crossing dependence of $\frac{ZDCwide}{BBCwide}$ can be safely ignored for the purposes of determining relative luminosity. Our final value of $A_{LL}(\frac{ZDCwide}{BBCwide})$, as determined from a fit to run-to-run calculations of the asymmetry, is $(0.88 \pm 1.8) \times 10^{-5}$. We see no systematic dependence of the asymmetry on spin pattern. We also scan over a range of values of k_S and k_N for the BBC and ZDC to estimate the systematic uncertainty that enters through the pileup correction. The resulting spread in $A_{LL}(\frac{ZDCwide}{BBCwide})$ over all scanned values of k_S and k_N is 1.3×10^{-5}, though the asymmetries calculated from all scanned values are consistent with one another. We nevertheless use the spread as an estimate of this systematic uncertainty.

While we seem to have the uncertainty from relative luminosity under control in Run 11 without needing to adjust error bars to account for poor χ^2/NDF values in the bunch fitting, it remains to be seen whether the approach set forth in this note will be as successful in Run 13. The increase in bunch-to-bunch luminosities in Run 13 may result in the crossing dependence of $\frac{ZDCwide}{BBCwide}$ being a critical problem. We have laid out ideas of where to look for the cause of the scaler ratio variation, but no single factor seems to explain everything. We may need to finally track down the source of the variation and correct for it to achieve similar precision in our relative luminosity measurement for Run 13 and beyond.

Chapter 5

MPC Calibration

To extract useful physics information from the MPC, we need to convert the "raw" information provided by the detector, essentially in the form of charge output and timing from the avalanche photodiodes attached to each crystal in the detector, to information about the energy deposited by particles incident on the detector. A comprehensive overview of this process is detailed in an analysis note written for the PHENIX collaboration[63]. In a condensed form, the conversion from charge to energy can be represented for each individual tower i by the following equation:

$$E_i = ADC_i \times G_i \times R_i(t), \tag{5.1}$$

where ADC_i (Analog-to-Digital Converter) is the charge measurement output by the detector for tower i, G_i is the gain, or the charge-to-energy conversion factor for tower i, and $R_i(t)$ is a factor that accounts for variations in crystal and APD output over time. Each of the terms on the right are the result of a subset of the MPC calibration. The ADC_i values depend on calibration of the MPC's front-end electronics module (FEM); the G_i are determined from a calibration process wherein the detector's ADC representations of energy are mapped to physical values via comparison to physical parameters, namely known energy spectra and the π^0 mass; and the $R_i(t)$ are measured by an LED monitoring system that tracks the response of the detector to stable pulses of light delivered to each crystal individually in the MPC.

5.1 FEM Calibration

What appears in Equation 5.1 as ADC_i is calculated offline as the combination of multiple measurements. From the discussion in subsection 2.3.3, we have

$$ADC_i = ADC_{post} - ADC_{pre} - (ADC_{post,pedestal} - ADC_{pre,pedestal}) \tag{5.2}$$

for both the low-gain ADC and the high-gain ADC. A conversion factor between the low-gain and high-gain ADC must be found to ensure that the low-gain and high-gain ADC give the same results. Also, we must determine the high-gain overflow value, above which the high-gain ADC is no longer suitable for use.

The pedestals are calibration constants that are measured when the MPC is operational but no beam is present. In practice, these values have been found to be stable over the course of the run and subtract to 0 in the above equation anyway. Therefore, they are ignored in our analysis.

Additionally, we determine when the low-gain ADC overflows, at which point the recorded ADC value is unreliable. TDC overflow values are also found and used to isolate towers in the MPC that are out of time from the particles associated with a collision of interest.

5.1.1 High-gain to low-gain conversion factor/high-gain cutoff

The amplified (high-gain) ADC yields a higher ADC value for a given energy than does the low-gain ADC. The readings from tower i are related by the following equation:

$$\frac{ADC_{i,high}}{C_i} = ADC_{i,low}. \tag{5.3}$$

The amplification factor for the high-gain ADC was set in the hardware to be around 16, but the actual value varies slightly from tower to tower. In the software, this amplification factor is divided out so that a single G_i can be used for each tower to convert from ADC to energy, regardless of whether the high-gain or low-gain ADC is used.

To find the high/low ratio C_i for a given tower, the point at which the high-gain ADC overflows must first be identified, as this gives the endpoint of the range where the high-gain ADCs are valid. To this end, we plot a histogram of the high-gain $ADC_{post} - ADC_{pre}$ values. The overflow is characterized by a large peak at the end of the falling ADC spectrum; any charge that would be measured as having an ADC value greater than 4095 is dumped into the last ADC bin. The peak is lower than 4095 and broadened because the ADC we record includes the subtracted ADC_{pre} value, which does not overflow and can vary. We find the characteristic peak at high ADCs and work back to lower ADCs to find the minimum of the spectrum in a certain range. The bins to the right of this minimum have increasing numbers of counts in contradiction to the expectation of a consistently falling spectrum, so high-gain ADCs in this range are potentially misleading overflows and cannot be used.

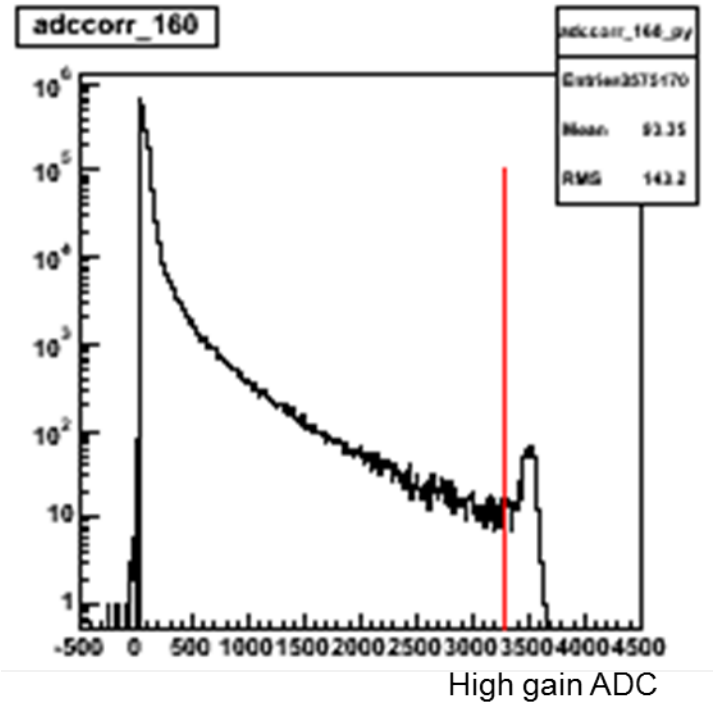

Figure 5.1: A plot of the high-gain ADC spectrum for one tower. The vertical red line is drawn where an algorithm determined the overflow to be.

Next, we compare the high-gain and low-gain ADC readings for a large number of hits in a given tower. We plot the low-gain ADC versus the high-gain ADC for each hit, and we fit a line in a range bounded on the low end by 0 and on the high end by the high-gain overflow values we found (see 5.2a). The inverse of the slope of this line gives us the constant C_i from Equation 5.3. Alternatively, we can generate a one-dimensional histogram of the ratio of the high-gain to low-gain ADC values for a tower. The peak (taken either as the mean of the histogram or as the peak of a Gaussian fit to the histogram) would also give us an estimate of C_i.

Figure 5.2: Methods for finding the low-gain conversion factor.

(a) Here, the low gain ADC is plotted vs. the high gain ADC, and the ratio is found from the slope of the line fit to the graph. The blue line represents the high gain overflow point and serves as the upper limit for the fit.

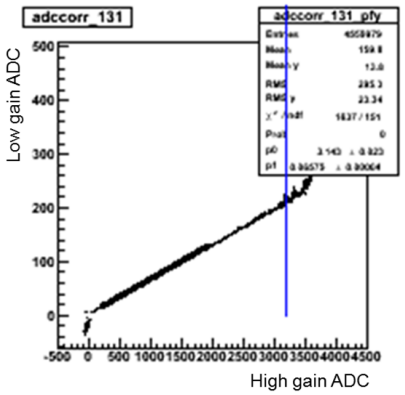

(b) The distribution of high gain ADC to low gain ADC ratios is shown. The conversion factor can be taken as the mean of this distribution.

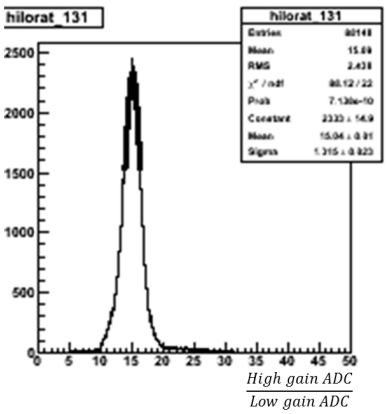

Ultimately, for each tower, we compared the resulting low-gain ADC spectrum and the high-gain ADC spectrum scaled by $\frac{1}{C_i}$, for each of the methods mentioned above for determining C_i. A "matching factor" M is defined: $M = \sum_k^{\#\,of\,bins} \frac{1}{\#\,of\,bins} |N_k(\frac{high\,ADC}{C_i}) - N_k(low\,ADC)|$, where the N_k are the number of counts N in histogram bin k. Whichever C_i gives the smallest value of M for tower i is the final value used.

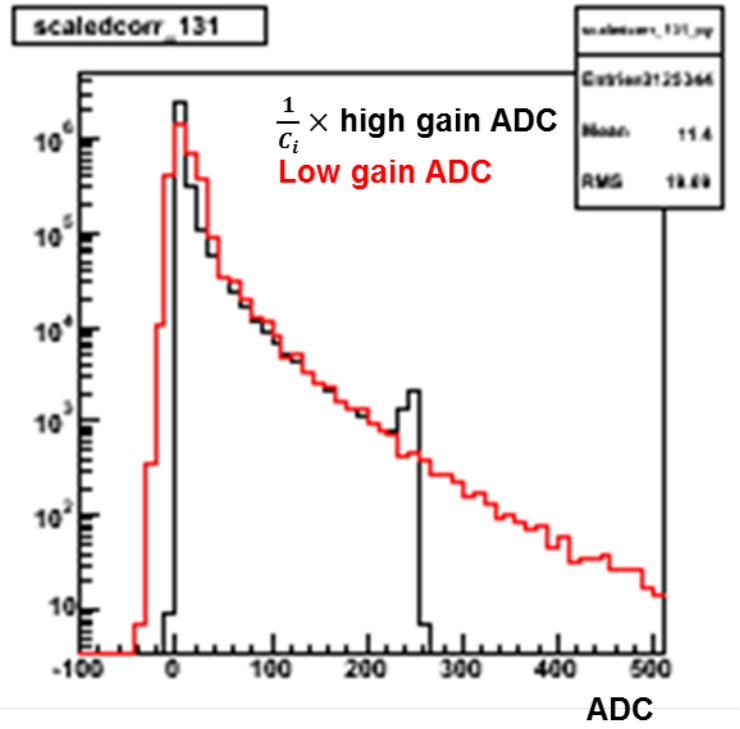

Figure 5.3: Comparison of the high gain ADC spectrum (black), scaled down by the conversion factor, to the low gain ADC spectrum (red).

5.1.2 ADC, TDC Overflows

The low gain ADCs and the TDCs for each tower can overflow in the same way as the high gain ADC overflows discussed in the previous section. The low gain ADC overflow corresponds to an amount of energy deposited in a crystal (or more directly, charge collected in the APD) that surpasses the dynamic range of the ADC. A TDC overflow for a channel indicates a hit that came too late for the TDC to receive the stop signal, where the TDC start time is determined by the BBC's measurement of the collision time. A cut based on the TDC overflow helps to eliminate out-of-time particles not originating from the *pp* collision.

The same procedure is used to find the overflows for the low-gain ADCs, the high-gain ADCs, and the TDCs. An example plot showing the overflow determination for the high-gain ADC was included in the previous section in Figure 5.1; we present examples for the low-gain ADCs and the TDCs in Figure 5.4.

Figure 5.4: Overflow examples for the low-gain ADC and the TDC.

(a) The low gain ADC spectrum for one tower from one run is shown. The vertical red line is drawn where the ADC overflows, represented by a spike in the spectrum at high ADC.

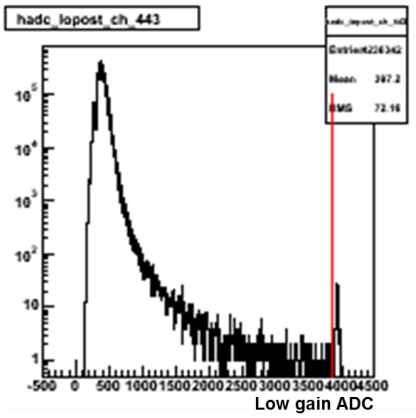

(b) The TDC distribution for one channel from one run with the overflow marked by a red line.

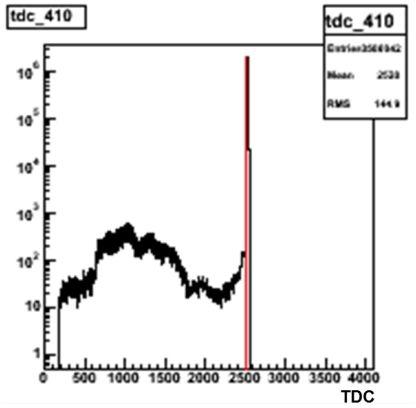

5.1.3 Confirmation of Channel Mapping

Each channel corresponds to a physical location, tracked by a mapping in the MPC calibration database from channel number to x, y, and z coordinates. This arrangement depends on consistent and accurate cabling from the APDs to the front-end electronics, but a swapped connection on the hardware side can lead to data from towers not appearing where it ought to in the data. We can check for mislocated towers by examining tower-to-tower correlations in energy deposits. First, we define two energy thresholds, a higher "primary" threshold and a lower "secondary" threshold. We then determine the probability $P(j \mid i)$ that if tower i registered an energy deposit greater than the primary threshold, tower j also reported a hit with energy greater than the secondary threshold. Conceptually, an electromagnetic shower that deposits significant energy on one tower will also deposit energy in neighboring towers. Therefore, the conditional probabilities $P(j \mid i)$ will be high for the towers surrounding tower i and low elsewhere. Problems in the channel locations can be spotted graphically by examining plots of the conditional probabilities mapped onto a graphical representation of the MPC.

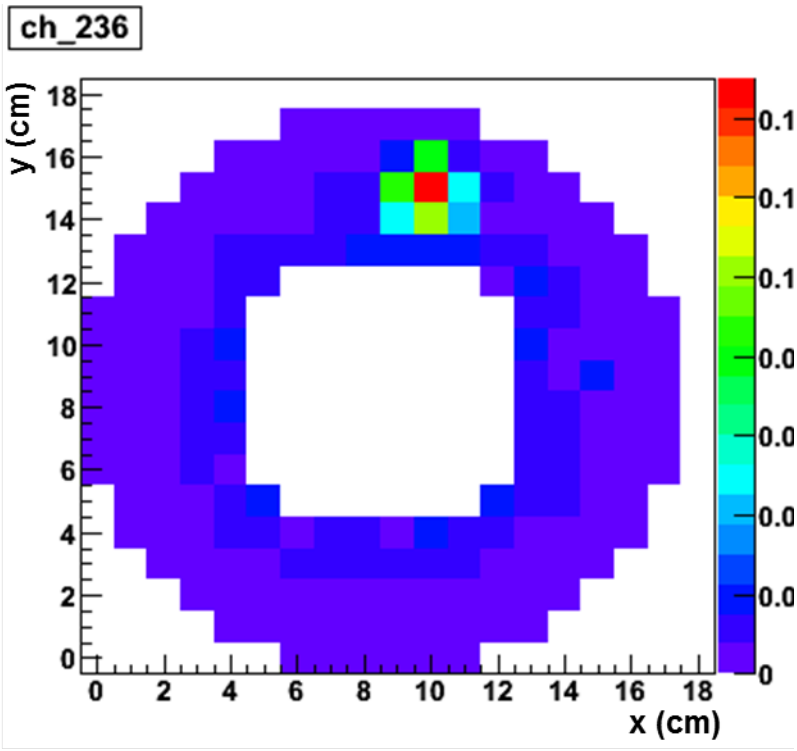

Figure 5.5: Conditional probabilities for a channel with correct location mapping. The tower in question has by definition $P(i \mid i) = 1$, but its value is set to 0.15 to avoid distorting the color axis. The bright colors surrounding the tower are neighboring towers with comparatively high $P(j \mid i)$, while the probabilities for towers further away to be hit are vanishingly small.

When scanning through the towers, we found a section of the MPC South affected by an accidental swapping of signal cables that send data from the MPC to a driver board.

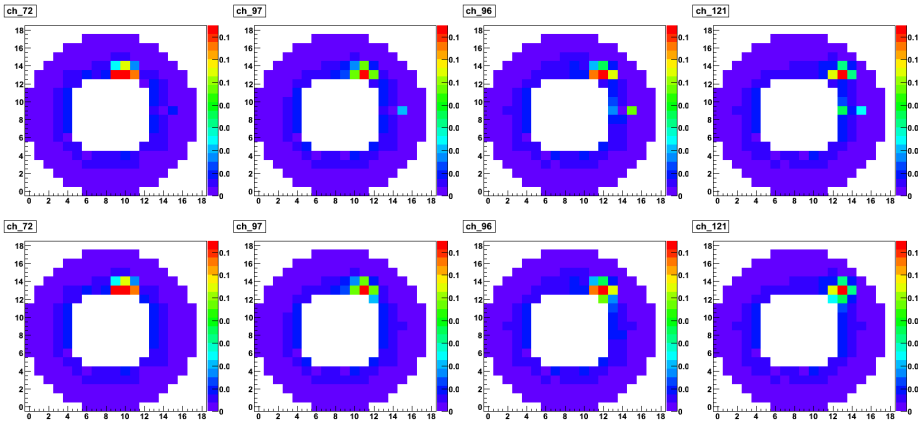

Figure 5.6: An error in the cabling for the MPC was uncovered through the channel mapping analysis. The top row shows a sequence of four adjacent towers before the mapping was corrected. The first two towers from the left are normal, but the third and fourth plots reveal towers that must be near each other in physical space but are separated in the data. The bottom row shows the same towers after the mapping was corrected.

Ultimately, we found that eleven towers were swapped one-to-one with eleven other towers. The issue was corrected in the reconstruction software by a simple reassignment of the affected channel numbers.

5.1.4 Noise subtraction from problematic driver board

A considerable excess of counts is present in both the low-gain and high-gain ADC spectra for one of the driver boards in the north arm of the MPC compared to other channels.

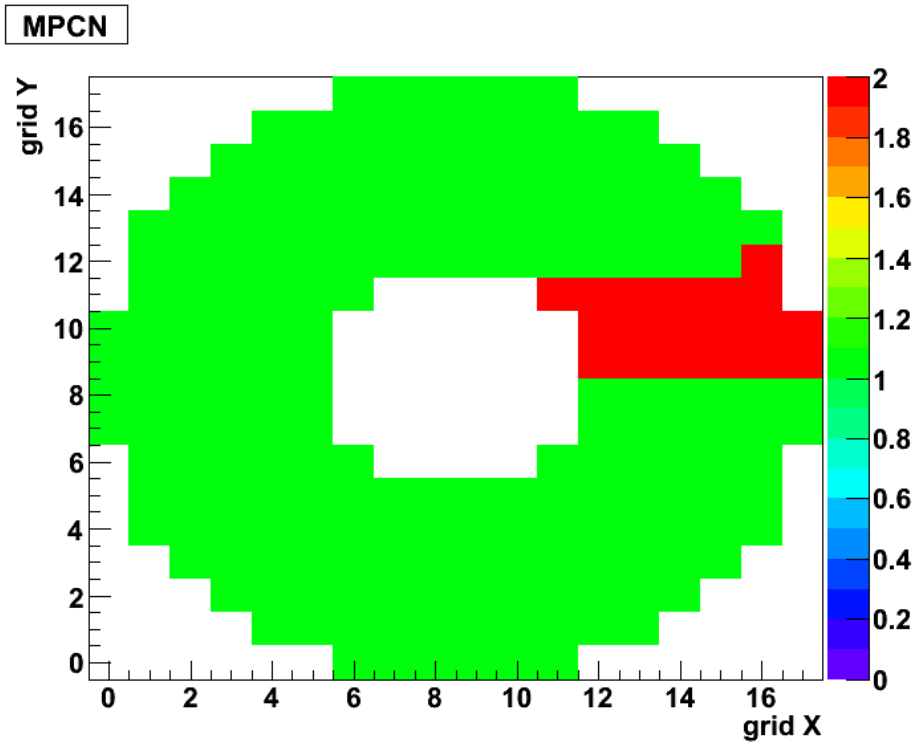

Figure 5.7: Location of the noisy driver board in the MPCN (driver board 19).

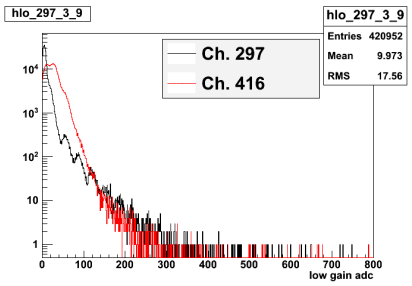

(a) Low-gain ADC spectrum from one run for Ch. 416 in the noisy driver board compared to an unaffected channel.

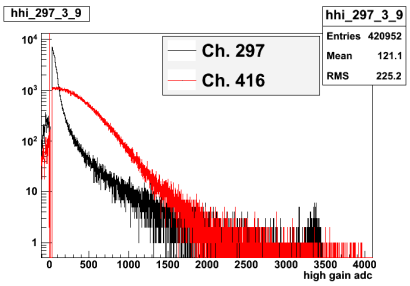

(b) High-gain ADC spectrum from one run for Ch. 416 in the noisy driver board compared to an unaffected channel.

Figure 5.8: The noisy driver board is evident in both the low-gain and high-gain ADC spectra.

We attempt to correct for the noise in the reconstruction code. If $> 50\%$ of the channels in the noisy driver board (at least 10 of the 19) register a hit, we calculate a truncated mean of the energies recorded by the noisy channels, excluding the two highest and two lowest energies. This truncated mean energy is then subtracted from each tower in the driver board, with the goal of removing the correlated noise in the channels while leaving real energy deposits from a particle shower intact.

5.2 LED Calibration

Analyzers have access to ADC measurements of a fixed amount of light delivered to the crystals from LEDs via optical fibers twice a second throughout Run 11 (see subsection 2.3.2). The mean ADC recorded from LED pulses for channel i for a run we write as $LED_i(run)$. We compare these values for each run and each tower to the values from a reference run to get the relative gain factor, $R_i(t)$. As we average LED measurements over the period of one run, we write

$$R_i(run) = (\frac{ADC_i(run)}{ADC_i(ref.)})^{-1},$$

where the inverse represents the concept that as the efficiency of the detector falls below what it was at the reference run (meaning $\frac{ADC_i(run)}{ADC_i(ref)} < 1$), we need to correct our measurements by a factor greater than one to compensate. There are occasional runs or towers for which the LED system drops out, so the values of $R_i(run)$ for those runs or towers are found from interpolating the values from nearby runs (since $R_i(t)$ is stable over short periods of time) or from nearby towers (since temperature and radiation aging effects should be similar for towers in close proximity).

In general, radiation damage throughout the running period causes light to be transmitted less efficiently in the $PbWO_4$ crystals as time goes on. The end result is that for the fixed amount of light delivered to the crystals, we measure smaller ADC values later in the year than early in the year. The towers closer to the beam pipe (at smaller r in the MPC) experience higher amounts of radiation, so the LED correction changes more over time for these towers. We present an example of this behavior in Figure 5.9.

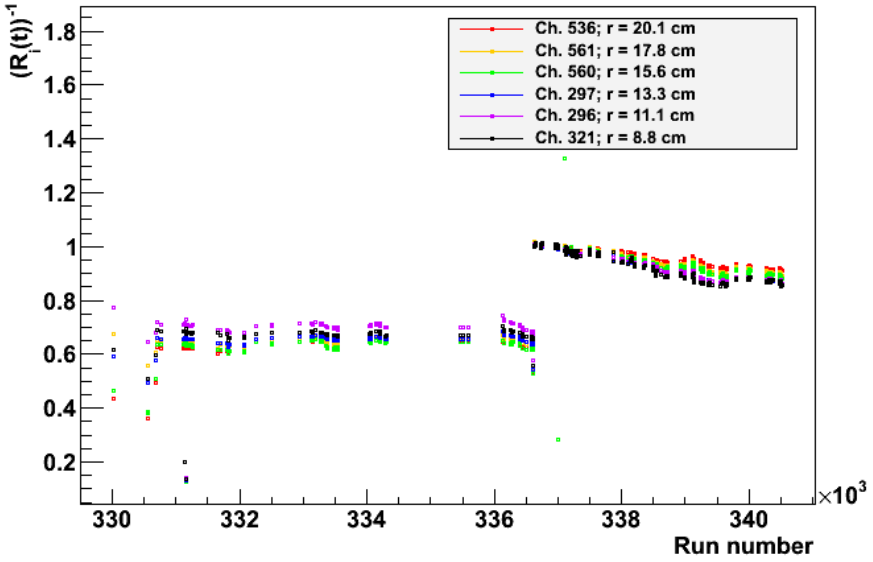

Figure 5.9: The average ADC measurement by run normalized to a reference run for a row of towers in the MPC at varying distances to the beam pipe r. We see that for long time scales, the ADC measurements decrease for each of the towers, while the decline is sharper for towers at small r closer to the beam pipe. The jump before run 336636 corresponds to a change in the high-voltage settings of the MPC (see text).

Fluctuations in the LED output as measured by the APDs can also result from temperature changes in the MPC. Previous studies have found that the effective gain of the APDs decreases by 2% per increase in temperature of one degree Celsius[41]. A general warming of the detector occurs throughout the run, which begins in January and ends in April, and temporary sharp fluctuations in temperature are attributable to the switching on or off of the electromagnet in the muon arm (5.10a). The brief variations in temperature correspond to adjustments in the LED correction factor as well (5.10b).

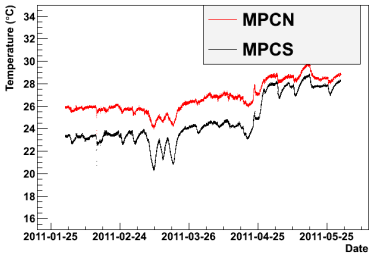

(a) Temperature variations in the MPCS and MPCN during Run 11.

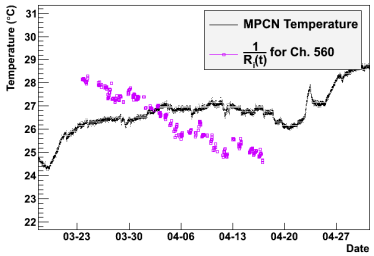

(b) Temperature in the MPCN along with the ADC response to the LED for one channel in the MPCN for a section of Run 11.

Figure 5.10: Temperature variations in the MPC.

A key feature of the LED data from Run 11 is the jump that occurs between runs 336610 and 336636. This point in time corresponds to when the high voltage setting on the MPC APDs was increased from M=10 to M=15 to compensate for the cumulative degradation of the detector response both during Run 11 and since the commissioning of the MPC. This change is reflected by the increase of the LED readings from ~ 0.7 before the jump to ~ 1.0 afterwards. We decided to use a single reference run early in the M=15 portion of Run 11, run 336739, as the M=15 portion is a higher percentage of the run and the LED system seems to have no problem accounting for the drastic change in the APD output.

5.3 Gain Calibration

With the FEM calibrated and time-dependent changes in detector response accounted for, the final step is to translate the ADC values to energies by finding the gain G_i for each tower. Previously, an initial estimate could be found using minimum ionizing particles (MIPs) in the MPC. Such particles lose a nearly fixed amount of energy per length in the MPC, meaning that the total energy they deposit can be calculated to be 234 MeV. One could find the peak corresponding to the minimum ionizing particles in the ADC spectrum of a tower, and the G_i would be simply the ratio of 234 MeV to the ADC value at this peak. The MIP peak was detectable in earlier runs at lower beam energies where the voltage to the APD was set to M=50. At higher beam energies, where M=10 or M=15 to increase the range of energies measurable by the ADC before it overflows, the MIP peak gets lost in background and electronics noise, meaning a different approach to approximate the gains was needed. Initially, we tried an assumption that the gains would be simply related by the ratio of the M values for the APDs, but this method was not successful. It appears that the cumulative aging effects on the MPC resulted in lower detector response than would be expected from this simple analysis, necessitating the use of larger gains.

5.3.1 Spectrum Matching

Knowing the energy spectrum for each tower from a previous run at the same center-of-mass energy gives another reference point that allows us to bypass a MIP analysis and find a rough estimate of the gain. For each tower, we can generate a histogram of hit energies from a reference run in Run 9[1], normalizing the histogram with the number of events in the sample. We can also generate ADC histograms for the same tower from Run 11, again normalizing the histogram with the number of events. Because the MPC is measuring the same physics in

[1]The MPC was calibrated in earlier runs based on test beam measurements and detector response to minimum ionizing particles which deposit a known amount of energy in the detector.

2011 as it was in 2009, we can determine which gain, when applied to the ADC spectrum for a tower, reproduces the "true" energy spectrum from Run 9.

We search for the approximate gain by comparing the counts in a range from 4 GeV to 12 GeV[2] of the energy histogram to a range in the ADC histogram. For the energy histogram, the bins to be integrated over begin with the bin centered at $E_{min} = 4\,GeV$ and end at $E_{max} = 12\,GeV$. For the ADC histogram, the low bin of the range is the bin containing $ADC_{min} = \frac{E_{min}}{G_i} \times R_i(t) = \frac{4\,GeV}{G_{i,itr}} \times R_i(t)$, where $R_i(t)$ is the relative gain factor taken from the LED measurements and $G_{i,itr}$ is the test gain value that we vary from 0 to 2.0 in steps of 0.001. Similarly, the high bin of the range is the bin containing $ADC_{max} = \frac{E_{max}}{G_i} \times R_i(t) = \frac{12\,GeV}{G_{i,itr}} \times R_i(t)$. For each iteration, starting at $G_{i,itr} = 0.001$, we find $R = \frac{\sum_{ibin=ADC_{min}}^{ibin=ADC_{max}} N_{ADC}(ibin)}{\sum_{ibin=E_{min}}^{ibin=E_{max}} N_E(ibin)}$, where the N_{ADC} and N_E refer to the counts in a bin of the ADC histogram and the energy histogram, respectively. Once we find $R \geq 1$, the iterative procedure is stopped, and we take that $G_{i,itr}$ as the approximate gain for tower i. The procedure works quite well for well-behaved towers, as can be seen in Figure 5.11, comparing a reference spectrum for a tower from Run 9 with an energy spectrum in Run 11 generated with the gain found using the above method.

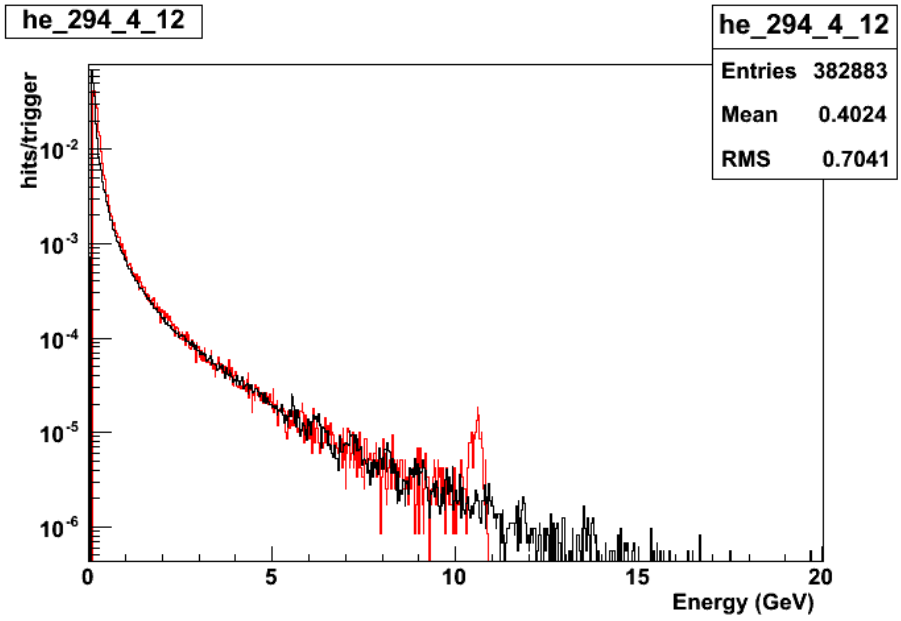

Figure 5.11: Sample results from spectrum matching method for finding. The black line is the reference energy spectrum from one tower in Run 9, while the red line is the Run 11 spectrum using the gains from the matching method.

For towers in the noisy driver board, we have mixed results. For some channels, the noise subtraction cleans up the spectra and allows for a successful

[2]Using this limited range avoids difficulties due to noise at low energy and poor statistics at high energy.

match; for others, the noise subtraction is not sufficient to salvage the channel.

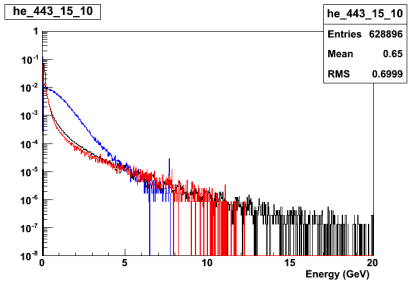

(a) Energy spectrum comparison for Ch. 443 between Run 9 (black) and Run 11 (red,blue). The red spectrum includes the noise subtraction algorithm while the blue does not, and improvement can be seen.

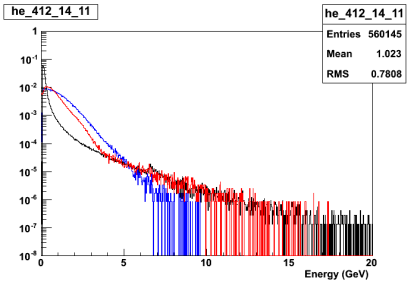

(b) Energy spectrum comparison for Ch. 412 between Run 9 (black) and Run 11 (red,blue). The red spectrum includes the noise subtraction algorithm while the blue does not. In this case, the noise subtraction does not correct the shape of the energy spectrum at low energy.

Figure 5.12: The noisy driver board is evident in both the low-gain and high-gain ADC spectra.

5.3.2 Iterative π^0 Calibration

Once we have an approximation of the correct gains for each tower, we finalize the gains by generating di-photon invariant mass spectra, identifying the π^0 mass peak, and comparing the mass to what we find from simulation. When a π^0 decays into two photons, each photon incident on the MPC initiates an electromagnetic shower which presents as a contiguous "cluster" of towers with energy deposits in the MPC. For each cluster, we have position and energy information which allow us to make selection cuts on the clusters entering into the di-photon mass spectrum and to calculate the invariant mass of the di-photon pair. To determine the expected reconstructed π^0 mass after energy-leakage and acceptance effects are accounted for, we use simulations based on the PYTHIA event generator as well as GEANT, a software package that emulates the specific geometry, materials, and response of the detector, giving us an idea even of how the showering and clustering of particles in the detector are expected to proceed[64]. The reconstructed π^0 masses in each tower from the simulations are given in Figure 5.13 and Figure 5.14. We find that the reconstructed masses are within $10\,MeV/c^2$ of the π^0 mass of $135\,MeV/c^2$, with more accurate reconstructions away from the edges of the detector where leakage and acceptance effects lead to smaller reconstructed masses.

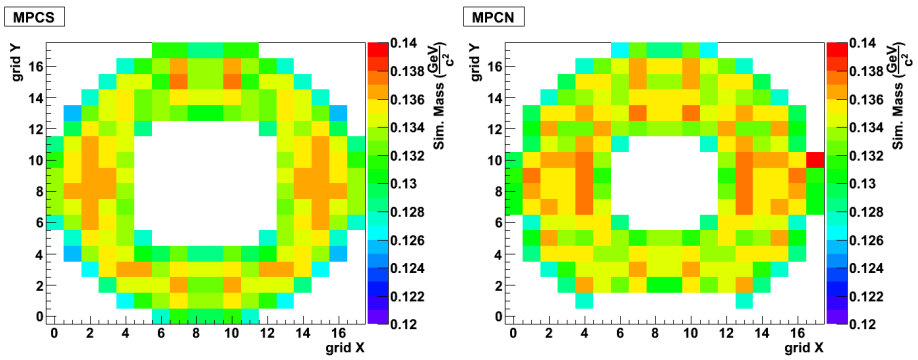

Figure 5.13: Reconstructed π^0 masses for each tower from simulation for the MPC South (left) and North (right).

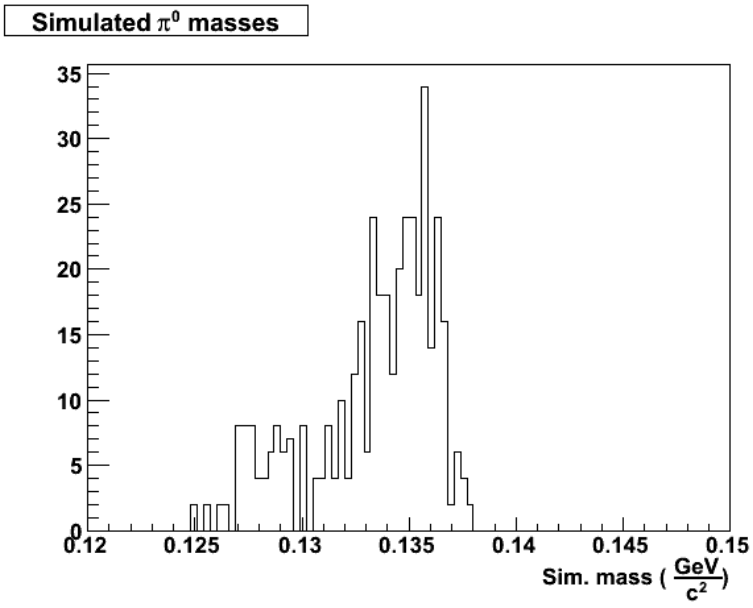

Figure 5.14: Distribution of tower-by-tower π^0 mass peaks as determined from simulation. The trueπ^0 mass is $135\,MeV/c$, but the segmentation of the MPC, acceptance effects, and the particular kinematic cuts we use affect the location of the peak of the di-photon invariant mass spectrum.

On the data side, we begin with a set of cuts on single clusters:

- Central tower of cluster not in warn map (flagged as a malfunctioning tower)
- $E_{clus} > 2\,GeV$
- $12\,cm < r_{clus} < 19\,cm$
- Dispersion $< 4.0\,cm^2$(a measure of lateral extent of the shower; the cut helps to distinguish EM from hadronic showers)

- $\chi^2/NDF < 3$ (comparison of shower shape to expected energy profile)
- No towers in cluster with an ADC overflow (see subsection 5.1.2)
- TDC from central tower of cluster is not an overflow (see subsection 5.1.2)
- Dispersion $> 0.0005\,cm^2$ (single tower background cut)
- # towers in cluster > 2 (single tower background cut)
- $\frac{E_{central\,tower}}{E_{clus}} < 0.95$ (single tower background cut)

From the set of all clusters that pass the above cuts, we calculate the invariant mass $M^2_{\gamma\gamma} = E^2_{\gamma\gamma} - p^2_{\gamma\gamma} = 2E_1E_2(1 - cos(\theta))$, where θ is the opening angle between the two clusters and $E_1$and E_2 are the energies of the two participating clusters. The cluster pairs are subject to additional cuts for the iterative π^0 calibration:

- $9\,GeV < E_{pair} < 17\,GeV$ (energy window matched to simulation; avoids noise at low energy and cluster merging at high energy)
- $p_{T,pair} > 0.5\,GeV/c$
- cluster separation $> 2.6\,cm$ (to avoid overlapping clusters and associated difficulties)
- $\alpha = \frac{|E_1-E_2|}{E_1+E_2} < 0.6$ (energy asymmetry cut; improves signal to background ratio)

For each pair that passes all of the above cuts, a histogram for the central towers of the two participating clusters is incremented at $M_{\gamma\gamma}$, weighted by the cluster's share of the pair's energy $\frac{E_{clus}}{E_1+E_2}$.

Once the invariant mass spectra for all towers are generated, we fit the peak near the π^0 mass with a Gaussian in a window with a width of $50\,MeV$ around the peak. We get the π^0 mass m_i for each tower i from the mean of this Gaussian. We find a correction factor to the gain as the ratio of the mass to the value from simulation, $\delta = \frac{m_i}{m_{i,sim}}$, and we adjust the tower gain accordingly. With the new tower gains, a simplified clustering algorithm is used to recalculate cluster energies, though to save computation time, we assume the cluster center positions are unchanged by the reshuffling of tower energies within the cluster. The new cluster energies in turn are used to find new π^0 mass peaks, and we converge on the final gains for all towers through successive iterations of gain adjustments and comparisons to the simulated mass peaks.

We find in the beginning that our estimated gains from the spectrum matching method are an underestimate as shown in Figure 5.15.

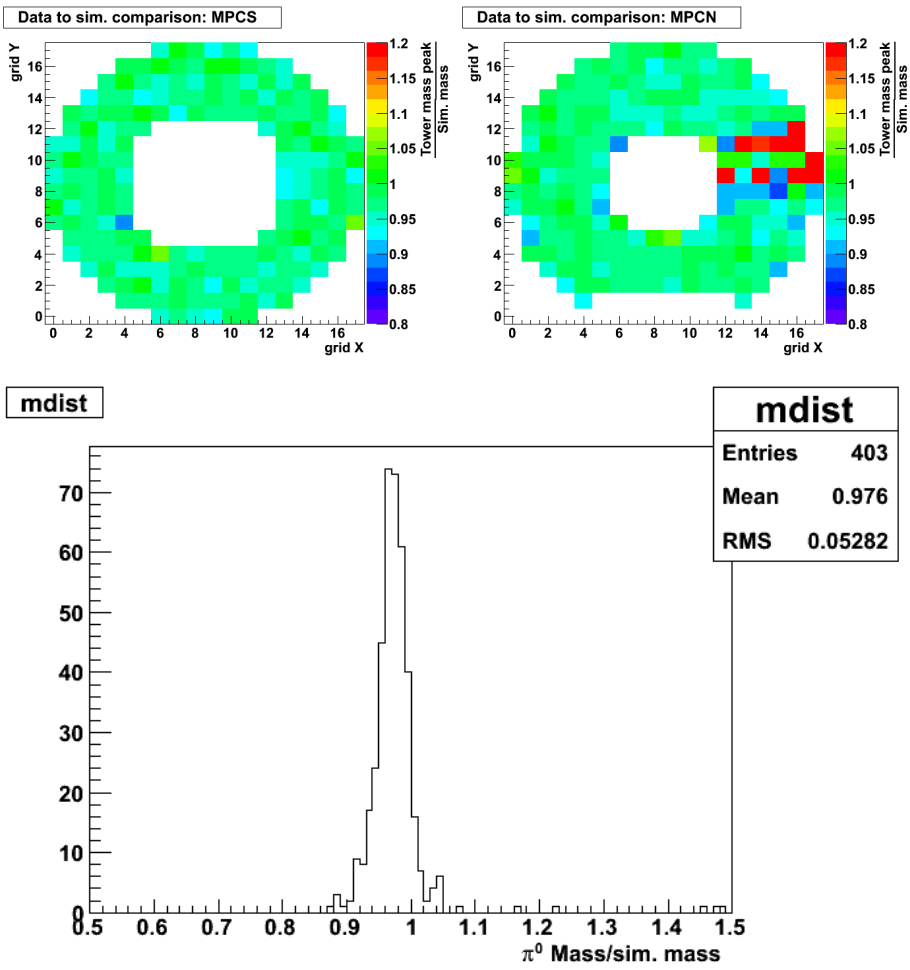

Figure 5.15: Initial comparison of reconstructed π^0 masses in data to simulation, using the gains from spectrum matching to determine tower energies.

During the course of the iterative process, some towers can be seen to have diverging behavior, often as a result of either far too few or far too many counts. These towers are added to the warn map (colored in the maps below with red diagonal lines) as they come up, and they are excluded from contributing to invariant mass distributions in other towers. With the exception of these misbehaving towers and the noisy driver board, the iterative procedure results in π^0 masses from nearly all towers that are within 5% of the target value from simulation. In Figure 5.16, we compare the final reconstructed π^0 masses to the value from simulation and plot the results for individual towers as well as a distribution. In Figure 5.17 and Figure 5.18, we show the final invariant mass distributions for each tower in the MPC South and MPC North. Finally, in Figure 5.19, we show by what factor the gains from each tower change over the course of the iterative procedure; the initial estimated gains were on the average adjusted upwards by $\sim 15\%$.

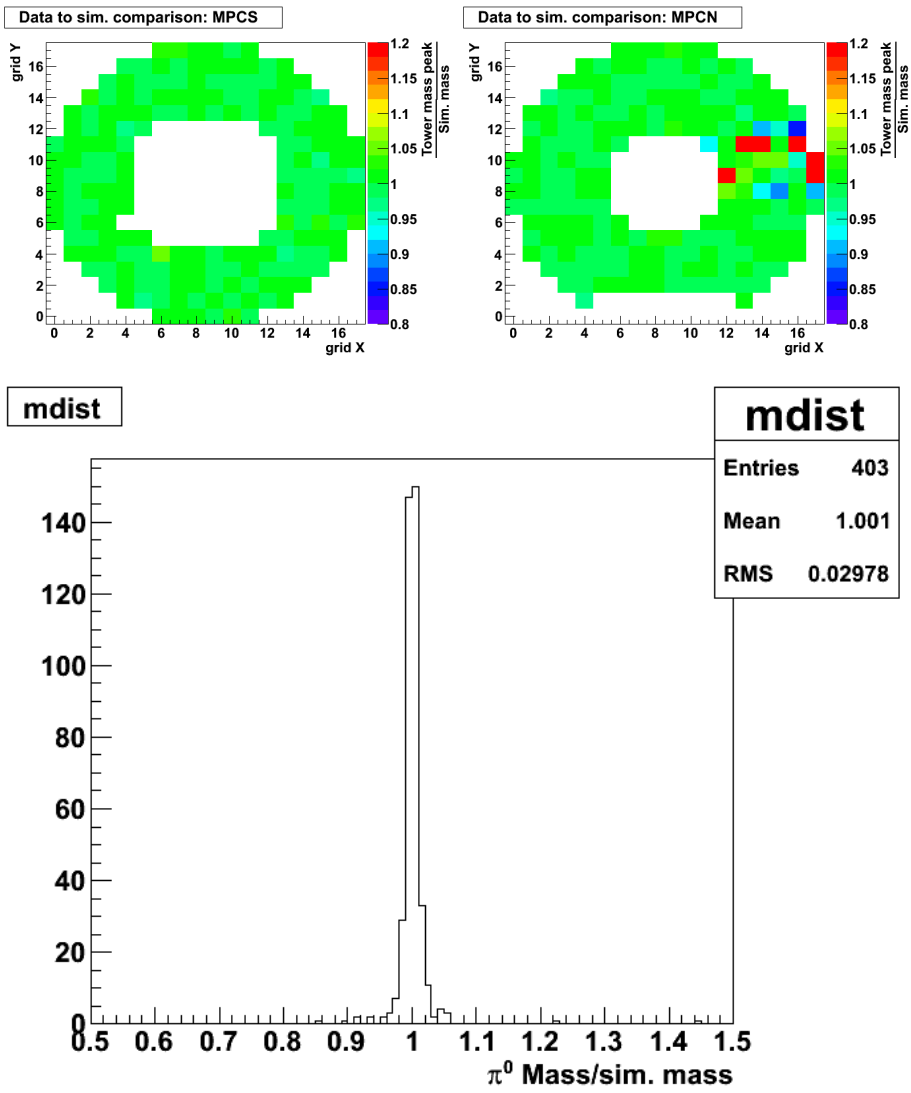

Figure 5.16: Comparison of reconstructed π^0 masses in data after iterative procedure to simulation, using gains adjusted during the iterative procedure.

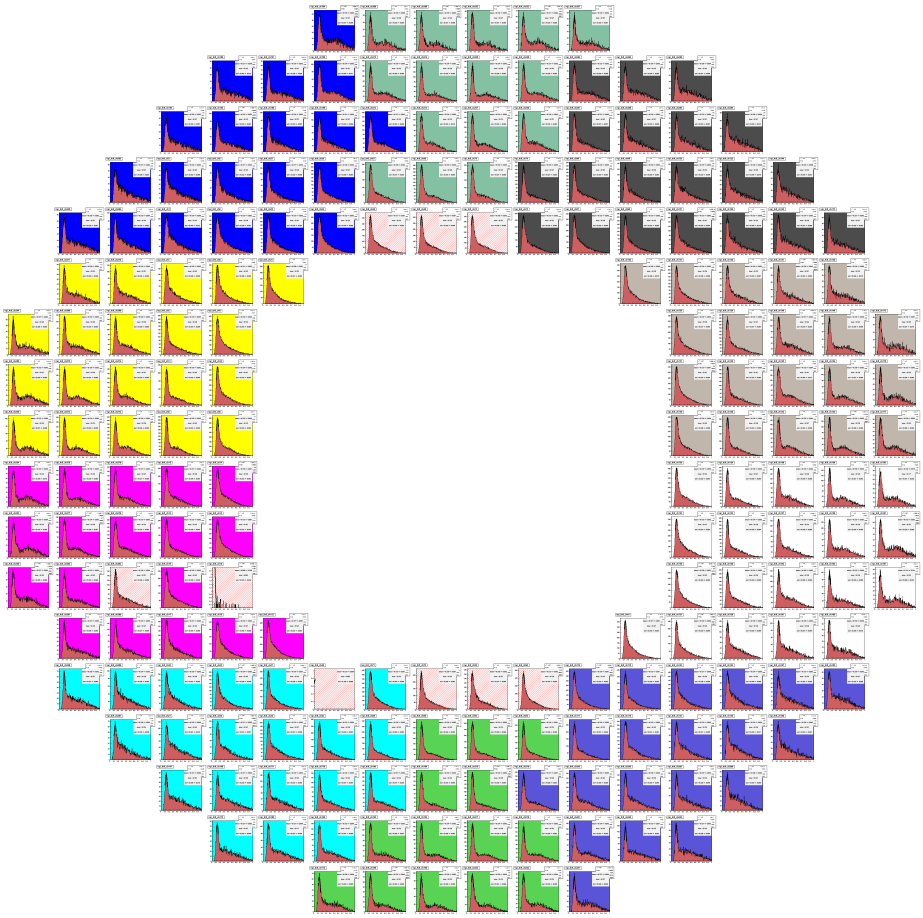

Figure 5.17: Map of the MPC South towers showing the invariant mass distributions in each tower at the end of the iterative procedure. Towers in the warn map are shaded with diagonal red lines. The shaded backgrounds in the towers represent different driver boards.

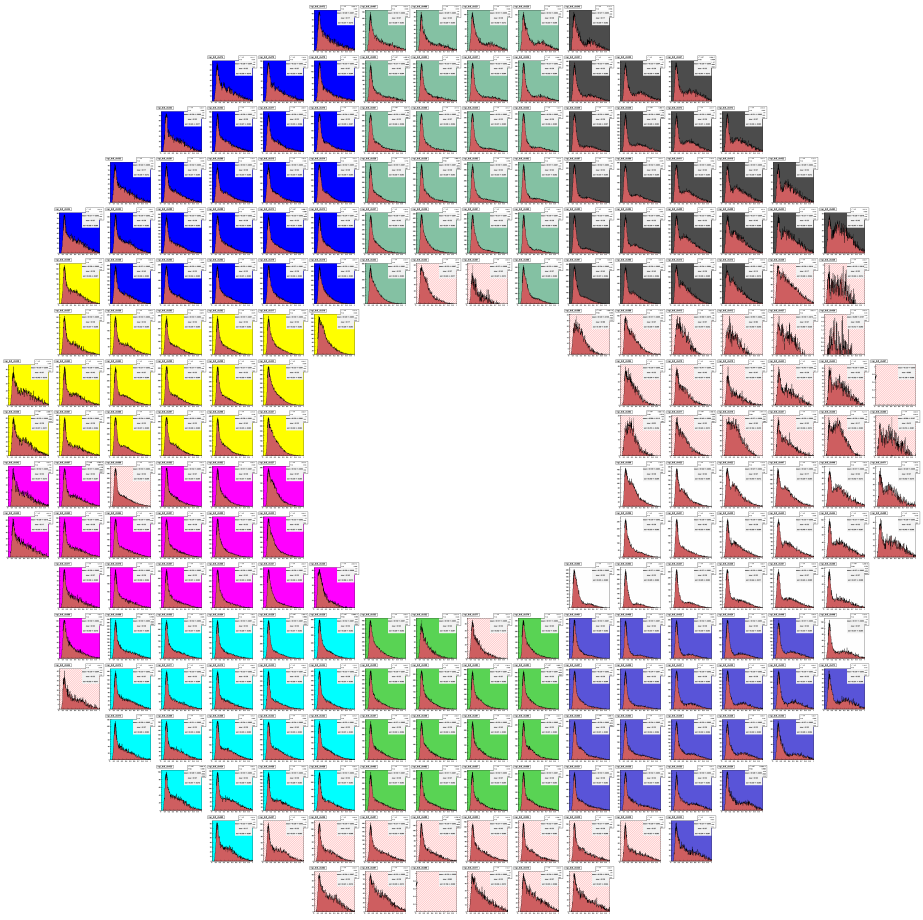

Figure 5.18: Map of the MPC North towers showing the invariant mass distributions in each tower at the end of the iterative procedure. Towers in the warn map are shaded with diagonal red lines. The shaded backgrounds in the towers represent different driver boards.

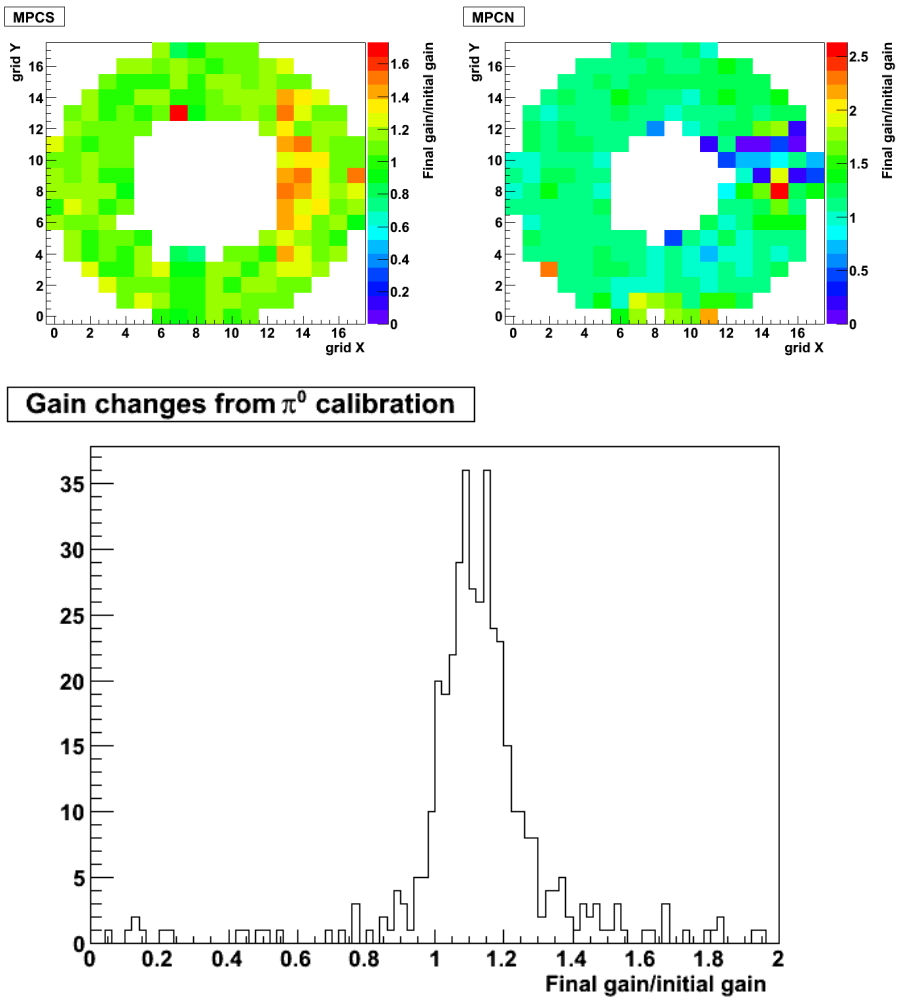

Figure 5.19: Plots showing the ratio $\frac{final\ gain}{initial\ gain}$ for each tower. In the top plot, the left map represents the MPC South, while the right represents the MPC North.

5.4 Warn map analysis

One of the standard cuts used in our final analysis is a simple exclusion of problematic towers in the MPC known as a warn map. The warn map is both an input and an output to the iterative π^0 calibration procedure. The warn map is needed as input because without a warn map, problematic towers can skew the invariant mass distributions in other towers and hinder our ability to accurately determine the correct gains. The warn map however is also an output from the iterative procedure because we need reasonable gains in order to determine if towers are "hot" or "cold," registering too many or too few hits, respectively, in comparison to other towers in the MPC. For this reason, we first identify towers that are clearly malfunctioning and remove them from the iterative π^0 analysis. Once the iterative π^0 calibration is run once, we use the

resulting gains to perform a more thorough analysis of hit rates in each tower.

Some care must be taken when comparing the number of hits between different towers. In general, particle production is a function of pseudorapidity η, and slices in η correspond to rings in the MPC. Rings closer to the center of the MPC contain fewer towers, so each tower gets a bigger share of the number of particles, $\frac{dN}{d\eta}$, for these rings. In other words, while each tower has the same geometrical size and shape, a tower's span in η and ϕ depend on r, the distance from the center of a tower to the center of the beam pipe. In the end, we find that the logarithm of the number of counts per trigger falls roughly linearly with increasing r. For each run, we find the number of counts per minimum bias trigger in six energy ranges for each tower. We plot $log_{10}(cts/trigger)$ vs. r and fit with a second degree polynomial (which tracks the relation better at small and large r), excluding the 15% of towers furthest from the fit to prevent outliers from dominating the fit. We then find the RMS, again excluding the outliers, and draw bands at $\pm 3\sigma$ from the fit as shown in Figure 5.20. Towers that fall outside of the bands are considered bad for that run and energy bin.

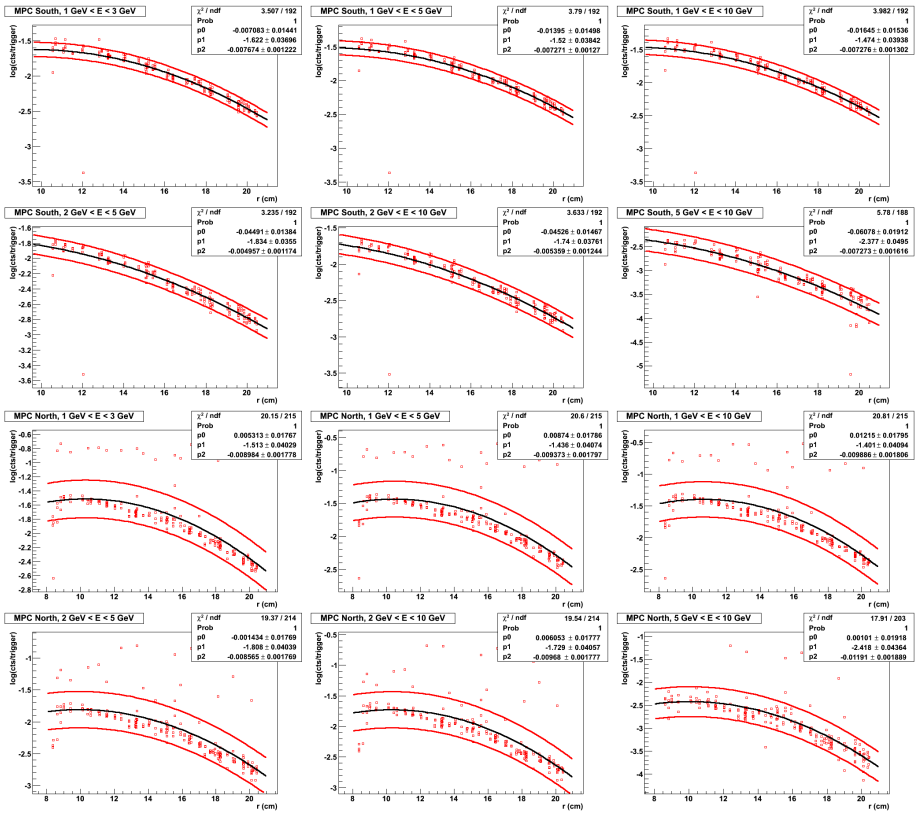

Figure 5.20: Example determination of hot and cold towers in the MPC South and North for the six energy bins for one run. The first two rows are for the MPC South while the last two are for the MPC North. Each individual plot represents counts per trigger in a particular energy bin labeled on the plot.

We consider the two sections of Run 11 with different high voltage settings

for the MPC separately, and if a tower is bad in more than 10% of runs in a section for a particular energy range, we say the tower is bad in that range. Then, if a tower is bad in at least three of the six energy ranges for a section, we consider it bad for the whole section.

The results for the warn map are shown in Figure 5.21 and Figure 5.22. The section of the MPCN corresponding to driver board 19 stands out as being bad as expected. A few of the towers are malfunctioning and were essentially inoperable during Run 11, while the cause of the other bad towers is less clear. In some cases, possibly again due to noise, the π^0 calibration did not converge on a fixed gain for a cluster of towers, as in the group on the middle-left of the MPCS in the M=10 section. The error in the gain applied to these towers could account for the towers showing up as cold or hot.

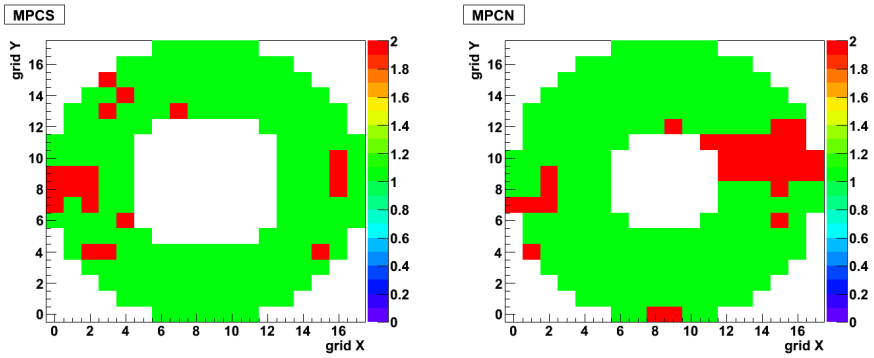

Figure 5.21: Warn map for the MPCS and MPCN for the M=10 section of Run 11 (runs before 336630), with bad towers marked red. Clusters with a tower in the warn map are excluded from the final analysis.

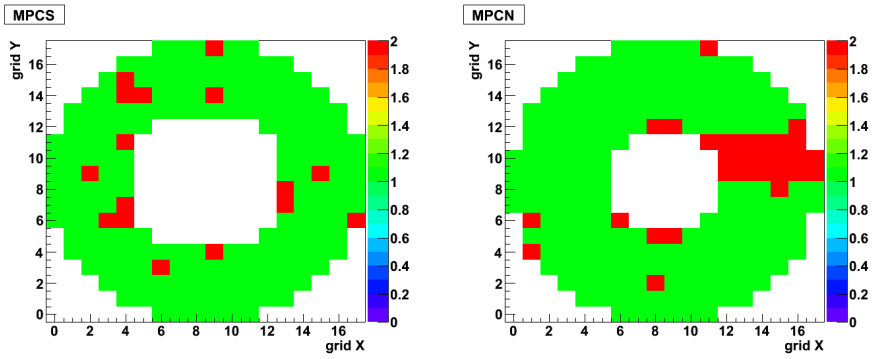

Figure 5.22: Warn map for the MPCS and MPCN for the M=15 section of Run 11 (runs after 336630), with bad towers marked red. Clusters with a tower in the map are excluded from the final analysis.

5.5 π^0 mass peak stability

As an overall check of our calibrations, we examine the π^0 mass peaks on a run-by-run basis. We generate the invariant mass distributions and fit the peaks as we do in subsection 5.3.2; however, because we are working with individual runs with limited statistics, we generate only a single distribution for each arm of the MPC, rather than one for each tower. We expect the locations and widths of the mass peaks to be consistent with respect to time. Any deviation in the measured π^0 mass can be attributed to the LED system imperfectly tracking the degradation in crystal performance over the course of the run. The widths of the π^0 peaks give information on the effective energy resolution of the detector and the precision of the gain calibrations.

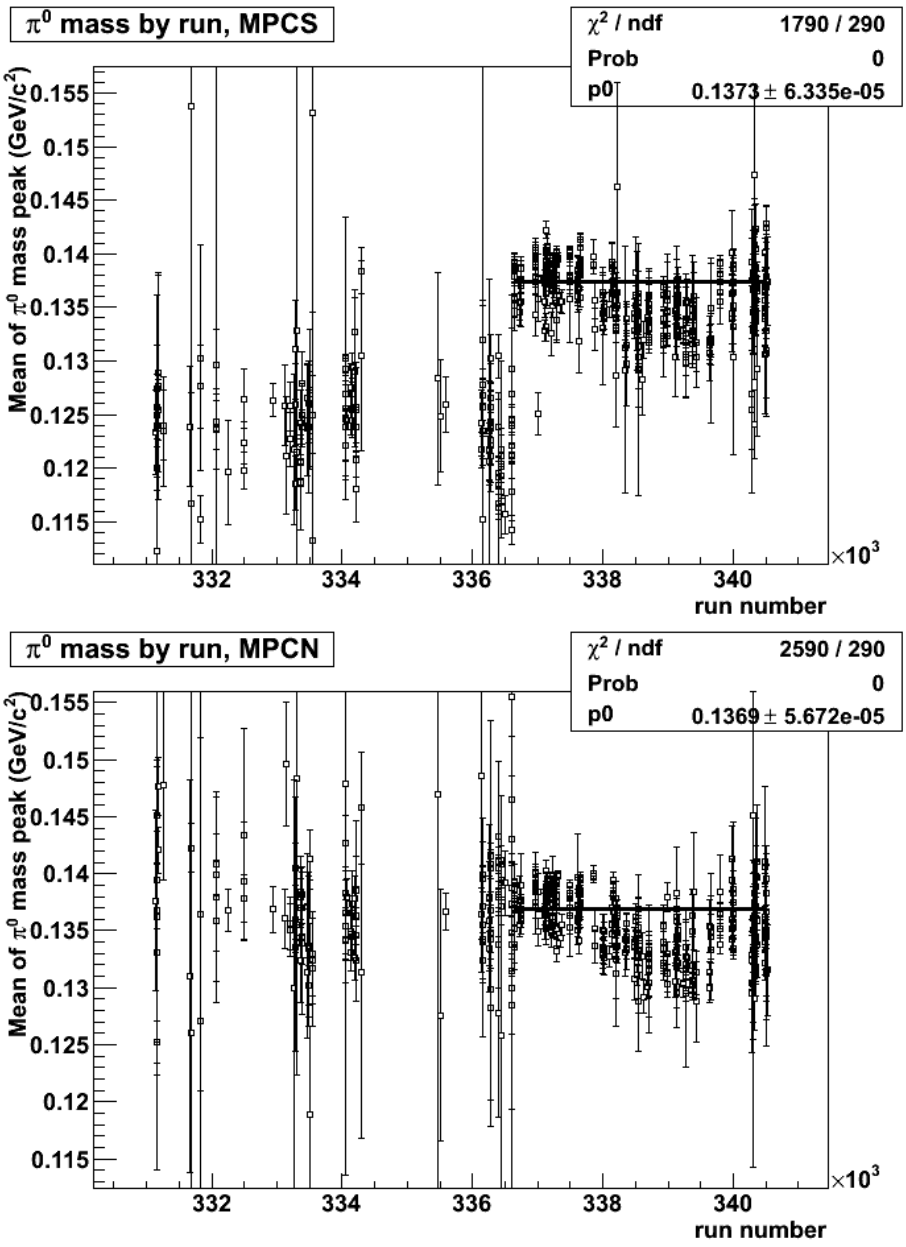

Figure 5.23: Stability of the π^0 mass as measured in the MPC South and North over the course of Run 11. A constant is fit to those runs in the M=15 section of Run 11.

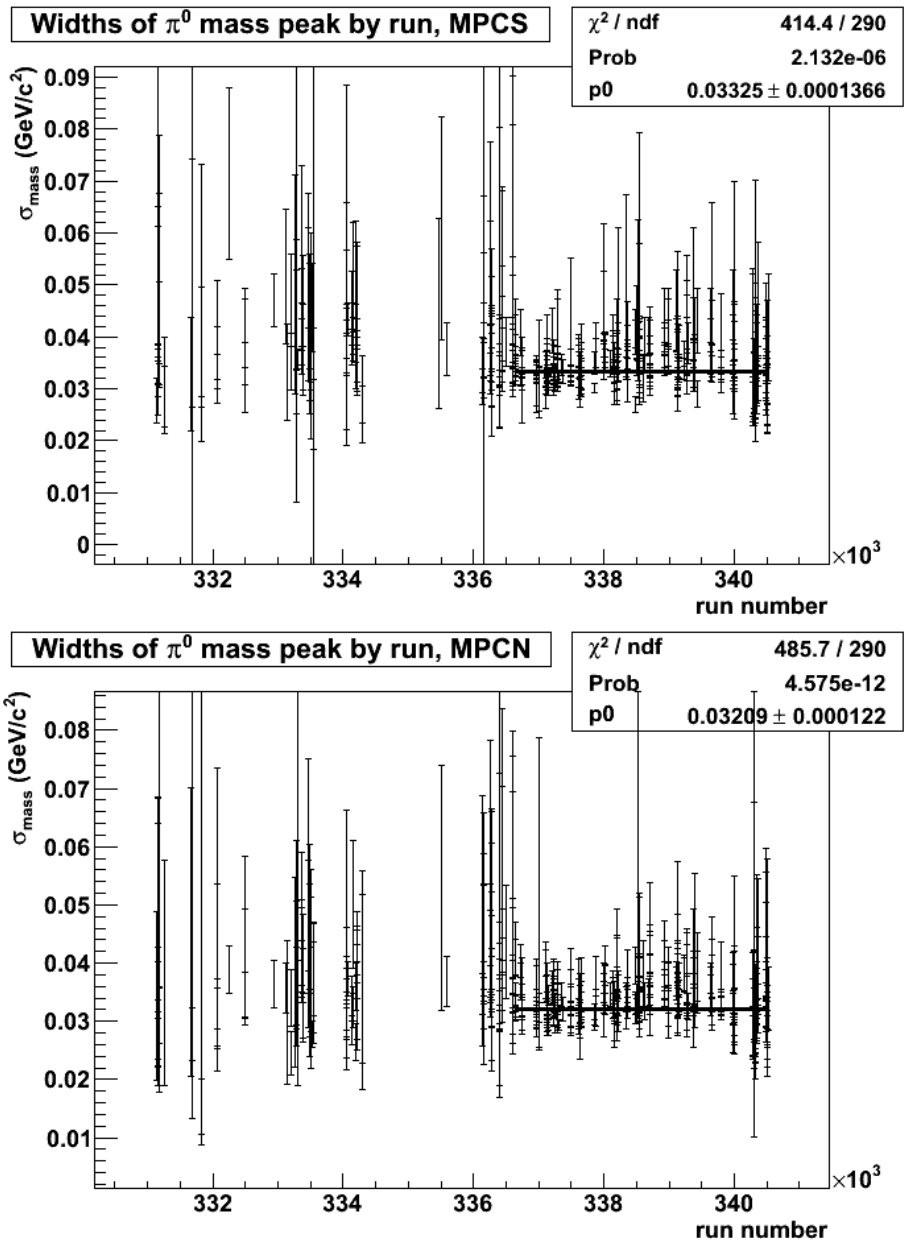

Figure 5.24: Stability of the π^0 width as measured in the MPC South and North over the course of Run 11. A constant is fit to those runs in the M=15 section of Run 11.

First, note in Figure 5.23 the poor statistics (as evidenced by the large error bars) and the poor quality of the calibration in general in the M=10 section of the run, before run 336636, especially in the south arm of the MPC. These factors weigh heavily against including the M=10 section of data in the final analysis. In the M=15 section of the run, the masses are comparatively very consistent, with a noticeable drop in the π^0 mass around run 339000 that nevertheless only amounts to around a 5% fluctuation. This decline in the

reconstructed π^0 mass appears correlated with increasing rates in RHIC around the same time (see Figure 5.25).

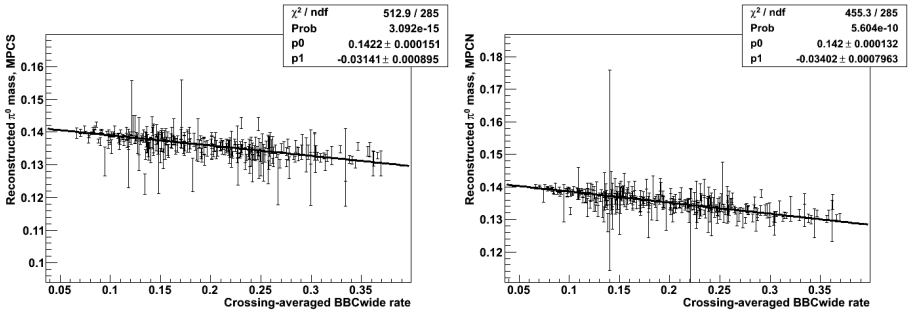

Figure 5.25: Correlation between BBCwide trigger rate and reconstructed π^0 mass in the MPCS (left) and MPCN (right).

I can only speculate about the nature of the correlation; it may be that the increased rates result in a higher fraction of crossings with multiple collisions, and the combinatorial background from clusters in the multiple collisions is not accounted for properly when fitting the mass peak. The 5% difference in the mass over the course of the M=15 section of the run is of comparable size to the spread in π^0 $\frac{data\,mass}{sim.\,mass}$ from tower to tower after running the iterative π^0 calibration.

The mass peak widths (Figure 5.24) are more or less stable in both the M=10 and M=15 segments of the run, with a value between 30 and 35 MeV/c^2. The widths are larger than those seen in Run 9 by about 10 MeV/c^2. The increased widths are seen in later runs as well, so the decreased resolution may be a result of the degradation of the detector with time or the necessity of running with lower high-voltage settings for the best dynamic range at center-of-mass energies of 500 or 510 GeV.

Chapter 6

Run 11 MPC $A_{LL}^{clus\cdot}$ analysis

Having covered in detail the technical tasks relating to the luminosity normalization for our measurement (chapter 4) as well as the calibration of the MPC (chapter 5), we turn to the final physics analysis where we determine the double longitudinal spin asymmetry in the production of electromagnetic clusters in the MPC. The $A_{LL}^{clus\cdot}$ analysis is similar in many respects to the $A_{LL}(\frac{ZDC}{BBC})$ analysis, but differences between the MPC and the luminosity detectors provide some additional complexity to the measurement. The main differences can be explained by the fact that the MPC reports much more than the "hit or no hit" information we typically use from the luminosity monitors; we record timing and energy information from each of 416 channels (196 in the south arm, 220 in the north).

One complication of the luminosity scaler analysis that for multiple reasons is not required for the MPC data is a pileup correction. We count clusters in the MPC for this analysis, rather than simple binary single-arm or coincidence counts. Therefore, there is no possibility of an accidental coincidence to worry about. Also, "missing" a hit in a tower because a second collision in the same crossing caused a hit in the same tower is unlikely on account of the segmentation of the MPC and the low rates of high p_T clusters in the MPC.

The additional information read out by the MPC compared to the ZDC and the BBC also allows for more detailed analysis of the detector's performance. For example, while we were restricted in our luminosity monitors to exclude data only on the crossing or run level, we are free to also eliminate sections or individual towers from the MPC on a run-to-run basis from our final analysis. The fact that we read out energies from the MPC towers also gives us more options in terms of detector QA since we can examine the detector response in various energy ranges. Finally, having knowledge of cluster energies also allows us to report the final asymmetry as a function of p_T, which is important for theoretical purposes as the p_T gives us a handle of the kinematics of a collision and therefore what momentum fraction of the proton is being probed.

6.1 Analyzing merged clusters

While the MPC can reconstruct π^0's from the two clusters resulting from the decay of the π^0 to two photons, as seen in our iterative π^0 calibration, restricting our analysis to reconstructed π^0's would severely limit our statistics for the measurement as well as the kinematic range we can cover. The difficulty is that the opening angle between the two photons resulting from a π^0 decay depends on the energy of the π^0 and how the energy is distributed between the photons. The invariant mass of a particle in the high-energy limit (where $E = |\boldsymbol{p}|$) in terms of the four momenta of its two decay products (photons in our case) is the scaler product of those four momenta:

$$m_{\gamma\gamma}^2 = p_\mu p^\mu = E^2 - \boldsymbol{p}^2 = 2E_1E_2(1 - cos\theta), \tag{6.1}$$

where θ is the angle between the three-momenta of the two photons and E_1 and E_2 are their energies. As the total angular diameter of the MPC at 220 cm is only 10°, we use the small-angle approximation to rewrite Equation 6.1 as $m_{\gamma\gamma}^2 = 2E_1E_2\frac{\theta^2}{2}$. We can immediately see that for the fixed mass of the π^0, the angle between the photon momenta decreases as the energy increases. We also define a total energy $E_{tot} = E_1 + E_2$ and an energy asymmetry $\alpha = \frac{|E_1 - E_2|}{E_{tot}}$ such that $\alpha^2 = \frac{E_1^2 - 2E_1E_2 + E_2^2}{E_{tot}^2} = \frac{E_{tot}^2 - 4E_1E_2}{E_{tot}^2}$, so $2E_1E_2 = \frac{E_{tot}^2(1-\alpha^2)}{2}$ and Equation 6.1 becomes

$$m_{\gamma\gamma}^2 = \frac{E_{tot}^2}{2}(1 - \alpha^2)\frac{\theta^2}{2}. \tag{6.2}$$

Our analysis requires a minimum separation of only 2.6 cm between clusters; however, the clusters cannot be cleanly resolved if their centers are in adjacent towers. The clusters can be considered a merged cluster if the separation between their centers is less than $2 \times 2.2\,cm$, corresponding to an angle at 220 cm of 0.022 radians. and a maximum α of 0.6. Plugging these values and the π^0 mass of 0.135 GeV/c^2 into Equation 6.2, we find that the highest-energy π^0 we can reconstruct has $E \approx 17\,GeV$ and a maximum p_T (for clusters at the outer edge of the MPC's acceptance) of $1.5\,GeV/c$. If we allow the smaller cluster separation of $2.6\,cm$ used in the iterative π^0 calibration, we can theoretically reconstruct a π^0 with $E \approx 28\,GeV$ and $p_T \approx 2.4\,GeV/c$. These limits are reduced further when considering cluster pairs with either no energy asymmetry or the average energy asymmetry around 0.25.

The theoretical framework of pQCD is applicable only for $p_T > 1\,GeV/c$ where hard interactions dominate, so we have theoretical motivation to focus on the higher-energy merged clusters as well. While is not practical to focus our analysis on reconstructed π^0's, simulations indicate that the merged clusters come predominantly from π^0's anyway. A study of 30 million PYTHIA events at $\sqrt{s} = 500\,GeV$ showed that around 80% of merged clusters above $p_T = 1\,GeV/c$ arise from π^0 decay, with smaller contributions from merged clusters from η meson decay, direct photons, and charged hadrons[65]. The cluster decomposi-

tion, showing the fraction of clusters arising from the various contributions as a function of p_T as determined from simulation, is shown in Figure 6.1.

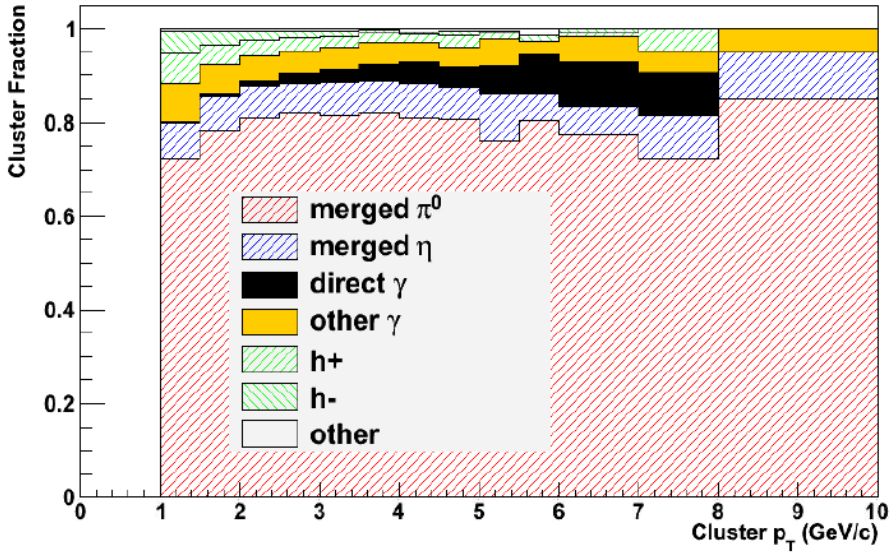

Figure 6.1: Cluster decomposition results from PYTHIA and GEANT at $\sqrt{s} = 500\,GeV$.

6.1.1 Single-tower background

There is a background signal that dominates the MPC-triggered data for high-energy clusters that is known as the single-tower background (Figure 6.2). The background consists of clusters that do not have any reasonable lateral extent; instead, what appears to be an unphysically large energy is deposited in a single tower, with little or no energy in surrounding towers. The energy spectra of these clusters is flat as well rather than falling off as a power law at high energies as would be expected for particles produced in a pp collision. This signal is thought to be produced by neutrons from interactions between high-energy particles and steel support structures in PHENIX. These neutrons do not initiate showers in the $PbWO_4$ crystals, but occasionally they can interact directly with the silicon in the APDs, kicking out a proton in a nuclear reaction and initiating an avalanche that in itself is indistinguishable from the avalanche resulting from scintillation light in the crystals. While the neutrons themselves have small energies on the order of a hundred MeV, they produce a signal corresponding to what a particle with tens of GeV of energy would yield through electromagnetic showering in the detector.

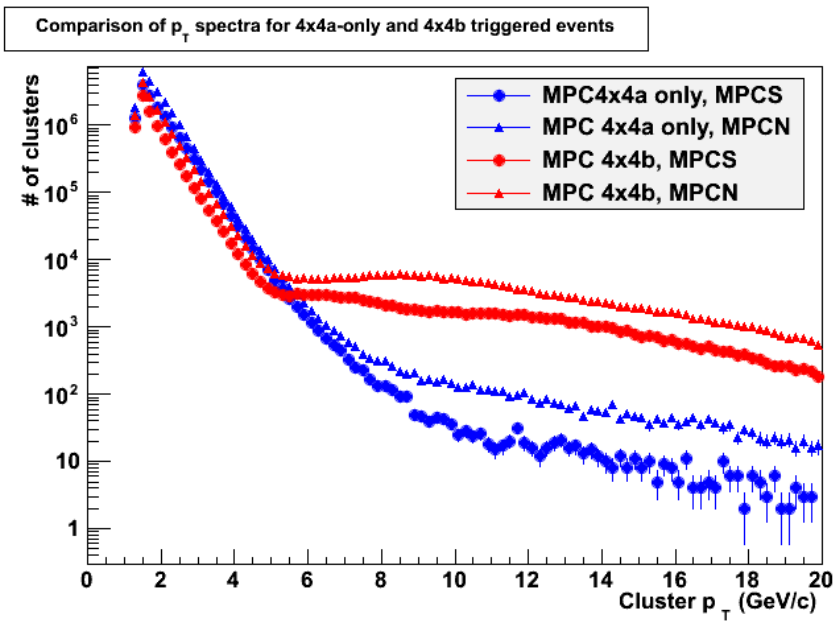

Figure 6.2: MPC 4x4a and 4x4b triggers. The spectrum for the 4x4b trigger is inflated by the presence of the single-tower background which is the dominant source of clusters with energy above $80\,GeV$ or p_T above $5\,GeV$ (see Figure 6.4).

We attempt to eliminate the single-tower background through a number of cuts on cluster parameters. These cuts all generally key on the fact that the background does not involve a shower, so there is no lateral spread of energy (unless by coincidence with another cluster). One simple cut would be to simply remove clusters with fewer than a certain number of towers. In the past, analyzers have removed clusters with fewer than three towers, though it seems this can be pushed further since many of the clusters with only two towers nevertheless appear normal by other measures. A more direct measure of the spatial extent of the shower is the dispersion, and requiring the dispersion to be larger than 0.001 essentially selects those clusters with a multiplicity of 1. In terms of the energy distribution, we know that a typical cluster centered at the center of a crystal will deposit around 90% of its energy in that crystal and 10% in other crystals. Single-tower background clusters will claim even larger fractions of the cluster energy in their central towers, so requiring that $\frac{E_{central\,tower}}{E_{cluster}}$ is smaller than some fraction[1] provides another overlapping cut against the background. Finally, as the position of a cluster's center is calculated as an energy-weighted average of the locations of towers in the cluster, clusters with one dominant tower will have their positions entirely determined by the one tower. This po-

[1] In calculating total cluster energies, only towers with $> 2\%$ of the total energy of towers in the cluster contribute to the cluster energy. A factor of $\frac{1}{0.918}$ is applied to the sum of the individual tower energies to compensate, meaning that for a truly single tower cluster, $\frac{E_{cent}}{E_{clus}} = 0.918$. A hypothetical electromagnetic shower depositing 90% of its energy in one tower and the other 10% in the eight surrounding towers will in contrast have $\frac{E_{cent}}{E_{clus}} \approx 0.83$.

sition shows up clearly as a single-bin spike in a histogram of cluster positions within a single tower. The actual width of the spike is even much smaller than shown in the histogram, and we can exclude clusters at the position of the spike.

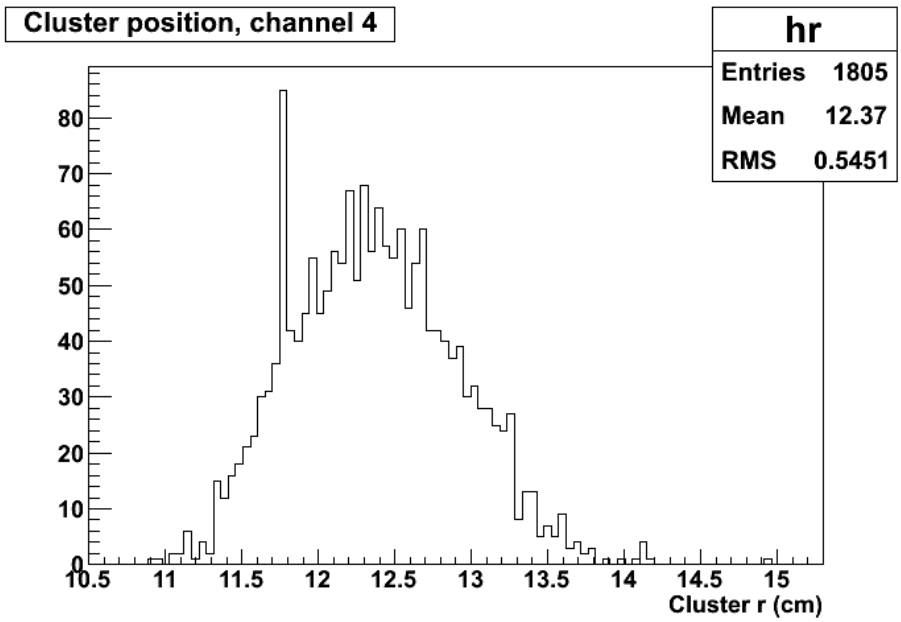

Figure 6.3: The distribution of cluster r for channel 4 shows a spike between 11.7 and 11.8 cm corresponding to the single tower background.

Unfortunately, the chances of at least one tower reporting a high-energy signal consistent with the single tower background are much higher than the chances of a tower recording a hit from a particle with the same high energy. As a result, there is a significant contamination of the triggered data set by the background signal, and perhaps as few as 5-10% of the clusters we see above 80 GeV in energy are of interest to us. The MPC4x4b trigger is especially hit hard owing to its higher threshold and correspondingly low rates of "real" triggers. We show the contamination of the total triggered data sample due to the single-tower background as well as the spectra after the background clusters are removed in Figure 6.4.

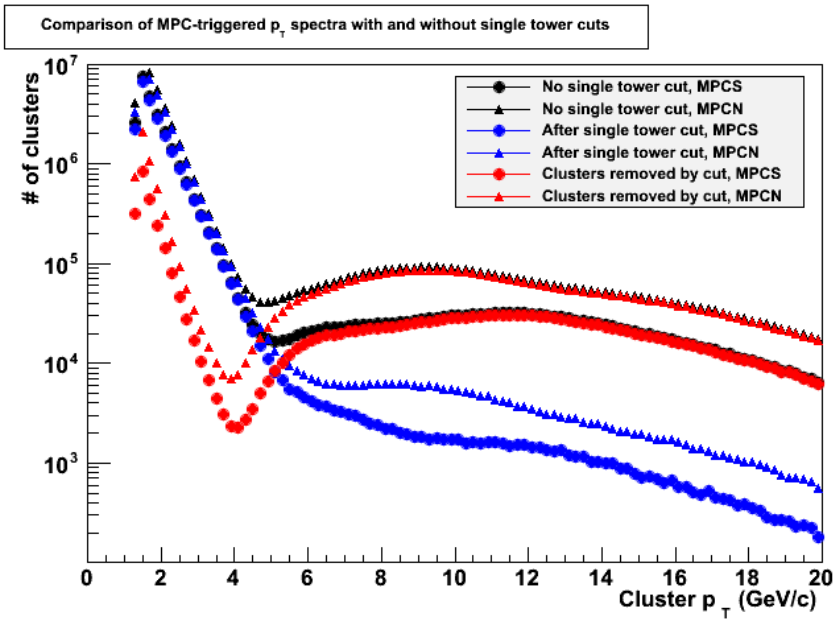

Figure 6.4: Effect of single tower background cut on cluster p_T spectrum. There are around ten times as many clusters removed by our single tower background cuts than there are good clusters for $p_T > 5\,GeV$.

6.1.2 MPC QA

Before computing the final cluster yields and asymmetries with data from the MPC, we must determine which runs and crossings are suitable for inclusion in our analysis. A number of runs and crossings are already excluded due to quality checks on data from the BBC and ZDC scalers. We summarize excluded runs and crossings here.

6.1.2.1 Run-level QA

We carry out checks similar to the ones we employed in the scaler data QA on a run-by-run level with the MPC data.

Missing data Of the 432 runs marked for physics use in the data acquisition database, 10 runs were not processed to generate the MPC data files.

MPC calibration difficulties Possibly due to the lower high-voltage settings on the MPC APDs in the M=10 section of Run 11 (before run 336636), or possibly in part due to the same beam stability issues that caused difficulties in analyzing the BBC and ZDC data before run 336000, we have been unable at this point to converge on a final set of gains for this section of Run 11. Our measurements of tower and cluster counts per trigger and bunch shuffling widths also show wide variations in this early part of Run 11 that are not present in the M=15 section. For these reasons, we exclude the portion of Run 11 where

the MPC is running at the M=10 setting, as well as the first fill at the M=15 setting. Most of this data is excluded due to the BBC and ZDC QA cuts as well.

PHENIX data acquisition problems Four runs were aborted very early on due to problems with the data acquisition system; data collected from these runs is unreliable.

Abort gap alignment For each run, we check that crossings 111 to 119 are empty, as no collisions occur in these crossings. A crossing shift for each run had been determined previously by analyzers in PHENIX's Spin Physics Working Group that corrects the crossing numbers reported in the original data. After applying the crossing shift, all runs were aligned as expected. However, eight runs had an abort gap that was one crossing too long as well as sporadic pairs of empty crossings throughout the rest of the first 110 crossings, so we exclude these runs from our analysis.

6.1.2.2 Crossing-level QA

To find outlying crossings that should be excluded, we looked at the number of clusters in each crossing that pass all of our analysis cuts. We fit a constant to these values from crossing 0 to crossing 110 and use ROOT's LTS regression method to only include 85% of the crossings (so the empty-full crossings, for example, do not have a disproportionate effect on the fit). Any crossing with fewer clusters than 0.5× the run average is flagged as bad. The number of good clusters for each crossing for a typical run along with the constant fit is shown in Figure 6.5.

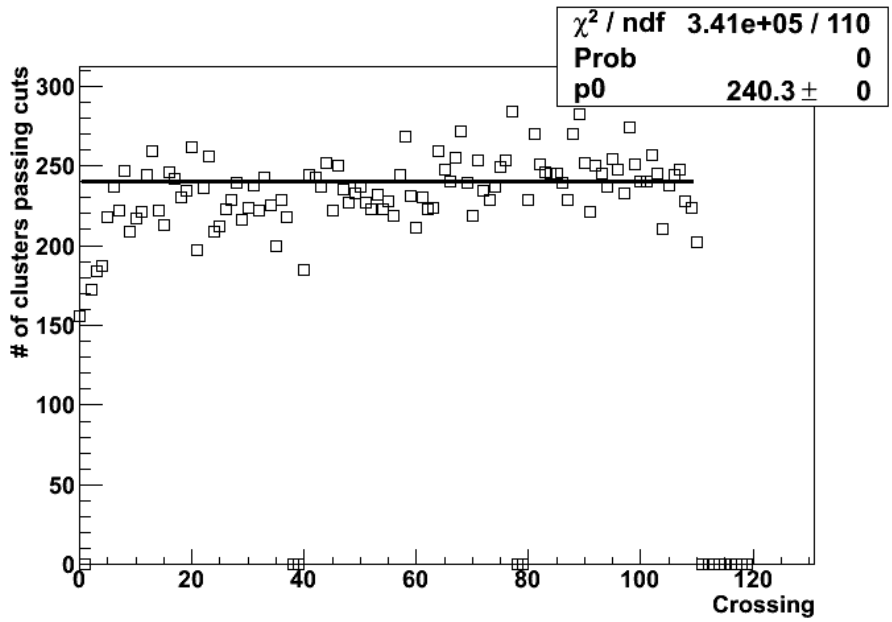

Figure 6.5: An example plot for one run showing clusters per crossing and the constant fit using LTS regression. Here, the only crossings excluded by the MPC crossing-level QA are the pairs of empty-full crossings at 38,39,78, and 79, the abort gap above crossing 110, and crossing 1 where the DAQ is set to busy.

6.1.3 Data characterization

6.1.3.1 Triggered vs. minimum bias data

For our final physics result, we analyze data from MPC-triggered data as opposed to minimum bias data. The high rate of minimum bias events necessitates a large prescale for those events, where data from only a small fraction of minimum bias events (every nth where n is the prescale factor) can be written to disk. However, the majority of these events do not result in high-p_T clusters in the MPC that we need for our analysis. Therefore, the triggered data set includes only those events where the MPC4x4a, MPC4x4b, and/or the MPC4x4c&ERT_LL12x2 trigger fired, indicating the presence of at least one of these clusters of interest. As the rate of high-p_T clusters is so much smaller than the rate for minimum bias events, we can collect this data with either a small prescale or no prescale at all. We show the effect of the MPC triggers by comparing spectra of cluster energies and p_T in the MPC for the minimum bias data set and the triggered data set in Figure 6.6. At energies below the lowest trigger threshold, there are relatively few clusters in the triggered sample compared to both the minimum bias sample and the triggered sample just above the trigger threshold[2]. The trigger then "turns on" at around $20\,GeV$, and the improved selection yielded by the trigger allows for a greater number

[2]There are still clusters in the spectrum below the threshold from events where a high-energy cluster fires the trigger and other clusters from the same event are recorded as well

of high-energy clusters to be collected, given bandwidth limitations, compared to the minimum bias trigger.

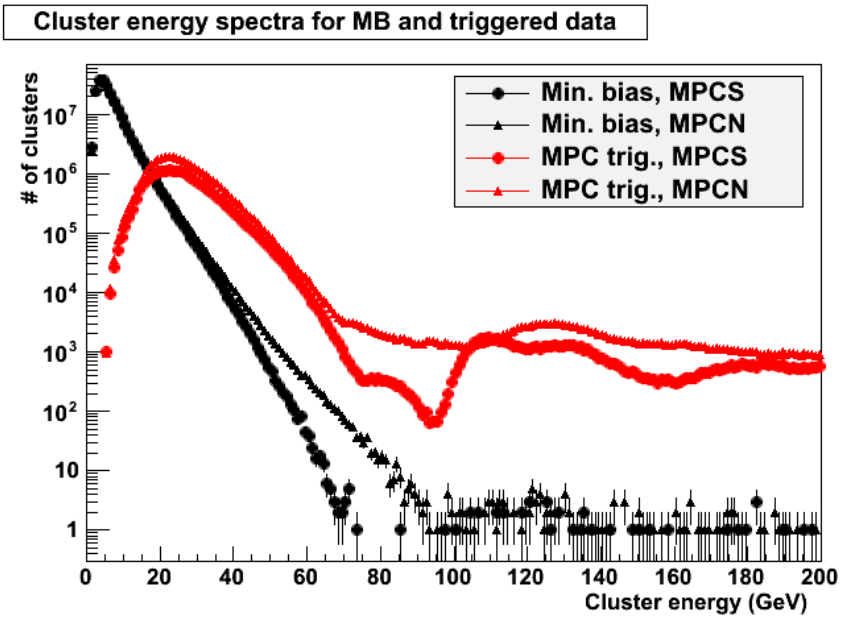

(a) Cluster energy spectra for minimum bias and triggered data.

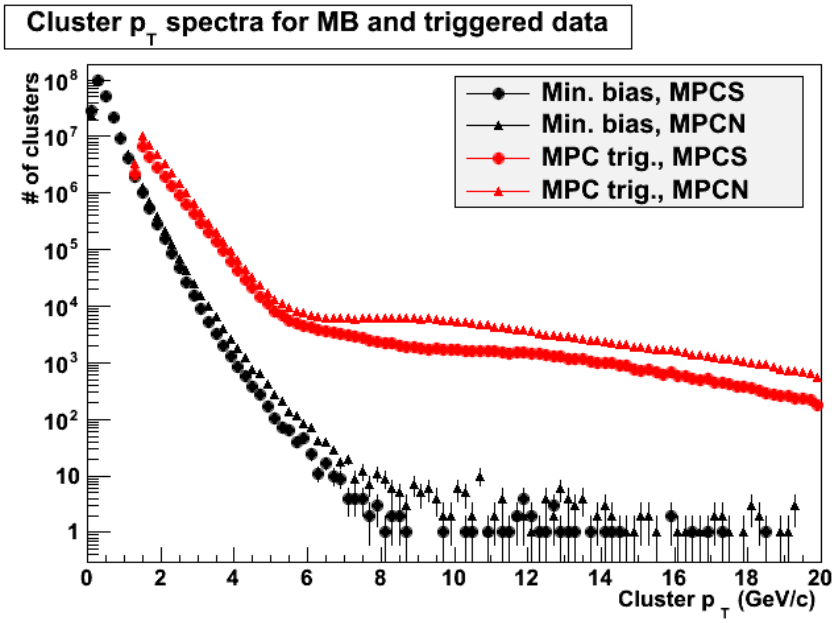

(b) Cluster p_T spectra for minimum bias and triggered data.

Figure 6.6: Comparison of cluster spectra in minimum bias and triggered data.

6.1.3.2 BBC vertex distribution

Figure 6.7 contains the BBC collision vertex distributions for MPC-triggered events. For each event, we also find the highest-energy cluster in the MPC (generally the one responsible for firing the trigger), and we separate the overall

vertex distribution into two distributions based on whether the leading cluster was in the north or south arm. The distribution for the MPCN is larger as expected due to its larger acceptance. The collision vertex locations are biased slightly towards the arm containing the leading cluster, as there is also a vertex-dependent acceptance effect in the MPC; for a given angle of a particle leaving the collision and the beam axis, more particles will hit the MPC if the vertex is closer to the detector.

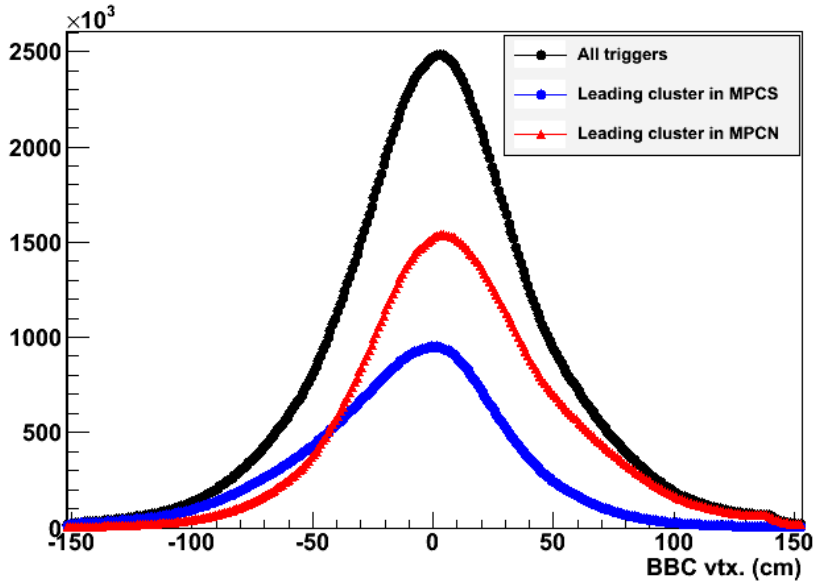

Figure 6.7: Distribution of collision vertices as determined by the BBC for MPC-triggered events.

6.2 Merged cluster identification

As discussed previously, for our final asymmetries, we consider single high-energy clusters in the MPC, the majority of which arise from overlapping pairs of clusters from π^0 decay. We apply cuts to clusters in the MPC to maximize the number of merged clusters in the analysis while minimizing the contribution from clusters from unmerged π^0's and the single tower background. The cuts used are the following:

- $E_{cluster} > 15\,GeV$
- $p_{T,\,cluster} > 1.5\,GeV/c$
- $12\,cm < r_{cluster} < 19\,cm$
- Central tower not in warn map
- ADC not overflowed

- TDC not overflowed
- $dispersion > 0.0005\,cm^2$
- At least three towers in the cluster
- Cluster r not in excluded tower-by-tower spike

6.3 Calculating the asymmetries

Recall the definitions for the parity-violating single-spin asymmetries $A_{L,b(y)}$ we use as a crosscheck and the double longitudinal spin asymmetry A_{LL}:

$$A_{L,b(y)}^{clus.} = \frac{1}{P_{b(y)}} \frac{N_{clus.}^{+} - RN_{clus.}^{-}}{N_{clus.}^{+} + RN_{clus.}^{+}},$$
$$A_{LL}^{clus.} = \frac{1}{|P_b P_y|} \frac{N_{clus.}^{++} - RN_{clus.}^{+-}}{N_{clus.}^{++} + RN_{clus.}^{+-}}. \tag{6.3}$$

As input to the asymmetry calculation for a given run, we need blue and yellow beam polarization values, cluster yields, and a measurement of relative luminosity. The blue and yellow beam polarizations can be found in a database provided by RHIC Spin[60] as in the relative luminosity analysis. We count clusters that pass all of our analysis cuts in p_T bins of 1.5-2.0, 2.0-2.5, 2.5-3.0, 3.0-4.0, 4.0-5.0, 5.0-6.0, 6.0-7.0, 7.0-8.0, and 8.0-12.0 GeV/c. The scaler counts for determining relative luminosity come from the *BBCwide* trigger, and the cluster yields and scaler yields are sorted by bunch according to the blue and yellow beam helicities ($h_b h_y$), where the helicities can be + or −. For $A_{LL}^{clus.}$, crossings are grouped into same-sign (++ or +−) crossings and opposite-sign (+− or −+) crossings, excluding crossings removed by data quality cuts (the same crossings are excluded when calculating both the scaler and cluster yields). For the single spin asymmetries, $A_{L,b(y)}^{clus.}$, we consider only the helicity of the blue or yellow bunch in grouping crossings. We calculate an asymmetry for each run individually, and the resulting run-by-run asymmetries are fit with a constant to determine the final overall asymmetry. We calculate asymmetries separately for even and odd crossings (due to slightly different thresholds in the separate trigger circuits for even and odd crossings) and for the north and south arms of the MPC. These are checked for consistency and then combined for the final result.

6.4 Single-spin asymmetries $A_{L,b(y)}^{clus.}$

We calculate $A_{L,b(y)}^{clus.}$ separately for even and odd crossings, blue and yellow beam, and the north and south arms of the MPC. An example of a fit of the run-by-run asymmetry to a constant is shown in Figure 6.8.

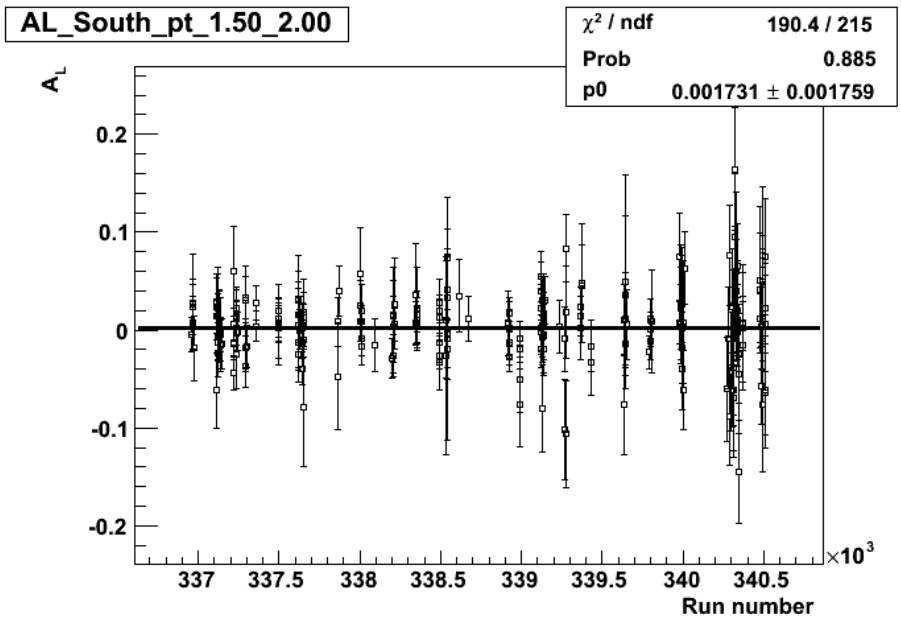

Figure 6.8: $A_{L,b}^{clus\cdot}(blue\,beam)$ by run for clusters in the MPC South in the lowest p_T bin from even crossings only.

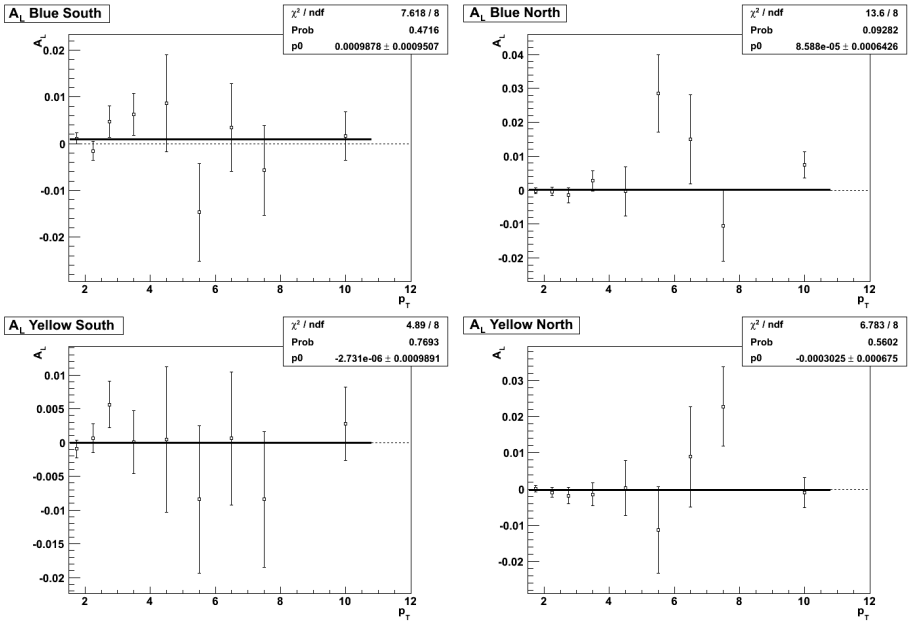

Figure 6.9: $A_{L,b(y)}^{cluster}$ vs. p_T for the blue (yellow) beam for clusters in the north and south arms of the MPC.

We also show $A_L^{clus\cdot}$ vs. p_T results for the blue and yellow beams and clusters in the MPCS and MPCN in Figure 6.9. We see reasonable numbers for χ^2/NDF, and the asymmetries (given by the fit parameters) are consistent with zero as expected due to the invariance of QCD interactions under a parity transformation. That the single-spin asymmetries are consistent with zero puts

a limit on the size of possible false asymmetries

6.5 Double longitudinal spin asymmetry, $A_{LL}^{clus.}$

We present in this section our results for $A_{LL}^{clus.}$ from the triggered data set, for even and odd crossings and the north and south arms of the MPC. As for the single-spin asymmetry results, we only include a sample plot of A_{LL} vs. run number (6.10a), the asymmetries vs. p_T separated by arm and even/odd crossings (6.10b), and a table of the results for those asymmetries (Table 6.1); the complete collection of plots can be found in Appendix B. We find asymmetries that are consistent over the course of Run 11 without any time-dependent effects, and the values of χ^2/NDF for the constant fits to the plots of asymmetry vs. run number are reasonable as well.

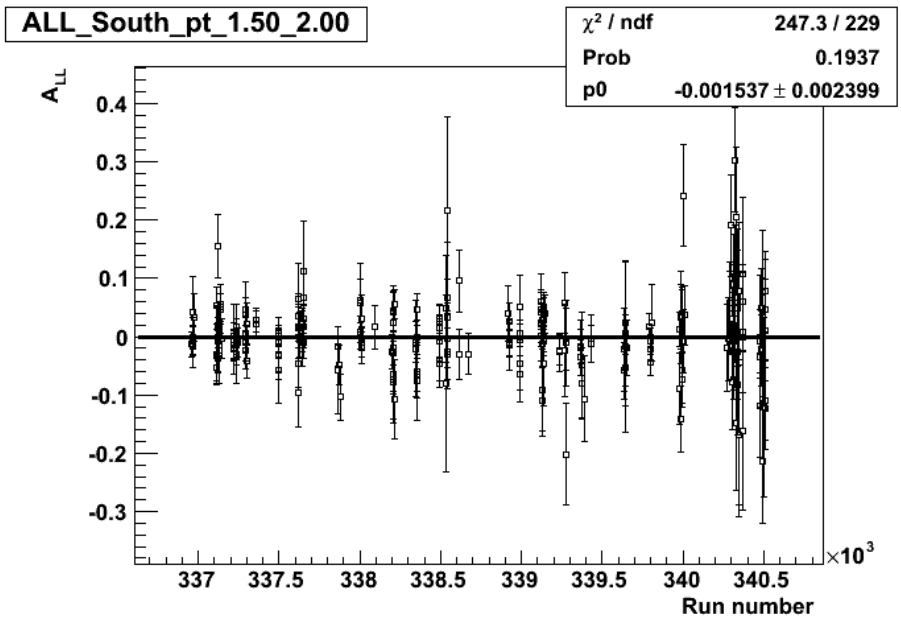

(a) $A_{LL}^{clus.}$ by run for clusters in the MPC South in the lowest p_T bin from even crossings only.

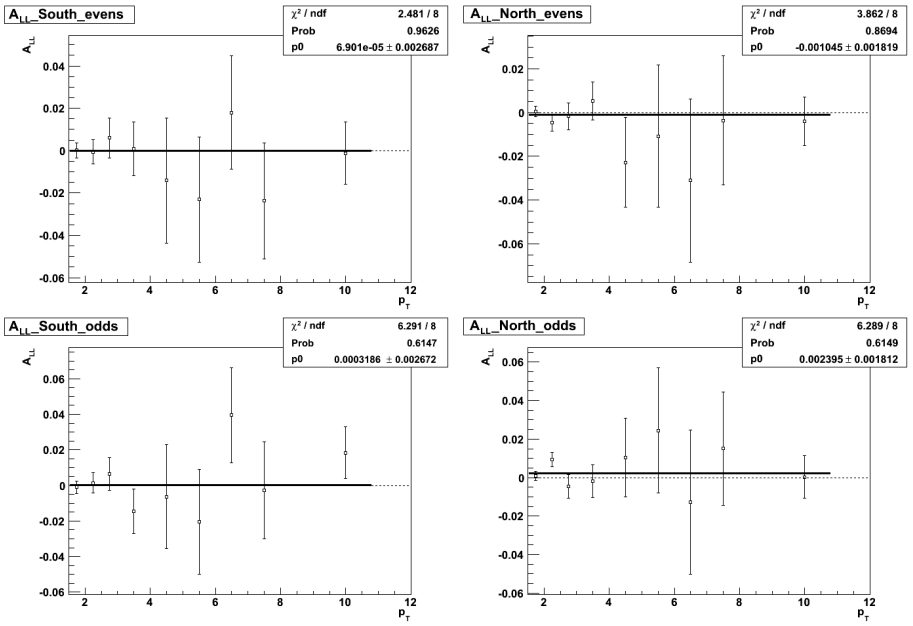

(b) $A_{LL}^{clus.}$ for even crossings, MPCS (upper-left), even crossings, MPCN (upper-right), odd crossings, MPCS (lower-left), odd crossings, MPCN (lower-right).

Figure 6.10: $A_{LL}^{clus.}$ results separated by even/odd crossings and MPC arm.

Table 6.1: $A_{LL}^{cluster}$ results for MPC-triggered data

$p_T^{min.}$	$p_T^{max.}$	Arm	Crossings	$A_{LL}^{cluster}$	$\delta A_{LL}^{cluster}$ $(stat.)$	χ^2/NDF
1.5	2	South	evens	8.74E-05	0.00350374	219.84/215
1.5	2	North	evens	0.000589329	0.00236312	209.947/215
1.5	2	South	odds	-0.00105821	0.00348314	223.497/215
1.5	2	North	odds	0.000911657	0.00235704	237.524/215
2	2.5	South	evens	-0.000572485	0.00579321	197.695/215
2	2.5	North	evens	-0.00464812	0.00377094	191.88/215
2	2.5	South	odds	0.00143051	0.00577246	223.396/215
2	2.5	North	odds	0.00924482	0.00375744	205.197/215
2.5	3	South	evens	0.00602013	0.00933998	186.998/215
2.5	3	North	evens	-0.00166943	0.00619408	239.691/215
2.5	3	South	odds	0.00639768	0.00931184	177.114/215
2.5	3	North	odds	-0.00467624	0.00614869	211.79/215
3	4	South	evens	0.0008295	0.0126835	187.851/215
3	4	North	evens	0.00532805	0.00862869	213.868/215
3	4	South	odds	-0.0146179	0.0125706	207.43/215
3	4	North	odds	-0.00184115	0.00853786	242.726/215
4	5	South	evens	-0.0141161	0.0296622	251.249/215
4	5	North	evens	-0.0227218	0.0206473	242.995/215
4	5	South	odds	-0.00629458	0.0292019	267.814/215
4	5	North	odds	0.0103657	0.0204816	215.677/215
5	6	South	evens	-0.0230577	0.0295705	264.104/214
5	6	North	evens	-0.0108052	0.0325265	196.98/214
5	6	South	odds	-0.0203544	0.0294782	210.414/214
5	6	North	odds	0.0245385	0.0324754	219.451/215
6	7	South	evens	0.0180156	0.0267388	243.567/214
6	7	North	evens	-0.0310115	0.0373504	255.458/212
6	7	South	odds	0.0394927	0.0266028	195.497/213
6	7	North	odds	-0.0127945	0.0373464	229.983/213
7	8	South	evens	-0.0237393	0.0273027	209.183/214
7	8	North	evens	-0.00361396	0.0295606	237.791/214
7	8	South	odds	-0.00270692	0.027246	186.997/214
7	8	North	odds	0.0150494	0.0294366	207.397/215
8	12	South	evens	-0.00122043	0.014753	191.961/215
8	12	North	evens	-0.00399833	0.0110609	223.818/215
8	12	South	odds	0.0184251	0.0146121	233.835/215
8	12	North	odds	0.000360406	0.0110379	268.267/215

6.5.1 Consistency between even and odd crossings and MPCS and MPCN results

To check for consistency between the asymmetries in each p_T bin between even and odd crossings and north and south arms, we employ a Student's T-test. For each p_T bin, we calculate a T-score,

$$T - score = \frac{A_{LL,1}(p_T) - A_{LL,2}(p_T)}{\sqrt{(\delta A_{LL,1}(p_T))^2 + (\delta A_{LL,2}(p_T))^2}}, \tag{6.4}$$

that gives the separation between the asymmetries in units of the statistical error. We then plot the distribution of T-scores, which is expected to follow a Student's t-distribution.

The bin-by-bin T-scores and the distributions are shown in Figure 6.11. We see no systematic difference between the asymmetries calculated from the even crossings versus the odd crossings, and the asymmetries in the MPCS and MPCN are consistent as well.

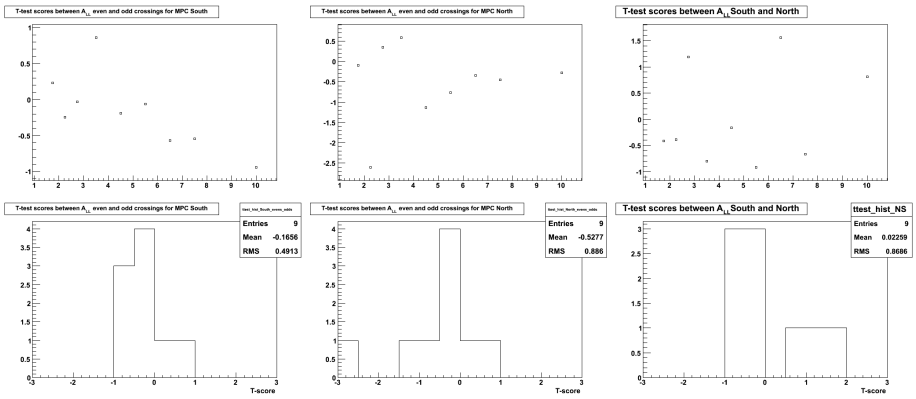

Figure 6.11: T-tests between asymmetries for even and odd crossings in the MPCS (left), even and odd crossings in the MPCN (middle), and the final (even/odd combined) MPCS and MPCN A_{LL} (right).

6.5.2 $A_{LL}^{clus.}$ by spin pattern

We also calculate $A_{LL}^{clus.}$ separately for the four spin patterns used in Run 11 to check for systematic effects that depend on the sequencing of bunch helicities in RHIC. For each of the four asymmetries, we perform the T-test described in the previous section and combine the asymmetries from even and odd crossings and north and south arms (Figure 6.12); again, we see nothing unusual in the T-scores. Finally, we look for discrepancies between patterns by performing T-tests between the two SOOS-type patterns P0 and P3, between the two OSSO-type patterns P1 and P2, and the between the combined SOOS and OSSO asymmetries. These three T-tests yield 9 T-scores each, and the distribution of all T-scores from the tests are plotted in one histogram (Figure 6.13). The final asymmetries for each pattern are shown in Figure 6.14. The asymmetries from

the four patterns show good agreement with one another, though pattern P0 is negative and slightly further from 0 (at 1.5σ) compared to the other patterns.

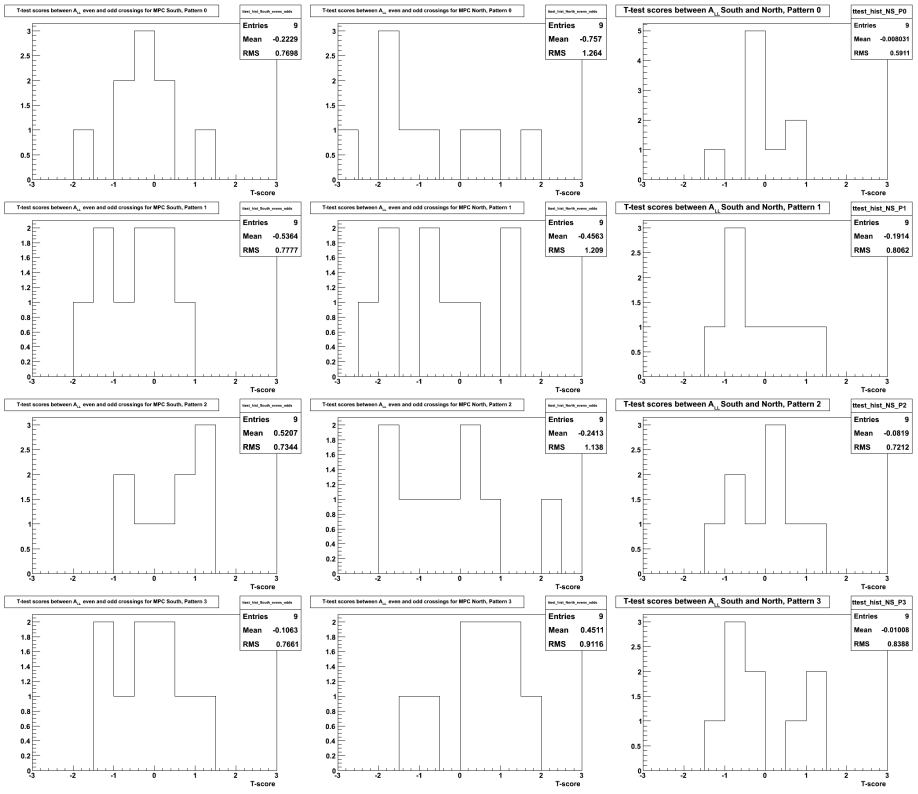

Figure 6.12: Compilation of T-tests for the four spin patterns. Each row represents one pattern, ordered sequentially with P0 at the top. The columns are the same tests shown in the previous section (MPCS even/odd, MPCN even/odd, MPCS/MPCN).

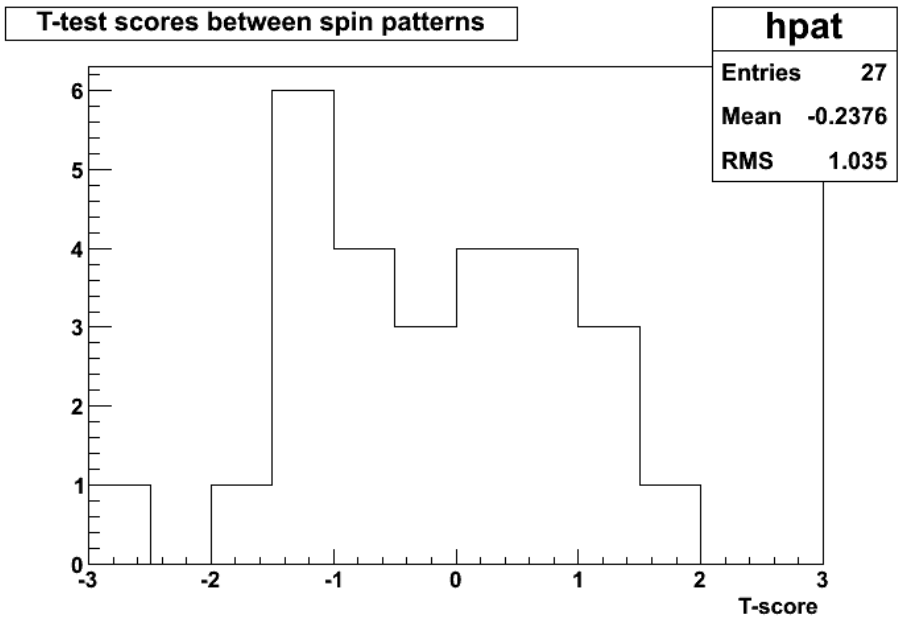

Figure 6.13: Combined T-scores from three T-tests, checking the consistency between patterns 0 and 3, patterns 1 and 2, and the combined asymmetry from patterns 0 and 3 and the combined asymmetry from patterns 1 and 2.

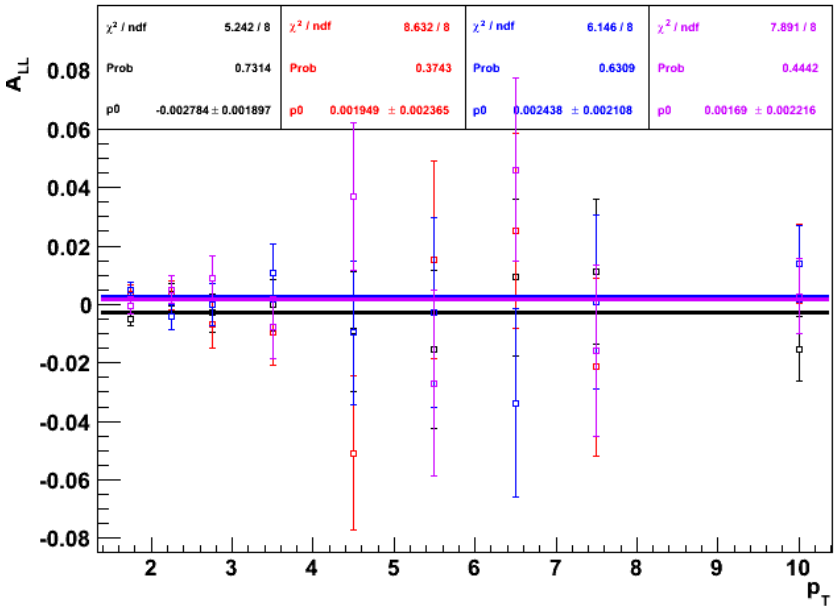

Figure 6.14: $A_{LL}^{clus.}$ calculated separately for each of the four spin patterns. The fit parameters and colors corresponding to the patterns are listed across the top of the plot, starting with P0.

6.5.3 Bunch shuffling

We again use the bunch shuffling method to check for errors causing a systematic offset of our calculated asymmetries and to check the accuracy of the size of our statistical errors. We randomize the beam helicities for each crossing and recalculate A_{LL} for each p_T bin. This process is repeated 10,000 times, and we plot the distribution of $A_{LL}/\delta A_{LL}$ in each p_T bin. The shuffling procedure ensures that the average effective beam polarization over the 10,000 shuffles is zero, so we should find that the mean of the error-normalized asymmetries should be zero. The width of the distribution should be approximately one if the statistical uncertainty δA_{LL} accurately reflects the spread we would hypothetically see if we could repeat our asymmetry measurement 10,000 times. We demonstrate in Figure 6.15 that the shuffled asymmetry distributions conform to expectations and do not point to problems with our calculations of $A_{LL}^{clus.}$ or its uncertainty. The means of the distributions lie near 0 (within the uncertainties of the Gaussian fits), and the widths of the distributions are around 1.02.

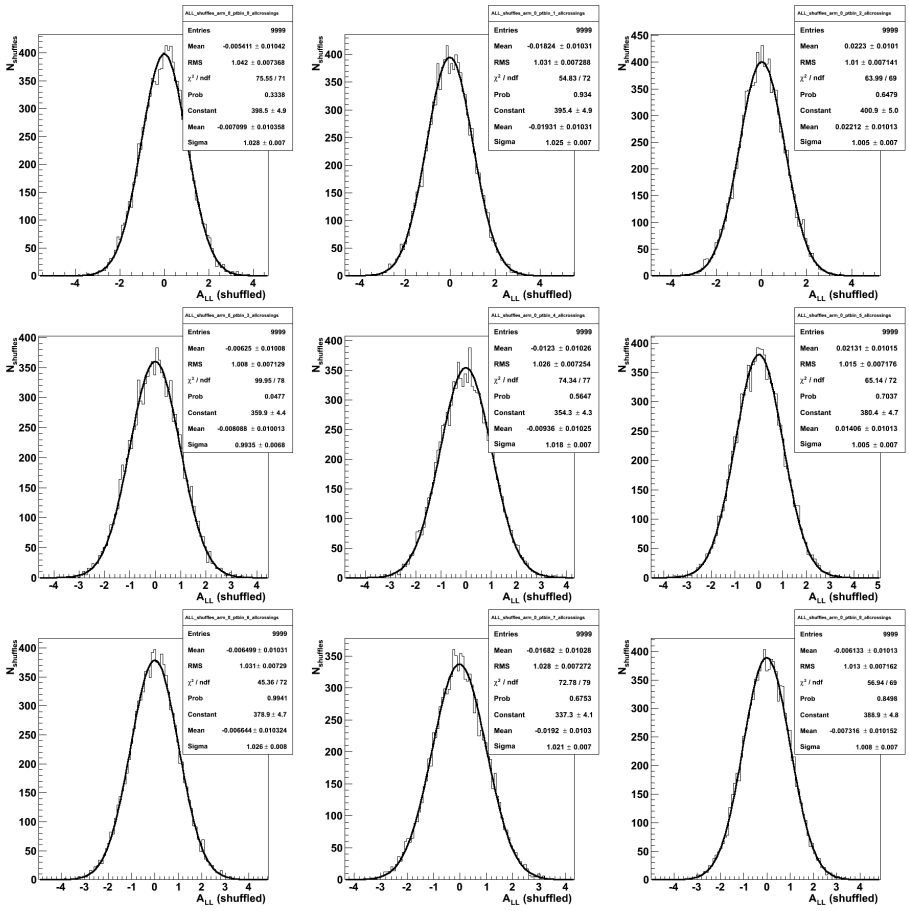

Figure 6.15: Bunch shuffling results for $A_{LL}^{clus.}$ for clusters in the MPCS, all crossings.

6.5.4 Final results for $A_{LL}^{clus.}(MPC)$

Having demonstrated that we calculate consistent asymmetries in the north and south arms and in even and odd crossings, we statistically combine the results to determine our final result for $A_{LL}^{clus.}$ in the MPC. First, the even and odd crossings are combined to give $A_{LL}^{clus.}$ for the north and south arms, and then the results from the north and south arms are combined. The resulting final asymmetry is shown in Figure 6.16, and the data points are given in Table 6.2. We see that the overall asymmetry is consistent with zero as are the asymmetries in each p_T bin. However, the statistical uncertainties, even in the lowest p_T bins, are on the order of 10^{-3}, meaning we are not sensitive to the small asymmetry we are looking for which is not expected to be larger than 5×10^{-4} or so (see subsection 3.2.3).

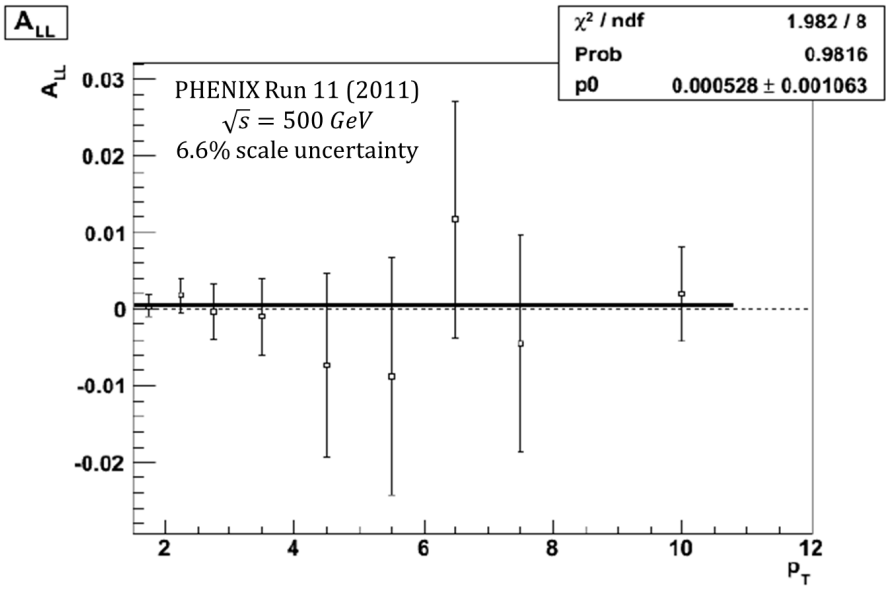

Figure 6.16: Final $A_{LL}^{clus.}(MPC)$ by p_T at $\sqrt{s} = 500\,GeV$. The uncertainty on the polarization measurement leads to an overall vertical scale uncertainty of 6.6%. The systematic uncertainty from the relative luminosity measurement of 2×10^{-5} is not shown here as it is dwarfed by the statistical uncertainties. The point in each p_T bin is plotted at the average p_T for the bin.

Table 6.2: Final bin-by-bin results for $A_{LL}^{clus.}(MPC)$ at $\sqrt{s} = 500\,GeV$. Units of p_T are GeV/c.

$p_T^{min.}$	$p_T^{max.}$	$< p_T >$	$A_{LL}^{clus.}(MPC)$	$\delta A_{LL}^{clus.}(stat.)$
1.5	2.0	1.71	0.000362416	0.00138283
2.0	2.5	2.21	0.00176058	0.00223072
2.5	3.0	2.71	-0.000323252	0.00363911
3.0	4.0	3.35	-0.00103407	0.00501924
4.0	5.0	4.40	-0.00738965	0.0119193
5.0	6.0	5.50	-0.00877294	0.0154528
6.0	7.0	6.51	0.0116827	0.0153475
7.0	8.0	7.52	-0.0044637	0.0141605
8.0	12.0	10.03	0.00198615	0.00624274

Chapter 7

Conclusions and outlook

With the A_{LL} measurements with the MPC, PHENIX will provide data to global QCD analyses that can constrain $\Delta g(x)$ for smaller x than is accessed by central arm measurements, helping to answer the question of how much spin in total the gluons contribute to the proton spin of $1/2$. The Run 9 measurements of the forward cluster A_{LL} at $\sqrt{s} = 200\,GeV$ and $\sqrt{s} = 500\,GeV$[65] and this measurement at $\sqrt{s} = 500\,GeV$ show asymmetries consistent with zero; however, the expected asymmetries according to our simulations were small to begin with, even for significant gluon polarizations, and these are not yet conclusively ruled out. In this thesis, we have shown how we reduced the uncertainty of our relative luminosity determination, the leading systematic uncertainty, from 1.3×10^{-3} to 2×10^{-5}. With this small systematic uncertainty, analysis of a much larger data set from 2013 will provide the statistical precision needed to distinguish between no asymmetry or a possible small asymmetry at forward rapidity, reducing the wide array of functional forms of $\Delta g(x)$ that are presently consistent with the DSSV analysis. This is crucial for constraining the gluon contribution to the proton spin for $x < 0.05$, where current fits allow for gluons in the small-x region alone to have total helicity ranging from more than $\frac{1}{2}\hbar$(the total spin of the proton) to $\frac{1}{4}\hbar$ in the opposite direction of the proton's spin. The potential impact of the A_{LL} measurements in the MPC was discussed with Rodolfo Sassot of the DSSV group at the 2014 PHENIX SpinFest analysis meeting in Urbana. Following the discussion, Rodolfo produced the plot shown in Figure 7.1 to quantify the importance of the MPC analyses to our understanding of the gluon polarization at low x. While PHENIX and STAR continue to provide data improving constraints on the gluon polarization for $x > 0.02$, the forward measurements will be the first to provide information on the gluon polarization for $x < 0.01$ as represented by the significant narrowing of the uncertainty band in Figure 7.1 once projected data from the forward measurements through 2015 are included.

The final word on gluon spin, however, is likely to come from a proposed electron-ion collider (EIC)[66]. The EIC would be the world's first polarized electron-proton collider and would run at extremely high luminosities, and as Figure 7.2 shows, the range of center-of-mass energies and Q^2 would be sufficient to constrain $\Delta g(x)$ even below $x \approx 10^{-4}$.

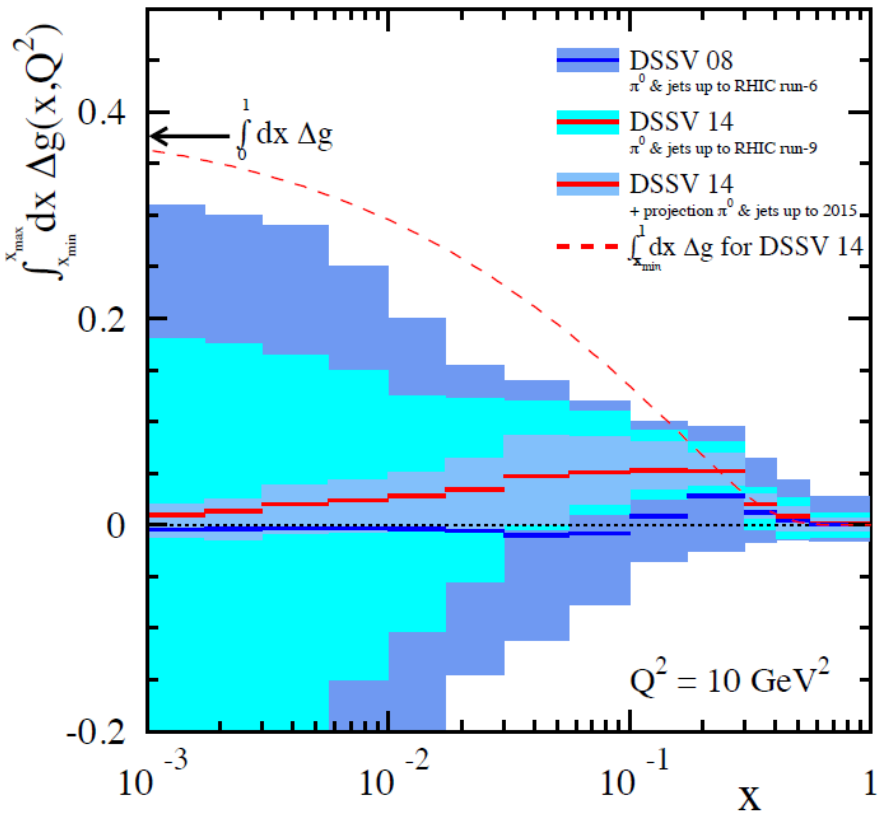

Figure 7.1: Here we show the projected impact of forward measurement of A_{LL} in the MPC through 2015 as well as similar measurements from STAR using their forward electromagnetic calorimeter[44]. In each bin of x, the contribution to the total gluon polarization from that range of x is plotted along with uncertainty bands corresponding to the 90% confidence interval. Results are shown for the original DSSV analysis including only RHIC data through 2006, the updated DSSV 14 analysis including RHIC data through 2009, and a projection that reflects the impact of data from simulations representing RHIC data through 2015 (with the forward measurements).

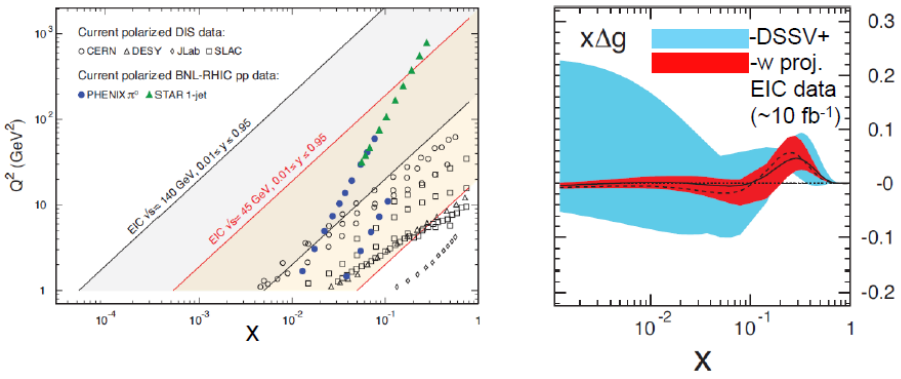

Figure 7.2: Plots showing the projected impact of an electron-ion collider on our knowledge of $\Delta g(x)$. The plot on the left shows the kinematic ranges covered by the EIC, while the plot on the right shows the projected impact on the uncertainty bands of the DSSV fit[66].

Appendix A

Runs used in final analysis

The runs passing the scaler data QA cuts and entering into the asymmetry calculations were the following:

336155 336156 336157 336158 336159 336160 336285 336286 336502 336596 336597 336598 336601 336603 336604 336609 336610 336962 336963 336964 336968 336969 336971 337113 337115 337116 337117 337118 337119 337120 337121 337122 337123 337131 337133 337140 337141 337142 337143 337217 337219 337220 337221 337222 337234 337236 337237 337238 337239 337240 337242 337290 337291 337292 337293 337302 337359 337360 337494 337495 337496 337497 337498 337499 337500 337618 337619 337620 337621 337622 337624 337627 337629 337642 337643 337645 337648 337649 337650 337651 337652 337653 337864 337865 337877 338003 338005 338006 338008 338009 338010 338012 338097 338203 338208 338209 338210 338211 338212 338213 338349 338350 338351 338352 338353 338354 338355 338490 338491 338492 338493 338494 338496 338535 338536 338539 338542 338543 338544 338545 338546 338613 338677 338920 338922 338925 338926 338927 338928 338992 338993 338994 338995 339118 339120 339122 339123 339124 339125 339127 339129 339130 339134 339135 339136 339138 339139 339140 339141 339142 339144 339238 339269 339273 339274 339277 339278 339364 339365 339367 339375 339376 339430 339432 339570 339572 339580 339583 339587 339591 339639 339640 339641 339646 339647 339648 339649 339795 339797 339801 339803 339805 339981 339982 339984 339985 339989 339992 339993 339994 339996 339999 340000 340006 340009 340273 340285 340287 340289 340296 340306 340308 340310 340312 340314 340315 340316 340321 340324 340326 340327 340334 340335 340336 340337 340342 340343 340344 340349 340367 340368 340369 340371 340476 340477 340478 340486 340489 340490 340491 340492 340493 340495 340496 340506 340508 340511 340512 340513.

Appendix B

Asymmetry plots

B.1 $A_L(\frac{ZDC}{BBC})$

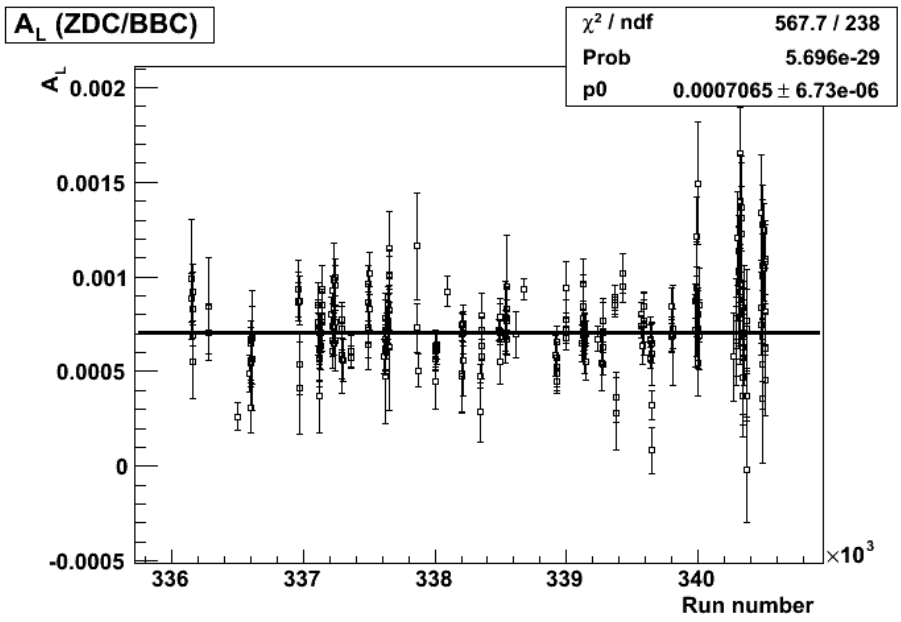

Figure B.1: $A_{L,b}(\frac{ZDC}{BBC})$ (blue beam) vs. run for all crossings.

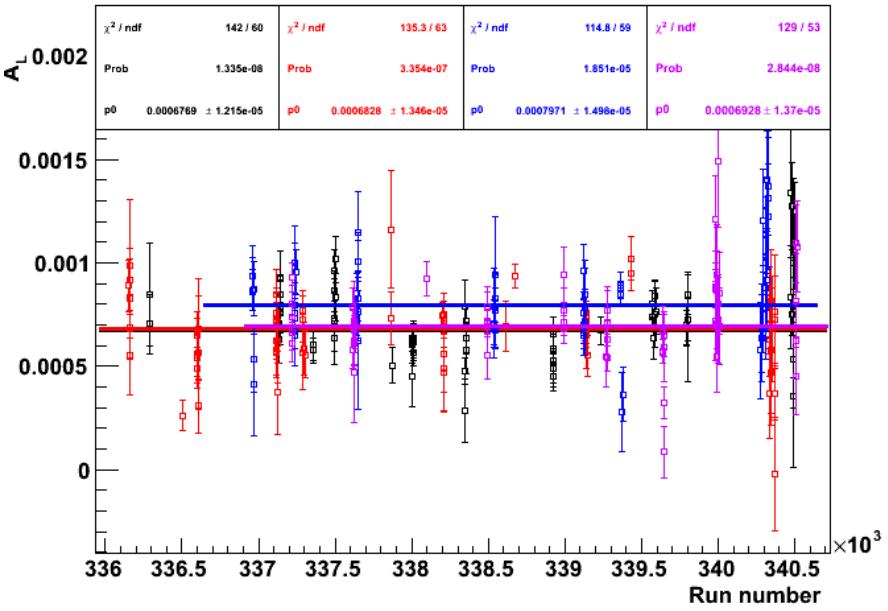

Figure B.2: $A_{L,b}(\frac{ZDC}{BBC})$ (blue beam) vs. run for all crossings, separated by spin pattern.

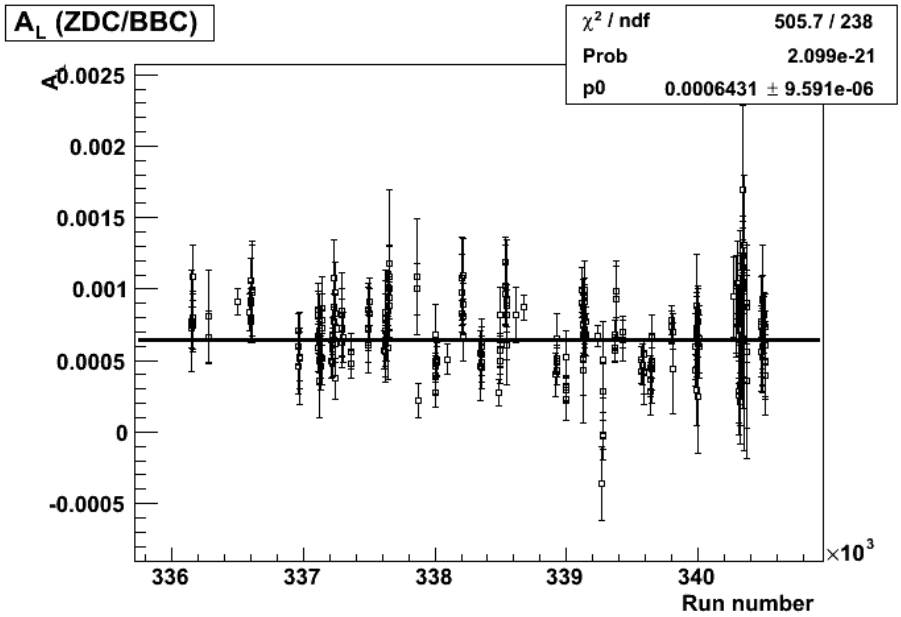

Figure B.3: $A_{L,y}(\frac{ZDC}{BBC})$ (yellow beam) vs. run for all crossings.

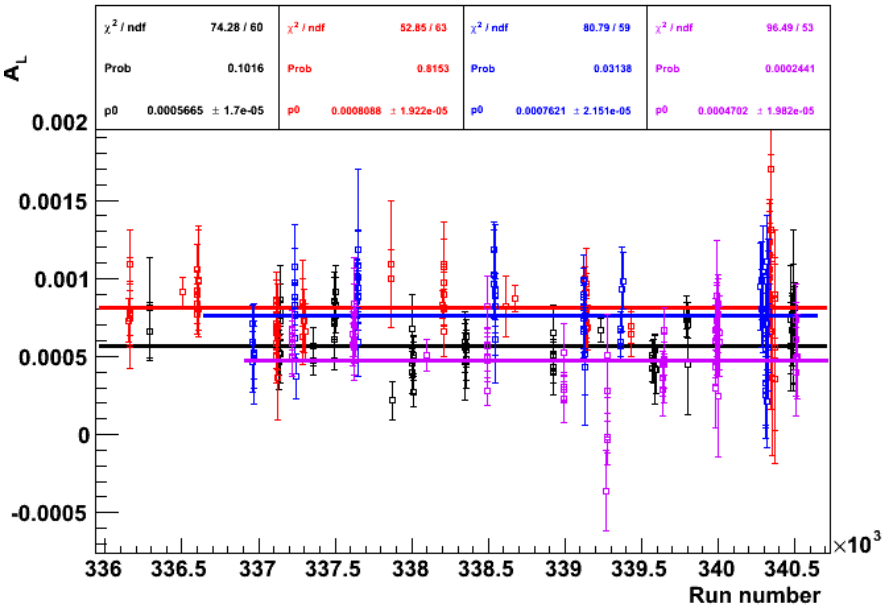

Figure B.4: $A_{L,y}(\frac{ZDC}{BBC})$ (yellow beam) vs. run for all crossings, separated by spin pattern.

B.2 $A_{LL}(\frac{ZDC}{BBC})$

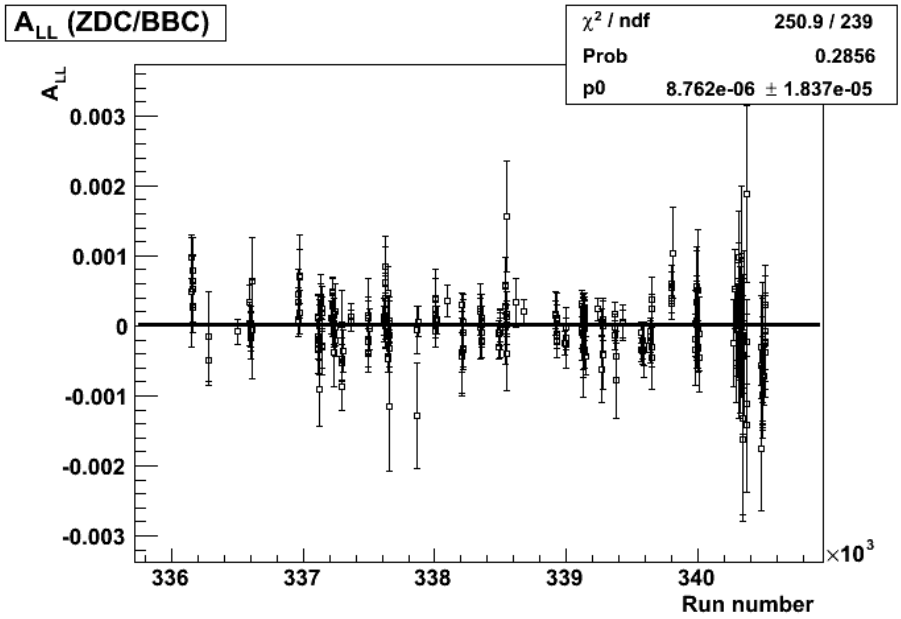

Figure B.5: $A_{LL}(\frac{ZDC}{BBC})$ vs. run for all crossings.

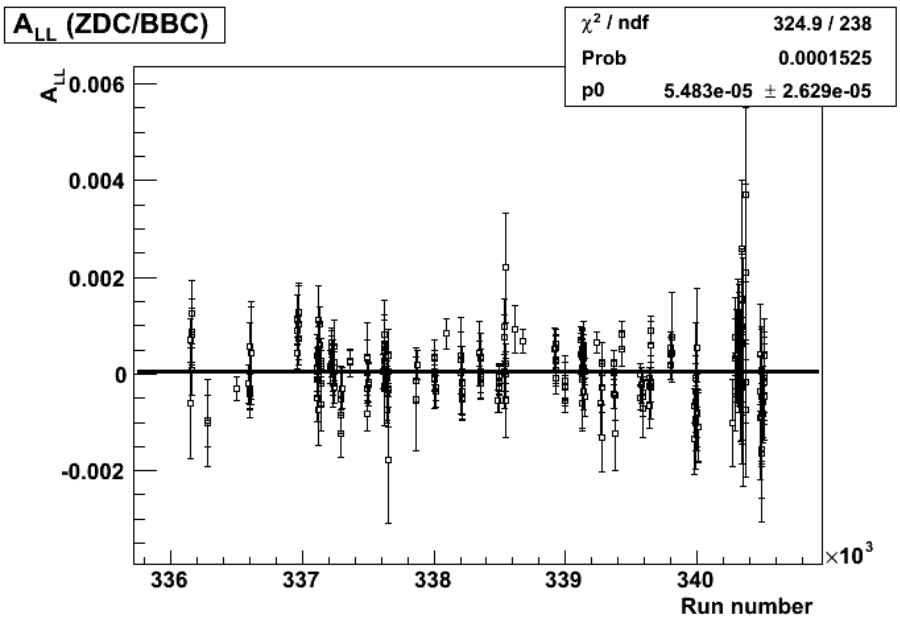

Figure B.6: $A_{LL}(\frac{ZDC}{BBC})$ vs. run for even crossings.

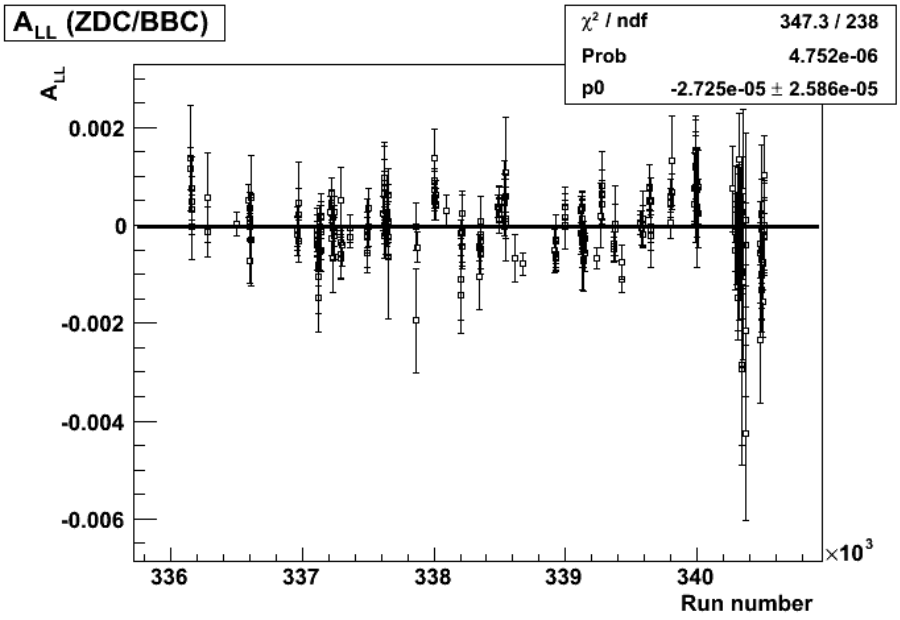

Figure B.7: $A_{LL}(\frac{ZDC}{BBC})$ vs. run for odd crossings.

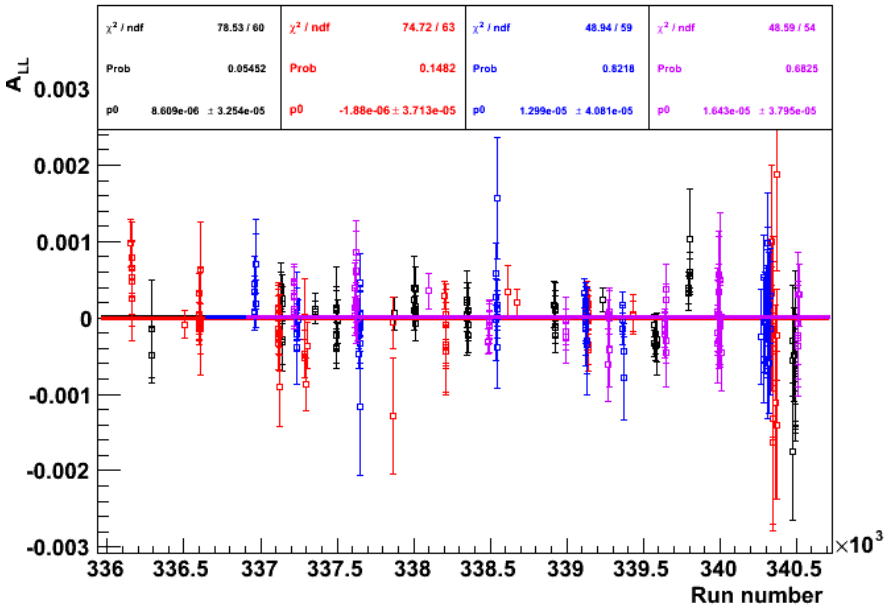

Figure B.8: $A_{LL}(\frac{ZDC}{BBC})$ vs. run for all crossings, separated by spin pattern.

B.3 MPC $A_{L,b(y)}^{clus.}$

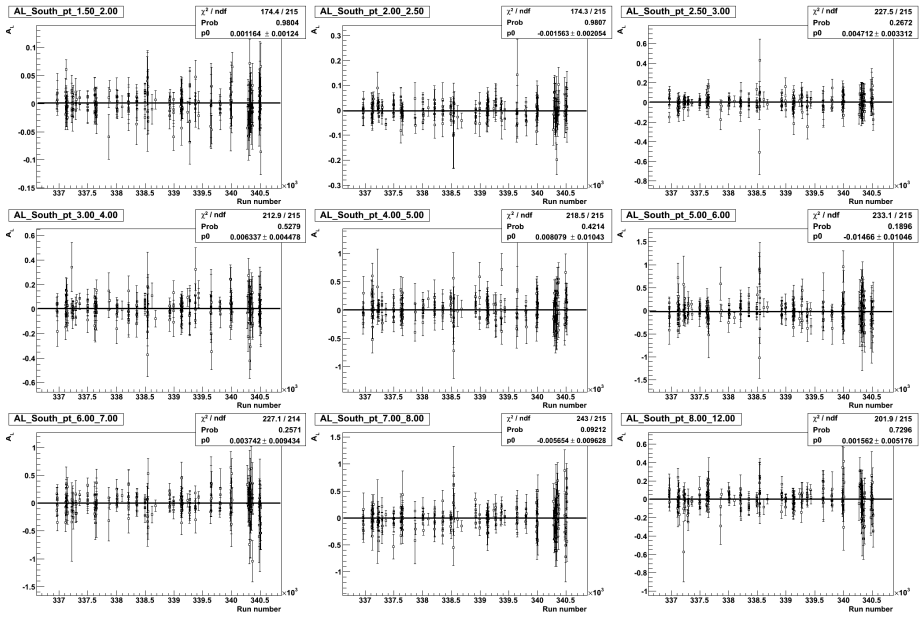

Figure B.9: MPC South $A_{L,b}^{clus.}$ (blue beam) vs. run for all crossings; each plot is one bin in p_T.

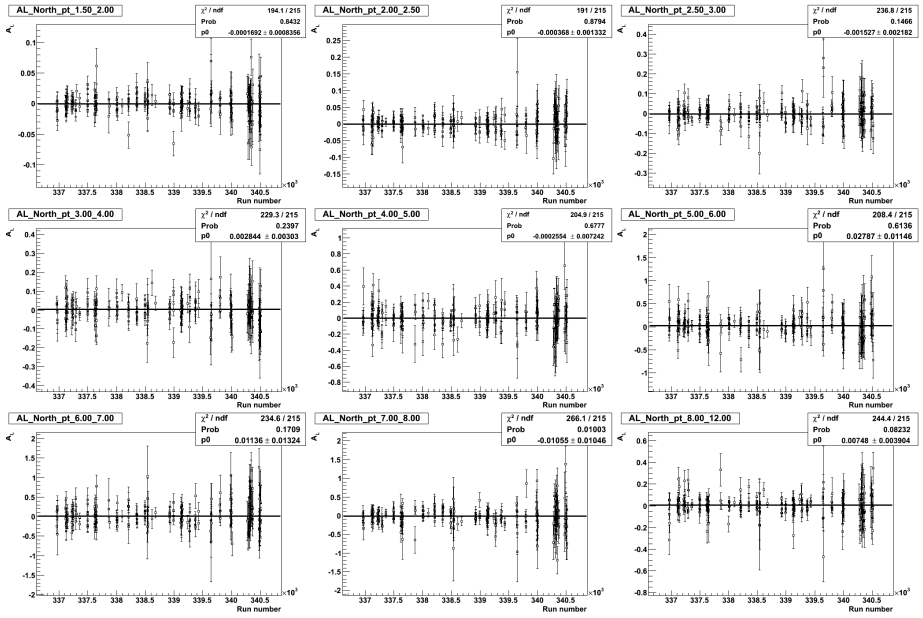

Figure B.10: MPC North $A_{L,b}^{clus.}$ (blue beam) vs. run for all crossings; each plot is one bin in p_T.

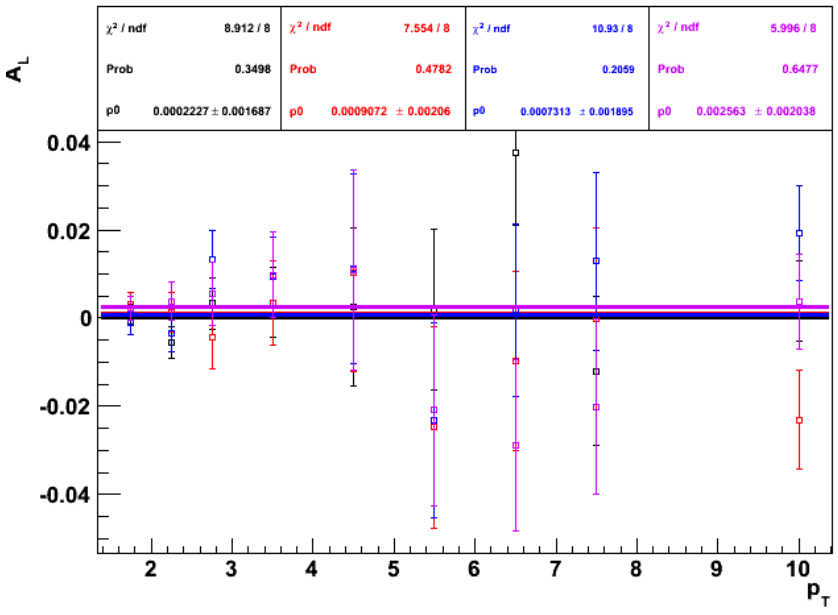

Figure B.11: MPC South $A_{L,b}^{clus.}$ (blue beam) vs. p_T for all crossings, separated by spin pattern.

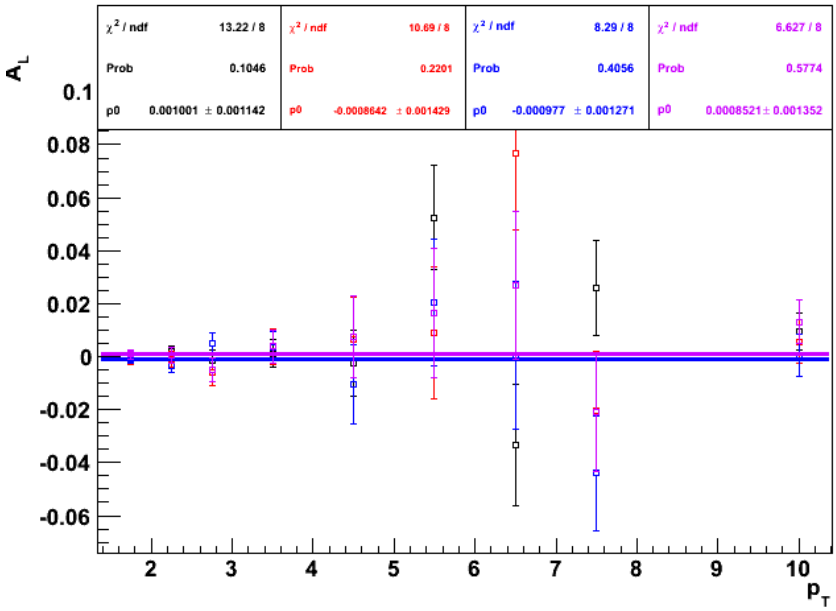

Figure B.12: MPC North $A_{L,b}^{clus.}$ (blue beam) vs. p_T for all crossings, separated by spin pattern.

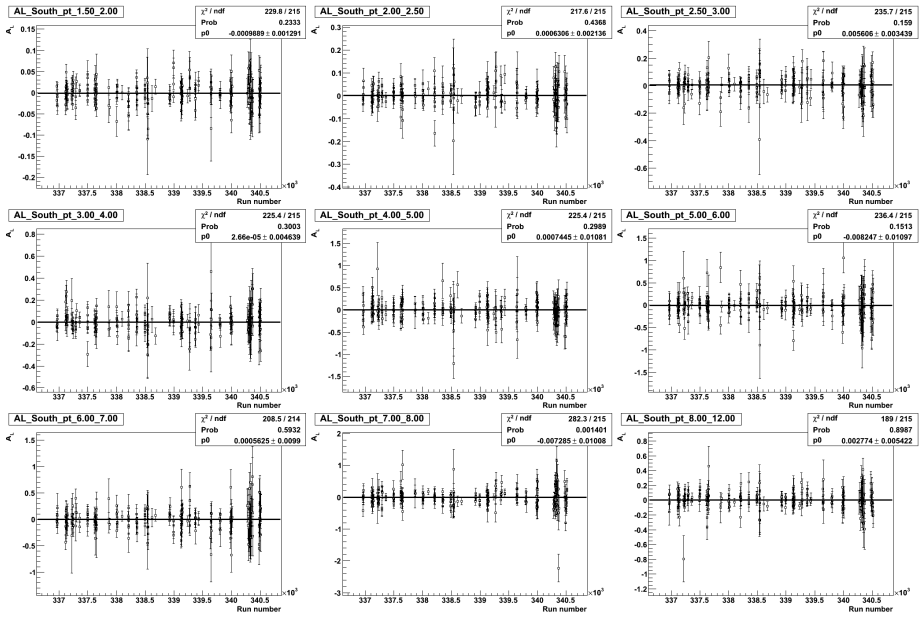

Figure B.13: MPC South $A_{L,y}^{clus.}$ (yellow beam) vs. run for all crossings; each plot is one bin in p_T.

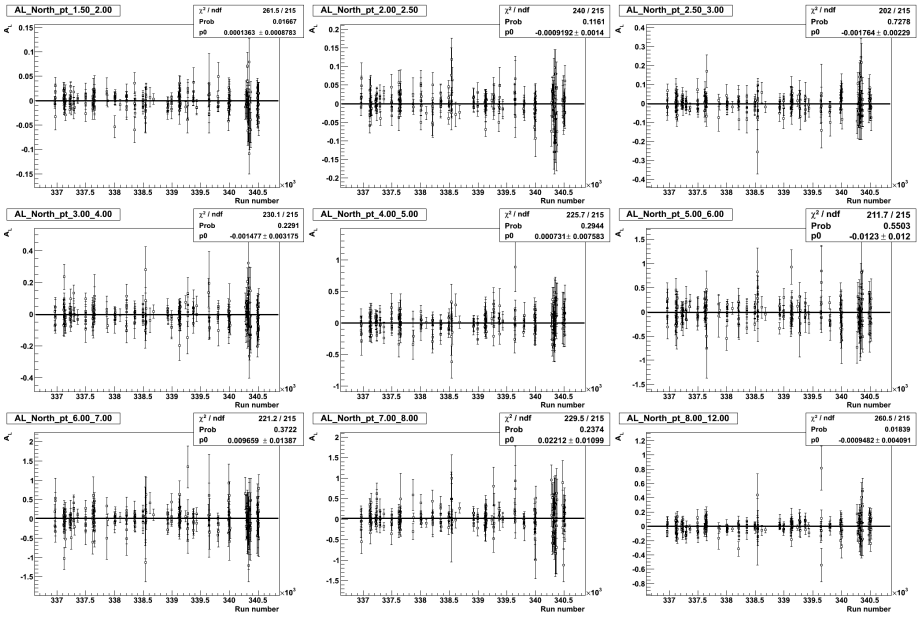

Figure B.14: MPC North $A_{L,y}^{clus.}$ (yellow beam) vs. run for all crossings; each plot is one bin in p_T.

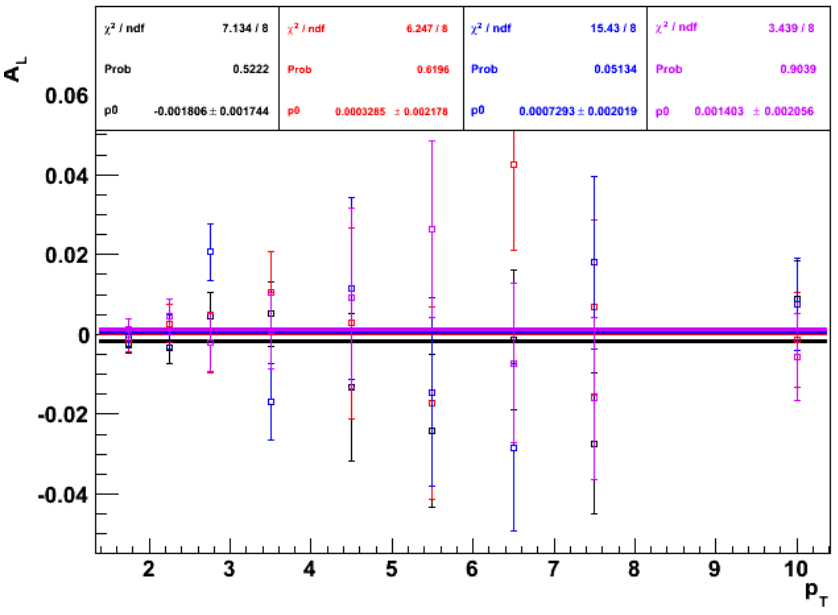

Figure B.15: MPC South $A_{L,y}^{clus.}$ (yellow beam) vs. p_T for all crossings, separated by spin pattern.

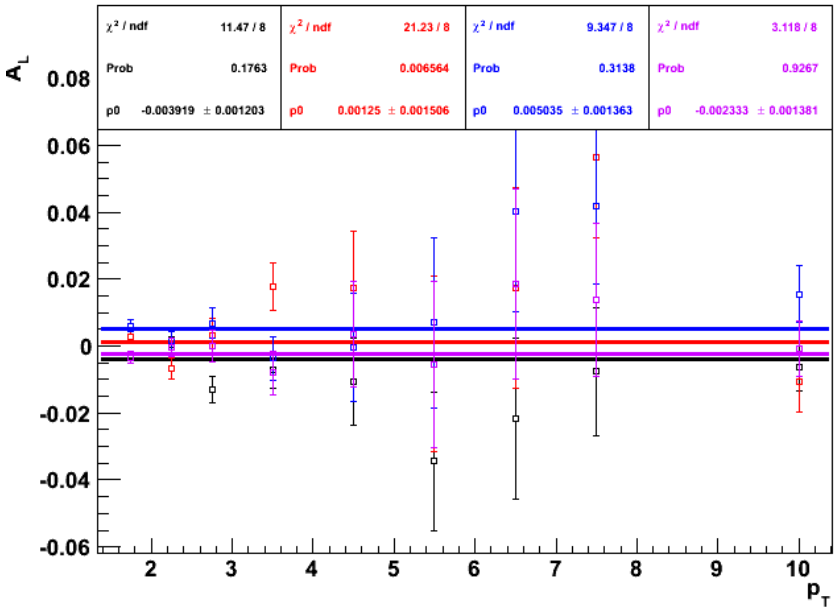

Figure B.16: MPC North $A_{L,y}^{clus.}$ (yellow beam) vs. p_T for all crossings, separated by spin pattern.

B.4 MPC $A_{LL}^{clus.}$

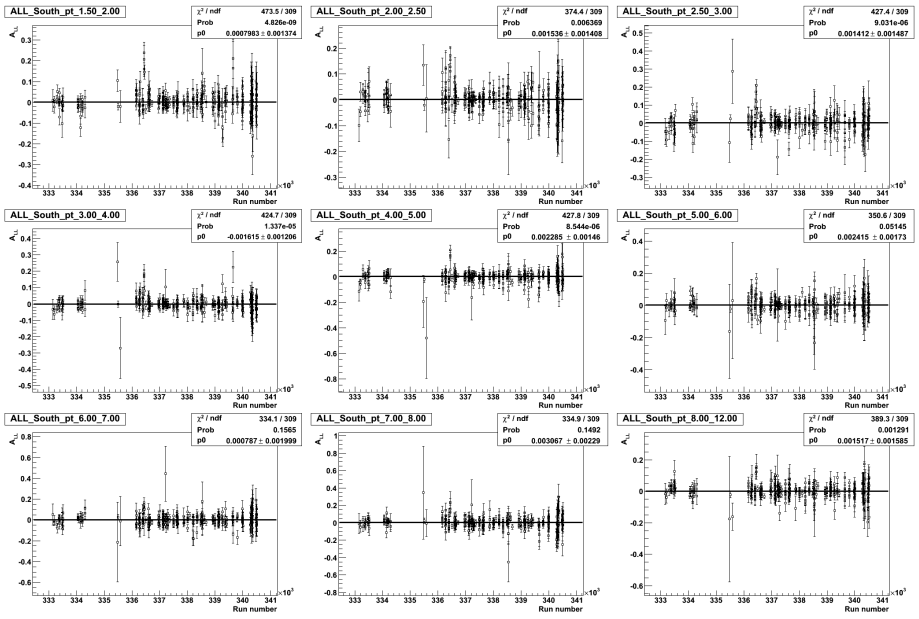

Figure B.17: MPC South $A_{LL}^{clus.}$ vs. run for all crossings; each plot is one bin in p_T.

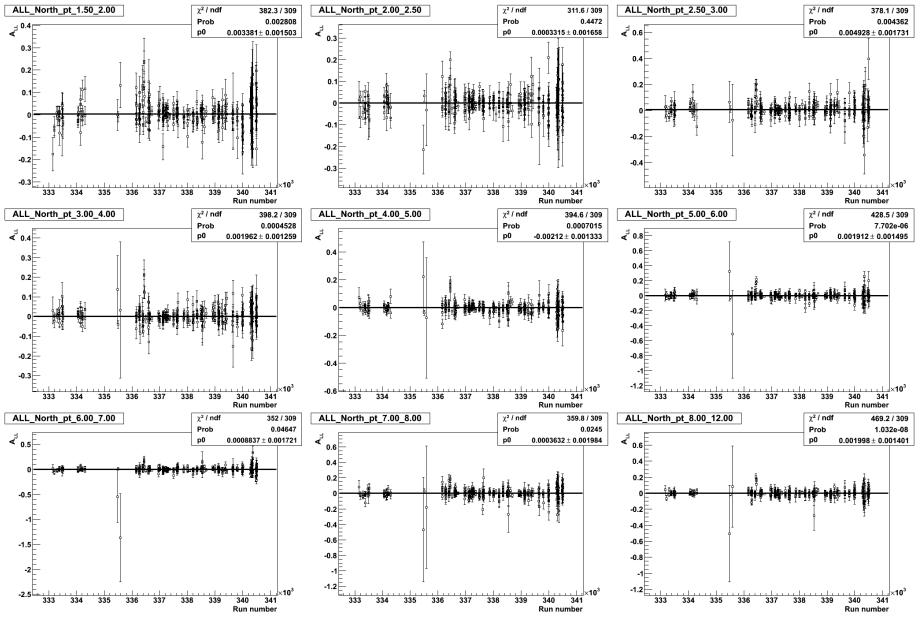

Figure B.18: MPC North $A_{LL}^{clus.}$ vs. run for all crossings; each plot is one bin in p_T.

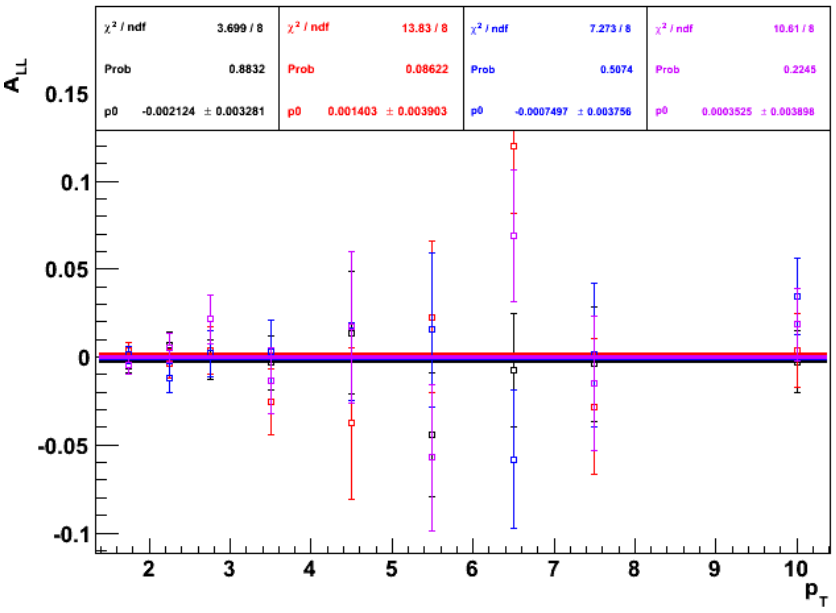

Figure B.19: MPC South $A_{LL}^{clus.}$ vs. p_T for all crossings, separated by spin pattern.

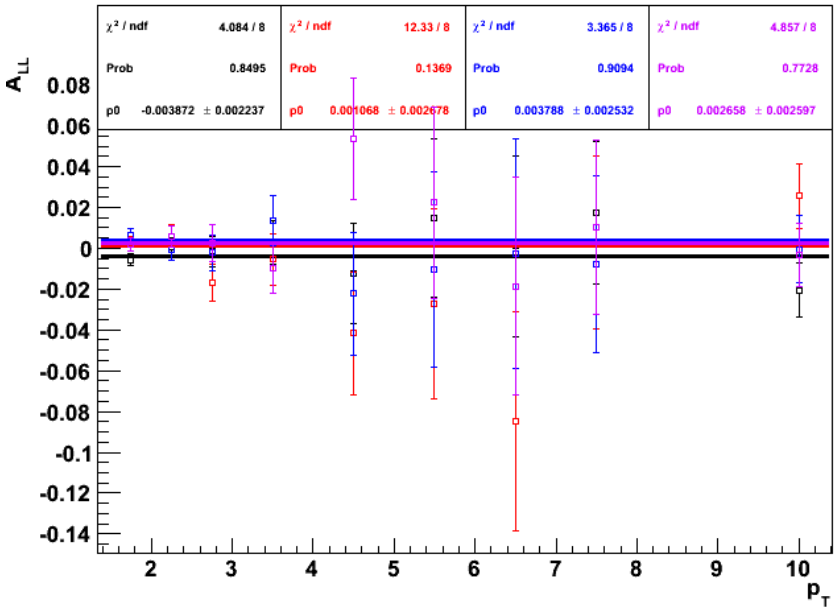

Figure B.20: MPC North $A_{LL}^{clus.}$ vs. p_T for all crossings, separated by spin pattern.

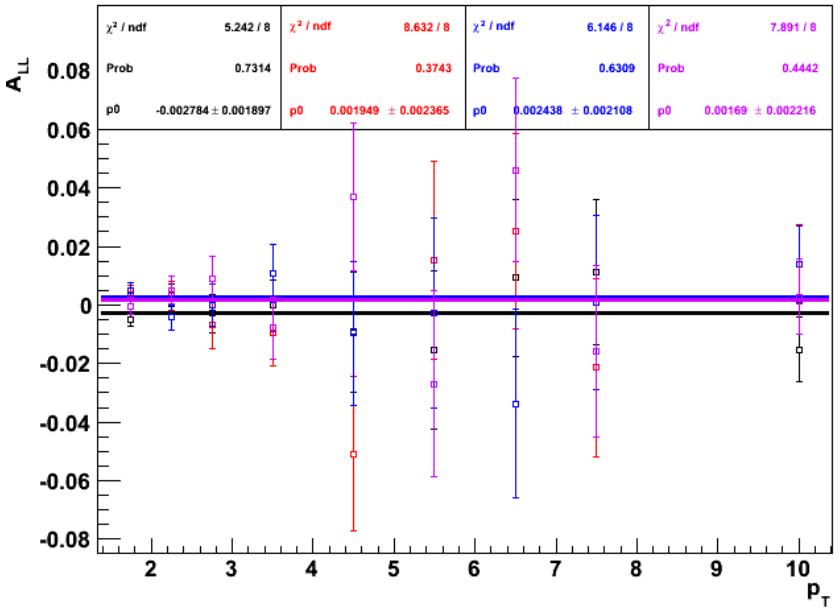

Figure B.21: MPC North and South combined $A_{LL}^{clus.}$ vs. p_T for all crossings, separated by spin pattern.

B.4.1 MPC $A_{LL}^{clus.}$ bunch shuffling

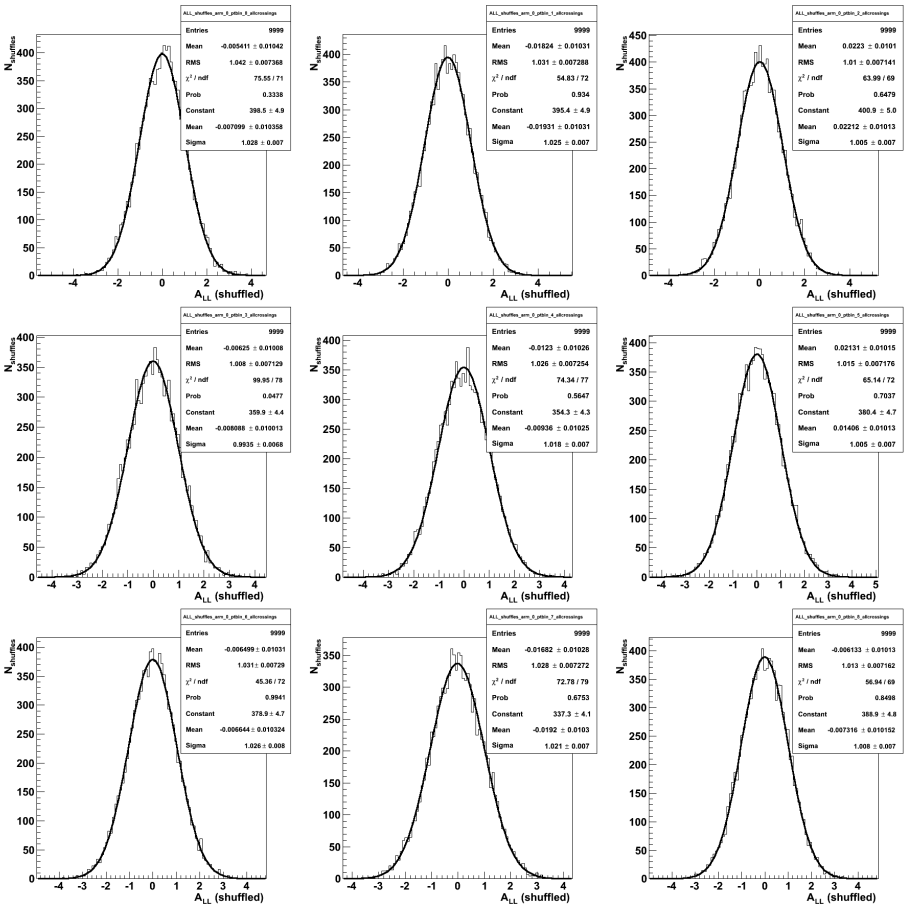

Figure B.22: Bunch shuffling results for $A_{LL}^{clus.}$ in the MPC South for all crossings; each plot is one p_T bin.

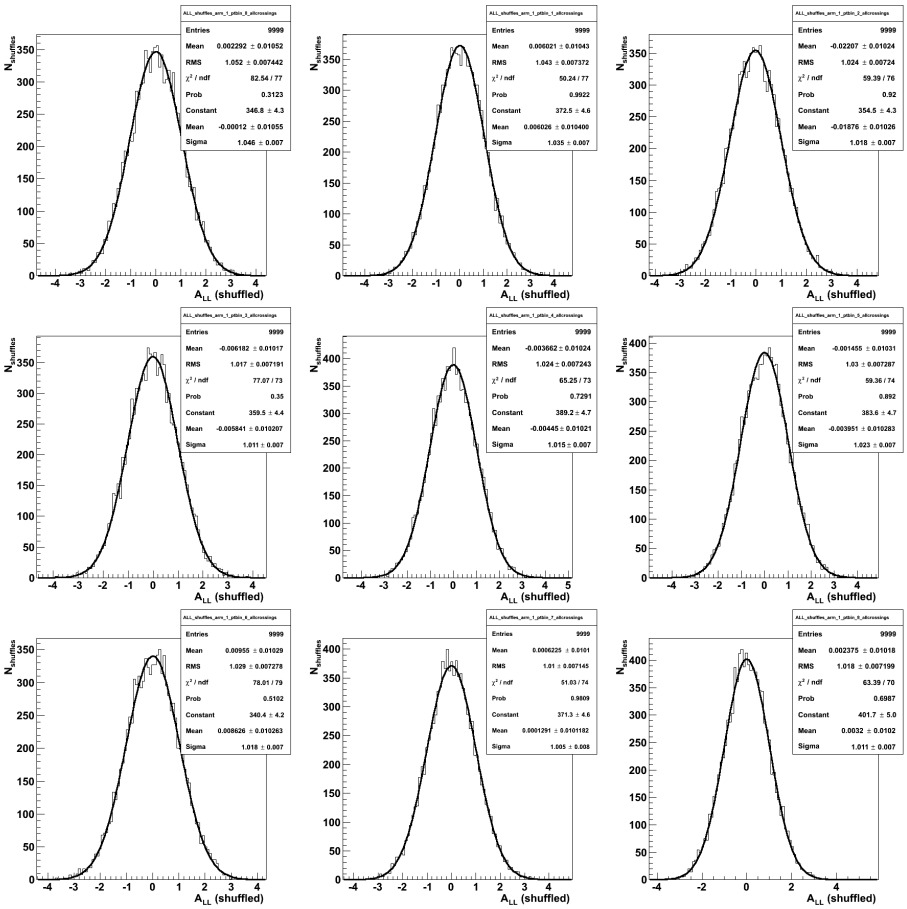

Figure B.23: Bunch shuffling results for $A_{LL}^{clus.}$ in the MPC North for all crossings; each plot is one p_T bin.

Bibliography

[1] Joseph John Thomson. XL. Cathode rays. *The London, Edinburgh, and Dublin Philosophical Magazine and Journal of Science*, 44(269):293–316, 1897.

[2] Joseph John Thomson. XXIV. On the structure of the atom: an investigation of the stability and periods of oscillation of a number of corpuscles arranged at equal intervals around the circumference of a circle; with application of the results to the theory of atomic structure. *The London, Edinburgh, and Dublin Philosophical Magazine and Journal of Science*, 7(39):237–265, 1904.

[3] Hans Geiger and Ernest Marsden. On a diffuse reflection of the α-particles. *Proceedings of the Royal Society of London. Series A, Containing Papers of a Mathematical and Physical Character*, 82(557):495–500, 1909.

[4] Ernest Rutherford. LXXIX. The scattering of α and β particles by matter and the structure of the atom. *The London, Edinburgh, and Dublin Philosophical Magazine and Journal of Science*, 21(125):669–688, 1911.

[5] Ernest Rutherford. LVII. The structure of the atom. *The London, Edinburgh, and Dublin Philosophical Magazine and Journal of Science*, 27(159):488–498, 1914.

[6] Ernest Rutherford. LIV. Collision of α particles with light atoms. IV. An anomalous effect in nitrogen. *The London, Edinburgh, and Dublin Philosophical Magazine and Journal of Science*, 37(222):581–587, 1919.

[7] Otto Stern. The method of molecular rays. Nobel lecture., 1946. `http://www.nobelprize.org/nobel_prizes/physics/laureates/1943/stern-lecture.pdf`.

[8] Martin Breidenbach, Jerome I Friedman, Henry W Kendall, et al. Observed behavior of highly inelastic electron-proton scattering. *Physical Review Letters*, 23(16):935, 1969.

[9] Richard P Feynman and Murray Gell-Mann. Theory of the Fermi interaction. *Physical Review*, 109(1):193, 1958.

[10] M. Gell-Mann. A schematic model of baryons and mesons. *Physics Letters*, 8(3):214–215, Feb 1964.

[11] George Zweig. An SU (3) model for strong interaction symmetry and its breaking. Version 1, 1964. `http://cds.cern.ch/record/570209/files/CERN-TH-412.pdf`.

[12] John Ellis. The discovery of the gluon. *International Journal of Modern Physics A*, 29(31), 2014.

[13] Xiangdong Ji, Jian-Hui Zhang, and Yong Zhao. Justifying the naive partonic sum rule for proton spin. *Physics Letters B*, 743:180–183, 2015.

[14] David Griffiths. *Introduction to elementary particles*. John Wiley & Sons, 2008.

[15] Francis Halzen and Alan D Martin. *Quark & Leptons: An Introductory Course In Modern Particle Physics*. John Wiley & Sons, 2008.

[16] Bogdan Povh, Martin Lavelle, Klaus Rith, Christoph Scholz, and Frank Zetsche. *Particles and nuclei: an introduction to the physical concepts*. Springer Science & Business Media, 2008.

[17] Gerry Bunce, Naohito Saito, Jacques Soffer, and Werner Vogelsang. Prospects for spin physics at RHIC. *Annual Review of Nuclear and Particle Science*, 50(1):525–575, Dec 2000.

[18] Werner Vogelsang. The spin structure of the nucleon. *Journal of Physics G: Nuclear and Particle Physics*, 34(7):S149, 2007.

[19] V.N. Gribov and L.N. Lipatov. Deep inelastic e p scattering in perturbation theory. *Sov.J.Nucl.Phys.*, 15:438–450, 1972.

[20] Guido Altarelli and G Parisi. Asymptotic freedom in parton language. *Nuclear Physics B*, 126(2):298–318, 1977.

[21] YL Dokshitzer. Calculation of the structure functions for deep inelastic scattering and e+ e- annihilation by perturbation theory in quantum chromodynamics. *Sov. Phys. JETP*, 46(4):641, 1977.

[22] Daniel de Florian, Rodolfo Sassot, Marco Stratmann, and Werner Vogelsang. Extraction of Spin-Dependent Parton Densities and Their Uncertainties. *Phys.Rev.*, D80:034030, 2009.

[23] M Glück, E Reya, M Stratmann, and W Vogelsang. Models for the polarized parton distributions of the nucleon. *Physical Review D*, 63(9):094005, 2001.

[24] Kieran Peter Boyle. *Measurements of the double helicity asymmetry in pion production in proton collisions s**(1/2) = 200-GeV and the resulting constraints on the polarized gluon distribution in the proton*. PhD thesis, SUNY, Stony Brook, 2008-05.

[25] J.F. Owens, A. Accardi, and W. Melnitchouk. Global parton distributions with nuclear and finite-Q^2 corrections. *Phys.Rev.*, D87(9):094012, 2013.

[26] H Hahn, E Forsyth, H Foelsche, et al. The RHIC design overview. *Nuclear Instruments and Methods in Physics Research Section A: Accelerators, Spectrometers, Detectors and Associated Equipment*, 499(2):245–263, 2003.

[27] M Harrison, T Ludlam, and S Ozaki. RHIC project overview. *Nuclear Instruments and Methods in Physics Research Section A: Accelerators, Spectrometers, Detectors and Associated Equipment*, 499(2):235–244, 2003.

[28] MJ Tannenbaum. Highlights from BNL-RHIC. *arXiv preprint arXiv:1201.5900*, 2012.

[29] Run Overview of the Relativistic Heavy Ion Collider. `http://www.rhichome.bnl.gov/RHIC/Runs/`.

[30] I Alekseev, C Allgower, M Bai, et al. Polarized proton collider at RHIC. *Nuclear Instruments and Methods in Physics Research Section A: Accelerators, Spectrometers, Detectors and Associated Equipment*, 499(2):392–414, 2003.

[31] K Adcox, SS Adler, M Aizama, et al. PHENIX detector overview. *Nuclear Instruments and Methods in Physics Research Section A: Accelerators, Spectrometers, Detectors and Associated Equipment*, 499(2):469–479, 2003.

[32] K Ikematsu, Y Iwata, K Kaimi, et al. A start-timing detector for the collider experiment PHENIX at RHIC-BNL. *arXiv preprint physics/9802024*, 1998.

[33] Clemens Adler, Alexei Denisov, Edmundo Garcia, et al. The RHIC zero degree calorimeters. *Nuclear Instruments and Methods in Physics Research Section A: Accelerators, Spectrometers, Detectors and Associated Equipment*, 470(3):488–499, 2001.

[34] Stephen Scott Adler, M Allen, G Alley, et al. PHENIX on-line systems. *Nuclear Instruments and Methods in Physics Research Section A: Accelerators, Spectrometers, Detectors and Associated Equipment*, 499(2):560–592, 2003.

[35] Rene Brun and Fons Rademakers. ROOT–an object oriented data analysis framework. *Nuclear Instruments and Methods in Physics Research Section A: Accelerators, Spectrometers, Detectors and Associated Equipment*, 389(1):81–86, 1997.

[36] H.J. Crawford, F.S. Bieser, and T. Stezelberger. The STAR Scaler Board, A 10 MHz 24-bit VME Memory Module. `http://www.star.bnl.gov/public/trg/TSL/Manual/scaler_paper.pdf`.

[37] John Koster. *Measurement of Transverse Spin Asymmetries in Polarized Proton-Proton Collisions and the Realization of New Electromagnetic Calorimeters for Forward Physics.* PhD thesis, University of Illinois at Urbana-Champaign, 2010.

[38] M. Chiu et al. Muon Piston Calorimeter Letter of Intent, 2005. `https://www.phenix.bnl.gov/WWW/p/draft/chiu/mpc/MPC_LOI_v3.pdf`.

[39] Christian W Fabjan and Fabiola Gianotti. Calorimetry for particle physics. *Reviews of Modern Physics*, 75(4):1243, 2003.

[40] William R Leo. Techniques for Nuclear and Particle Physics Experiments. *Dr155*, 1990.

[41] J. Koster, M. Chiu, and A. Kazantsev. MPC Run 08 Monitoring System. PHENIX Technical Note 440.

[42] L Aphecetche, TC Awes, J Banning, et al. PHENIX calorimeter. *Nuclear Instruments and Methods in Physics Research Section A: Accelerators, Spectrometers, Detectors and Associated Equipment*, 499(2):521–536, 2003.

[43] M. Chiu, M. Grosse Perdekamp, A. Kazantsev, J. Koster, and B. Meredith. MPC Clustering: Description, Performance, and Comparison of Run8 p+p Data and Simulation. PHENIX Analysis Note 949.

[44] Elke-Caroline Aschenauer, Alexander Bazilevsky, K Boyle, et al. The RHIC spin program: achievements and future opportunities. *arXiv preprint arXiv:1304.0079*, 2013.

[45] L. Adamczyk et al. Longitudinal and transverse spin asymmetries for inclusive jet production at mid-rapidity in polarized p+p collisions at s= 200 GeV. *Physical Review D*, 86(3):032006, 2012.

[46] Djawotho, P. for the STAR Collaboration. Gluon polarization and jet production at STAR. *arXiv preprint arXiv:1303.0543*, 2013.

[47] A Adare, S Afanasiev, C Aidala, et al. Inclusive cross section and double helicity asymmetry for π 0 production in p+ p collisions at s= 62.4 GeV. *Physical Review D*, 79(1):012003, 2009.

[48] A Adare, S Afanasiev, C Aidala, et al. Gluon-Spin Contribution to the Proton Spin from the Double-Helicity Asymmetry in Inclusive π 0 Production in Polarized p+ p Collisions at s= 200 GeV. *Physical review letters*, 103(1):012003, 2009.

[49] A. Adare et al. Inclusive double-helicity asymmetries in neutral-pion and eta-meson production in p + p collisions at s= 200 GeV. *Physical Review D*, 90(1):012007, 2014.

[50] B. Meredith. *A Study of Nuclear Effects Using Forward-Rapidity Hadron Production and Di-hadron Angular Correlations in* $\sqrt{S_{NN}}$ *= 200 GeV d+Au and p+p Collisions with the PHENIX Detector at RHIC.* PhD thesis, University of Illinois at Urbana-Champaign, 2011.

[51] Torbjörn Sjöstrand, Stephen Mrenna, and Peter Skands. PYTHIA 6.4 physics and manual. *Journal of High Energy Physics*, 2006(05):026, 2006.

[52] Anne M Sickles, PHENIX Collaboration, et al. The next decade of physics with PHENIX. *Journal of Physics G: Nuclear and Particle Physics*, 38(12):124129, 2011.

[53] O Martin and A Schafer. $\Delta G(x, \mu^2)$ from jet and prompt photon production at RHIC. *arXiv preprint hep-ph/0005320*, 2000.

[54] Robert L Jaffe and Nobuhiko Saitô. QCD selection rules in polarized hadron collisions. *Physics Letters B*, 382(1):165–172, 1996.

[55] Jonathan Pumplin, Daniel Robert Stump, Joey Huston, et al. New generation of parton distributions with uncertainties from global QCD analysis. *Journal of High Energy Physics*, 2002(07):012, 2002.

[56] K. Boyle, A. Deshpande, and P. Kline. Relative Luminosity in Run9 Polarized p+p Collisions at $sqrts = 200GeV$. PHENIX Analysis Note 881.

[57] A. Manion. Method For Determining Relative Luminosity From Detection Probabilities (Run9 200 GeV). PHENIX Analysis Note 953.

[58] M. Chiu, M. Grosse Perdekamp, and S. Wolin. New Ideas on Relative Luminosity Determination in Run09 500 GeV Polarized Proton Collisions. PHENIX Analysis Note 1184.

[59] G. Aad et al. Luminosity Determination in pp Collisions at sqrt(s)=7 TeV Using the ATLAS Detector at the LHC. *Eur.Phys.J.C*, 71:1630,2011, January 2011.

[60] RHIC Spin Collaboration. Run 11 Polarization, 2012. https://wiki.bnl.gov/rhicspin/Run_11_polarization.

[61] K. Boyle and A. Manion. Beam Angles at PHENIX: A Systematic Study at *sqrts* = 200 GeV in Run12 p+p. PHENIX Analysis Note 1028.

[62] P. Kline. Run 11 Vernier Scan Update, 2011. PHENIX Spin PWG Presentation. https://www.phenix.bnl.gov/cdsagenda/askArchive.php?base=agenda&categ=a11519&id=a11519s1t1/moreinfo.

[63] M. Chiu, M. Grosse Perdekamp, J. Koster, B. Meredith, and S. Wolin. Muon Piston Calorimeter Calibration. PHENIX Analysis Note 927.

[64] Rene Brun, Federico Carminati, Simone Giani, et al. GEANT detector description and simulation tool. *CERN program library long writeup W*, 5013:1993, 1993.

[65] S. Wolin. *Measuring the Contribution of Low Bjorken-x Gluons to the Proton Spin with Polarized Proton-Proton Collisions*. PhD thesis, University of Illinois at Urbana-Champaign, 2013.

[66] A Accardi, JL Albacete, M Anselmino, et al. Electron Ion Collider: The Next QCD Frontier-Understanding the glue that binds us all. *arXiv preprint arXiv:1212.1701*, 2012.